Numerical Studies on the Influence of Dissipative Effects on Electromechanical Properties of Dielectric Polymers

Zur Erlangung des akademischen Grades Doktor-Ingenieur (Dr.-Ing.)
genehmigte Dissertation von Dagmar Eder-Goy aus Arheilgen
Tag der Einreichung: 13.02.2019, Tag der Prüfung: 04.06.2019
Darmstadt — D 17

1. Gutachten: Prof. Bai-Xiang Xu
2. Gutachten: Prof. Dietmar Gross

TECHNISCHE UNIVERSITÄT DARMSTADT

MECHANICS of FUNCTIONAL MATERIALS

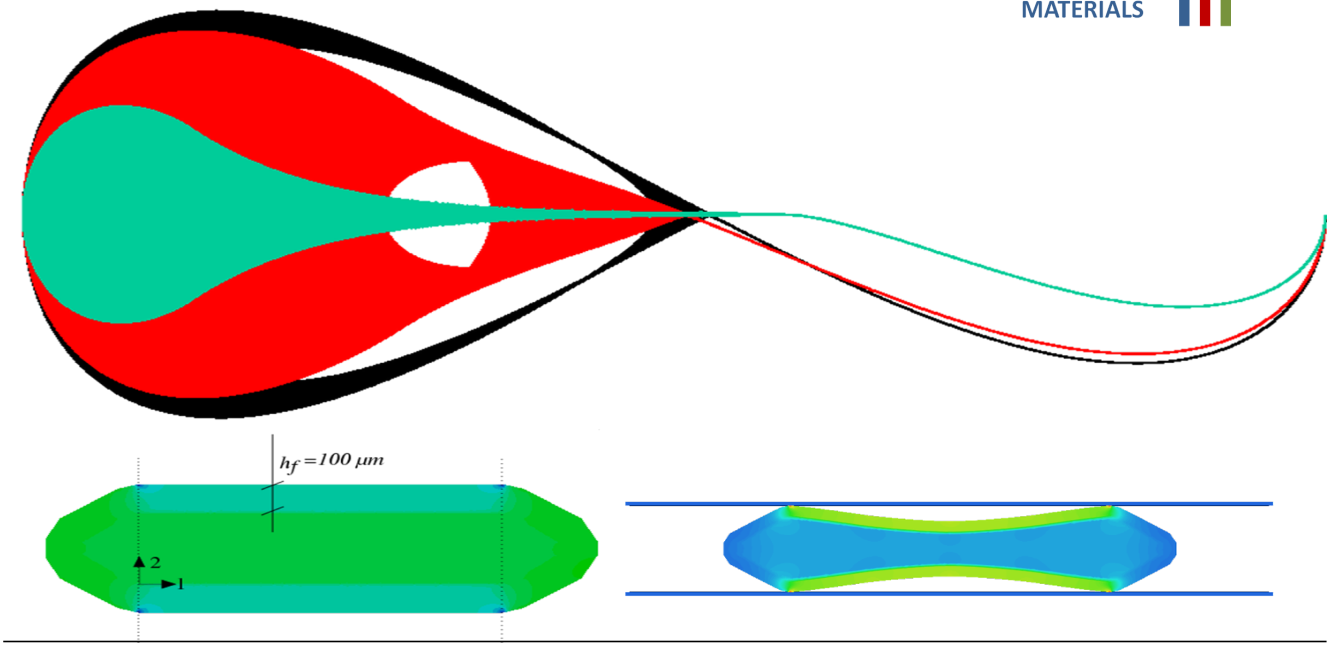

Numerical Studies on the Influence of Dissipative Effects on Electromechanical Properties of Dielectric Polymers

Genehmigte Dissertation von Dagmar Eder-Goy aus Arheilgen

1. Gutachten: Prof. Bai-Xiang Xu
2. Gutachten: Prof. Dietmar Gross

Tag der Einreichung: 13.02.2019
Tag der Prüfung: 04.06.2019

Darmstadt — D 17

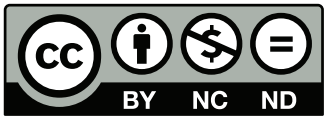

Contents

Erklärung zur Dissertation

Hiermit versichere ich, die vorliegende Dissertation ohne Hilfe Dritter nur mit den angegebenen Quellen und Hilfsmitteln angefertigt zu haben. Alle Stellen, die aus Quellen entnommen wurden, sind als solche kenntlich gemacht. Diese Arbeit hat in gleicher oder ähnlicher Form noch keiner Prüfungsbehörde vorgelegen.

Darmstadt, den November 3, 2019

(Dagmar Eder-Goy)

Abstract

Dielectric polymers find an increased interest in research and development due to an intensive demand of soft and flexible materials for electromechanical components. Dielectric polymers are excellent energy converters because of high efficiency and energy density and have a vast area of application; primarily, they are used in sensors and actuators. Due to tissue-like deformation properties, they are applied for artificial muscles, prosthesis or implants, and are suitable for wearable and foldable electronics. In this work, the viscoelastic behaviour of dielectric polymers is focussed, the frequently investigated acrylic elastomer VBH49, which shows a pronounced viscous deformation, was chosen as material example.

A rectangular, dielectric elastomer membrane with compliant electrodes was selected as an example for an actuator. Static and dynamic, voltage-controlled deformation of this idealised dielectric elastomer actuator (DEA) is investigated numerically. Moreover, a global, structural failure mode called “Pull-in instability“ is examined with regard to pre-stretch and viscous effects. The Euler-Lagrange formalism is used at this to obtain equation of motion and viscous evolution equation. Using an energy approach, a stability analysis is conducted to determine the critical parameters for instantaneous and time-delayed dynamic Pull-in. The impact of cross-linking on dynamic deformation is investigated using a viscoelastic Arruda-Boyce material.

Continuum mechanical models for electro-viscoelastic behaviour of solid dielectrics, based on a coupling of electrostatic and mechanical stress, are formulated and implemented for small and large deformation applying the Hooke and St.Vernant material law. Numerical solutions for a split of energy function and deformation gradient into elastic and viscoelastic fractions are investigated in reference to a similar split of the stress tensor. Benchmark tests are carried out to validate the models.

Non-polar dielectric polymers are used for the manufacturing of pseudo-piezoelectric structures denoted as ferro- or piezoelectrets. Ferroelectrets show piezo- and inverse piezoelectric properties after an electric poling, whereby charge is trapped in the interface of layers with different susceptibility. In this work, ferroelectret structures consisting of air-filled polymer cells from fluorinated ethylene propylene (FEP) are investigated. In contrast to piezoceramics, these ferroelectrets are flexible and allow large deformation; due to their ultra-softness they are suitable for applications activated by sound or vibration. The micro-cellular ferroelectret structures, with measured d_{33} piezoelectric coefficients up to $160\,\mathrm{pC\,N^{-1}}$, are analysed by means of Finite-Element simulation. A volume interface element is formulated therefore to map the charging process and the behaviour under compression. The influence of geometry and mechanical boundary conditions on the effective Young’s modulus and the d_{33} coefficient is studied using a linear model. Electrical and mechanical field distributions are analysed finally for three geometries that either replicate a real cell structure, a simple rectangular structure, or a structure gained from the simulation of FEP-tube compression.

Zusammenfassung

Aufgrund der intensiven Nachfrage nach weichen und flexiblen, elektromechanischen Bauteilen, erfahren elektroaktive Polymere (EAPs) vermehrtes Interesse im Bereich Forschung und Entwicklung. Wegen ihrer hohen Energiedichte und ihres hohen Wirkungsgrades sind sie exzellente Energiewandler. EAPs finden Anwendung im Bereich Sensoren, Aktuatoren und Generatoren; sie können in künstlichen Muskeln, Prothesen und Implantaten, sowie in trag- und faltbarer Elektronik eingesetzt werden. In dieser Arbeit wurde das zur Gruppe der elektronischen EAPs zugehörige Acrylatelastomer VHB49 als Materialbeispiel für einen dielektrischen Elastomeraktuator (DEA) ausgewählt.

Untersucht wird das elektrisch aktivierte, statische und dynamische Verformungsverhalten dieses idealisierten Aktuators, bestehend aus einer Elastomermembran und nachgiebigen Elektroden. Ferner wird ein globaler, struktureller Versagensmodus, bezeichnet als „Pull-in Instabilität“, in Hinblick auf den Einfluss von Vorspannung und viskosen Effekten analysiert. Der Euler-Lagrange Formalismus wird verwendet, um die Bewegungsgleichung des Systems und eine Evolution für die viskose Streckung zu ermitteln. Der Einfluss der Molekülkettenvernetzung auf die dynamische Verformung wird anhand eines viskoelastischen Arruda-Boyce Materials untersucht. Ausgehend von der freien Energie des Systems wird zur Bestimmung der kritischen Parameter für instantanen oder zeitverzögerten Pull-in eine Stabilitätsanalyse durchgeführt.

Elektro-viskomechanische Materialmodelle, basierend auf einer Kopplung zwischen elektrostatischer und mechanischer Spannung, werden für kleine und große Verformungen unter Verwendung von Hooke und St.Vernant Material formuliert. Die Modelle für kleine Deformationen dienen hierbei als Referenz für den Vergleich mit experimentellen Ergebnissen. Der Einfluss auf die numerische Lösung bei einer Zerlegung des Spannungstensors in elastische- und viskoelastische Anteile wird im Vergleich zu einer entsprechenden Zerlegung von Energiefunktion und Deformationsgradient untersucht. Hierfür werden Benchmark Tests durchgeführt.

Nonpolare dielektrische Elastomere werden zur Herstellung von pseudo-piezoelektrischen Materialen, sogenannten Ferro- oder Piezoelektrets verwendet. Diese Materialien zeigen piezo- und invers piezoelektrische Effekte nach einer elektrischen Polung, bei der freie Ladung in den Grenzflächen zwischen Schichten mit unterschiedlicher Suszeptibilität eingeschlossen wird. In dieser Arbeit wird eine Ferroelektretstruktur bestehend aus luftgefüllten Polymerzellen aus dem Fluorcopolymer Tetrafluorethylen-Hexfluorpropylen-Copolymer (FEP) untersucht. Im Gegensatz zu Piezokeramiken sind diese Materialien flexibel und hochgradig deformierbar. Aufgrund ihrer Weichheit eignen sie sich für Anwendungen die durch Schall- oder Vibrationswellen aktiviert werden. Die mikrozellularen Ferroelektrestrukturen, mit d_{33} Koeffizienten bis $160\,\mathrm{pC\,N^{-1}}$, werden unter Verwendung von Finite-Elemente Simulationen analysiert. Zur Abbildung des Polarisierungsprozesses und des Verhaltens unter mechanischer Kompression wird ein Volumengrenzflächenelement zur Steuerung der Grenzflächenpolarisation formuliert.

Der Einfluss von Geometrie und mechanischen Randbedingungen auf den effektiven E-Modul und den d_{33} Koeffizienten wird mit einem linearen Modell untersucht. Abschließend werden elektrische und mechanische Feldgrößenverteilungen anhand dreier Zellgeometrien, einer idealen Zelle, die eine reale Struktur abbildet, einer rechteckigen Zelle und einer virtuellen Zelle, basierend auf Verformungssimulationen von FEP-Röhrchen, untersucht.

Acknowledgements

I would like to express my deep gratitude to Prof. Bai-Xiang Xu for giving me the possibility to work within the group Mechanics of Functional Materials. I would like to offer my special thanks to Prof. Dietmar Gross for the spontaneous willingness to serve as co-referee and for helpful suggestions. I would also like to extend my thanks to Prof. Ralf Müller and Prof. Karsten Durst to be my auditors. I like to thank Prof. Heinz von Seggern for his strategical understanding and scientific passion and especially Dr. Sergey Zhukov who supported my work and barrier-free research. I would like to acknowledge the Deutsche Forschungsgemeinschaft (DFG) for financial support. Special thanks to my colleagues Dr. Peter Stein, the administrator of my computer, Prof. Min Yi, Dr. Yangbin Ma, Dr. Shuai Wang and Mammun Al-Siraj. I would also like to thank Prof. Wolfgang Ensinger for the temporary place of work and the support by his working group and Dipl.-Ing Hansgeorg Haupt for the invitations. I am particularly grateful to Bell who encouraged me and Eckhard who helped in linguistic questions. Finally, I'd like to thank my husband Oliver, my daughter Janne, my son Jonas and grandmas for food and child care.

List of symbols and abbreviations

$\cdot$	scalar product between two vectors
:	scalar product between two tensors
$\otimes$	dyadic product
ε_f	strain in direction of electric field
ε	component of linearised strain tensor
$\boldsymbol{\varepsilon}$	linearised strain tensor
$\overline{\varepsilon}$	mean value of a strain component
E	electric field component
Y	Young's modulus
$Y^{'}$	storage part of complex Young's modulus
$Y^{''}$	loss part of complex Young's modulus
Y_{E}	effective Young's modulus of a ferroelectret cell
μ	shear modulus, Lamé constant
μ, G	shear modulus
$G^{'}$	storage part of complex shear modulus
$G^{''}$	loss part of complex shear modulus
K	bulk modulus
p_A	actuation pressure
A	surface
U_e	electrostatic energy
V_{B}	breakdown voltage
χ_s	susceptibility
ϵ_0	vacuum permittivity
ϵ_r	relative permittivity
$\mathbf{F}_{\mathrm{c}}$	Coulomb force vector

q	point charge
ρ_f	averaged charge density free charges
ρ_p	averaged charge density polarisation charges
ρ	total averaged charge density current configuration
ρ_0	total averaged charge density reference configuration
ϕ	electrostatic potential
ϕ_{max}	peak value of a time function of an electrostatic potential
$\mathbf{E}, \mathbf{E}_0$	electric field vector current configuration, reference configuration
E_c	critical electric field
$\boldsymbol{\sigma}^{\text{E}}$	Maxwell stress tensor, assuming linear theory
$\mathbf{S}^{\text{E}}$	Maxwell stress tensor, assuming non-linear theory
$\mathbf{P}$	polarisation vector
$\mathbf{P}_{\text{O}}$	orientation polarisation vector
$\mathbf{D}, \mathbf{D}_0$	dielectric displacement vector current configuration, reference configuration
σ, p	surface charge density
$\mathbf{x}, \mathbf{X}$	position vector current configuration, reference configuration
$\mathbf{u}, \mathbf{U}$	displacement vector current configuration, reference configuration
$\mathbf{1}$	unit tensor second order
$\mathbb{1}$	unit tensor fourth order
$\mathbf{F}$	deformation gradient
$\mathbf{F}_{\text{pre}}$	deformation gradient due to pre-stretch
$\hat{\mathbf{F}}$	deviatoric part deformation gradient
$\hat{\mathbf{F}}_{\text{e}_\alpha}$	deviatoric part deformation gradient Maxwell element
$\hat{\mathbf{F}}_{\text{v}_\alpha}$	deviatoric part deformation gradient dashpot
J	determinant of $\mathbf{F}$
χ	push-forward
χ^{-1}	push-backward
$\mathbf{h}, \mathbf{H}$	displacement gradient tensor current configuration, reference configuration
$\mathbf{l}$	velocity gradient tensor current configuration

$d\mathbf{x}, d\mathbf{X}$	line element current configuration, reference configuration
$d\mathbf{s}, d\mathbf{S}$	surface element current configuration, reference configuration
$d\mathbf{v}, d\mathbf{V}$	volume element current configuration, reference configuration
$\mathbf{R}$	rotation tensor
$\mathbf{U}$	right stretch tensor
$\mathbf{v}$	left stretch tensor
$\mathbf{C}$	right Cauchy-Green deformation tensor
$\mathbf{b}$	left Cauchy-Green deformation tensor
$\mathbf{A}$	Green-Lagrange strain tensor
$\mathbf{a}$	Euler-Almansi strain tensor
$\hat{\mathbf{H}}$	Hencky strain tensor reference configuration
$\mathbf{S}$	2.Piola-Kirchhoff stress tensor
$\mathbf{S}_\infty$	time-independent part of the 2.Piola-Kirchhoff stress tensor
$\mathbf{S}_\mathrm{v}$	time-dependent, viscous part of the 2.Piola-Kirchhoff stress tensor
$\mathbf{P}$	1.Piola-Kirchhoff stress tensor
$\boldsymbol{\tau}$	Kirchhoff stress tensor
$\mathscr{L}_\mathrm{v}$	Lie time derivative
m	mass
ρ	density
$\mathbf{v}, \mathbf{V}$	velocity vector current configuration, reference configuration
$\mathbf{L}$	linear momentum
$\mathbf{J}$	angular momentum
$\mathbf{M}$	momentum
$\mathbf{F}_\mathrm{m}$	mechanical force
$\sum F_\mathrm{reac}$	sum of reaction forces
$\mathbf{t}$	Cauchy vector
$\mathbf{b}, \mathbf{B}$	body force vector current configuration, reference configuration
E_kin	kinetic energy
E_pot	potential energy

$\mathrm{E}_{\mathrm{ext}}$	external energy
G	thermal energy
g_n, G_n	heat flux over surface current configuration, reference configuration
r, R	heat source current configuration
$\mathbf{n}, \mathbf{N}$	normal vector current configuration, reference configuration
$\mathrm{P}_{\mathrm{int}}$	internal mechanical work
Γ	total entropy production
$\tilde{\mathrm{G}}$	rate of entropy input
Θ	absolute temperature
s_c, s	specific entropy current configuration, reference configuration
S	entropy
u	specific internal energy density
$\tilde{\mathrm{U}}$	internal energy
u	internal energy density
$\tilde{\mathrm{F}}$	Helmholtz free energy
$\tilde{\mathrm{H}}$	enthalpy
$\tilde{\mathrm{G}}$	Gibbs free enthalpy
T	temperature
$\mathbf{X}_{\mathrm{v}}$	viscous internal variable
$\mathscr{D}$	dissipation
$\mathscr{D}_\Theta$	thermal dissipation
$\mathscr{D}_{\mathrm{v}}$	viscous dissipation
Ψ	free energy
Ψ_0	hyperelastic free energy
Ψ_{el}	vacuum part of electric free energy
Ψ_{P}	polarisation part of electric free energy
$\Psi_{\mathrm{P_v}}$	visco-electric part of electric free energy
Ψ_{v}	visco-hyperelastic or viscoelastic free energy
$\mathbf{C}_{\mathrm{v}}$	viscous right Cauchy-Green deformation tensor

$\boldsymbol{\tau}_{\mathrm{v}}$	viscous part of Kirchhoff stress
$\mathbf{b}_{\mathrm{e}_\alpha}$	tensor of elastic strain in a Maxwell element, current configuration
$\mathbf{M}_\nu$	Mandel type referential stress
T	relaxation time
η	shear viscosity
η_E	elongation viscosity
φ_0	fluidity
η_0	viscosity after infinite time
τ	shear stress
γ	shear strain
α_T	thermal expansion
C	heat capacity
T_g	glass transition temperature
T_s	melting temperature
t	time
$J(t)$	creep function
$G(t)$	relaxation function
l_d	deformation-dependent load
W	work done by external load
β	positive factor > 0, determing the proportion of viscous stiffness in relation to total stiffness
γ	positive factor > 0, determing the proportion of dissipative resistance to total resistance
H, L	geometry parameters
λ	stretch, chain stretch, Lamé constant
λ_{pe}	pre-stretch
λ_ν	viscous stretch
λ_c	critical stretch
λ_f	stretch at failure
t_f	time until failure

c_1, c_2	constants
P	external load
N	number of cross-links
Λ	chain stretch
Λ_v	viscous part of chain stretch
r	chain length
r_0	chain length undeformed chain
I_1	first invariant of left Cauchy-Green tensor
$\overline{h}$	mean value of displacement in compression direction
Δ	time interval
$\mathbb{C}$	fourth order elasticity tensor, elasticity tensor St.Vernant material
E_{B}	electric breakdown field
E_{m}	electric field component perpendicular to an interface

1 Introduction

Electroactive polymers (EAPs) play an important role as material for electromechanical components. EAPs are subdivided into ionic and electronic EAPs, distinguished by their chemical bond. In conductive, ionic EAPs [1, 2], free ions are transported due to diffusion processes. Electronic EAPs [3] exhibit spontaneous or permanent dipoles where the electric charge is locally fixed. The electroactive behaviour is caused by slight displacement or rotation of charge, called, dielectric displacement. Electrostrictive, ferroelectric, as well as dielectric elastomers belong to this group whereby the first two types require a crystal lattice. The latter type includes amorphous polymers. Dielectric elastomer (DE) denotes primarily amorphous, cross-linked polymers that are interesting due to superb and reversible, hyperelastic deformability even for large deformation. Since the deformation behaviour of DEs is similar to that of human tissue, they are appropriate for artificial muscles in robots, implants in human bodies, prostheses, wearable, and foldable electronics.

Most DEs are viscoelastic what is observable in a time-dependent creep- and relaxation behaviour and goes along with a dissipation of energy. The cause of macroscopic viscous phenomena is a readjustment of the thermodynamic equilibrium, which can be described by the mechanism of non-Fickian diffusion. Dielectric dissipation in polar or polarised DEs, which is orientation or re-orientation of dipoles or charge, is a mechanism that takes place in a measurable time interval. Continuum mechanical models to describe viscoelastic dissipation are well known for elastic and hyperelastic materials, whereas models to describe transient viscous and dielectric processes simultaneously are rare.

It is verified that viscoelastic and dielectric dissipation can be formulated using similar mathematical expressions by assuming an “ideal“ dielectric; in an ideal dielectric there is no interaction between identical dipoles and relaxation times are equal for all dipoles [4]. Dielectric dissipation can be described then by a relation formulated by Debye in 1913, known also as Debye relaxation that defines a linear rate for orientation polarisation [5]. A linear evolution equation for the viscous strain is given by the Maxwell element, which represents a standard component in rheological models.

Most polymers are not ideal concerning the dipole interaction. In such cases, dielectric dissipation is described by alternatives to Debye, e.g. Cole-Cole, Havriliak–Negami, which reproduce special functions of loss and storage moduli of permittivity. What is more, specific dissipation functions can be found by dielectric impedance spectroscopy (DIS) including several methods. DIS can be used to determine frequency-dependent, relative dielectric constants [6]. For the determination of frequency-dependent, viscoelastic parameters, like relaxation time and Young’s modulus, dynamic mechanical analysis (DMA) can be applied [7]. Using this method, samples are tested at fixed frequency by variation of temperature or vice versa. Dielectric and viscous parameters are recorded for a small frequency or temperature range

and are extrapolated using the Williams-Landel-Ferry (WLF) relation [8] or approaches based on the Arrhenius function.[1]

It is well known that dielectric and viscous relaxation behaviour is strongly influenced by the microstructure.[2] An individual consideration of the polymeric material is therefore relevant when material models are developed [9, 10]. Since this work has a numerical orientation, experimental characterisation of materials is beyond the author's working scope. The model structure is therefore kept simple to demonstrate an approach and to acquire a reference.[3]

Two materials are focussed, the amorphous, polar, acrylic dielectric elastomer VHB49, produced by 3M, was chosen since extensive scientific data and results are available in literature so that for an access to the subject of this thesis a detailed picture can be placed in the background. The copolymer fluorinated ethylene propylene (FEP) is a variant of Teflon with a lower melt viscosity. The thermoplastic, nearly crystalline polymer, is non-polar and was used in the ferroelectret structures investigated in this work in chapter 7 and 6. Since this work is in the theoretical realm material parameters are obtained from literature which is assumed to be verified.

The thesis is structured as follows: Chapter 1 includes the argumentation of motives of this work. Following, physical properties of focussed materials are described and applications for dielectric polymers are introduced. In chapter 2, the underlying theory of electrostatics, mechanics, polymer physics and numerics is explained. A continuum mechanical description of a viscous, dielectric Neo-Hooke material is used to formulate the free energy of an ideal, pre-stretched dielectric elastomer actuator (DEA) in chapter 3. [4] Dynamic deformation and stability behaviour of the DEA is investigated for voltage-control by means of the equation of motion and critical values for Pull-in instability. An Arruda-Boyce material is analysed alternatively to estimate the influence of chain-cross-linking. Three different models, A, B, C for electro-viscoelasticity are introduced in chapter 4. A is a merely linear model, B and C are models for large deformation using a St.Vernant material where the stress-strain relation is still linear. In model B, the stress tensor, in model C, energy function and deformation gradient are split. A comparison between analytical and numerical solutions for types of model is presented by the analysis of benchmark tests under stress-, strain- and voltage-control. Chapter 5 introduces FE-models for the interface polarisation of polymeric ferroelectrets for small and large deformation. Chapter 6 is concerned with the analysis of structural effects like cell geometry and mechanical boundary conditions on the effective Young's modulus and the d_{33} coefficient of a ferroelectret cell, denoted as „ideal cell“, inspired by structures manufactured and experimentally investigated in the working group of Prof. Heinz von Seggern. An inward orientated pre-deformation that results from hot-forming is analysed by means of elasto-plastic Finite-Element simulation. Simulation results for “ideal cell“, and two other geometry variations, “rect-

[1] The equivalence of mathematical description of dielectric and viscous dissipation is used in the continuum mechanical formulation of electro-viscoelasticity in chapter 4.

[2] The specific molecule mass is an important parameter in this context.

[3] From the author's viewpoint it makes no sense to treat more sophisticated material descriptions if no experimental verification is at hand.

[4] Since experiments and calculations show that pre-stretching of electroactive membranes has an positive influence on the electromechanical performance and stability, the activation energy is reduced because of geometric effects [11], electric breakdown field is increased [12], and resonance frequencies can be shifted [13], the energy due to pre-stretch is included into free energy additionally.

angular cell“ and “virtual cell“, are presented in chapter 7. In chapter 8 results are finally summarised and an outlook is given.

1.1 Motivation

Numerical simulation based on the Finite-Element method has established as an successful tool in design processes for a variety of engineering disciplines. Its importance and effectiveness will be increased in future because of the improvement of computing power and the will for precision and cost saving by digitisation and automation. Precision and quality of a numerical solution depends to a great extent on the chosen material model. An intensive exploration of material behaviour and an adequate model formulation is therefore worthwhile. The acquisition of knowledge about continuum mechanical description and implementation of dissipative, time-dependent features of dielectric polymers is the overall intention of this thesis that is subdivided in four arguments.

1. High actuation voltage is necessary to activate dielectric polymer structures because permittivity of those materials is low. One possibility to increase the electric field and thus the deformation is a thickness reduction of the structure which leads to thin film applications. Besides electric breakdown, material and structural instabilities like polymer specific creasing and electro-creasing as well as global electromechanical buckling (Pull-in) determine the film thinness. Pull-in instability is a prominent failure mode and was examined by including inertia effects, for dynamic assumptions are closer to reality.

2. In the merely mechanical description of materials, a consideration of large deformation is state-of-the-art and already implemented in commercial software. The assumption of large deformation in context with dielectric polarisation is still object of research. A dissipative continuum model for large deformation orientation polarisation is therefore introduced.

3. A further motivation for this treatise was to have the possibility to estimate the piezoelectric coefficient of cellular ferroelectret structures by means of numerical simulation. Since in context with questions concerning the commercialisation of those structures, the time stability of piezoelectric coefficient is of great interest, and experiments have shown that the time stability of cellular ferroelectret structures is influenced by viscous and dielectric relaxation, a 3D model taking into account viscous and dielectric dissipation is formulated.

4. This treatise also serves as an evaluation for the proposed numerical models and as guide for the development of more specific material models.

1.2 Materials

The next two subsections introduce two polymers, FEP and VHB, that are relevant in the investigated context.

1.2.1 Fluoropolymer

The most prominent fluoropolymer is polytetrafluorethylen (PTFE), also denoted by the trade name Teflon [14]. PTFE is non-polar and the interaction of molecule chains is rather modest. PTFE behaves thermoplastically what is attributed to a crystalline fraction up to 98 %. It has a very high melt viscosity and a good heat resistance (T_s=325 °C-335 °C). PTFE is synthesised from chloroform. Rheological investigation of PTFE is outlined in Calleja et al. [15] where in particular the transition behaviour was examined. PTFE has two amorphous phases that relax at different glass transition temperatures of T_{g1}=−103 °C and T_{g2}=116 °C. Copolymers made of PTFE and other fluoropolymers with lower viscosity due to shorter molecules have been created to gain a better thermoplastic processability [16]. One of these polymers is the copolymer fluorinated ethylene propylene (FEP), which has a lower thermal resistivity (T_s=255 °C-285 °C) in comparison to PTFE, and exhibits a better temperature stability for electric charge. The Young's modulus is about 500 MPa. FEP is primarily used as cable insulation material. Its structural formula is

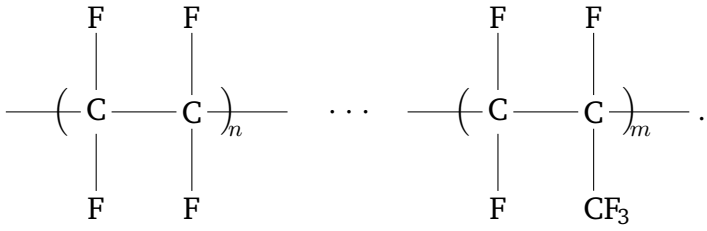

Figure 1.2.1.: Chemical structure of FEP.

The left part of the structural formula in Fig. 1.2.1, describes fluoroethylene where hydrogen atoms of ethylene are substituted by fluorine. The part on the right symbolises fluoropropylene where three hydrogen atoms are substituted by fluorine and one hydrogen atom by trifluoromethyl (CF_3). Cross-linking of FEP 100 by irradiation has been investigated in [17]. The irradiation shows different effects on the molecular structure. Cross-linking predominates over degradation for temperatures above the glass I transition. It has been reported that an increase of cross-links by irradiation has no influence on relative electric permittivity, which is in the order of 2 for room temperature, whereas viscosity is raised. This can be observed in the curve progressions in Fig. 1.2.2 which show higher shear stresses in the cross-linked material for a similar shearing rate. Shear-thickening flow behaviour of original and irradiated FEP is shown by the rising of curves before the turn-off point. Linear curve progression in the double-log plot indicates non-linear viscous behaviour of FEP.

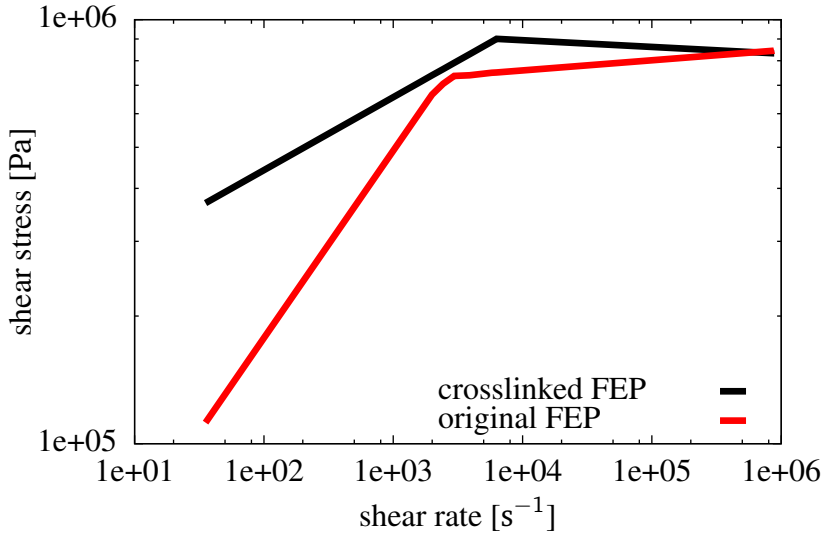

Figure 1.2.2.: Flow curve of original FEP 100 and cross-linked FEP, experimental results from [17].

1.2.2 Dielectric Elastomer

Dielectric elastomers (DEs) are discovered as attractive materials for soft sensors and actuators in the early 1990s [18, 19, 20]. Four polymer groups: acrylic elastomers, silicones, polyurethanes and natural rubber, have been intensively discussed in literature. A very good energy conversion or electromechanical performance was observed in particular for acrylic elastomers and silicones [21], which are compared in Capri et al. [22]. By Pelrine et al. [23], the electromechanical performance of a dielectric elastomer is defined by the compression ε_f of the elastomer that stores an energy U_e, and has the charges Q^+ and Q^- on opposite electrode surfaces A.

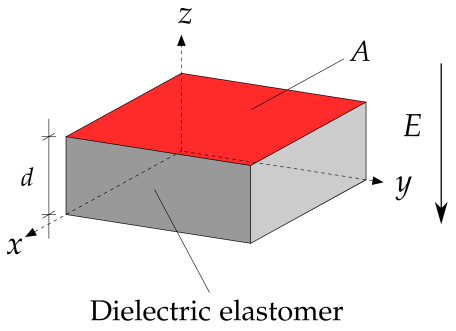

Figure 1.2.3.: Rectangular dielectric elastomer with thickness d and electrode surfaces A.

In case of a rectangular geometry with volume $V = Ad$, as shown in Fig. 1.2.3, the electrostatic energy is given by $U_e = 1/2\varepsilon E^2 Ad$, where $\varepsilon = \varepsilon_0\varepsilon_r$ is the permittivity of the elastomer and E is the electric field. A variation of the thickness $\mathrm{d}d$ changes the surface $\mathrm{d}A$ and the potential energy $\mathrm{d}U_e$

$$\mathrm{d}U_e = \frac{1}{2}\varepsilon E^2 A\,\mathrm{d}d - \frac{1}{2}\varepsilon E^2\,\mathrm{d}A\,d. \tag{1.2.1}$$

For an incompressible material follows $\mathrm{d}A/A = -\mathrm{d}d/d$. Therefore $\mathrm{d}U = \varepsilon E^2 A\ \mathrm{d}d$. The actuation pressure is

$$p_A = \left(\frac{1}{A}\right)\left(\frac{\mathrm{d}U_e}{\mathrm{d}d}\right) = \varepsilon E^2. \tag{1.2.2}$$

The compression ε_f is the actuation pressure divided by the mechanical resistance of the elastomer, given by the Young's modulus

$$\varepsilon_f = -\frac{p_A}{Y}. \tag{1.2.3}$$

Fig. 1.2.4 shows the electromechanical performances of DEs in comparison with natural muscle. Acrylic elastomer has the highest deformability that is clearly better as for natural muscle and silicones.

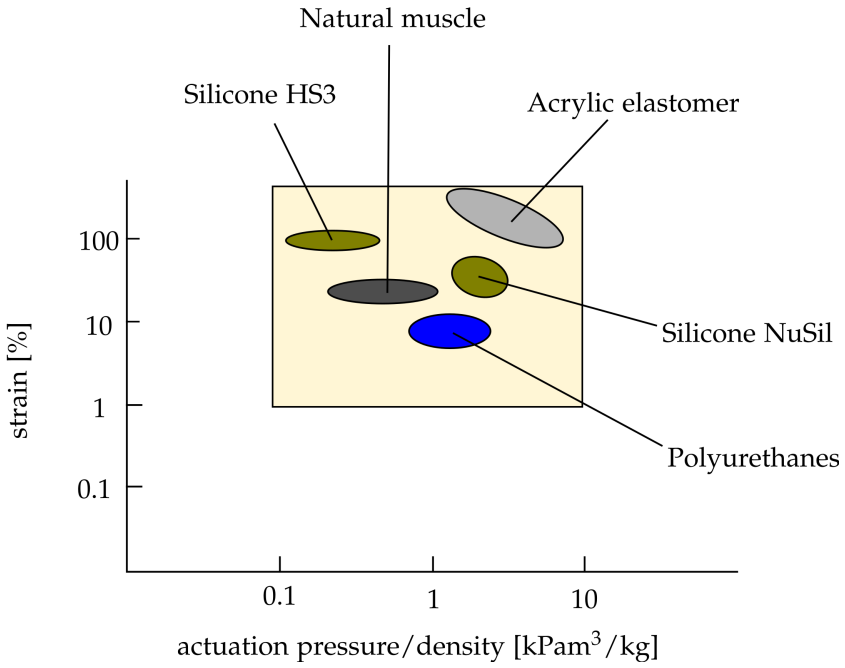

Figure 1.2.4.: Logarithmic electromechanical performances of natural muscle and dielectric elastomer [24].

Acrylic Elastomer

Acrylic elastomer is a promising material because of an outstanding electromechanical performance, especially under pre-stretch, which is applied if small forces at low voltages are needed as signal output [25]. The acrylic elastomer VBH 4905/10, produced by 3M, has been frequently investigated. The 05 or 10 stands for the elastomer's thickness expressed in 1×10^{-4} m. VHB is available as tape, pad or film, single- or double-sided adhesive. VBH 49 is a copolymer consisting of polyacrylates that differ in the substituent. The structural formula is shown in Fig. 1.2.5. The Young's modulus is in the order of 500 kPa. The microstructure of VBH 49 is amorphous whereby molecular chains are cross-linked. Viscoelastic properties are very pronounced and were studied in detail in Michel et al. and Sahu and Patra [21, 26] where strain-rate, time- and cyclic effects have been investigated. Hyperelastic behaviour is characterised for strains up to 1300 % at a strain rate of $0.16\,\mathrm{s}^{-1}$. The stress-strain curve shows that

a description with a Neo-Hooke behaviour is reasonable for strains up to 200 %. Up to 600 % a Yeoh or Gent material law can be applied. The stress-strain curve for higher strain cannot be described by an established model for hyperelasticity. A discrete viscoelastic spectrum for VHB49 was determined based on uniaxial experiments in [27]. It is shown that at least 20 Maxwell elements are necessary to map the viscoelastic behaviour between $-40\,^{\circ}\mathrm{C}$ and $60\,^{\circ}\mathrm{C}$.

Pre-stretching of VBH 4910 improves its electromechanical performance, its relative electric permittivity of 4.7 is thereby decreased [28, 29]. Interpenetrating networks (IPNs) formed by chemical bonds, see Fig. 1.2.6b, can have a similar effect on ε_f but do not change the permittivity. Using IPNs has further the advantage that the construction of applications can be simplified [30].

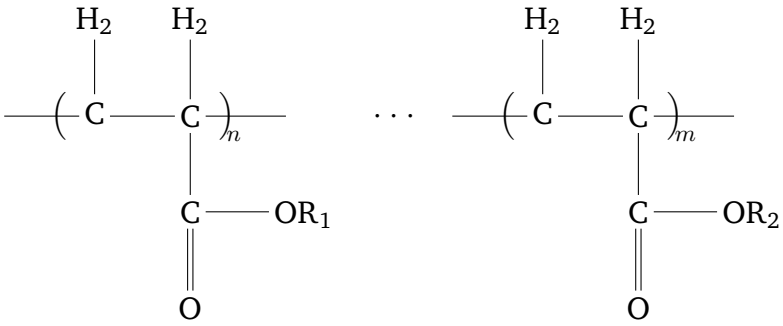

Figure 1.2.5.: Chemical structure of VHB [31]

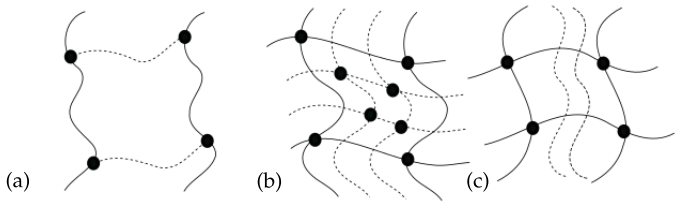

Figure 1.2.6.: Polymer network: (a) Cross-linked polymer, (b) Interpenetrating polymer network of two cross-linked polymers, (c) Semi-interpenetrating polymer network of two cross-linked polymers, picture schematically taken over from [32].

1.3 Applications

1.3.1 Electrets

In 1919, the first electret, a composite of Carnauba and bee wax polarised in an electric field at elevated temperature, was manufactured by the Japanese scientist Mototaro Eguchi [33]. Electrets are dielectric materials or composites of dielectric materials that show piezoelectric behaviour after an electric polarisation. Different classes of electrets can be defined by the poling method [34] whereby efficiency is influenced by the chemical composition and microstructure. Electrets can be poled in an electric, magnetic or mechanical force field under the influence of electromagnetic radiation or temperature, or by

combinations. That way, elevated temperature can increase the penetration depth and leads to a better time stability of charge.

In the context of this thesis, structures of open, lined-up polymeric ferroelectret cells, consisting of a polymer frame enclosing air are investigated.[5] The structures are manufactured by hot-forming of adjacent FEP-tubes. After sputtering of silver electrodes on lower and upper surface, direct charging with voltages between 3 kV and 5 kV is used to trap free charge in the inner polymer edge layers what leads to a remanent space charge polarisation. Free charge is generated by triggering breakdown events of the enclosed air. The breakdown voltage or sparking potential depends on the gap width between opposite charged electrodes and is defined by Paschen's law, formulated first by Townsend

$$V_{\mathrm{B}} = \frac{B}{\ln(Apd) - \ln\left[\ln(1+\gamma^{-1})\right]} pd. \tag{1.3.1}$$

V_{B} is the breakdown voltage, A and B are constants[6]. p is the gas pressure, d the gap's width between electrodes and γ the Townsend coefficient. Paschen's law refers to a plate condenser and is derived from the probability of impact ionisation.[7]

The breakdown voltage as function of d was measured for FEP/ePTFE[8]/FEP sandwich structures with d_{33} coefficients between $100\,\mathrm{pC\,N^{-1}}$ and $1600\,\mathrm{pC\,N^{-1}}$ for a constant gas pressure in [38]. In reference to the Paschen's curve of air, the curve for the sandwich is shifted to higher electric fields by a factor of $50\,\mathrm{kV\,cm^{-1}}$ and decreases with the thickness of the porous layer. Electric (Paschen's) breakdown events or atmospheric dielectric barrier discharges (DBDs) in air are associated with a donation of electrons from N_2 that was found by means of optical emission spectroscopy in Kozlov et al. [39]. With this method light impulses are observable when micro-discharge takes place [40]. For a trapezoidally voltage function applied on a tubular channel PP film, three voltage levels for Paschen's breakdown were identified in Qiu et al. [41, 42]. The first level is defined by the breakdown voltage, the second is observable at higher voltages and the third during the ramp down of voltage when a reversed electric field is built and back discharge takes place.

Polypropylene (PP) is a classical non-polar material for voided ferroelectrets. Its melting temperature T_s is about 160 °C and the space charge is stable up to 60 °C [45]. In latest research FEP is focussed because of its high temperature resistivity, which allows charging at higher temperature that stabilises the charge up to the poling temperature [46]. Besides temperature stability, the time stability of the d_{33} coefficient is decisive for the use; the d_{33} is influenced by viscous and dielectric relaxation, and in closed structures by air flow effects[9]. For the open FEP/ePTFE/FEP sandwich discussed above, a

---

5 See Fig. 1.3.1a

6 $A = \frac{\pi r_I^2}{k_B T}$, $B = \frac{\pi r_I^2 E_I}{k_B T e}$, k_B is the Boltzmann constant, T the temperature, r_I the radius of an ion, E_I the energy of a charged particle and e=1.62 × 10^{-19} C the unit charge.

7 Paschen's curve is not clearly determined for gaps in the order between 1 µm-10 µm [35] where an interaction of two discharge mechanisms takes place. Surface and avalanche discharge mechanism are still object of scientific investigation [36, 37].

8 The abbreviation ePTFE stands for expanded PTFE.

9 For a mainly closed pore structure of cellular PP, an increase of d_{33} with time is reported in [47]. Measurements show an initial d_{33} about $110\,\mathrm{pC\,N^{-1}}$ that grows to $250\,\mathrm{pC\,N^{-1}}$ within one hour. In Gaal et al. [48] viscoelastic

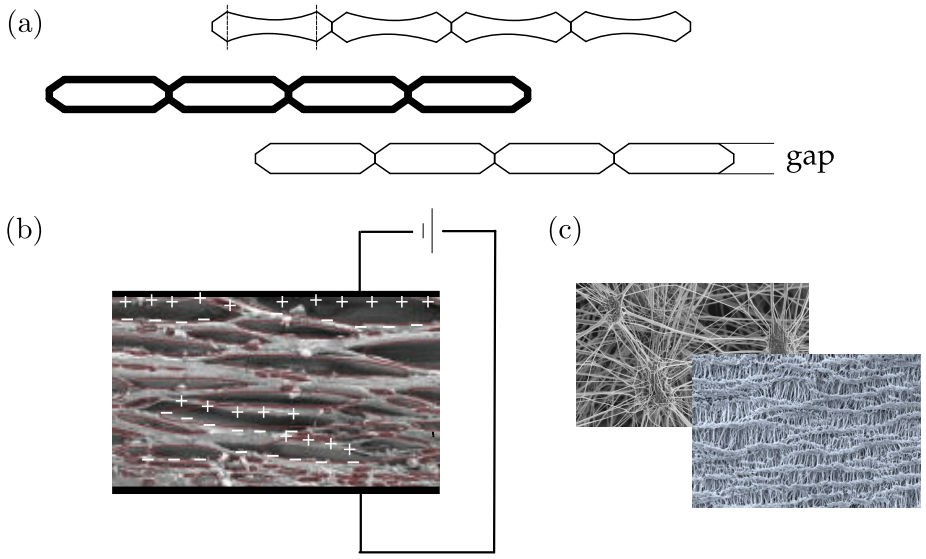

Figure 1.3.1.: Possible ferroelectret geometries: (a) Cellular structures. (b) Sandwich structure with cellular PP, SEM picture PP [42]. (c) Possible structures of ePTFE [43, 44].

strong decrease of d_{33} from $800\,\mathrm{pC\,N^{-1}}$ to $400\,\mathrm{pC\,N^{-1}}$ under the impact of a static mechanical force of $3.93\,\mathrm{kPa}$ during a time period of six days is reported in [46]. Creeping of the softer ePTFE layer is assumed to be the reason for the reduction. Experiments also show viscoelastic behaviour of the described cell structures from FEP-tubes, which is attributed to the viscous properties of FEP.[10]

1.3.2 Dielectric elastomer applications

The design of DE based applications starts in the 1990s with the work of Kornbluh et al. [24] who investigated dielectric elastomers as material for artificial muscle. First, the usage for planar, linear, actuators similar to Fig. 3.3.1, was examined [51, 52]. Design alternatives like linear rolled or bended as well as folded or stacked structures followed.[11] Three overviews, Capri et al., Kornbluh et al., O'Halloran et al. [22, 56, 57], in which prototypes are introduced, are recommended to the interested reader. Clamped, circular membranes covered with compliant electrodes, called diaphragm actuators are of particular interest and can be used for pumps, electric generators, loud speakers or in tactile feedback devices [58]. Circular membranes are lenticular deformed in the rest state to avoid non-axialsymmetric deformation modes; shaping by means of a support is illustrated in the left of Fig. 1.3.3 where the work method of a buckling dielectric elastomer actuator (DEA) is demonstrated. In electric activation, the membrane, which is fixed in a rigid frame, deforms out-of-plane due to electrostatic instability. A

properties of cellular PP ferroelectrets are examined for different excitation frequencies. Dynamic mechanical analysis (DMA) was used to investigate frequency dependence of in-plane and out-of-plane Young's moduli Y_{11} and Y_{33} in the lower frequency range (1Hz). Laser doppler vibrometry (LDV) was applied to analyse Y_{33} for higher frequencies. The DMA method shows a non-linear frequency dependence of storage component Y'_{33}, while the LDV method shows linear behaviour. Air flow between pores is presumed to increase the d_{33} in DMA experiments. Also, Kressmann [49] have reported that airflow between bubbles and surrounding air leads to growing of the d_{33} for low frequencies

[10] Viscous properties of FEP are studied in [50]

[11] See Fig. 1.3.2.

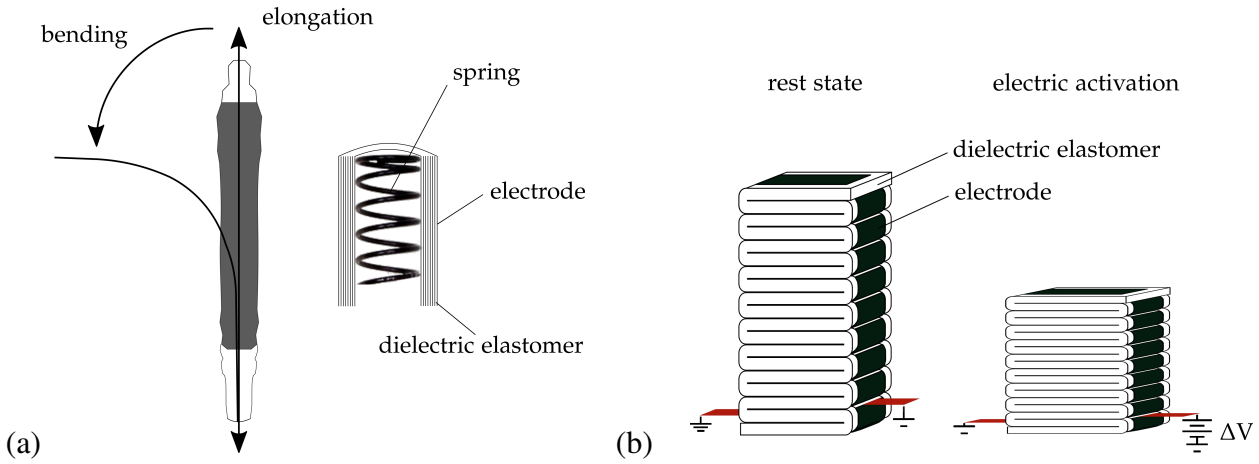

Figure 1.3.2.: (a) Rolled DEA with a bending and an elongation deformation mode that can be controlled by activation of different electrode surfaces [53, 54]. (b) Folded DEA structure [55].

buckling DEA array is shown in the right of Fig. 1.3.3. Such a design can be used e.g. for smart surfaces. A flat dynamic loudspeaker that works on the same principle is introduced in Rustighi et al. [59]. Due to stiff microscopically perforated electrodes a homogeneous strain distribution and constant device dimensions can be achieved.

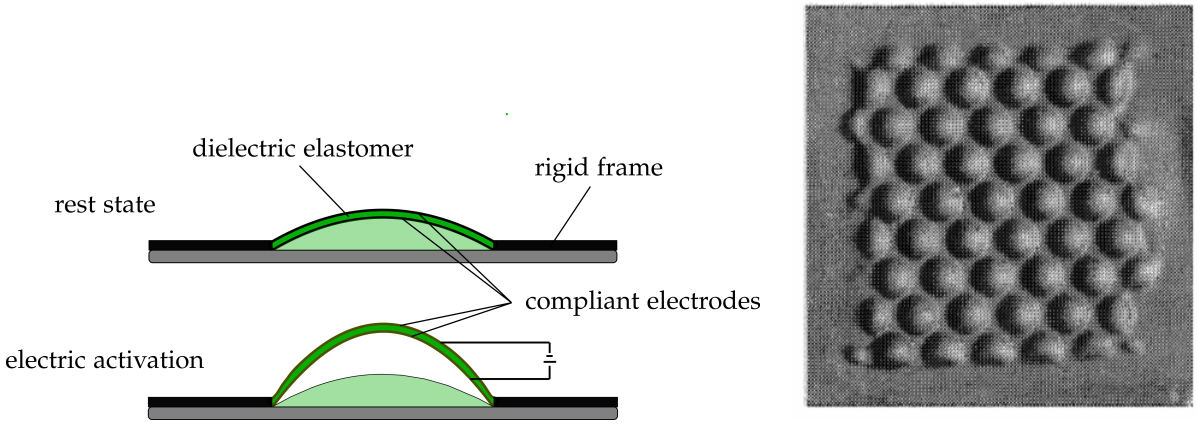

Figure 1.3.3.: Diaphragm DEA [60], [61].

Sensors, which transduce mechanical into electrical signals, are a further application for DE. In large area compression sensors sandwiches of dielectric material and electrode surface are stretched by compression of waved profiles, like illustrated in Fig. 1.3.4. The thickness of the dielectric is thereby reduced and capacitance is enlarged [62]. This kind of sensors is usable for sensor mats to determine a weight distribution, e.g. in car seats or medical applications.

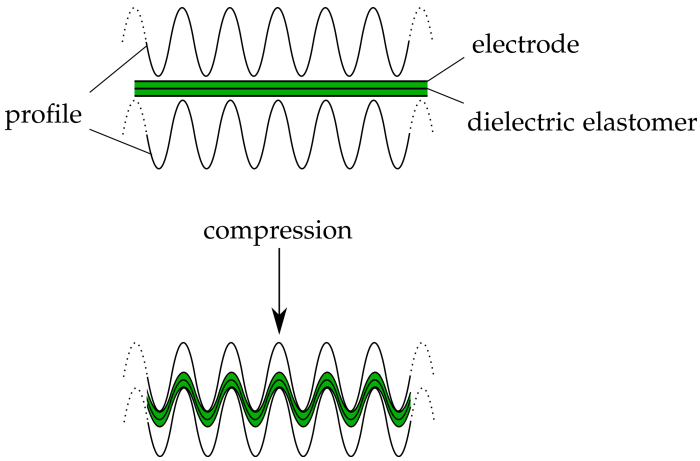

Figure 1.3.4.: Operating principle of a DE sensor mat. An electrode-dielectric sandwich is deformed by the compression of two waved profiles.

What is more, capacitive pressure sensors can be used in foldable keyboards; a programmable polydimethylsiloxane PMDS silicon rubber keyboard detecting touch in two dimensions is introduced in Xu et al. [63]. DE capacitive pressure sensors can be found, in wearable or implantable electronics, their use however is limited due to low sensitivity and slow response because of the small Young's modulus of elastomers [64]. The use of DE is customary e.g. for planar or lens-shaped sensor and actuator components [65, 66].

2 Theoretical background

2.1 Dielectric polarisation mechanisms

Mechanical strain due to a displacement of point charge within a crystal lattice is called electrostriction, which is parametrised by the electrostriction coefficient. A generation of electric fields by charge displacement due to mechanical force is called piezoeffect [67]. This definition as well as the definition of the inverse-piezoeffect, which is a mechanical response to an electric field, is independent of the microstructure.

In this work, polymeric dielectrics are regarded where lattice effects play a subordinate role and charge displacement is attributed to four types of polarisation [68]. The first type is electronic polarisation that takes place on the atomic scale by a displacement of the centre of negative electron cloud relative to nucleus position. Atomic polarisation, the second type, is displacement of atoms or molecules as consequence of electronic polarisation. Electronic and atomic polarisation occur within a very short time-period in the order of 10×10^{-10} s, which can be considered as instantaneous. Both types are hardly influenced by temperature because these phenomena are intra molecular, strain and polarisation is proportional to the applied electric field. Amorphous polymers consist of macromolecules that can have permanent dipoles. Organic dielectric fluids or dielectric gases consist of freely rotatable dipoles. The moving of dipoles is called orientation polarisation which is the third mechanism described by relaxation times in the order of 10×10^{-5} s [34]. The fourth polarisation type is space charge polarisation which includes a mechanism called interface polarisation. This type specifies diffusion of charge carriers along an applied electric field. Space charge polarisation takes place in higher electric fields and is the mechanisms to charge interfaces of the FEP-ferroelectret structures introduced in detail in chapter 6.

2.2 Electrostatics

The basic equations of electrostatics in vacuum and medium are summarised in reference to Landau and Lifshitz, Meschede, Wipf, Fließbach [4, 67, 69, 70].

2.2.1 Electrostatics in vacuum

Coulomb's law is given here for the SI-system, it defines the interaction or Coulomb force $\mathbf{F}_\mathrm{c}$ between two static point charges q_1 and q_2

$$\mathbf{F}_\mathrm{c}(\mathbf{x}) = \frac{q_1 q_2}{4\pi\epsilon_0 x^2}\mathbf{x}_0 = \frac{q_1 q_2}{4\pi\epsilon_0}\frac{\mathbf{x}_1 - \mathbf{x}_2}{|\mathbf{x}_1 - \mathbf{x}_2|^3}. \tag{2.2.1}$$

x is the distance between the points and $\mathbf{x}_0$ is their connection vector. $\mathbf{x}_1$ and $\mathbf{x}_2$ are the position vectors of the point charges q_1 and q_2. From the right side of Eq. (2.2.1) can be seen that the Coulomb force has a $1/x^2$ dependence. The pre-factor $1/4\pi\epsilon_0$ defines the interaction strength. ϵ_0 is the vacuum permittivity (ϵ_0=8.854 187 817 $\times$ 10^{-12} F m^{-1}). In the Gauss-system this pre-factor is set to 1. Interaction between one point charge q and point charges $q_1, ..., q_N$ with positions $\mathbf{x}_1, ..., \mathbf{x}_N$ results in a force

$$\mathbf{F}_\mathrm{c}(\mathbf{x}) = \sum_{\mathrm{i}=1}^{\mathrm{N}} \frac{q\, q_i}{4\pi\epsilon_0} \frac{\mathbf{x}-\mathbf{x}_i}{|\mathbf{x}-\mathbf{x}_i|^3} = q\, \mathbf{E}(\mathbf{x}). \tag{2.2.2}$$

The electric field vector $\mathbf{E}(\mathbf{x})$ is the electrostatic force divided by the point charge q

$$\mathbf{E}(\mathbf{x}) = \frac{\mathbf{F}_\mathrm{c}(\mathbf{x})}{q} = \sum_{\mathrm{i}=1}^{\mathrm{N}} \frac{q_i}{4\pi\epsilon_0} \frac{\mathbf{x}-\mathbf{x}_i}{|\mathbf{x}-\mathbf{x}_i|^3}. \tag{2.2.3}$$

A charge density $\varrho(\mathbf{x}) = \frac{\text{charge}}{\text{volume}}$ summarises the charge of N point charges on the microscopic scale.

$$\varrho(\mathbf{x}) = \sum_{i=1}^{N} q_i\, \delta(\mathbf{x}-\mathbf{x}_i). \tag{2.2.4}$$

The electric field of a charge density is approximated by discrete point charges q_i of position $\mathbf{x}_i$ assigned to a partial volume V_i, see appendix A.1. V_ref is the sum of the partial volumes and is assumed to be much larger than an atomic volume. A formulation of the Coulomb's law referring to a charge density, with $\mathbf{x}'$ as position of a reference point in V_ref is given as

$$\mathbf{E}(\mathbf{x}) = \frac{1}{4\pi\epsilon_0} \int\limits_{V_\mathrm{ref}} \varrho(\mathbf{x}') \frac{\mathbf{x}-\mathbf{x}'}{|\mathbf{x}-\mathbf{x}'|^3}\, dV. \tag{2.2.5}$$

The electrostatic potential $\phi(\mathbf{x})$ can be derived from Eq. (2.2.5) using

$$\mathrm{grad}\, \frac{1}{|\mathbf{x}-\mathbf{x}'|} = -\frac{\mathbf{x}-\mathbf{x}'}{|\mathbf{x}-\mathbf{x}'|^3}, \tag{2.2.6}$$

$$\mathbf{E}(\mathbf{x}) = \frac{1}{4\pi\epsilon_0} \int\limits_{V_\mathrm{ref}} \varrho(\mathbf{x}') \frac{\mathbf{x}-\mathbf{x}'}{|\mathbf{x}-\mathbf{x}'|^3}\, dV = -\mathrm{grad}\, \frac{1}{4\pi\epsilon_0} \int\limits_{V_\mathrm{ref}} \frac{\varrho(\mathbf{x}')}{|\mathbf{x}-\mathbf{x}'|}\, dV = -\mathrm{grad}\, \phi(\mathbf{x}), \tag{2.2.7}$$

with

$$\phi(\mathbf{x}) = \frac{1}{4\pi\epsilon_0} \int\limits_{V_\mathrm{ref}} \frac{\varrho(\mathbf{x}')}{|\mathbf{x}-\mathbf{x}'|}\, dV. \tag{2.2.8}$$

The electrostatic potential of a point charge is

$$\phi(\mathbf{x}) = \frac{1}{4\pi\epsilon_0} \frac{q}{|\mathbf{x}-\mathbf{x}_0|}. \tag{2.2.9}$$

The Maxwell equations for time-independent fields can be derived from (2.2.7) when the Laplace operator is applied on the electrostatic potential ϕ, defined in Eq. (2.2.8) [1]

$$\operatorname{div} \mathbf{E}(\mathbf{x}) = \frac{1}{\epsilon_0} \varrho(\mathbf{x}), \tag{2.2.10}$$

$$\operatorname{rot} \mathbf{E}(\mathbf{x}) = 0, \text{ with} \tag{2.2.11}$$

$$\Delta\phi(\mathbf{x}) = -\frac{\varrho(\mathbf{x})}{\epsilon_0}. \tag{2.2.12}$$

Eq. (2.2.12) is denoted as Poisson's equation. In case the reference volume is free from electric loading, the right side of Eq. (2.2.12) vanishes and Eq. (2.2.12) becomes the Laplace's equation. Eq. (2.2.10) can be written as an integral in case the Gauss's theorem is applied

$$\oint_{\mathrm{A}} \mathbf{E}(\mathbf{x}) \cdot \mathrm{d}\mathbf{A} = \int_V \frac{1}{\epsilon_0} \varrho(\mathbf{x}) \, \mathrm{d}V = Q_V. \tag{2.2.13}$$

Eq. (2.2.13) is denoted as Gauss's law, where Q_V is the volume charge. The Coulomb force resulting from a charge density $\varrho(\mathbf{x})$ can be derived from [2]

$$\begin{aligned} \mathbf{F}_{\mathrm{c}}(\mathbf{x}) &= \int_V \mathbf{f}^{\mathrm{E}}(\mathbf{x}) \, \mathrm{dV} = \int_V \varrho(\mathbf{x}) \mathbf{E}(\mathbf{x}) \, \mathrm{d}V = \int_V \epsilon_0 \left[\operatorname{div} \mathbf{E}(\mathbf{x})\right] \mathbf{E}(\mathbf{x}) \, \mathrm{d}V \\ &= \int_V \epsilon_0 \left[\operatorname{div} (\mathbf{E} \otimes \mathbf{E}) - \operatorname{grad}\mathbf{E}\mathbf{E}\right] \, \mathrm{d}V = \epsilon_0 \operatorname{div} \int_V \left(\mathbf{E} \otimes \mathbf{E} - \frac{1}{2} (\mathbf{E} \cdot \mathbf{E}) \mathbf{1} \right) \, \mathrm{d}V, \end{aligned} \tag{2.2.14}$$

where $\mathbf{f}^{\mathrm{E}}$ is the electric force density formulated via Gauss's law as

$$\mathbf{f}^{\mathrm{E}} = \operatorname{div} \boldsymbol{\sigma}^{\mathrm{E}}. \tag{2.2.15}$$

By inserting Eq. (2.2.15) into Eq. (2.2.14) the Maxwell stress in vacuum is written as [3]

$$\boldsymbol{\sigma}^{\mathrm{E}} = \epsilon_0 \left(\mathbf{E} \otimes \mathbf{E} - \frac{1}{2} (\mathbf{E} \cdot \mathbf{E}) \mathbf{1} \right). \tag{2.2.16}$$

2.2.2 Maxwell stress tensor in solid dielectrics for large deformation

The Maxwell stress for large deformation can be described by a material-inherent and strain-dependent permittivity. Measurements of strain-dependent permittivity were conducted for VHB whereby results have a massive scattering as reported in [71]. A stretch of 5 % modifies the permittivity between nearly zero and up to 44 % [72, 73]. In a mirostructural approach, the variation of permittivity is associated with

[1] $\Delta \frac{1}{|\mathbf{x}-\mathbf{x}_0|} = -4\pi\delta(\mathbf{x}-\mathbf{x}_0)$.

[2] $E_k E_{j,k} = -E_i \phi_{,jk} = E_k E_{k,j} = \left(\frac{1}{2} E_k E_k \delta_{ij}\right)_{,i}$, $\operatorname{div}(\mathbf{u} \otimes \mathbf{v}) = \mathbf{u} \operatorname{div} \mathbf{v} + (\operatorname{grad} \mathbf{u})\mathbf{v}$

[3] $\mathbf{1}$ is the second order unit tensor.

a strain induced change of the birefringence. Based on this observation, a model to describe the permittivity as a function of strain was developed using statistical mechanics in Jiménez and McMeeking [71].

2.2.3 Electrostatics in dielectric solids

"The fundamental property of dielectrics is that a constant current cannot flow in them.", is stated by Landau and Lifshitz [4] in 1960. Dielectrics have the possibility to trap charges and to restrict and slow down their moveability; under the influence of an electric field, charge is slightly moved due to polarisation mechanisms. Positive charge is orientated in direction of the applied electric field, negative charge in the opposite direction. Charge or dielectric displacement is described by the polarisation vector $\mathbf{P}(\mathbf{x})$, see Eq. (2.2.18), which is composed of fractions of the four polarisation types: electronic, atomic, orientation and space charge polarisation, described in section 2.1.[4] Orientation polarisation $\mathbf{P}_\mathrm{O}(\mathbf{x})$ arise by the orientation of dipole moments between point charges, $\mathbf{P}_\mathrm{O} = q\mathbf{x}$. Assuming a continuous charge density the dipole moment in the regarded volume is

$$\int_{V_\mathrm{ref}} \mathbf{r}' \varrho_p(\mathbf{x}')\,\mathrm{d}V = \int_{V_\mathrm{ref}} \mathbf{P}_\mathrm{O}(\mathbf{x}')\,\mathrm{d}V. \tag{2.2.17}$$

For the ideal case, polarisation is a linear function of the electric field where the susceptibility χ_s is the slope

$$\mathbf{P}(\mathbf{x}) = \mathbf{D}(\mathbf{x}) - \epsilon_0\mathbf{E}(\mathbf{x}) = (\epsilon_r - 1)\mathbf{E}(\mathbf{x})\epsilon_0 = \chi_s\mathbf{E}(\mathbf{x})\epsilon_0, \tag{2.2.18}$$

$\mathbf{D}(\mathbf{x})$ is the dielectric displacement or induction. The component of $\mathbf{P}$ normal to the surface of the dielectric defines the surface charge density σ

$$\sigma = P_n. \tag{2.2.19}$$

The superposition of a polarisation charge density ϱ_p with a mobile charge density ϱ_f gives the total charge ϱ

$$\varrho(\mathbf{x}) = \varrho_f(\mathbf{x}) + \varrho_p(\mathbf{x}) = \varrho_f(\mathbf{x}) - \operatorname{div}\mathbf{P}(\mathbf{x}). \tag{2.2.20}$$

Inserting Eq. (2.2.10) into Eq. (2.2.20) leads to

$$\operatorname{div}\mathbf{E}(\mathbf{x}) = \frac{1}{\epsilon_0}\varrho(\mathbf{x}) = \frac{1}{\epsilon_0}\varrho_f(\mathbf{x}) - \frac{1}{\epsilon_0}\operatorname{div}\mathbf{P}(\mathbf{x}). \tag{2.2.21}$$

Defining the dielectric displacement as

$$\mathbf{D}(\mathbf{x}) = \epsilon_0\mathbf{E}(\mathbf{x}) + \mathbf{P}(\mathbf{x}), \tag{2.2.22}$$

Eq. 2.2.21 can be written as

$$\operatorname{div}\mathbf{D}(\mathbf{x}) = \varrho_f(\mathbf{x}). \tag{2.2.23}$$

[4] A description of polarisation types is given in Kao [34].

The component of the dielectric displacement perpendicular to a surface of a dielectric body surrounded by vacuum is[5]

$$D_n = -\epsilon \frac{\partial \phi}{\partial \mathbf{n}} = \sigma, \tag{2.2.24}$$

where $\mathbf{n}$ is the surface normal. ϵ_r is the relative permittivity, $\epsilon = \epsilon_0 \epsilon_r$ the absolute permittivity.

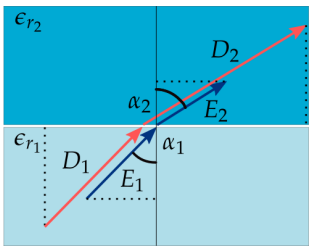

Figure 2.2.1.: Refraction of electric and dielectric displacement. Field lines in adjacent dielectrics with different electric permittivities ϵ_{r_1} and ϵ_{r_2}, whereby $\epsilon_{r_2} > \epsilon_{r_1}$.

Following relation holds for an interface between two dielectric materials with different permittivities

$$[[\mathbf{D} \cdot \mathbf{n}]] = (\mathbf{D}^+ - \mathbf{D}^-) \cdot \mathbf{n} = (\mathbf{D}_2 - \mathbf{D}_1) \cdot \mathbf{n} = p, \text{ with } \mathbf{D}_2 > \mathbf{D}_1 \tag{2.2.25}$$

where p is free interface charge. The electric field in the interface does not have a tangential component,

$$(\mathbf{E}_1 - \mathbf{E}_2) \cdot \mathbf{t} = 0, \text{ with } \mathbf{E}_2 > \mathbf{E}_1 \tag{2.2.26}$$

where $\mathbf{t}$ is the tangential vector of the surface. For a charge-free interface, refraction of electric field lines is described by

$$|\mathbf{E}_1| \sin \alpha_1 = |\mathbf{E}_2| \sin \alpha_2, \ |\mathbf{D}_1| \cos \alpha_1 = |\mathbf{D}_2| \cos \alpha_2, \tag{2.2.27}$$

from which follows

$$\frac{\tan \alpha_2}{\tan \alpha_1} = \frac{\epsilon_{r_2}}{\epsilon_{r_1}}, \text{ with } \epsilon_{r_2} > \epsilon_{r_1}. \tag{2.2.28}$$

In a conductor, $\epsilon_r \to \infty$. Therefore Eq.2.2.28 leads to $\alpha_1 = 0$. The electric field lines in the dielectric with ϵ_{r_1} are then perpendicular to the interface.

[5] In this thesis the surface charge density σ is also denoted as p in case free interface charge is meant.

2.3 Mechanics

2.3.1 Basics of continuum mechanics

The subject of continuum mechanics is the mathematical description of time-dependent movement and deformation of bodies in space seen from a macroscopic viewpoint. A body is imagined as an accumulation of particles or material points. Two different configurations or frames are defined to formulate the kinematics: The reference configuration, which defines an initial state at $t = t_0$ before movement, described by material coordinates (X_1, X_2, X_3), and the current configuration regarding the body after motion at time $t = t_n$, described by spatial coordinates (x_1, x_2, x_3). Fig. 2.3.1 illustrates both states: (a), reference configuration with volume Ω_0 and (b), current configuration with volume Ω. The boundary of the body is exposed to external impacts that can be electrical (ϕ, q), mechanical (T, t) or thermal (G, g) in the context with this thesis. (B, b) and (R, r) are internal force- and thermal sources. χ denotes the motion or deformation of the body from reference into current configuration.

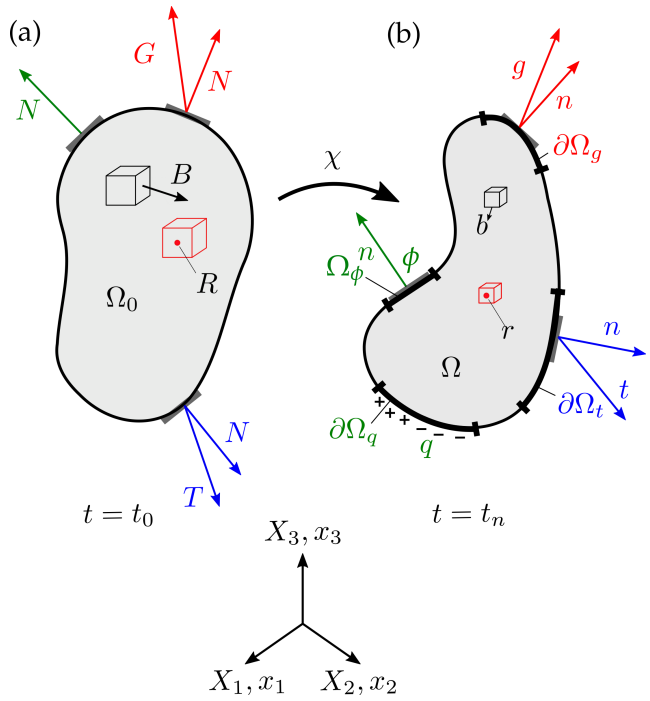

Figure 2.3.1.: Body as part of a time-space continuum: (a) Reference configuration, (b) Current configuration. Electric boundary conditions are defined on boundaries $\partial\Omega_\phi$ and $\partial\Omega_q$. An electric potential is prescribed on $\partial\Omega_\phi$, whereas on $\partial\Omega_q$ a charge density is given.

The vectors $\mathbf{x}$ and $\mathbf{X}$ describe positions of material particles in Ω and Ω_0, respectively. $\mathbf{x}$ and $\mathbf{X}$ are transferred into each other due to the deformation χ of the body, which is invertible.

$$\begin{aligned} \mathbf{x} &= \chi(\mathbf{X}, t), \\ \mathbf{X} &= \chi^{-1}(\mathbf{x}, t). \end{aligned} \tag{2.3.1}$$

A tensorial measure of deformation is the deformation gradient $\mathbf{F}$ and its inverse $\mathbf{F}^{-1}$

$$\begin{aligned} \mathbf{F}(\mathbf{X}, t) &= \frac{\partial \chi(\mathbf{X}, t)}{\partial \mathbf{X}} = \operatorname{Grad} \mathbf{x}(\mathbf{X}, t), \\ \mathbf{F}^{-1}(\mathbf{x}, t) &= \frac{\partial \chi^{-1}(\mathbf{x}, t)}{\partial \mathbf{x}} = \operatorname{grad} \mathbf{X}(\mathbf{x}, t). \end{aligned} \tag{2.3.2}$$

The displacement from positions $\mathbf{x}$ to $\mathbf{X}$ is given as spatial or material displacement field $\mathbf{u}$ or $\mathbf{U}$

$$\begin{aligned} \mathbf{u}(\mathbf{X}, t) &= \mathbf{x}(\mathbf{X}, t) - \mathbf{X}, \\ \mathbf{U}(\mathbf{x}, t) &= \mathbf{x} - \mathbf{X}(\mathbf{x}, t). \end{aligned} \tag{2.3.3}$$

The spatial and the material displacement gradient tensors $\mathbf{h}$ and $\mathbf{H}$ are

$$\begin{aligned} \mathbf{h} &= \operatorname{grad} \mathbf{u} = \operatorname{grad} \mathbf{x} - \operatorname{grad} \mathbf{X}(\mathbf{x}, t) = \mathbf{1} - \mathbf{F}^{-1}(\mathbf{X}, t), \\ \mathbf{H} &= \operatorname{GRAD} \mathbf{U} = \operatorname{GRAD} \mathbf{x}(\mathbf{X}, t) - \operatorname{GRAD} \mathbf{X} = \mathbf{F}(\mathbf{X}, t) - \mathbf{1}. \end{aligned} \tag{2.3.4}$$

The spatial velocity gradient is defined by

$$\mathbf{l}(\mathbf{x}, t) = \frac{\partial \mathbf{v}(\mathbf{x}, t)}{\partial \mathbf{x}} = \operatorname{grad}\mathbf{v}\,(\mathbf{x}, t) = \dot{\mathbf{F}}\mathbf{F}^{-1}. \tag{2.3.5}$$

Line, surface and volume elements can be transferred from the reference configuration into the current configuration as follows

$$\begin{aligned} \mathrm{d}\mathbf{x} &= \mathbf{F}(\mathbf{X}, t)\mathrm{d}\mathbf{X}, \\ \mathrm{d}\mathbf{s} &= J\mathbf{F}^{-T}(\mathbf{x}, t)\mathrm{d}\mathbf{S}, \\ \mathrm{dv} &= J\mathrm{dV}, \end{aligned} \tag{2.3.6}$$

with $J = \det\mathbf{F}$. The second equation in Eq. (2.3.6) is known as Nanson's formula. The deformation gradient can be decomposed in a rigid body rotation and a stretching or contraction

$$\begin{aligned} \mathbf{F} &= \mathbf{R}\mathbf{U} = \mathbf{v}\mathbf{R}, \\ &\text{whereby} \\ \mathbf{R}^{\mathrm{T}}\mathbf{R} &= \mathbf{1},\ \mathbf{U} = \mathbf{U}^{T},\ \mathbf{v} = \mathbf{v}^{T}. \end{aligned} \tag{2.3.7}$$

R is called rotation tensor. **U** and **v** are called right and left stretch tensor. Previously in the text, **U** describes the material displacement vector. This ambiguity is common in literature. In the remainder of this chapter **U** denotes the right stretch tensor. Quadratures of **U** and **v** give the right- and the left Cauchy Green tensor. Left and right are thereby referred to the position in the decomposition of deformation gradient in Eq. (2.3.7).

$$\begin{aligned} \mathbf{U}^2 &= \mathbf{C}, \\ \mathbf{v}^2 &= \mathbf{b}. \end{aligned} \tag{2.3.8}$$

Stresses and strains

Stress and strain measures are distinguished by their configuration into Lagrangian and Eulerian; that specifies also the perspective of the observer.[6] Their formulation is based on the deformation measures **F**, **R**, **U**, introduced in the previous subsection. $\mathbf{C} = \mathbf{F}^T\mathbf{F}$ is the right Cauchy-Green tensor, assigned to reference configuration, and $\mathbf{b} = \mathbf{F}\mathbf{F}^T$ the left Cauchy-Green tensor assigned to current configuration. The Green-Lagrange strain tensor, here denoted as **A** [7]

$$\mathbf{A} = \frac{1}{2}(\mathbf{C} - \mathbf{1}) = \frac{1}{2}(\mathbf{F}^{\mathrm{T}}\mathbf{F} - \mathbf{1}), \tag{2.3.9}$$

is used in the formulation of large deformation material laws in this thesis. The Euler-Almansi strain tensor, denoted as **a**, is the counterpart of the Cauchy-Green tensor allocated to current configuration

$$\mathbf{a} = \frac{1}{2}(\mathbf{1} - \mathbf{b}^{-1}) = \frac{1}{2}(\mathbf{1} - \mathbf{F}^{-\mathrm{T}}\mathbf{F}^{-1}). \tag{2.3.10}$$

Strain measures can be transformed into each other using a push-forward $\chi(\bullet)$ or a pull-back $\chi^{-1}(\bullet)$ operation

$$\begin{aligned} \mathbf{a} &= \mathbf{F}^{-\mathrm{T}}\mathbf{A}\mathbf{F}^{-1} = \chi(\mathbf{A}), \\ \mathbf{A} &= \mathbf{F}^{\mathrm{T}}\mathbf{a}\mathbf{F} = \chi^{-1}(\mathbf{a}). \end{aligned} \tag{2.3.11}$$

The Lagrangian Hencky strain tensor $\hat{\mathbf{H}}$ is defined as in [74]

$$\hat{\mathbf{H}} = \ln\mathbf{U} = \frac{1}{2}\ln\left(\mathbf{F}^{\mathrm{T}}\mathbf{F}\right) = \frac{1}{2}\ln\mathbf{C}. \tag{2.3.12}$$

The choice of the strain measure has to be synchronised with experimental data, for numerical values of strains vary with the used strain measure as discussed in chapter 3 of Altenbach [74]. Strain and stress measures are work-conjugated. The symmetric, Eulerian Cauchy stress tensor $\boldsymbol{\sigma}$ is equivalent to true stress and conjugated to Hencky strain. The symmetric, Lagrangian 2.Piola-Kirchhoff stress **S** is

[6] Reference configuration is associated to the Lagrangian specification where the observer follows an individual particle as if it moves through space and time. The current configuration uses the Eulerian specification that implies a perspective as if the observe is sitting on the particle and watching the moving surrounding.

[7] In literature, the Green-Lagrange strain tensor is usually denoted as **E** or **G** but these symbols are used otherwise in this thesis.

conjugated to Green-Lagrange strain. The 2.Piola-Kirchhoff stress tensor is often denoted as “Pseudo stress“ because it has no physical meaning and is rather a definition based on the asymmetrical 1.Piola-Kirchhoff stress. The 2.Piola-Kirchhoff tensor can be obtained from the Cauchy stress tensor

$$\mathbf{S} = J\mathbf{F}^{-1}\boldsymbol{\sigma}\mathbf{F}^{-\mathrm{T}}. \tag{2.3.13}$$

The asymmetric 1.Piola-Kirchhoff stress tensor $\mathbf{P}$ is defined by

$$\mathbf{P} = \mathbf{FS}. \tag{2.3.14}$$

Lie time derivative

The Lie time derivative describes a temporal change of a spatial field $f(\mathbf{x}, t)$ relative to a material field $F(\mathbf{X}, t)$

$$\mathscr{L}_{\mathrm{v}} = \chi\left(\frac{\mathrm{D}}{\mathrm{Dt}}\chi^{-1}f\right) = \chi(\dot{F}). \tag{2.3.15}$$

The spatial field $f(\mathbf{x}, t)$ is first transformed into reference configuration where the time derivative is carried out, and then transformed back to current configuration. Thus an objective rate of a spatial field can be obtained. The Lie time derivative is used for the spatial formulation of dissipation rates in viscoelastic materials.

Split of the deformation gradient

The state-of-the-art in continuum mechanical formulation of plasticity and viscoelasticity is to assign the dissipative part of free energy to the deviatoric part of deformation. Coming from metal plasticity where dislocation movement can explain this assignment, the concept is used for polymers too, since appropriate models enable a good adjustment to measurement curves.

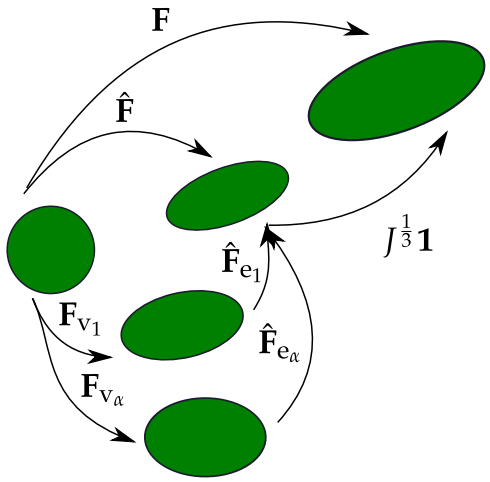

Figure 2.3.2.: Split of the deformation in a Maxwell element.

A split of the deformation in a Maxwell element, which covers the time-dependent behaviour and consists of spring and dashpot, is carried out by a decomposition of the deformation gradient multiplicatively by

$$\mathbf{F} = J^{\frac{1}{3}}\hat{\mathbf{F}},\ J = \det\mathbf{F}. \tag{2.3.16}$$

$J^{\frac{1}{3}}\mathbf{1}$ is the isochoric and $\hat{\mathbf{F}}$ the deviatoric part. Assuming a rheological model containing α parallel Maxwell elements, deviatoric parts are further split into instantaneous and time-dependent parts

$$\hat{\mathbf{F}} = \hat{\mathbf{F}}_{\mathrm{e}_\alpha}\mathbf{F}_{\mathrm{v}_\alpha}. \tag{2.3.17}$$

$\hat{\mathbf{F}}$ can be interpreted as 3D formulation of the sum of stretches in the Maxwell elements, see Fig. 2.6.2 whereby $\hat{\mathbf{F}}_{\mathrm{e}_\alpha}$ is the stretch in the springs and $\mathbf{F}_{\mathrm{v}_\alpha}$ maps the motion of the dashpots.

Balance laws

Physical and chemical processes underlie balance principles. Mechanical and electrostatic balance laws, interesting for this work, are recapitulated in this section. Fundamentally, it has to be distinguished between **closed systems** without any kind of flux over the boundary $\partial\Omega$, and **open systems** that have an exchange of material or energy with the environment. In a closed system, **conservation of mass** is expressed by

$$m(\Omega_0) = m(\Omega) > 0. \tag{2.3.18}$$

For all times t, the mass rate is assumed as

$$\dot{m} = \frac{\mathrm{D}}{\mathrm{D}t}\int\limits_{\Omega_c}\rho(\mathbf{x},t)\mathrm{d}v = 0. \tag{2.3.19}$$

In an open system, the mass rate in a control volume Ω_c is equal to the negative flux $\rho\mathbf{v}$ over the boundary

$$\dot{m} = \frac{\mathrm{D}}{\mathrm{D}t}\int\limits_{\Omega_c}\rho(\mathbf{x},t)\mathrm{d}v = -\int\limits_{\partial\Omega_c}\rho(\mathbf{x},t)\mathbf{v}(\mathbf{x},t)\cdot\mathbf{n}\mathrm{d}s. \tag{2.3.20}$$

Equivalent relations can be assumed for the **conservation of charge density**. In case charge sources are taken into account, follows for the charge rate

$$\dot{Q}_V = \frac{\mathrm{D}}{\mathrm{D}t}\int\limits_{\Omega_c}\varrho(\mathbf{x},t)\mathrm{d}v = -\int\limits_{\partial\Omega_c}\varrho(\mathbf{x},t)\mathbf{v}(\mathbf{x},t)\cdot\mathbf{n}\mathrm{d}s + \int\limits_{\Omega_c}\varrho(\mathbf{x},t)\mathrm{d}v. \tag{2.3.21}$$

Another two mechanical balance laws are the **balance of linear and angular momentum**, here described for an open system

$$\dot{\mathbf{L}}(t) = \frac{\mathrm{D}}{\mathrm{D}t}\int\limits_{\Omega}\rho\mathbf{v}\,\mathrm{d}v = \frac{\mathrm{D}}{\mathrm{D}t}\int\limits_{\Omega_0}\rho_0\mathbf{V}\,\mathrm{d}V = \mathbf{F}_{\mathrm{m}}(t), \tag{2.3.22}$$

$$\dot{\mathbf{J}}(t) = \frac{\mathrm{D}}{\mathrm{D}t}\int_{\Omega} \mathbf{r} \times \rho \mathbf{v}\, \mathrm{d}v = \frac{\mathrm{D}}{\mathrm{D}t}\int_{\Omega} \mathbf{r} \times \rho_0 \mathbf{V}\, \mathrm{d}V = \mathbf{M}(t). \tag{2.3.23}$$

The force $\mathbf{F}_{\mathrm{m}}(t)$ consists of two parts

$$\mathbf{F}_{\mathrm{m}}(t) = \int_{\partial\Omega} \mathbf{t}\, \mathrm{d}s + \int_{\Omega} \mathbf{b}\, \mathrm{d}v, \tag{2.3.24}$$

$\mathbf{t}$ is the traction vector on the boundary and $\mathbf{b}$ is the body force.

2.4 Thermodynamics of continua

Material behaviour of dielectric solids is governed by thermodynamic principles that are explained in this section. The **first law of thermodynamics** describes the **conservation of energy** in a system. It may be understood as an extension of the balance of mechanical energy that follows from the balance of the linear momentum, Baehr [75]. [8] The first law in energy rates is formulated as in Holzapfel [76]

$$\frac{\mathrm{d}}{\mathrm{d}t}\mathrm{E}_{\mathrm{kin}}(t) + \frac{\mathrm{d}}{\mathrm{d}t}\tilde{\mathrm{U}}(t) = \mathrm{E}_{\mathrm{ext}}(t) + \mathrm{G}(t). \tag{2.4.1}$$

$\mathrm{E}_{\mathrm{kin}}$ is the kinetic energy in the regarded volume [9]

$$\mathrm{E}_{\mathrm{kin}} = \int_{\Omega} \frac{1}{2}\rho \mathbf{v}^2 \,\mathrm{d}v. \tag{2.4.2}$$

The internal energy $\tilde{\mathrm{U}}$, which is a thermodynamic potential, given in the current configuration as $\int_{\Omega} \rho \mathrm{u}(\mathbf{x})\ \mathrm{dv}$, and in the reference configuration as $\int_{\Omega_0} \rho_0 \mathrm{U}(\mathbf{X})\ \mathrm{dV}$, is the integral of the specific internal energy density.[10] The right side of Eq. (2.4.1) contains work rates of external forces like

$$\begin{aligned}
\mathrm{E}_{\mathrm{ext}} &= \underbrace{\int_{\partial\Omega} \mathbf{t}\cdot\mathbf{v}\,\mathrm{d}s + \int_{\Omega} \mathbf{b}\cdot\mathbf{v}\,\mathrm{d}v}_{\text{mechanical}} \underbrace{- \int_{\partial\Omega} \phi \frac{\mathrm{d}(\varrho\,\mathrm{d}s)}{\mathrm{d}t} + \int_{\Omega} \phi \frac{\mathrm{d}(\varrho\,\mathrm{d}v)}{\mathrm{d}t}}_{\text{electric}} \\
&= \underbrace{\int_{\partial\Omega} \mathbf{t}\cdot\mathbf{v}\,\mathrm{d}s + \int_{\Omega} \mathbf{b}\cdot\mathbf{v}\,\mathrm{d}v}_{\text{mechanical}} \underbrace{- \int_{\partial\Omega} \phi \frac{\mathrm{d}(\mathbf{D}\cdot\mathbf{n}\,\mathrm{d}s)}{\mathrm{d}t} + \int_{\Omega} \phi \frac{\mathrm{d}(\mathbf{D}\cdot\mathbf{n}\,\mathrm{d}v)}{\mathrm{d}t}}_{\text{electric}} \\
\mathrm{G} &= \underbrace{\int_{\partial\Omega} \mathrm{g_n}\,\mathrm{d}s + \int_{\Omega} \rho \mathrm{r}\,\mathrm{d}v}_{\text{thermal}}
\end{aligned} \tag{2.4.3}$$

G is the rate of thermal work, g_n the heat flux, normal to the surface of volume

$$\mathrm{g_n}(\mathbf{x}, \mathbf{n}) = -\mathbf{g}(\mathbf{x})\cdot\mathbf{n}. \tag{2.4.4}$$

$\rho \mathrm{r}(\mathbf{x}, \mathrm{t})$ is a scalar field that denotes specific heat sources.[11] External power rates due to charge displacement are derived from the incremental work of a charge density [4]

$$\delta\Pi = \int_V \phi \delta\varrho \,\mathrm{d}V. \tag{2.4.5}$$

[8] See Eq. 2.3.22.
[9] Time-dependence is assumed, but omitted in the notation to simplify expressions.
[10] The integral of specific internal energy density is described in Eq. (2.4.11).
[11] See Fig. 2.3.1.

In case the system is in the current configuration, electric power in Eq. (2.4.3) is not only changed by charge rate, but also by geometry variation; the time derivative has to be considered for volume and surface increments. For the time derivatives following interrelations are used [12]

$$\begin{aligned}\dot{\mathrm{d}\mathbf{s}} &= (\dot{J}\mathbf{F}^{-\mathrm{T}} + J\dot{\mathbf{F}}^{-\mathrm{T}})\mathrm{d}\mathbf{S} = (\mathrm{div}\,\mathbf{v}\,\mathbf{1} - \mathbf{l}^T)J\mathbf{F}^{-T}\mathrm{d}\mathbf{S},\\ &= \mathrm{div}\,\mathbf{v}\,\mathrm{d}\mathbf{s} - \mathbf{l}^T\,\mathrm{d}\mathbf{s},\\ \dot{\mathrm{d}v} &= \dot{J}\mathrm{d}V = \mathrm{div}\,\mathbf{v}\,\mathrm{d}v.\end{aligned} \tag{2.4.6}$$

With $\mathrm{d}\mathbf{s} = \mathrm{d}s\mathbf{n}$, the electric parts of external energy are written as

$$\begin{aligned}\int_{\partial\Omega}\phi\frac{\mathrm{d}(\mathbf{D}\cdot\mathbf{n}\,\mathrm{d}s)}{\mathrm{d}t} &= \int_{\partial\Omega}\phi\left[\dot{\mathbf{D}} + \mathbf{D}(\mathrm{div}\,\mathbf{v}\,\mathbf{1} - \mathbf{l}^T)\right]\mathbf{n}\mathrm{d}s,\\ &= \int_{\partial\Omega}\phi\left[\dot{\varrho} + \varrho(\mathrm{div}\,\mathbf{v}\,\mathbf{1} - \mathbf{l}^T)\right]\mathrm{d}s,\\ \int_{\Omega}\phi\frac{\mathrm{d}(\varrho\,\mathrm{d}v)}{\mathrm{d}t} &= \int_{\Omega}\phi\,(\dot{\varrho} + \varrho\,\mathrm{div}\,\mathbf{v})\,\mathrm{d}v.\end{aligned} \tag{2.4.7}$$

Assuming that potential and kinetic energy are equal to zero, the first law in Eq. (2.4.1) can be formulated for the reference configuration

$$\frac{\mathrm{d}}{\mathrm{d}t}\int_{\Omega_0}\rho_0\mathrm{U}\,\mathrm{d}V = \int_{\partial\Omega_0}\left(\mathbf{T}\cdot\mathbf{V} + \mathrm{G_N} - \phi\dot{\mathbf{D}}_0\cdot\mathbf{N}\right)\,\mathrm{d}S + \int_{\Omega_0}\left(\mathbf{B}\cdot\mathbf{V} + \rho_0\mathrm{R} + \mathbf{E}_0\cdot\dot{\mathbf{D}}_0\right)\mathrm{d}V. \tag{2.4.8}$$

By applying the divergence theorem on electric boundary forces[13], and

$$\int_{\Omega_0}\mathbf{P}:\dot{\mathbf{F}} = \int_{\partial\Omega_0}\mathbf{T}\cdot\mathbf{V}\,\mathrm{d}S + \int_{\Omega_0}\mathbf{B}\cdot\mathbf{V}\,\mathrm{d}V, \tag{2.4.10}$$

follows

$$\frac{\mathrm{d}}{\mathrm{d}t}\int_{\Omega_0}\rho_0\mathrm{U}\,\mathrm{d}V = \int_{\Omega_0}\left(\mathbf{P}:\dot{\mathbf{F}} + \mathbf{E}_0\cdot\dot{\mathbf{D}}_0 - \mathrm{DIV}\,\mathbf{G} + \rho_0\mathrm{R}\right)\mathrm{d}V \tag{2.4.11}$$

for the rate of internal energy. It should be mentioned that the internal energy rate in entropic elastic, rubber-like materials is nearly zero. Internal energy does almost not change with deformation (purely entropic theory) or only in dependency of hydrostatic deformation (modified entropic theory). By as-

[12] Compare [76], chapter 2.7.

[13]
$$\int_{\partial\Omega_0}\phi\frac{\mathrm{d}(\mathbf{D}_0\cdot\mathbf{N}\,\mathrm{d}S)}{\mathrm{d}t} = \int_{\Omega_0}\mathrm{DIV}\left(\phi\dot{\mathbf{D}}_0\right)\,\mathrm{d}V = \int_{\Omega_0}\left(-\mathbf{E}_0\cdot\dot{\mathbf{D}}_0 + \phi\,\mathrm{DIV}\,\dot{\mathbf{D}}_0\right)\,\mathrm{d}V, \tag{2.4.9}$$

.

suming that the volume, taken into account, is arbitrary, a **local** specific internal energy rate with respect to the reference configuration is obtained

$$\rho_0 \dot{\mathrm{U}} = \mathbf{P} : \dot{\mathbf{F}} + \mathbf{E}_0 \cdot \dot{\mathbf{D}}_0 - \mathrm{DIV}\,\mathbf{G} + \rho_0 \mathrm{R}. \tag{2.4.12}$$

For the current configuration follows

$$\rho \dot{\mathrm{u}} = \boldsymbol{\sigma} : \mathbf{d} + \mathbf{E} \cdot \dot{\mathbf{D}} - \mathrm{div}\,\mathbf{g} + \rho \mathrm{r}, \tag{2.4.13}$$

where $\mathbf{d}$ is the symmetric part of the spacial velocity gradient $\mathbf{l}$.[14]
The **Second law of thermodynamics** explains the **directionality of natural processes** referring to the entropy, which is a state variable and can be seen in relation to the number of possible micro processes in a system. The second law states that entropy can never decrease with time in a closed system [77]. The specific entropy is denoted as $\mathrm{s_c} = \mathrm{s_c}(\mathbf{x})$ in the current, and as $\mathrm{s} = \mathrm{s}(\mathbf{X})$ in the reference frame whereby $\mathrm{S} = \int_\Omega \rho \mathrm{s_c}(\mathbf{x})\ \mathrm{dv} = \int_{\Omega_0} \rho_0 \mathrm{s}(\mathbf{X})\ \mathrm{dV}$. By the definition of Clausius, the second law states that the total entropy production is always greater or equal to zero

$$\Gamma = \frac{\mathrm{d}}{\mathrm{d}t}\mathrm{S} - \tilde{\mathrm{G}} \geq 0. \tag{2.4.14}$$

$\tilde{\mathrm{G}}$ is the rate of entropy input

$$\tilde{\mathrm{G}} = -\int_{\partial\Omega} \frac{\mathbf{g}}{\Theta} \cdot \mathbf{n} \mathrm{d}s + \int_\Omega \frac{\rho \mathrm{r}}{\Theta}\,\mathrm{d}v = -\int_{\partial\Omega_0} \frac{\mathbf{G}}{\Theta} \cdot \mathbf{N} \mathrm{d}s + \int_{\Omega_0} \frac{\rho_0 \mathrm{R}}{\Theta}\,\mathrm{d}V, \tag{2.4.15}$$

which is equal to the rate of thermal power, divided by the absolute temperature Θ. Inserting $\tilde{\mathrm{G}}$ into Eq. (2.4.14) gives the **Clausius-Duhem inequality**

$$\Gamma = \frac{\mathrm{d}}{\mathrm{d}t}\int_\Omega \rho \mathrm{s_c}\,\mathrm{d}v + \int_{\partial\Omega} \frac{\mathbf{g}}{\Theta} \cdot \mathbf{n} \mathrm{d}s - \int_\Omega \frac{\rho \mathrm{r}}{\Theta}\,\mathrm{d}v = \frac{\mathrm{d}}{\mathrm{d}t}\int_{\Omega_0} \rho_0 \mathrm{s}\,\mathrm{d}V + \int_{\partial\Omega_0} \frac{\mathbf{G}}{\Theta} \cdot \mathbf{N} \mathrm{d}s - \int_{\Omega_0} \frac{\rho_0 \mathrm{R}}{\Theta}\,\mathrm{d}V \geq 0. \tag{2.4.16}$$

The divergence theorem is applied to derive a local energy density from Eq. (2.4.16). The formulation for the reference configuration follows by an elimination of heat source R using Eq. (2.4.12)

$$\rho_0 \Theta \dot{\mathrm{s}} - \frac{1}{\Theta}\mathbf{G} \cdot \mathrm{GRAD}\,\Theta - \rho_0 \dot{\mathrm{u}} + \mathbf{P} : \dot{\mathbf{F}} + \mathbf{E}_0 \cdot \dot{\mathbf{D}}_0 \geq 0. \tag{2.4.17}$$

Common thermodynamic potentials of dielectric systems and their incremental forms are described subsequently in Tab.2.1.

[14] See Eq. (2.3.5).

Thermodynamic potential				Increment		
Internal energy, variation of p	$\tilde{\mathrm{U}}$			$\mathrm{d}\tilde{\mathrm{U}}$	$=$	$\mathrm{T}\mathrm{d}\mathrm{S} + \mathbf{E}_0 \cdot \mathrm{d}\mathbf{D}_0$
Internal energy, variation of ϕ	$\tilde{\mathrm{U}}$			$\mathrm{d}\tilde{\mathrm{U}}$	$=$	$\mathrm{T}\mathrm{d}\mathrm{S} - \mathbf{E}_0 \cdot \mathrm{d}\mathbf{D}_0$
Helmholtz free energy	$\tilde{\mathrm{F}}$	$=$	$\tilde{\mathrm{U}} - \mathrm{TS}$	$\mathrm{d}\tilde{\mathrm{F}}$	$=$	$-\mathrm{S}\mathrm{d}\mathrm{T} - \mathbf{E}_0 \cdot \mathrm{d}\mathbf{D}_0$
Enthalpy	$\tilde{\mathrm{H}}$	$=$	$\tilde{\mathrm{U}}$	$\mathrm{d}\tilde{\mathrm{H}}$	$=$	$\mathrm{T}\mathrm{d}\mathrm{S} - \mathbf{E}_0 \cdot \mathrm{d}\mathbf{D}_0$
Gibbs free enthalpy	$\tilde{\mathrm{G}}$	$=$	$\tilde{\mathrm{H}} - \mathrm{TS}$	$\mathrm{d}\tilde{\mathrm{G}}$	$=$	$-\mathrm{S}\mathrm{d}\mathrm{T} - \mathbf{E}_0 \cdot \mathrm{d}\mathbf{D}_0$

Table 2.1.: Thermodynamic potentials and their incremental forms.

The Helmholtz energy is used to describe processes in which the temperature remains constant. In case a chemical potential is included in the energy balance, e.g. for investigation of phase transitions or in context with electromechanical couplings, Gibbs enthalpy is used. For constant temperature, Helmholtz energy and Gibbs free enthalpy are equal for the kind of electromechanical systems discussed here.[15] Free energy density is therefore unspecifically denoted as Ψ. A Legendre transformation of Ψ relates the free with internal energy density [16]

$$\Psi = \rho_0 \left(\mathrm{u} - \Theta \mathrm{s}\right) - \mathbf{E}_0 \cdot \mathbf{D}_0, \tag{2.4.18}$$

and has a time derivative

$$\dot{\Psi} = \rho_0 \left(\dot{\mathrm{u}} - \dot{\Theta}\mathrm{s} - \Theta\dot{\mathrm{s}}\right) - \dot{\mathbf{E}}_0 \cdot \mathbf{D}_0 - \mathbf{E}_0 \cdot \dot{\mathbf{D}}_0. \tag{2.4.19}$$

By inserting Eq. (2.4.19) into Eq. (2.4.17), Θ and $\mathbf{E}$ become the independent variables. When the energy rate is influenced by viscous dissipation follows

$$\begin{aligned} \dot{\Psi} &= \underbrace{\frac{\partial \Psi}{\partial \mathbf{F}} : \dot{\mathbf{F}}}_{\text{mechanical}} + \underbrace{\frac{\partial \Psi}{\partial \mathbf{E}_0} : \dot{\mathbf{E}}_0}_{\text{electric}} + \underbrace{\frac{\partial \Psi}{\partial \Theta}\dot{\Theta}}_{\text{thermal}} + \underbrace{\sum_{\alpha=1}^{n} \frac{\partial \Psi}{\partial \mathbf{X}_{\mathrm{v}_\alpha}} : \dot{\mathbf{X}}_{\mathrm{v}_\alpha}}_{\text{viscous}} \\ &= -\rho_0 \dot{\Theta}\mathrm{s} - \frac{1}{\Theta}\mathbf{G}\,\mathrm{GRAD}\,\Theta - \dot{\mathbf{E}}_0 \cdot \mathbf{D}_0 + \mathbf{P} : \dot{\mathbf{F}}, \end{aligned} \tag{2.4.20}$$

where $\mathbf{X}_{\mathrm{v}_\alpha}$ represent α tensors of internal variables. Eq. (2.4.20) can be combined to

$$\left(\mathbf{P} - \frac{\partial \Psi}{\partial \mathbf{F}}\right) : \dot{\mathbf{F}} - \left(\mathbf{D}_0 + \frac{\partial \Psi}{\partial \mathbf{E}_0}\right) : \dot{\mathbf{E}}_0 - \left(\rho_0 \mathrm{s} + \frac{\partial \Psi}{\partial \Theta}\right) : \dot{\Theta} - \frac{1}{\Theta}\mathbf{G}\,\mathrm{GRAD}\,\Theta - \sum_{\alpha=1}^{n} \frac{\partial \Psi}{\partial \mathbf{X}_{\mathrm{v}_\alpha}} : \dot{\mathbf{X}}_{\mathrm{v}_\alpha} \geq 0. \tag{2.4.21}$$

In case the 2.Piola-Kirchhoff stress tensor is used, it follows

$$\left(\mathbf{S} - 2\frac{\partial \Psi}{\partial \mathbf{C}}\right) : \frac{1}{2}\dot{\mathbf{C}} - \left(\mathbf{D}_0 + \frac{\partial \Psi}{\partial \mathbf{E}_0}\right) : \dot{\mathbf{E}}_0 - \left(\rho_0 \mathrm{s} + \frac{\partial \Psi}{\partial \Theta}\right) : \dot{\Theta} - \frac{1}{\Theta}\mathbf{G}\,\mathrm{GRAD}\,\Theta - \sum_{\alpha=1}^{n} \frac{\partial \Psi}{\partial \mathbf{X}_{\mathrm{v}_\alpha}} : \dot{\mathbf{X}}_{\mathrm{v}_\alpha} \geq 0. \tag{2.4.22}$$

[15] See Tab.2.1

[16] A formulation for an entropic elastic material is given on page 335 in Holzapfel [76].

According to the argumentation in Coleman and Noll [78] follows

$$\mathbf{S} = 2\frac{\partial \Psi}{\partial \mathbf{C}}, \tag{2.4.23}$$

$$\mathbf{D}_0 = -\frac{\partial \Psi}{\partial \mathbf{E}_0}, \tag{2.4.24}$$

$$\rho_0 \mathrm{s} = -\frac{\partial \Psi}{\partial \Theta}. \tag{2.4.25}$$

The rest of Eq. (2.4.22) defines the energy dissipation

$$\mathscr{D} = \underbrace{-\frac{1}{\Theta}\mathbf{G}\,\mathrm{GRAD}\,\Theta}_{\mathscr{D}_\Theta} \underbrace{-\sum_{\alpha=1}^{n} \frac{\partial \Psi}{\partial \mathbf{X}_{\mathrm{v}_\alpha}} : \dot{\mathbf{X}}_{\mathrm{v}_\alpha}}_{\mathscr{D}_\mathrm{v}} \geq 0, \tag{2.4.26}$$

where $\mathscr{D}_\Theta$ is the thermal and $\mathscr{D}_\mathrm{v}$ the viscous part.

2.5 Evolution of viscous dissipation

Different approaches to describe the evolution of viscous dissipation can be found in literature. In Reese and Govindjee [79, 80], viscous dissipation $\mathscr{D}_\mathrm{v}$ is formulated in an positive definite, quadratic form.

$$\mathscr{D}_\mathrm{v} = -\sum_{\alpha=1}^{n} \frac{\partial \Psi}{\partial \mathbf{C}_{\mathrm{v}_\alpha}^{-1}} : \dot{\mathbf{C}}_{\mathrm{v}_\alpha}^{-1} = -\frac{1}{2}\sum_{\alpha=1}^{n} \boldsymbol{\tau}_{\mathrm{v}_\alpha} : (\mathscr{L}_\mathrm{v}\mathbf{b}_{\mathrm{e}_\alpha} \cdot \mathbf{b}_{\mathrm{e}_\alpha}{}^{-1}). \tag{2.5.1}$$

$\boldsymbol{\tau}_{\mathrm{v}_\alpha}$ is the non-equilibrium Kirchhoff stress in the α-th Maxwell element.[17] $\mathscr{L}_\mathrm{v}\mathbf{b}_{\mathrm{e}_\alpha}$ is the Lie time derivative of the α-th contravariant tensor $\mathbf{b}_{\mathrm{e}_\alpha} = \mathbf{F}_{\mathrm{e}_\alpha}\mathbf{F}_{\mathrm{e}_\alpha}{}^T$, which describes the elastic strain in the α-th Maxwell element.[18] $\mathbf{C}_{\mathrm{v}_\alpha}^{-1} = \mathbf{F}_{\mathrm{v}_\alpha}^{-1}\mathbf{F}_{\mathrm{v}_\alpha}^{-T} = \mathbf{X}_{\mathrm{v}_\alpha}$ is the α-th tensor of internal variables. A non-linear viscoelastic evolution is given by

$$-\frac{1}{2}\mathscr{L}_\mathrm{v}\mathbf{b}_\mathrm{e} \cdot \mathbf{b}_\mathrm{e}{}^{-1} = \frac{1}{\hat{\eta}_\mathrm{dev}(\mathbf{b}_\mathrm{e})}\mathrm{dev}\,[\boldsymbol{\tau}_{\mathrm{v}_1}] + \frac{2}{9\hat{\eta}_\mathrm{vol}(\mathbf{b}_\mathrm{e})}\,(\boldsymbol{\tau}_{\mathrm{v}_1} : \mathbf{1})\,\mathbf{1}. \tag{2.5.2}$$

$\hat{\eta}_\mathrm{dev}$ and $\hat{\eta}_\mathrm{vol}$ are the isochoric and hydrostatic dynamic viscosity.[19] A power law type evolution is formulated in Ask et al. [81]

$$\dot{\mathbf{C}}_{\mathrm{v}_\alpha} = \frac{1}{2}\frac{\dot{\gamma}_{0_\alpha}}{M_{0_\alpha}}\mathbf{C}_{\mathrm{v}_\alpha}\mathbf{M}_{\mathrm{v}_\alpha}^{\mathrm{dev}^T} = \dot{\Gamma}_\alpha \mathbf{C}_{\mathrm{v}_\alpha}\mathbf{M}_{\mathrm{v}_\alpha}^{\mathrm{dev}^T} \tag{2.5.3}$$

[17] See Fig. 2.6.2a
[18] See section 3.3.
[19] See section 2.6.2.

where $\dot{\gamma}_{0_\alpha} > 0$ and $M_{0_\alpha} > 0$ are material parameters. $\mathbf{M}_{\mathrm{v}_\alpha}$ is a Mandel type referential stress given as

$$\mathbf{M}_{\mathrm{v}_\alpha} = -\rho_0 \mathbf{C}_{\mathrm{v}_\alpha} \cdot \frac{\partial \Psi_\alpha}{\partial \mathbf{C}_{\mathrm{v}_\alpha}} = \rho_0 \frac{\partial \Psi_\alpha}{\partial \mathbf{C}_{\mathrm{v}_\alpha}^{-1}} \cdot \mathbf{C}_{\mathrm{v}_\alpha}{}^{-1}. \tag{2.5.4}$$

By Bonet [82], a linear rate that follows from the standard linear solid model is defined by

$$\dot{\mathbf{C}}_{\mathrm{v}_\alpha} = -\frac{1}{T_\alpha} \left[\frac{\partial \mathbf{S}_{\mathrm{v}_\alpha}}{\partial \mathbf{C}_{\mathrm{v}_\alpha}} \right]^{-1} : \mathbf{S}_{\mathrm{v}_\alpha}. \tag{2.5.5}$$

2.6 Polymer physical consideration of viscous effects

Polymer physical correlations are essential to understand viscous effects in polymers. In this section a very short summary of physical descriptions and models for viscous behaviour is given that starts with an explanation of the glass transition and goes further to show basic rheology concepts and some aspects of micromechanical mechanisms and rubber elasticity.[20] This section primarily demonstrates that the background of viscoelastic effects in polymers is diverse as chemical structures and earns a more intensive treatment than what can be achieved in the frame of this thesis.

2.6.1 Glass/rubber transition

In polymers, the order of transition is specified by the degree of crystallinity. In crystalline polymers occur first order transitions from solid to liquid, whereas amorphous or semicrystalline polymers have second order transitions. The glass transition is a second order transition, named after the softening of ordinary glass. The glass transition is the most important parameter for the classification of mechanical behaviour for amorphous polymers whereby the glass transition temperature T_g marks the separation between the glassy and the viscous state. T_g is indicated by discontinuities of thermodynamic state functions or variables like volume, entropy or enthalpy, and by discontinuities of material parameters like thermal expansion and heat capacity. T_g is identifiable also in the temperature functions of mechanical moduli (G, Y)[21] and in loss parts of complex moduli $(G^{''}, Y^{''})$, which have a maximum at T_g.[22]

In the temperature function of Young's modulus of amorphous polymers, five sections can be identified like illustrated in Fig. 2.6.1. In section (1), the glassy region, the Young's modulus is constant. This section can be approximated by using the Lennard-Jones potential for polymers, which describes the interaction between a pair of isolated molecules or carbon-carbon bonds. In the glass transition region, section (2), between 20 °C and 30 °C, the Young's modulus drops down with a factor of 1000. The polymer behaves leatherlike. On the rubbery plateau, section (3), the Young's modulus does not strongly vary within a temperature range and typical elastomer behaviour is given. For section (4), the rubbery

[20] A derivation of mathematical expressions to describe viscous behaviour is not reviewed. For the interested reader Schwarzl [83] is recommended.

[21] See Fig. 2.6.1

[22] See appendix A.2.

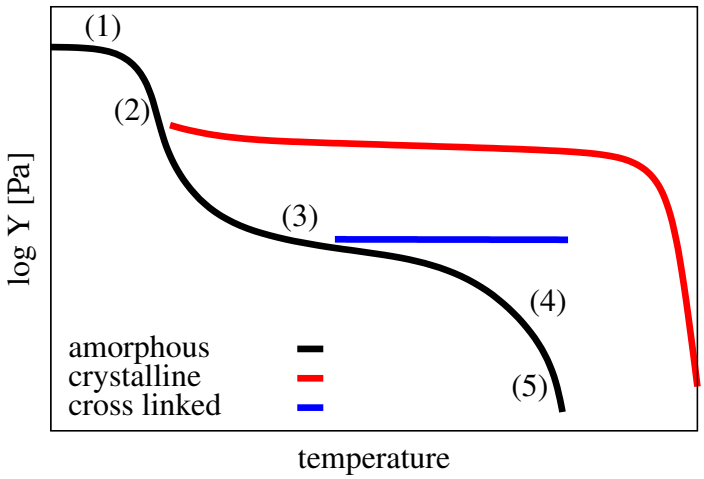

Figure 2.6.1.: Qualitative presentation of the temperature dependence of polymer's Young's modulus. Black line is valid for amorphous polymers and can be divided into 5 sections: (1) glassy region, (2) glass transition region, (3) rubbery plateau, (4) rubbery flow region and (5) liquid flow region.

flow region, a combination of hyperelastic and viscous behaviour can be assumed. Section (5) is called the liquid flow region, where the polymer behaves like a liquid.

2.6.2 Rheology

The field of rheology is concerned with the flow properties of solid bodies observable by the two macroscopic phenomena relaxation and creep. Viscous processes are parametrised by the physical quantity η with unit [Pa s], which determines the shear or dynamic viscosity. Ideal viscous behaviour is described by $\tau = \eta\dot{\gamma}$, where τ is the shear stress and $\dot{\gamma}$ the shear rate.[23]

Rheological models illustrate the viscous, time-dependent deformation of solids. Different types of flow behaviour can be modelled by combining rheological elements like springs, dashpots, friction-, gap- or fractional elements. Kinematical expressions can be derived from these models. The basic elements to map linear viscoelastic behaviour are spring and dashpot. Plastic behaviour is modelled using friction elements. For viscoelastic polymers mainly two classical rheological models are of interest[24]: The Generalised Maxwell or Wiechert model, and the Generalised Kelvin model. Both models are shown subsequently in Fig. 2.6.2.

[23] For the normal stress follows $\sigma = \eta_E\dot{\varepsilon}$ where $\eta_E = 3\eta$ is the elongation viscosity [84].

[24] Less common are rheological models which contain fractional elements that describe time-dependent behaviour by the sum of fractional derivatives, governed by an order parameter [85, 86].

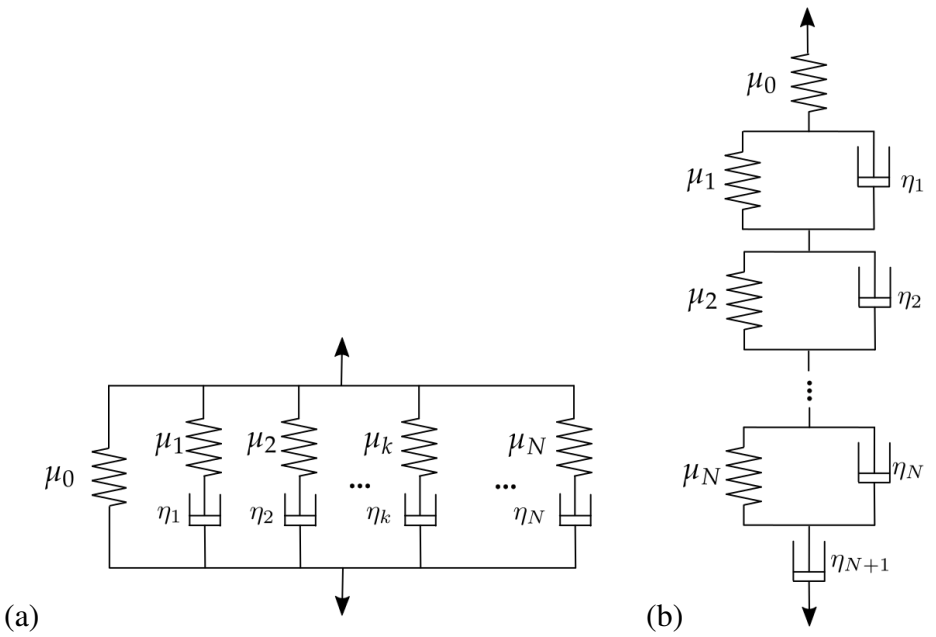

Figure 2.6.2.: (a) Generalised Maxwell or Wiechert model with Maxwell elements $\alpha = 1, .., N$, (b) Generalised Kelvin model.

Viscous behaviour is described by two time functions, creep function $J(t)$ and relaxation function $G(t)$ that have following properties

$$\left.\begin{array}{l} J(t) > 0 \\ \\ \dot{J}(t) \geq 0 \end{array}\right\} \quad 0 \leq t < \infty$$

$$\left.\begin{array}{l} G(t) \geq 0 \\ \\ \dot{G}(t) \leq 0 \end{array}\right\} \quad 0 \leq t < \infty.$$

The limits for $t \rightarrow 0$ are J_0 and G_0. The relation $J(t) \cdot G(t) \leq 1$ is hold $\forall\ t$. The Boltzmann time-temperature superposition can be applied to describe viscous behaviour within a frequency-, temperature- or time-range.[25] Within a time-range, time-dependent stresses can be summarised as $\sum_{i=1}^{n} \tau_i(t)$ that generates a sum of time-dependent deformations $\sum_{i=1}^{n} \gamma_i(t)$. The superposition principle, applicable for linear viscosity, enables the formulation of discrete relaxation and creep spectra, which are in reference to a Generalised Maxwell model given as

$$\begin{aligned} G(t) &= \mu_0 + \sum_{\alpha=1}^{n} \mu_\alpha e^{-\frac{t}{T_\alpha}}, \\ J(t) &= J_0 + \sum_{\alpha=1}^{m} b_i \left[1 - e^{-\frac{t}{T_a}}\right] + \frac{t}{\eta_0}. \end{aligned} \tag{2.6.1}$$

[25] The Boltzmann superposition principle is applied also in the Williams-Landel-Ferry (WLF) equation that extrapolates frequency or time-dependent material data from measured data.

Herein b_i are material parameters and η_0 is the reciprocal of the fluidity φ_0, which is the slope of the creep function at infinite time

$$\lim_{t\to\infty} \dot{J}(t) = \varphi_0 = \frac{1}{\eta_0}. \tag{2.6.2}$$

Microscopic mechanism of viscosity

On the micro-scale physical and chemical mechanisms are involved in viscous processes. Five of them are listed down here [87]:

1. Chain scission due to oxidative degradation and hydrolysis that causes stress relaxation,
2. Bond interchange, at polyesters and polysiloxanes,
3. Viscous flow caused by chain slipping under stress,
4. Thiriton relaxation, recovery of cross-links and entanglements,
5. Molecular relaxation, near the glass transition temperature.

Rubber elasticity

In rubber or entropic elastic materials the internal energy is hardly changed by mechanical stretch. Polymer chains are smoothed by tension and entropy is therefore reduced which releases heat. When tension is taken back, the polymer chain entanglement becomes stronger, the entropy is increased and the polymer cools down. This phenomenon of thermoelastic coupling is referred to as Gough-Joule effect. The consideration of this specific effect can be important in context with electromechanical coupling, since the permittivity is temperature dependent.[26]

2.7 Numerics

It is assumed that common numerical basics like the Finite-Element method [90, 91] including the isoparametric concept, Gaussian quadrature, Newton-Raphson method are known by the reader, so that they need not to be repeated here. In the frame of this thesis, a numerical concept to describe a deformation-dependent load was applied, which is outlined in this section.

2.7.1 Deformation-dependent load

Loads that act perpendicular to a surface change their direction if the surface is deformed, the load magnitude can be changed also.[27] The former situation where load magnitude remains unchanged is

[26] One approach to describe thermo-viscoelastic behaviour assuming an Ogden material is made in [79]. A thermo-viscoelastic model is presented also in [88, 89].

[27] The Coulomb force due to polarised surfaces is direction-dependent and described with the numerical concept depicted in this section.

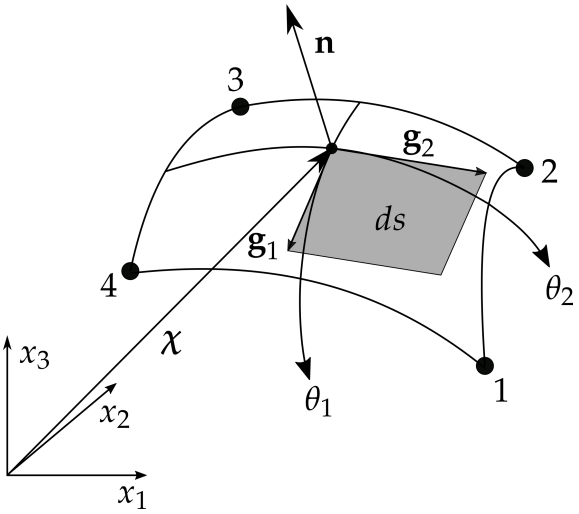

Figure 2.7.1.: Surface-dependent load.

assumed here to formulate the virtual work $g_{l_d}(\boldsymbol{\chi}, \delta\boldsymbol{\chi})$ of a direction depending load l_d with respect to current configuration

$$g_{l_d}(\boldsymbol{\chi}, \delta\boldsymbol{\chi}) = \int\limits_{\partial\Omega_{l_d}} l_d \, \mathbf{n} \cdot \delta\boldsymbol{\chi} \, ds. \tag{2.7.1}$$

$\partial\Omega_{l_d}$ represents a physical surface, and $\delta\boldsymbol{\chi}$ is a virtual displacement. The surface normal $\mathbf{n}$ on a surface increment ds can be expressed by the cross product of tangents to curvilinear axes (θ_1, θ_2), like shown in Fig. 2.7.1. The tangent vectors $\mathbf{g}_1$ and $\mathbf{g}_2$ are calculated by the derivative of the midpoint position vector $\boldsymbol{\chi}$ with respect to convective coordinates

$$\mathbf{g}_\alpha = \boldsymbol{\chi}_{,\alpha} = \frac{\partial \boldsymbol{\chi}}{\partial \theta_\alpha}, \ \alpha = 1, 2. \tag{2.7.2}$$

The surface normal is defined by

$$\mathbf{n} = \frac{\mathbf{g}_1 \times \mathbf{g}_2}{||\mathbf{g}_1 \times \mathbf{g}_2||}, \tag{2.7.3}$$

the surface increment is

$$ds = ||\mathbf{g}_1 \times \mathbf{g}_2|| \, d\theta_1 d\theta_2. \tag{2.7.4}$$

From inserting equation Eq. (2.7.2), Eq. (2.7.3) and Eq. (2.7.4) into Eq. (2.7.1), it follows the virtual work with respect to curvilinear coordinates

$$g_{l_d}(\boldsymbol{\chi}, \delta\boldsymbol{\chi}) = \int\limits_{\theta_1} \int\limits_{\theta_2} l_d \, \left(\boldsymbol{\chi}_{,1} \times \boldsymbol{\chi}_{,2}\right) \cdot \delta\boldsymbol{\chi} \, d\theta_1 d\theta_2. \tag{2.7.5}$$

Assuming $\boldsymbol{\chi} = \mathbf{u} + \mathbf{X}$[28] and thus $\boldsymbol{\chi}_{,\alpha} = \mathbf{u}_{,\alpha} + \mathbf{X}_{,\alpha}$, the linearisation of Eq. (2.7.5) is given as in [92]

$$Dg_{l_d} \cdot \Delta\mathbf{u} = \Delta g_{l_d} = \int\limits_{\theta_1} \int\limits_{\theta_2} l_d \, \left(\Delta\mathbf{u}_{,1} \times \boldsymbol{\chi}_{,2} + \boldsymbol{\chi}_{,1} \times \Delta\mathbf{u}_{,2}\right) \cdot \delta\boldsymbol{\chi} \, d\theta_1 d\theta_2. \tag{2.7.6}$$

[28] See Eq. (2.3.1) and Eq. (2.3.3)

For the current configuration follows

$$Dg_{l_d} \cdot \Delta\mathbf{u} = \Delta g_{l_d} = \int\limits_{\partial\Omega_{l_d}} l_d \frac{\left(\Delta\mathbf{u}_{,1} \times \boldsymbol{\chi}_{,2} + \boldsymbol{\chi}_{,1} \times \Delta\mathbf{u}_{,2}\right)}{||\boldsymbol{\chi}_1 \times \boldsymbol{\chi}_2||} \cdot \delta\boldsymbol{\chi}\, ds. \tag{2.7.7}$$

A transformation of Eq. (2.7.7) into the reference configuration can be carried out by using following relations

$$\frac{ds}{dS} = \frac{||\mathbf{g}_1 \times \mathbf{g}_2||}{||\mathbf{G}_1 \times \mathbf{G}_2||} = \frac{||\boldsymbol{\chi}_{,1} \times \boldsymbol{\chi}_{,2}||}{||\mathbf{X}_{,1} \times \mathbf{X}_{,2}||}. \tag{2.7.8}$$

Assuming the natural coordinates ξ, η instead of convective, the concept for direction-dependent load can be included into the isoparametric concept.

3 Viscous Pull-in instability

3.1 Introduction

Experimental examination of dielectric elastomers (DEs) starts with the work of Kornbluh et al. 1991 and Pelrine et al. 1997 who suggested dielectric elastomer as material for artificial muscles and microactuators. A strong scientific interest leads to continuum models to describe non-linear electromechanical coupled behaviour [93, 94, 95, 96]. Of particular interest for this work are the large deformation models introduced in Dorfmann and Ogden [94, 96] where hyperelastic energy density functions for dielectric material are defined, and a theoretical framework of governing equations for the analysis of electromechanical boundary value problems is given.

Viscous effects like relaxation, creep and rate dependency which also show in rate sensitive deformation behaviour, play an important role in hyperelastic dielectrics because of the working range of elastomers lies above the glass transition temperature. Torsional dynamic mechanical thermal analysis (DMTA) of VHB 4910 has shown that the mechanical loss factor or phase shift $\tan\,\delta$ is a highly non-linear function of temperature.[1] The phase shift is especially strong between $-25\,^{\circ}\mathrm{C}$ and $25\,^{\circ}\mathrm{C}$.

Large deformation continuum models for viscoelastic dielectric elastomers using the Finite-Element method are introduced in [81, 97, 98, 99, 100, 101, 102, 103] whereby in particular the descriptions in Ask et al., Park and Nguyen, Büschel et al., Ask et al. [81, 101, 102, 103] were regarded intensively. None of these models include pre-stretch that is however important to improve the electromechanical performance.

The chapter is organised as follows: The free energy density Ψ, and stresses for a dielectric, incompressible, pre-stretched, viscous Neo-Hooke material are introduced in section 3.2 of this chapter. In section 3.3 this energy formulation is used to analyse the deformation behaviour and the "Pull-in instability" of a rectangular dielectric elastomer membrane of VBH49 under voltage control. The impact of cross-linking on the dynamic deformation behaviour is examined in subsection 3.3.1 by exchanging the Neo-Hooke energy with an Arruda-Boyce energy formulation.[2]

[1] See Michel et al. [21]. Guo et al. [27] show clearly that about 20 Maxwell elements are necessary to map the relaxation spectrum of a Generalised Maxwell model.

[2] A further reason for the use of an Arruda-Boyce energy was the popularity of this model in context with continuum mechanical descriptions of fluoropolymers [104]. The application in an analytical example enables a better understanding of such kind of models.

3.2 Free energy density considering pre-stretch

The free energy density of a **dielectric**, elastic or **hyperelastic**, **pre-stretched** material is assumed to consist of four parts: Instantaneous elastic energy Ψ_0, viscoelastic or time-dependent energy $\sum_\alpha \Psi_{\mathrm{v}_\alpha}$, electrostatic energy Ψ_{el} and external energy due to pre-stretch W.[3] The free energy density Ψ is[4]

$$\Psi(\mathbf{C}, \mathbf{C}_{\mathrm{v}_\alpha}) = \underbrace{\Psi_0(\mathbf{C})}_{\text{instantaneous}} + \underbrace{\sum_\alpha \Psi_{\mathrm{v}_\alpha}(\mathbf{C}, \mathbf{C}_{\mathrm{v}_\alpha})}_{\text{time-dependent}} + \underbrace{\Psi_{\mathrm{el}}(\mathbf{C})}_{\text{electric}} - \underbrace{\mathrm{W}(\mathbf{F}_{\mathrm{pe}}{}^{\mathrm{T}}\mathbf{F})}_{\text{pre-stretch}}, \tag{3.2.1}$$

with

$$\begin{aligned} \mathbf{C} &= \mathbf{F}^{\mathrm{T}}\mathbf{F}, \\ \mathbf{C}_{\mathrm{v}_\alpha} &= \mathbf{F}_{\mathrm{v}_\alpha}^{\mathrm{T}}\mathbf{F}_{\mathrm{v}_\alpha}. \end{aligned} \tag{3.2.2}$$

$\mathbf{C}$ is the right Cauchy-Green tensor, $\mathbf{C}_{\mathrm{v}_\alpha}$ the viscous right Cauchy-Green tensor. $\mathbf{F}_{\mathrm{v}_\alpha}$ is the α's viscous part of deformation gradient containing 6 internal variables that are convertible into each other in case of isotropy and uniaxial stress. With the sum over α, several nonequilibrium parts are given simultaneously. The condition $\det \mathbf{F}_{\mathrm{v}_\alpha} = 1$ describes the isochoric character of viscous deformation. In case an equilibrium state is reached the movement of dashpots stop and $\det \mathbf{F}_{\mathrm{v}_\alpha} = \det \mathbf{F}$. Because the system's energy is changed by pre-stretch an external work W has to be considered and pre-stretches have to be included in the deformation gradient. A pre-stretch augmented Cauchy-Green tensor is written as

$$\mathbf{C} = \mathbf{F}^{\mathrm{T}}\mathbf{F}_{\mathrm{pe}}\mathbf{F}_{\mathrm{pe}}{}^{\mathrm{T}}\mathbf{F}. \tag{3.2.3}$$

The free energy density of an incompressible Neo-Hooke material can be assumed as

$$\Psi_0(\mathbf{C}) = \frac{1}{2}\mu(\operatorname{tr}\mathbf{C} - 3), \tag{3.2.4}$$

μ is interpreted as the shear modulus of single spring in the Generalised Maxwell model. From Eq. (3.2.4) a viscous energy density

$$\Psi_{\mathrm{v}_\alpha}(\mathbf{C}, \mathbf{C}_{\mathrm{v}_\alpha}) = \frac{1}{2}\beta_\alpha\mu(\mathbf{C} : \mathbf{C}_{\mathrm{v}_\alpha}^{-1} - 3) \tag{3.2.5}$$

is determined for the Maxwell elements [82]. $\beta_\alpha \in \mathbb{R}^+$ are material parameters. $\beta_\alpha\mu$ comply with the shear moduli of springs in α-Maxwell elements.

The electrostatic energy in vacuum is given according to Dorfmann and Ogden [94] for compressibility and incompressibility as

$$\Psi_{\mathrm{el}}(\mathbf{C}) = -\frac{1}{2}\epsilon_0 J\mathbf{E}_0 \cdot (\mathbf{C}^{-1}\mathbf{E}_0), \tag{3.2.6}$$

[3] Dielectric dissipation is not considered in this approach.

[4] A split of the deformation gradient into volumetric and isochoric parts is not carried out, for the material is incompressible.

and

$$\Psi_{\text{el}}(\mathbf{C}) = -\frac{1}{2}\epsilon_0 \mathbf{E}_0 \cdot (\mathbf{C}^{-1}\mathbf{E}_0). \tag{3.2.7}$$

$\mathbf{E_0}$ is the electric field vector in the reference configuration, ϵ_0 the dielectric constant. The external energy due to pre-stretch is not described in detail because it is not considered in the element stiffness matrix. The entries of $\mathbf{F}_{\text{pre}}$ can be stored as history variables defined in an upstream calculation and are read in as initial condition. The model introduced here is modified for the description of dielectric bulk material in ferroelectret structures in chapter 4.

The mechanical stress parts are obtained by the partial derivative of energy parts with respect to deformation. The stresses are given here with respect to the reference configuration using the 2.Piola-Kirchhoff stress tensor[5]

$$\mathbf{S} = 2\frac{\partial \Psi}{\partial \mathbf{C}}. \tag{3.2.8}$$

The hyperelastic and visco-hyperelastic stress parts are[6]

$$\begin{aligned} \mathbf{S}_0 &= \mu(\mathbf{1} - \frac{1}{3} I_1 \mathbf{C}^{-1}),\ I_1 = \text{tr}\ \mathbf{C}, \\ \mathbf{S}_{\text{v}_\alpha} &= \beta_\alpha \mu \left[\mathbf{C}_{\text{v}_\alpha}^{-1} - \frac{1}{3}(\mathbf{C} : \mathbf{C}_{\text{v}_\alpha})\mathbf{C}^{-1} \right]. \end{aligned} \tag{3.2.9}$$

The derivative of electrostatic energy for a compressible material by assuming J=1, leads to a Maxwell stress tensor of[7].

$$\mathbf{S}^{\text{E}} = \epsilon_0 \mathbf{E}_0 \cdot \left[\left(\mathbf{C}^{-1} \otimes \mathbf{C}^{-T} \right)^{\overset{23}{T}} \mathbf{E}_0 \right] - \epsilon_0 \frac{1}{2} \mathbf{C}^{-1} \left[\mathbf{E}_0 \cdot \left(\mathbf{C^{-1}} \mathbf{E}_0 \right) \right]. \tag{3.2.10}$$

3.3 Viscous, dynamic Pull-in instability

DE actuators suffer from failure mechanisms. One relevant structural failure is **electromechanical** or **Pull-in instability** that occurs for voltage-control. Pull-in instability arises when the energy stored in the material can no longer compensate the electric energy. This happens when a critical membrane compression is reached under the influence of an electric field between compliant electrodes. Usually a collapse of the device is initiated then; this shows in a snap-trough for rotation symmetric membranes. In experiments for other geometries that have constrained edges, wrinkle patterns are an indication of Pull-in instability. Godaba et al. [105] propose that wrinkled regions and snap-through are two structural modi that go along with an electromechanical phase transition. Pull-in instability is the dominant failure mechanism for low stretch rates and pre-stretches up to 10 for circular actuators [29]. In this work of Plante and Dubowsky experiments were conducted also for diamond actuators which show similar trends for pre-stretches up to 20. Dynamic Pull-in is experimentally investigated in Fox and Goulbourne

[5] See Eq. (2.4.23).

[6] For more details see [82].

[7] $\overset{23}{T}$ means that the 2. and the 3. component of the tensor are transposed.

and Gonçalves et al. [106, 107]. For the unconstrained rectangular DEA regarded here, instantaneous Pull-in becomes obvious by a divergence of the numerical solution of the equation of motion (EOM), reflected in an asymptotical increase of compression, and kinetic energy. Electric fields smaller than a critical value initiate a delayed Pull-in; the viscous dissipation leads to a time-dependent thinning of the membrane.

Analytical prediction methods in literature consider primarily two mechanical boundary conditions and membrane geometries whereby viscoelastic effects are neglected. A rectangular geometry with free edges was assumed by Zhao and Suo [108, 109] who proposed a method based on the positive definiteness of the Hessian. This method was applied for stability analysis of other materials also [110, 111, 112]. Using Lagrange multipliers, Xu et al. [113] presented an explicit solution for the estimation of the critical electric field in biaxially stretched hyperelastic rectangular DEAs. Zhu et al., Rudykh et al., Li et al. [114, 115, 116] have investigated diaphragm DEAs that have clamped edges. De Tommasi et al. [117] calculated critical values for Pull-in and Wrinkling Instability for an biaxially stretched rectangular actuator of Neo-Hookean material. They have assumed that Wrinkling instability is connected with compression stresses that cannot be transferred by a membrane. Suo et al. [118] used a Hadamard type condition to determine local bifurcation. Dorfmann and Ogden [119] have presented an incremental formulation of non-linear electrostatics and investigated the buckling stability of a half space in plane strain state. Calculation results show a dependence of the critical stretch on dielectric displacement. The same authors have investigated diffuse modes of instability of an electroelastic plate whereby the plate thickness was taken into account [120]. They have demonstrated that plate thickness influences the buckling stretch; this dependence cannot be reproduced by the Hessian approach. Making use of the framework of Dorfmann and Ogden, Rudykh and Bhattacharya [121, 122] have examined the material stability of layered DE composites as a function of lamination angle and phases. If the lamination angle is greater than $\pi/4$, instabilities only arise under tension. By increasing the stiffer phase fraction, stable regions are expanded.

Initially investigated in the 1950s in context of metal structures at elevated temperatures [123, 124, 125], many publications are concerned with the influence of viscous effects on buckling behaviour. In Ziegler [126] and Hoff [127] static and kinetic assumptions in context of stability analysis of merely mechanical systems were compared. From the discussion was concluded, that non-conservative systems can only be analysed well by using kinetic stability criteria.

Dynamic stability of DEAs has been less frequently investigated. One approach was introduced by Xu et al. [128] who made use of the Euler-Lagrange equation to derive an EOM for hyperelastic DEAs, and studied the stability behaviour for constant and sinusoidal voltage. Based on the Hessian, Zhu [129] derived an EOM which includes pre-stretch. In particular they provided numerical studies of stability under cyclic voltage. Joglekar [130, 131] proposed an interesting analytical model to extract the critical values of dynamic responses for pre-stretched DEAs excited by a step voltage; the obtained critical values show a good agreement with numerical results published in Xu et al. [128].

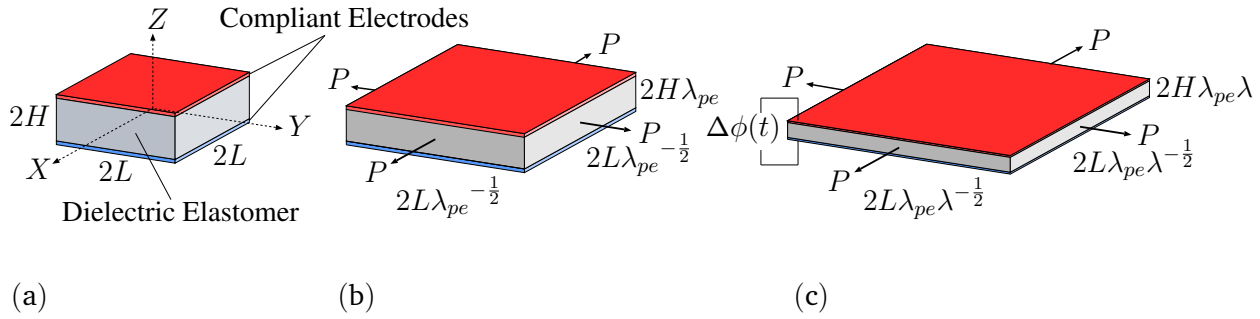

Figure 3.3.1.: Deformation of an electroactive membrane due to biaxial pre-loads P, and voltage perpendicular to membrane plane: (a) Undeformed state, (b) Pre-loads in equilibrium position, (c) Pre-stretched DEA deformed by voltage.

In Eder-Goy et al. [132] an energy approach is described to calculate critical Pull-in parameters considering viscous and inertia effects. To obtain the EOM for a system like illustrated in Fig. 3.3.1.[8], a non-conservative Euler-Lagrange scheme is used.

$$\frac{d}{dt}\left(\frac{\partial \mathcal{L}}{\partial \dot{q}_i}\right) - \frac{\partial \mathcal{L}}{\partial q_i} + \frac{\partial \mathscr{D}_\mathrm{v}}{\partial \dot{q}_i} = 0 \quad i = 1, 2. \tag{3.3.1}$$

In the scheme, written in Eq. (3.3.1), $\mathcal{L}$ is the Lagrangian, $\mathscr{D}_\mathrm{v}$ is the dissipation function and q_i are the generalised coordinates. A hyperelastic, incompressible material like in Eq. (3.2.1) is assumed. For the isotropic material, uniaxial compression is formulated in main stretches [133]. Hence, the deformation gradient after relaxation of the viscous overpotential due to pre-stretch is written as

$$\mathbf{F}_\mathrm{pre}\mathbf{F}^\mathrm{T} = \begin{bmatrix} \lambda_{pe}^{-\frac{1}{2}}\lambda^{-\frac{1}{2}} & 0 & 0 \\ 0 & \lambda_{pe}^{-\frac{1}{2}}\lambda^{-\frac{1}{2}} & \\ 0 & 0 & \lambda_{pe}\lambda \end{bmatrix}. \tag{3.3.2}$$

Viscous behaviour is modelled by one Maxwell element therefore $\alpha = 1$. The deformation in the Maxwell element expressed by $\mathbf{F}_{\mathrm{M}_1}$ does not contain pre-stretch, for an equilibrium state is assumed to be reached when voltage is applied.

$$\mathbf{F}_{\mathrm{M}_1} = \mathbf{F}_{\mathrm{e}_1}{\mathbf{F}_{\mathrm{v}_1}}^{-1} = \begin{bmatrix} \lambda^{-\frac{1}{2}}\lambda_v^{\frac{1}{2}} & 0 & 0 \\ 0 & \lambda^{-\frac{1}{2}}\lambda_v^{\frac{1}{2}} & \\ 0 & 0 & \lambda{\lambda_v}^{-1} \end{bmatrix}. \tag{3.3.3}$$

The motion of system is described by two independent degrees of freedom (DOFs) q_1 and q_2 in direction of compression: $q_1 = \lambda = \lambda_3$ is the external stretch, and $q_2 = \lambda_v = \lambda_{v_3}$ is the internal viscous stretch. Since the volume is conserved $\lambda_1\lambda_2\lambda_3 = 1$, and due to symmetry about the x- and y-axis follows $\lambda_1 = \lambda_2 = 1/\sqrt{\lambda_3}$, and one variable $\lambda = \lambda_3$ which is sufficient to describe the external deformation.

[8] Compare with [132].

The out-of-plane pre-compression λ_{pe} is a constant. The Lagrangian is defined by $\mathcal{L} = \mathrm{E_{kin}} - \mathrm{E_{pot}}$. $\mathrm{E_{kin}}$ is the kinetic energy also referred to as T, and $\mathrm{E_{pot}}$ the potential energy also referred to as U. $\mathrm{E_{pot}}$ for the system at hand is

$$\begin{aligned}\mathrm{E_{pot}} = 8L^2H\frac{\mu}{2}[&\underbrace{2\lambda_{pe}^{-1}\lambda^{-1} + \lambda_{pe}^2\lambda^2 - 3}_{\text{hyperelastic}} + \underbrace{\beta_1(2\lambda^{-1}\lambda_v + \lambda^2\lambda_v^{-2} - 3)}_{\text{viscohyperelastic}} \\ &\underbrace{-4(\lambda_{pe}^{-\frac{1}{2}} - \lambda_{pe}^{\frac{5}{2}})(\lambda_{pe}^{-\frac{1}{2}}\lambda^{-\frac{1}{2}} - 1)}_{\text{pre-stretch}} \underbrace{-\frac{\epsilon}{\mu}\lambda_{pe}^{-2}\lambda^{-2}E_0^2}_{\text{electric}}]\,.\end{aligned} \tag{3.3.4}$$

Herein, $\epsilon = \epsilon_0\epsilon_r$ is the permittivity of the dielectric. E_0 is the electric field due to a step voltage, and referred to the reference configuration. The external work done by pre-load is[9]

$$W = 4\int_L^{\lambda_{pe}^{-1/2}\lambda^{-1/2}L} P\,\mathrm{d}x = 4PL(\lambda_{pe}^{-\frac{1}{2}}\lambda^{-\frac{1}{2}} - 1)\,. \tag{3.3.5}$$

The pre-load P is determined by the derivative of potential energy with respect to λ at $t = 0$ when the membrane is relaxed and voltage is not applied yet

$$\frac{\partial \mathrm{E_{pot}}(t=0)}{\partial\lambda} = 8L^2H\frac{\mu}{2}(-2\lambda_{pe}^{-2}\lambda^{-2} + 2\lambda_{pe}^{-2}\lambda^{-2} + \frac{1}{2}\frac{P}{\mu HL}\lambda_{pe}^{-\frac{3}{2}}\lambda^{-\frac{3}{2}}) = 0\,. \tag{3.3.6}$$

Transposing leads to

$$P = 4\mu HL(\lambda_{pe}^{-\frac{1}{2}} - \lambda_{pe}^{\frac{5}{2}})\,. \tag{3.3.7}$$

$\mathrm{E_{kin}}$ is calculated with respect to the current configuration as

$$\mathrm{E_{kin_\Omega}} = \int_\Omega \frac{1}{2}\rho(\dot{x}^2 + \dot{y}^2 + \dot{z}^2)\,\mathrm{d}\Omega \tag{3.3.8}$$

if it is assumed that the membrane rotates around a fixed centre of mass. In the reference configuration the kinetic energy is written like

$$\mathrm{E_{kin_{\Omega_0}}} = \rho(\frac{2}{3}L^4H\dot{\lambda}^2\lambda^{-3}\lambda_{pe}^{-1} + \frac{4}{3}L^2H^3\dot{\lambda}^2\lambda_{pe}^2)\,. \tag{3.3.9}$$

ρ denotes the density of the elastomer. A Rayleigh function is chosen to describe the viscous dissipation

$$\mathscr{D}_\mathrm{v} = \frac{1}{2}\eta\lambda_{pe}\dot{\lambda}_v^2\,8HL^2\,. \tag{3.3.10}$$

[9] See Fig. 3.3.1b

η is the viscous friction or dynamic viscosity. The case derivatives of Eq. (3.3.4), Eq. (3.3.9) and Eq. (3.3.10) are inserted into the Euler-Lagrange scheme, a system of two differential equations follows for the system state shown in Fig. 3.3.1c

$$\begin{aligned}
&\frac{d}{dt}\left(\frac{\partial \mathcal{L}}{\partial \dot{\lambda}}\right) - \frac{\partial \mathcal{L}}{\partial \lambda} = 0 = \\
&\ddot{\lambda} - \frac{3}{2}\frac{1}{\lambda(1+c_1\lambda_{pe}^3\lambda^3)}\dot{\lambda}^2 \\
&+ c_2\lambda_{pe}\left[\frac{\lambda_{pe}^2\lambda^4 - \lambda_{pe}^{-1}\lambda + \frac{\epsilon}{\mu}\lambda_{pe}^{-2}E_0^2 + \beta(\lambda^4\lambda_v^{-2} - \lambda\lambda_v) + (\lambda_{pe}^{-\frac{1}{2}} - \lambda_{pe}^{\frac{5}{2}})\lambda_{pe}^{-\frac{1}{2}}\lambda^{\frac{3}{2}}}{(1+c_1\lambda_{pe}^3\lambda^3)}\right].
\end{aligned} \tag{3.3.11}$$

$$\begin{aligned}
&-\frac{\partial L}{\partial \lambda_v} + \frac{\partial \mathscr{D}}{\partial \dot{\lambda}_v} = 0 = \\
&-8HL^2\beta\mu(-\lambda^{-1} + \lambda^2\lambda_v^{-3}) + 8HL^2\eta\lambda_{pe}\dot{\lambda}_v,
\end{aligned} \tag{3.3.12}$$

with constants: $c_1 = 2H^2/L^2$ and $c_2 = 6\mu/\rho L^2$. Eq. (3.3.11) is the EOM and Eq. (3.3.11) yields an evolution for the internal variable λ_v

$$\dot{\lambda}_v = \frac{1}{\lambda_{pe}T}(-\lambda^{-1} + \lambda^2\lambda_v^{-3}), \quad \text{with} \quad T = \frac{\eta}{\beta\mu}\,. \tag{3.3.13}$$

T is the relaxation time. Using the software Octave, the differential equation system is solved numerically for the initial state at t=0 for a variety of applied electric fields E_0. Geometry parameters are assumed with H=1 $\times$ 10^{-3} m and L=5 $\times$ 10^{-3} m and material parameters for Mat.1 and Mat.2 were taken from appendix A.4.

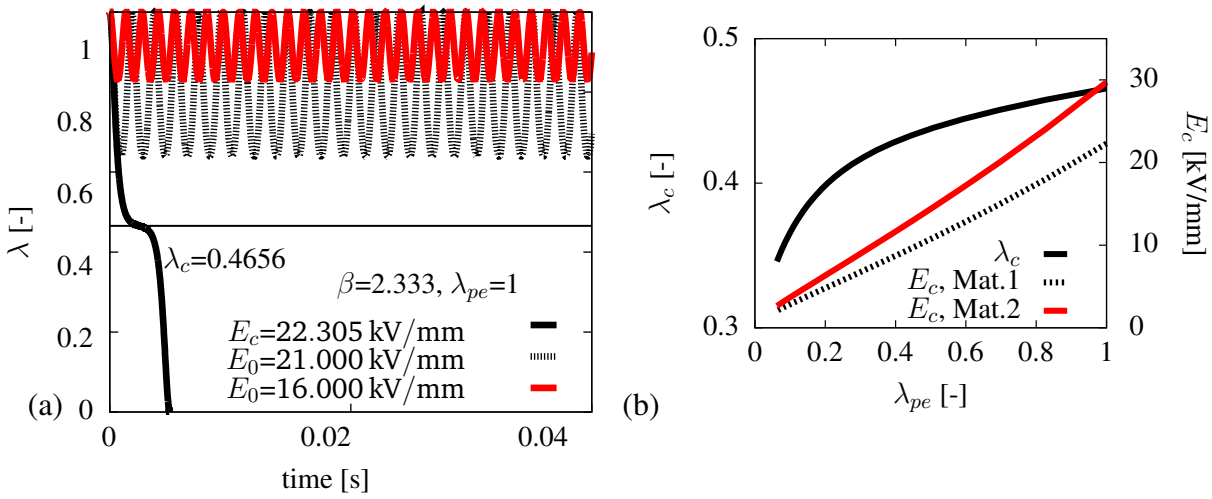

Figure 3.3.2.: Dynamic stretch $\lambda(t)$ and critical Pull-in parameters E_c and λ_c of a rectangular VHB49 membrane (Mat.1) under step voltage.: (a) Functions of $\lambda(t)$ for specified E_0, (b) Impact of pre-stretch on E_c and λ_c.

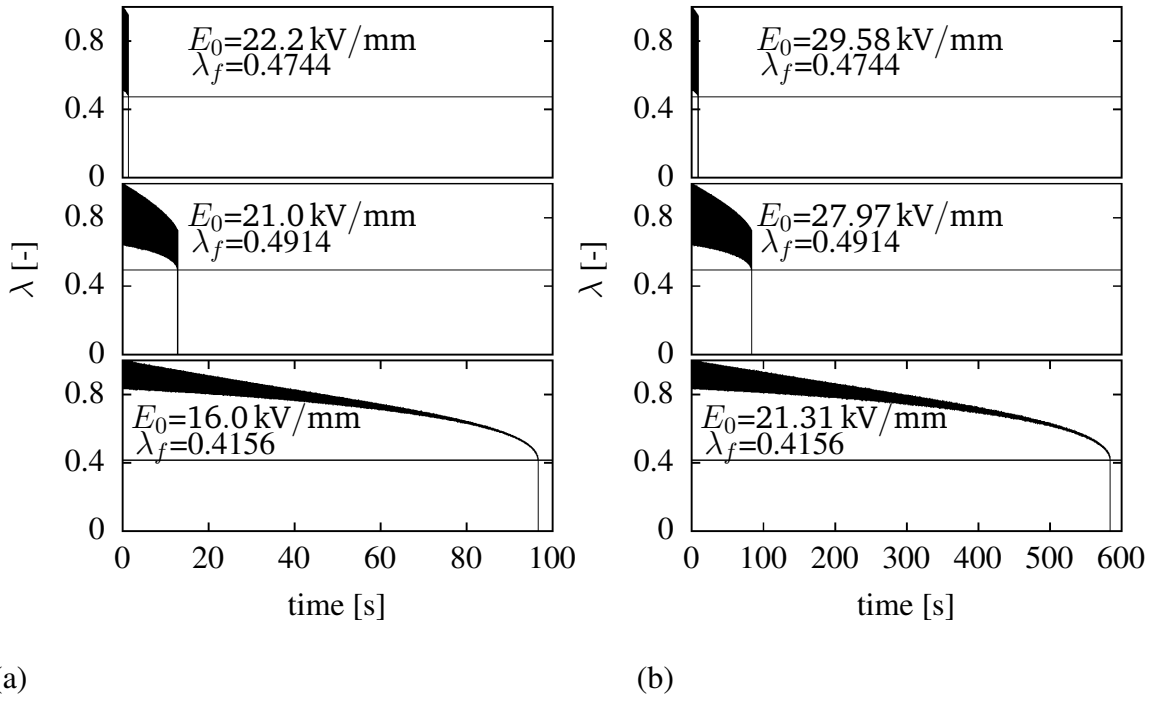

Figure 3.3.3.: Pull-in failure for electric fields below E_c for an unprestretched membrane: (a) Mat.1 (T=72.377 s), (b) Mat.2 (T=200 s). Applied electric fields E_0 are assumed as similar percentages of the material dependent critical field E_c. The stretch at failure λ_f is independent of material parameters. The time to failure t_f is influenced by relaxation time T.

Fig. 3.3.2 shows that the dynamic Pull-in instability is governed by the electric field strength. Pull-in occurs if a critical electric field E_c is applied. The critical stretch λ_c is reached almost instantaneously; the numerical solution is diverging, which is indicated by an asymptotical decrease of λ. An harmonic oscillation of $\lambda(t)$ is observed for electric fields below E_c.[10] Fig. 3.3.2b illustrates that pre-stretch reduces E_c and λ_c. In Fig. 3.3.3 can be seen that the working stroke and the envelopes steadily decrease until the stretch at failure λ_f is reached. The curves in Fig. 3.3.3a and b show that the time to a delayed Pull-in, t_f, is material sensitive, whereas λ_f is a geometry parameter also. For similar percentages in relation to a material-immanent E_c an equal value for λ_f is determined. The lower the electric field, the larger is t_f.[11]

The phase diagrams in Fig. 3.3.4a make clear that λ_c is independent of viscous effects. The viscous phase diagrams in Fig. 3.3.4b show a non-linear, non-monotonic dependence of λ_f on E_0. This can be seen more clearly in Fig. 3.3.5a where a maximum of λ_f is observed between a ratio E_0/E_c of 0.9 and 1.0, whereas the viscous stretch λ_{vf} is strictly decreasing. The same tendencies are discernible under the influence of pre-stretch that shifts the curves for λ_f and λ_{vf} to larger compression like it can be seen in Fig. 3.3.5b.

[10] Compare Fig. 3.3.2.
[11] Material parameters for Mat.1 and Mat.2 are summarised in A.4.

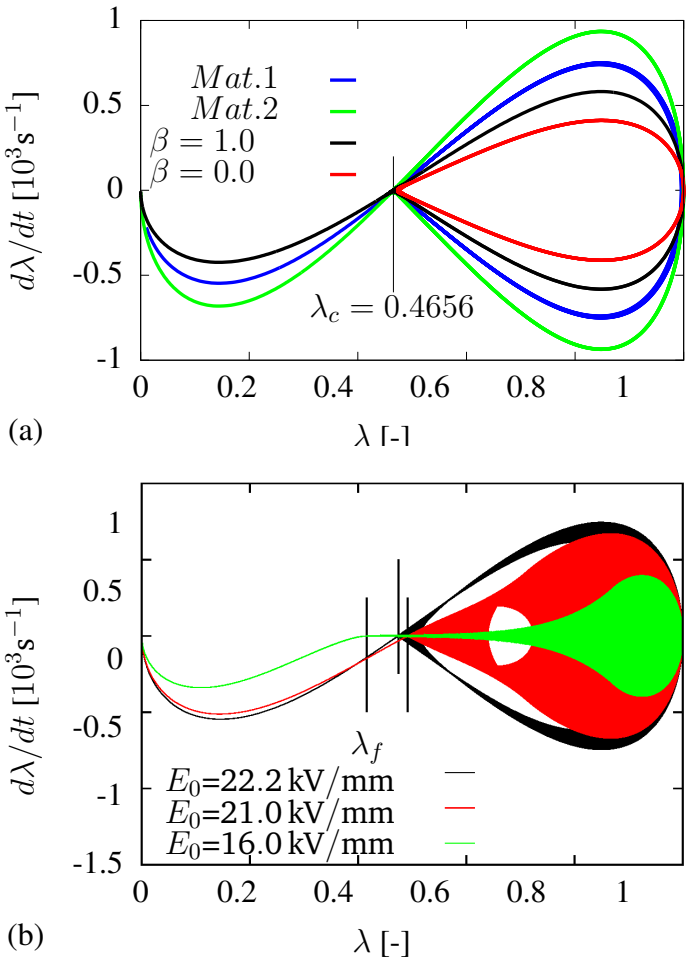

Figure 3.3.4.: Solution of EOM: (a) Phase diagram for Mat.1 and Mat.2. and two values of β for critical electric fields. The curve for $\beta = 0.0$ describes an elastic material. (b) Phase diagrams and stretch at failure λ_f for variations of E_0 for Mat.1 and $\lambda_{pe} = 1.0$.

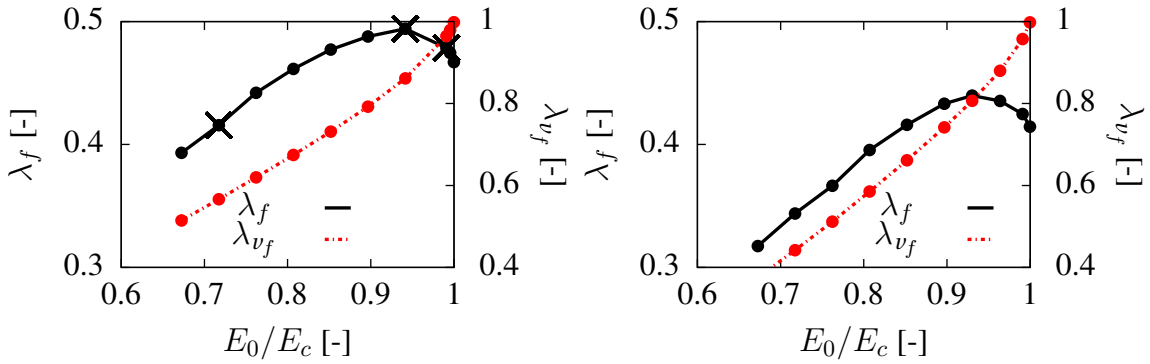

Figure 3.3.5.: Stretch at failure λ_f and corresponding viscous strain λ_{v_f} as functions of E_0/E_c, assuming Mat.1.: (a) $\lambda_{pe} = 1$, (b) $\lambda_{pe} = 1/4$.

Following observations are important: The critical stretch λ_c and the stretch at failure λ_f are geometry parameters in case viscosity is described with the Maxwell model that implements the Boltzmann superposition principle. A comparison between static and dynamic Pull-in parameters for the viscoelastic membrane at hand is made in [132]. Dynamic parameters of the investigated membrane are λ_c=0.4656 and E_c=0.647$\sqrt{\mu/\epsilon(1+\beta)}$, static parameters are λ_c=0.63 and E_c=0.69$\sqrt{\mu/\epsilon(1+\beta)}$. This shows that the system is more sensitive for Pull-in for dynamic assumptions, although the difference of E_c with $2\,\%$ is very small. Furthermore, the λ_c shows that the dynamic system is more compliant than the quasi static system.

The long-term behaviour in dependence on the number of cross-links, governed by viscous effects is investigated in the next section; this aspect is interesting, for the cross-link density and type can be adjusted during the production process of acrylic elastomers.

3.3.1 Influence of cross-links on dynamic deformation

Besides energy functions that are designed by means of empirical observation, energy functions based on microstructure are available in the context with hyperelastic material behaviour. The models by Arruda and Boyce [134] take the contour length of molecular chains and chain movement into account; a parameter N considers the number of cross-links, which governs the elastomeric behaviour. An eight chain invariant based Arruda Boyce model according to Steinmann et al. [133], for an incompressible viscous material, is used here for investigation of the impact of cross-links on the dynamic Pull-in parameters; the energy density is given as

$$\Psi_0(\mathbf{C}) = \mu N \left[\sqrt{N^{-1}}\Lambda\gamma + \ln\left(\frac{\gamma}{\sinh\gamma}\right)\right] \quad \text{with} \tag{3.3.14}$$

$$\Lambda = \frac{r}{r_0} = \frac{r}{\sqrt{Nl}} = \sqrt{\frac{I_1}{3}} = \sqrt{\frac{2\lambda^{-1}+\lambda^2}{3}} \quad \text{and} \tag{3.3.15}$$

$$\gamma = \mathscr{L}^{-1}(\Lambda\sqrt{N^{-1}}) \approx \Lambda\sqrt{N^{-1}}\frac{3N-\Lambda^2}{N-\Lambda^2}. \tag{3.3.16}$$

Λ is the chain stretch that is the actual stretch r divided by the initial end to end chain length r_0 of the undeformed chain, which has a length of $\sqrt{Nl}$ according to random walk statistics. N is the number of cross-links or Kuhn segments that are fictive rigid beams of length l with an arbitrary rotation [134]. I_1 is the first invariant, the trace of the right Cauchy-Green tensor. The right side of equation (3.3.16) is the Padé approximation which substitutes the inverse Langevin's function $\mathscr{L}^{-1}$ used in the formulation of

the free energy of a single Langevin chain [135], μ is the shear modulus. The viscous parts are assumed to be proportional to the time-independent energy Ψ_0

$$\begin{aligned}
\Psi_{\mathrm{v}_\alpha}(\mathbf{C},\mathbf{C}_{\mathrm{v}_\alpha}) = \beta_\alpha \Psi_0(\mathbf{C}_{\mathrm{e}_\alpha}) = \beta_\alpha \mu N \left[\sqrt{N^{-1}}\Lambda_\nu \gamma_\nu + \ln\left(\frac{\gamma_\nu}{\sinh\gamma_\nu}\right)\right] \quad \text{with} \\
\mathbf{C}_{\mathrm{v}_\alpha} = \mathbf{F}_{\mathrm{v}_\alpha}{}^{\mathrm{T}}\mathbf{F}_{\mathrm{v}_\alpha}, \\
\mathbf{C}_{\mathrm{e}_\alpha} = \mathbf{C}\mathbf{C}_{\mathrm{v}_\alpha}{}^{-1} = \mathbf{F}_{\mathrm{e}_\alpha}{}^{\mathrm{T}}\mathbf{F}_{\mathrm{e}_\alpha} \quad \text{and} \\
\Lambda_\nu = \sqrt{\frac{\mathbf{C}:\mathbf{C}_{\mathrm{v}_\alpha}^{-1}}{3}} = \sqrt{\frac{2\lambda^{-1}\lambda_\nu + \lambda^2\lambda_\nu^{-2}}{3}} \quad \text{where} \\
\gamma_\nu \approx \Lambda_\nu \sqrt{N^{-1}} \frac{3N - \Lambda_\nu^2}{N - \Lambda_\nu^2}.
\end{aligned} \tag{3.3.17}$$

The electrostatic energy is chosen as in the model previously introduced in section 3.3, and the dissipation function and geometry as well. Pre-stretch is not considered and an evolution of the internal variable is assumed as for the Neo-Hooke material. The EOM for an Arruda-Boyce material is

$$\ddot{\lambda} - \frac{3}{2}\frac{1}{\lambda(1+c_1\lambda^3)}\dot{\lambda}^2 + c_2 \frac{(\lambda^3 N(A+\beta A_\nu) + \frac{\epsilon_0\epsilon_r}{\mu}E_0^2)}{(1+c_1\lambda^3)} = 0 \quad \text{with} \tag{3.3.18}$$

$$A = \sqrt{N^{-1}}\left(\frac{\partial\Lambda}{\partial\lambda}\gamma + \Lambda\frac{\partial\gamma}{\partial\lambda}\right) + \frac{\partial a}{\partial\lambda},\ A_\nu = \sqrt{N^{-1}}\left(\frac{\partial\Lambda_\nu}{\partial\lambda}\gamma_\nu + \Lambda_\nu\frac{\partial\gamma_\nu}{\partial\lambda_\nu}\right) + \frac{\partial a}{\partial\lambda_\nu}, \tag{3.3.19}$$

$$\begin{aligned}
\frac{\partial\Lambda}{\partial\lambda} &= 0.5\left(\frac{-2\lambda^{-2}+2\lambda}{3}\right)\left(\frac{2\lambda^{-1}+\lambda^2}{3}\right)^{-\frac{1}{2}} \\
\frac{\partial\Lambda_\nu}{\partial\lambda} &= 0.5\left(\frac{-2\lambda^{-2}\lambda_\nu+2\lambda\lambda_\nu^{-2}}{3}\right)\left(\frac{2\lambda^{-1}\lambda_\nu+\lambda^2\lambda^{-2}}{3}\right)^{-\frac{1}{2}} \\
\frac{\partial\gamma}{\partial\lambda} &= \sqrt{N^{-1}}\left[\frac{\partial\Lambda}{\partial\lambda}\left(\frac{3N-\Lambda^2}{N-\Lambda^2}\right) + \Lambda\left(\left(\frac{2\lambda^{-2}-2\lambda}{3(N-\Lambda^2)}\right) + \left(3N-\Lambda^2\right)\left(\frac{2\lambda^{-2}-2\lambda}{3(N-\Lambda^2)}\right)\right)\right], \\
\frac{\partial\gamma_\nu}{\partial\lambda} &= \sqrt{N^{-1}}\left[\frac{\partial\Lambda_\nu}{\partial\lambda}\left(\frac{3N-\Lambda_\nu^2}{N-\Lambda_\nu^2}\right) + \Lambda_\nu\left(\left(\frac{2\lambda^{-2}\lambda_\nu-2\lambda\lambda_\nu^{-2}}{3(N-\Lambda_\nu^2)}\right) + \left(3N-\Lambda_\nu^2\right)\left(\frac{2\lambda^{-2}\lambda_\nu-2\lambda\lambda_\nu^{-2}}{3(N-\Lambda_\nu^2)}\right)\right)\right] \\
\frac{\partial a}{\partial\lambda} &= \frac{\partial \ln\left(\frac{\gamma}{\sinh\gamma}\right)}{\partial\lambda} = \frac{\sinh\gamma - \gamma\cosh\gamma}{\gamma\sinh\gamma}\frac{\partial\gamma}{\partial\lambda},\ \frac{\partial a_\nu}{\partial\lambda} = \frac{\sinh\gamma_\nu - \gamma_\nu\cosh\gamma_\nu}{\gamma_\nu\sinh\gamma_\nu}\frac{\partial\gamma_\nu}{\partial\lambda}
\end{aligned} \tag{3.3.20}$$

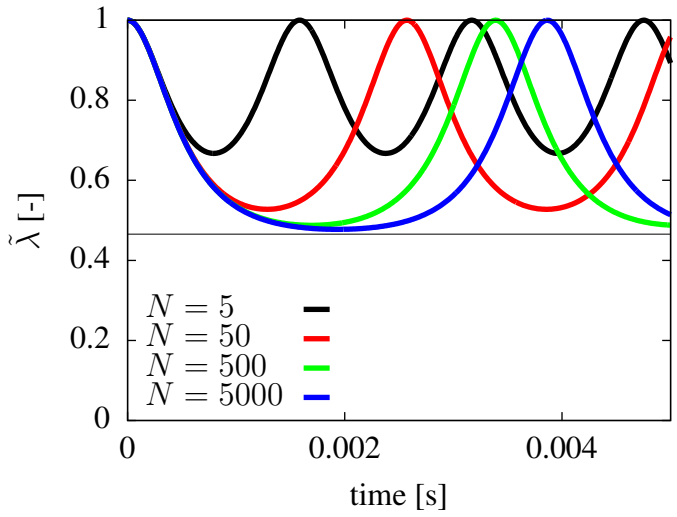

Figure 3.3.6.: Dynamic stretch $\lambda(t)$ of a rectangular VHB49 membrane (Mat.1) under step voltage assuming a viscous Arruda-Boyce material and different numbers of cross-links. The electric field is equal to $E_0 = 22.3\,\mathrm{kV\,mm^{-1}}$.

Fig. 3.3.6 shows the numerical solution of the EOM for different numbers of cross-links. By increasing N, the material becomes more compliant, which shows in a larger compression amplitude that almost coincides the curve of a hyperelastic material for $N = 5000$.

4 Electro-viscoelastic material

4.1 Introduction

Multiphysical material models are complex in particular if non-linearity is included in the description of material and kinematics. For the creation of numerical code it is therefore important to have a reference either in form of analytical equations or experiments to control the implementation by verification of solutions. Within the scope of this work an adequate experimental classification by creep and relaxation tests was not available for support therefore it was referred to analytical solutions, which can be found in literature. A linear FE-model, model A, for electro-viscoelasticity is formulated to have a direct comparison to them.

A straightforward model for large deformation electro-viscoelastic behaviour was envisaged, for an FE-model including contact analysis was set up, which need large computational power due to a small iteration step size. Two classical approaches to describe large deformation viscoelasticity are compared. The models use either a split of stress tensor that can be undertaken without great expense, applied in a model B, or a split of deformation gradient and energy function which is more expensive and applied in a model C. Both variants are augmented with an electrostatic energy part, and what is more, model C is able to map dielectric dissipation.

Model A is related to the viscoelastic, thermomechanical model that has been introduced in Taylor et al. [136]. This model uses a convolution integral to describe time history.

Model B is inspired by the large deformation viscoelastic model in Simo [137]. In this approach, the 2.Piola-Kirchhoff stress tensor is split into volumetric and deviatoric part, which includes internal variables; by using a Neo-Hooke material this method is equivalent to a multiplicative decomposition of the deformation gradient. Simo has used a linear rate equation that leads to a linearised formulation of kinematics. Model B is directly derived from the descriptions presented in Kaliske [138] where the stress tensor for small and large deformation is first split into volumetric and deviatoric part, and secondly, the deviatoric part is split into one elastic and several viscoelastic parts similar to the model in the previous chapter 3. Time-dependent strain is described by the sum of convolution integrals according to the Boltzmann superposition. For this method, thermodynamic compatibility with regard to the 2nd law is not proven for all admissible processes [139]. Nevertheless, this method is implemented in many simulation programs. The usability of this simple approach is evaluated here in the context of electro-viscoelasticity.

Model C applies an additive split of the energy function and a multiplicative spilt of the deviatoric part of deformation gradient into elastic and viscoelastic parts. This procedure was originally used for the implementation of large deformation plasticity and follows the work of Green and Tobolsky [140]

and Lubliner [141]. Govindjee and Reese [139] refer to Sidoroff [142] and have assumed that there exists a set of internal variables representing several viscous parts of the deformation gradient, and propose a viscous evolution in a quadratic form.[1] Bonet [82] refers directly to the Generalised Maxwell model that specifies a linear rate equation, see section 2.5. An alternative approach to describe electro-viscohyperelasticity, which is not retraced here, is introduced in Saxena et al. [143], where a split of the deformation gradient and the electric field has been performed. To compare numerical solutions for model A, B and C, a St.Vernant material that defines geometric non-linearity is used in the large deformation models B and C.

This chapter is structured as follows: In the next section 4.2, the linear model A, is presented. In section 4.3 the two large deformation electro-viscoelastic models B and C are introduced. In section 4.4, numerical simulation of creep and relaxation tests validate models B and C against the analytical solutions.

4.2 Linear electro-viscoelasticity

It is uncomplicated to implement electro-viscoelasticity if elastic, viscoelastic, and electric energy are assumed to be uncoupled and dielectric dissipation is neglected. In such a case the Cauchy stress $\boldsymbol{\sigma}$ is split into four parts: Hydrostatic stress $\operatorname{vol}\boldsymbol{\sigma}$, instantaneous deviatoric stress $\operatorname{dev}\boldsymbol{\sigma}_0$, viscous stresses $\sum_\alpha \boldsymbol{\sigma}_{\mathrm{v}_\alpha}$, and electrostatic stress $\boldsymbol{\sigma}^{\mathrm{E}}$

$$\boldsymbol{\sigma} = \operatorname{vol}\boldsymbol{\sigma} + \operatorname{dev}\boldsymbol{\sigma} + \boldsymbol{\sigma}^{\mathrm{E}} = \operatorname{vol}\boldsymbol{\sigma} + \operatorname{dev}\boldsymbol{\sigma}_0 + \sum_\alpha \boldsymbol{\sigma}_{\mathrm{v}_\alpha} + \boldsymbol{\sigma}^{\mathrm{E}}. \tag{4.2.1}$$

The split into hydrostatic and deviatoric part is adopted from plasticity theory and follows the "general observation" that plastic deformation causes very small volume changes and can be interpreted as "distortion" [144]. For linear theory, the time-dependent behaviour can be calculated in case creep or relaxation functions are known. In the numerical implementation of time-dependency, the viscous deviatoric stress tensors $\sum_\alpha \boldsymbol{\sigma}_{\mathrm{v}_\alpha}$, also denoted as $\sum_\alpha \mathbf{h}_\alpha$, which stands for "**h**istory", as well as the total deviatoric stresses $\operatorname{dev}\boldsymbol{\sigma}$ are saved in each time step as history variables. The derivation of an algorithm is presented in [138] where a relaxation test is formulated for the 1D case with a continuous relaxation function G for an infinitesimal strain step $\mathrm{d}s$ in a time interval $[0, t]$.[2]

$$\sigma(t) = \int_0^t G(t-s)\,\frac{\partial \varepsilon(s)}{\partial s}\,\mathrm{d}s, \tag{4.2.2}$$

where

$$G(t-s) = Y_0 + \sum_{\alpha=1}^{N} Y_\alpha e^{\left(-\frac{t-s}{T_j}\right)}. \tag{4.2.3}$$

[1] See section 2.5

[2] In the context of this work, a tensile test is supposed.

In reference to the Generalised Maxwell model, Y_0 is the Young's modulus of the single spring and Y_α are α's Young's moduli of the springs in the Maxwell elements. A decomposition of Eq. (4.2.2) into an instantaneous and time-dependent stress parts is given as

$$\begin{aligned}\sigma(t) &= \int_0^t Y_0 \varepsilon(t) + \sum_{\alpha=1}^{N} \int_0^t Y_\alpha e^{\left(-\frac{t-s}{T_\alpha}\right)} \frac{\partial \varepsilon(s)}{\partial s} \, \mathrm{d}s \\ &= \sigma_0(t) + \sum_{\alpha=1}^{N} h_\alpha(t).\end{aligned} \tag{4.2.4}$$

Where T_α are relaxation times and $\varepsilon(t) = \frac{\sigma_0(t)}{Y_0}$. With $\beta_\alpha = \frac{Y_\alpha}{Y_0}$ follows the viscous stress variables $h_\alpha(t)$

$$h_\alpha(t) = \int_0^t \beta_\alpha e^{\left(-\frac{t-s}{T_\alpha}\right)} \frac{\partial \sigma_0(s)}{\partial s} \, \mathrm{d}s. \tag{4.2.5}$$

For the numerical implementation, a time step $\Delta t = t_{n+1} - t_n$ is defined that is used to segment the exponential function

$$e^{\left(-\frac{t_{n+1}}{T_\alpha}\right)} = e^{\left(-\frac{t_n + \Delta t}{T_\alpha}\right)} = e^{\left(-\frac{t_n}{T_\alpha}\right)} e^{\left(-\frac{\Delta t}{T_\alpha}\right)}. \tag{4.2.6}$$

Eq. (4.2.6) splits the time history into two intervals: $0 \leq s \leq t_n$ and $t_n \leq s \leq t_{n+1}$. Viscous stress variables are consequently written as

$$\begin{aligned} h_\alpha(t_{n+1}) &= \beta_\alpha \int_0^{t_{n+1}} e^{\left(-\frac{t_{n+1}-s}{T_\alpha}\right)} \frac{\partial \sigma_0(s)}{\partial s} \, \mathrm{d}s \\ &= \beta_\alpha e^{\left(-\frac{\Delta t}{T_\alpha}\right)} \int_0^{t_n} e^{\left(-\frac{t_n - s}{T_\alpha}\right)} \frac{\partial \sigma_0(s)}{\partial s} \, \mathrm{d}s \\ &+ \beta_\alpha \int_{t_n}^{t_{n+1}} e^{\left(-\frac{t_{n+1}-s}{T_\alpha}\right)} \frac{\partial \sigma_0(s)}{\partial s} \, \mathrm{d}s \\ &= e^{\left(-\frac{\Delta t}{T_\alpha}\right)} h_\alpha(t_n) + \beta_\alpha \int_{t_n}^{t_{n+1}} e^{\left(-\frac{t_{n+1}-s}{T_\alpha}\right)} \frac{\partial \sigma_0(s)}{\partial s} \, \mathrm{d}s. \end{aligned} \tag{4.2.7}$$

The differential expression for deviatoric strain $\frac{\partial \sigma_0(s)}{\partial s}$, is formulated for a discrete time step Δt as

$$\frac{\partial \sigma_0(s)}{\partial s} = \lim_{\Delta t \to 0} \frac{\Delta \sigma_0(s)}{\Delta s} = \lim_{\Delta t \to 0} \frac{\sigma_0^{n+1} - \sigma_0^n}{\Delta t}. \tag{4.2.8}$$

Eq. (4.2.8) inserted into Eq. (4.2.7) yields

$$h_\alpha^{n+1} = e^{\left(-\frac{\Delta t}{T_\alpha}\right)} h_\alpha^n + \beta_\alpha \int_{t_n}^{t_{n+1}} e^{\left(-\frac{t_{n+1}-s}{T_\alpha}\right)} \mathrm{d}s \frac{\sigma_0^{n+1} - \sigma_0^n}{\Delta t}. \tag{4.2.9}$$

After integration with respect to $\mathrm{d}s$ follows

$$h_\alpha^{n+1} = e^{\left(-\frac{\Delta t}{T_\alpha}\right)} h_\alpha^n + \beta_\alpha \frac{1 - e^{\left(-\frac{\Delta t}{T_\alpha}\right)}}{\frac{\Delta t}{T_\alpha}} \left[\sigma_0^{n+1} - \sigma_0^n\right]. \tag{4.2.10}$$

For 3D case scalar expressions of strain and stress are substituted by tensorial expressions in the current time increment. The split into hydrostatic and deviatoric stress part gives

$$\boldsymbol{\sigma}^{n+1} = \text{vol}\, \boldsymbol{\sigma}^{n+1} + \text{dev}\, \boldsymbol{\sigma}^{n+1} = K\, \text{vol}\, \boldsymbol{\varepsilon}^{n+1} + \text{dev}\, \boldsymbol{\sigma}^{n+1} = K \frac{1}{3} \mathrm{I}_\varepsilon^{n+1} + \text{dev}\, \boldsymbol{\sigma}^{n+1} \tag{4.2.11}$$

where K is the bulk modulus and $\mathrm{I}_\varepsilon = \mathbf{tr}\, \varepsilon$. Deviatoric stresses are split into instantaneous and time-dependent parts

$$\text{dev}\, \boldsymbol{\sigma}^{n+1} = \text{dev}\, \boldsymbol{\sigma}_0^{n+1} + \sum_\alpha \mathbf{h}_\alpha^{n+1}, \tag{4.2.12}$$

with

$$\text{dev}\, \boldsymbol{\sigma}_0^{n+1} = (\boldsymbol{\varepsilon} - \mathrm{I}_\varepsilon^{n+1})\, \mathbb{C}_{\text{dev}}\,. \tag{4.2.13}$$

The incremental viscous history variables are

$$\mathbf{h}_\alpha^{n+1} = e^{\left(-\frac{\Delta t}{T_\alpha}\right)} \mathbf{h}_\alpha^n + \beta_\alpha \frac{1 - e^{\left(-\frac{\Delta t}{T_\alpha}\right)}}{\frac{\Delta t}{T_\alpha}} \left[\text{dev}\, \boldsymbol{\sigma}_0^{n+1} - \text{dev}\, \boldsymbol{\sigma}_0^n\right]. \tag{4.2.14}$$

The viscoelastic material tangent is divided into three parts

$$\begin{aligned} \mathbb{C} := \frac{\partial \boldsymbol{\sigma}^{n+1}}{\partial \boldsymbol{\varepsilon}^{n+1}} &= \mathbb{C}_{\text{vol}} + \left(1 + \sum_\alpha \beta_\alpha \frac{1 - e^{\left(-\frac{\Delta t}{T_\alpha}\right)}}{\frac{\Delta t}{T_\alpha}}\right) \mathbb{C}_{\text{dev}} \\ &= K(\mathbf{1} \otimes \mathbf{1}) + \left(1 + \sum_\alpha \beta_\alpha \frac{1 - e^{\left(-\frac{\Delta t}{T_\alpha}\right)}}{\frac{\Delta t}{T_\alpha}}\right) 2\mu_0 \left(\mathbb{1} - \frac{1}{3}(\mathbf{1} \otimes \mathbf{1})\right). \end{aligned} \tag{4.2.15}$$

Electrostatic and electromechanical material tangents due to coupling are discussed in detail in chapter 5.

4.3 Geometric non-linear electro-viscoelasticity

The ferroelectret structures at hand have been investigated by mechanical compression tests whereby the compression was in a range of 1 and 50 %. Since a specific material classification was not available the simplest way to describe large deformation elasticity was to use the St.Vernant material, which was augmented by dissipative and electrostatic parts; an advantage of this choice is that results from linear analytical solutions and non-linear calculations are comparable.

4.3.1 Split of stress tensor, model B

The stress tensor split is justified when the material equations are linear, which is the case for the St.Vernant material. The incremental scheme presented in the last section 4.2 can be adopted and the Cauchy stress $\boldsymbol{\sigma}$ is substituted by the 2.Piola-Kirchhoff stress $\mathbf{S}$ derived from the energy function.

4.3.2 Split of energy and deformation gradient, model C

The implementation of material non-linearity, e.g. hyperelastic material like Neo-Hooke, Gent, Ogden, Arruda-Boyce, description of dielectric dissipation, or distinction between polarised and non-polarised material, requires a split of energy function and deformation gradient. A free energy density function for a compressible dielectric material that includes viscous and dielectric dissipation is given by

$$\begin{aligned}\Psi(\mathbf{C}, \mathbf{C}_{\mathrm{v}_\alpha}) = &\underbrace{\Psi_{\mathrm{vol}}(\mathbf{C})}_{\text{hydrostatic}} + \underbrace{\Psi_{\mathrm{dev}_0}(\mathbf{C})}_{\text{deviatoric instant.}} + \underbrace{\Psi_{\mathrm{el}}(\mathbf{C})}_{\text{el. vacuum}} + \underbrace{\Psi_{\mathrm{P}}(\mathbf{C})}_{\text{el. polarisation}} \\ &+ \underbrace{\sum_\alpha \Psi_{\mathrm{v}_\alpha}(\mathbf{C}_{\mathrm{e}_\alpha})}_{\text{viscous dissipation}} + \underbrace{\sum_\alpha \Psi_{\mathrm{P}_{\mathrm{v}_\alpha}}(\mathbf{C}_{\mathrm{e}_\alpha})}_{\text{dielectric dissipation}} .\end{aligned} \tag{4.3.1}$$

Here, the electrostatic energy parts are separated into vacuum part $\Psi_{\mathrm{el}}(\mathbf{C})$ and matter part $\Psi_{\mathrm{P}}(\mathbf{C})$. $\Psi_{\mathrm{P}}(\mathbf{C})$ is the polarisation. The kind of polarisation can be defined via specific expressions of the polarisability e.g. discussed in [34]. Dielectric dissipation $\sum_\alpha \Psi_{\mathrm{P}_{\mathrm{v}_\alpha}}(\mathbf{C}_{\mathrm{e}_\alpha})$ is formulated equivalent to viscous dissipation assuming a sum of simultaneous processes. For a non-polar material $\Psi_{\mathrm{P}}(\mathbf{C})$ and $\sum_\alpha \Psi_{\mathrm{P}_{\mathrm{v}_\alpha}}(\mathbf{C}_{\mathrm{e}_\alpha})$ are omitted. Keeping the assumption of a St.Vernant material with free energy density

$$\Psi(\mathbf{C}) = \frac{\lambda}{2}\left(\mathrm{tr}\mathbf{A}\right)^2 + \mu\,\mathrm{tr}\mathbf{A}^2, \tag{4.3.2}$$

volumetric and deviatoric parts of Eq. (4.3.2) are

$$\begin{aligned}\Psi_{\mathrm{vol}}(\mathbf{C}) &= \frac{1}{2}K\left[\mathrm{tr}\left[\frac{1}{2}\left(\mathbf{C}-\mathbf{1}\right)\right]\right]^2 \text{ and} \\ \Psi_{\mathrm{dev}}(\mathbf{C}) &= G\left[\mathrm{tr}\left[\frac{1}{2}\left(\mathbf{C}-\mathbf{1}\right)\right]^2 - \frac{1}{3}\left[\mathrm{tr}\left[\frac{1}{2}\left(\mathbf{C}-\mathbf{1}\right)\right]\right]^2\right].\end{aligned} \tag{4.3.3}$$

According to [82] viscous, dissipative parts are assumed to be proportional to the elastic energy. It follows

$$\Psi_{\mathrm{v}_\alpha}(\mathbf{C}_{\mathrm{e}_\alpha}) = \beta_\alpha\,\Psi_{\mathrm{dev}}(\mathbf{C}_{\mathrm{e}_\alpha}) = \beta_\alpha\,G\left[\mathrm{tr}\left[\frac{1}{2}\left(\mathbf{C}_{\mathrm{e}_\alpha}-\mathbf{1}\right)\right]^2 - \frac{1}{3}\left[\mathrm{tr}\left[\frac{1}{2}\left(\mathbf{C}_{\mathrm{e}_\alpha}-\mathbf{1}\right)\right]\right]^2\right]. \tag{4.3.4}$$

The vacuum part of the electrostatic energy Ψ_{el} is given by Eq. (4.3.5). A similar quadratic approach is chosen for the polarisation fraction Ψ_{P}. Dielectric dissipation is assumed to be proportional to the instantaneous polarisation whereby γ_α is an positive factor.[3]

$$\begin{aligned}
\Psi_{\text{el}}(\mathbf{C}) &= -\frac{1}{2}\epsilon_0 J\mathbf{E}_0 \cdot (\mathbf{C}^{-1}\mathbf{E}_0),\\
\Psi_{\text{P}}(\mathbf{C}) &= -\frac{1}{2}\epsilon_0\, \chi_s\, \mathbf{E}_0 \cdot (\mathbf{C}^{-1}\mathbf{E}_0),\\
\Psi_{\text{P}_{\text{v}_\alpha}}(\mathbf{C}_{\text{e}_\alpha}) &= -\frac{1}{2}\,\gamma_\alpha\, \epsilon_0\, \chi_s\, \mathbf{E}_0 \cdot (\mathbf{C}_{\text{e}_\alpha}^{-1}\mathbf{E}_0).
\end{aligned} \tag{4.3.5}$$

The dielectric displacement with respect to the reference configuration is[4]

$$\mathbf{D}_0(\mathbf{C}, \mathbf{C}_{\text{v}_\alpha}) = -\frac{\partial \Psi}{\partial \mathbf{E}_0} = -\frac{\partial \left(\Psi_{\text{el}} + \Psi_{\text{P}} + \sum\limits_\alpha \Psi_{\text{P}_{\text{v}_\alpha}}\right)}{\partial \mathbf{E}_0} \tag{4.3.6}$$

with

$$\begin{aligned}
\mathbf{D}_{0_{\text{vac}}}(\mathbf{C}) &= \underbrace{\epsilon_0 J\, \mathbf{C}^{-1}\, \mathbf{E}_0}_{\text{vacuum}},\\
\mathbf{D}_{0_{\text{P}}}(\mathbf{C}) &= \underbrace{\epsilon_0 \chi_s\, \mathbf{C}^{-1}\, \mathbf{E}_0}_{\text{polarisation}},\\
\mathbf{D}_{0_{\text{v}_\alpha}}(\mathbf{C}, \mathbf{C}_{\text{v}_\alpha}) &= \underbrace{\gamma_\alpha\, \epsilon_0\, \chi_s\, \mathbf{C}_{\text{e}_\alpha}\, \mathbf{E}_0}_{\text{dielectric relaxation}}.
\end{aligned} \tag{4.3.7}$$

For stresses follows

$$\mathbf{S}(\mathbf{C}, \mathbf{C}_{\text{v}_\alpha}) = 2\frac{\partial \Psi}{\partial \mathbf{C}} = 2\frac{\partial \left(\Psi_{\text{vol}} + \Psi_{\text{dev}_0} + \sum\limits_\alpha \Psi_{\text{v}_\alpha} + \Psi_{\text{el}} + \Psi_{\text{P}} + \sum\limits_\alpha \Psi_{\text{P}_{\text{v}_\alpha}}\right)}{\partial \mathbf{C}} \tag{4.3.8}$$

[3] FEP shows a piezoelectric effect if free charge is brought into the material [145]. An investigation about space charge distribution in dependence of wall thickness in corona charged ferroelectret structures was conducted using a Laser-Intensity Modulation Method (LIMM) [146]. Measurement of the space charge distribution in the ferroelectret structures at hand is recommended as well as an assessment of the specific dielectric relaxation model.

[4] See Eq. (2.4.20).

with[5]

$$
\begin{aligned}
\mathbf{S}_{\text{vol}}(\mathbf{C}) &= \frac{1}{2}K(\text{tr}\mathbf{C} - \text{tr}\mathbf{1})\mathbf{1}, \\
\mathbf{S}_{\text{dev}_0}(\mathbf{C}) &= G\left[\frac{1}{2}\left[\left[(\mathbf{C}\otimes\mathbf{1})^{\overset{23}{T}} + \left(\mathbf{1}\otimes\mathbf{C}^T\right)^{\overset{23}{T}}\right] : \mathbf{1} - 2\mathbf{1}\right] - \frac{1}{3}\left[\text{tr}\left(\mathbf{C}-\mathbf{1}\right)\right]\mathbf{1}\right], \\
\mathbf{S}_{\text{v}_\alpha}(\mathbf{C},\mathbf{C}_{\text{v}_\alpha}) &= 2\frac{\partial\Psi_{\text{v}_\alpha}}{\partial\mathbf{C}} = \beta_\alpha\, G\left[\frac{1}{2}\left[\left[\left(\mathbf{C}{\mathbf{C}_{\text{v}_\alpha}}^{-1}\otimes\mathbf{1}\right)^{\overset{23}{T}} - \left(\mathbf{1}\otimes\mathbf{C}{\mathbf{C}_{\text{v}_\alpha}}^{-1}\right)^{\overset{23}{T}}\right] : \mathbf{1}{\mathbf{C}_{\text{v}_\alpha}}^{-1} - 2{\mathbf{C}_{\text{v}_\alpha}}^{-1}\mathbf{1}\right]\right. \\
&\quad \left. - \frac{1}{3}\left[\text{tr}\left(\mathbf{C}{\mathbf{C}_{\text{v}_\alpha}}^{-1} - \mathbf{1}\right)\right] : \mathbf{1}{\mathbf{C}_{\text{v}_\alpha}}^{-1}\right], \\
\mathbf{S}^{\text{E}}(\mathbf{C},\mathbf{C}_{\text{v}_\alpha}) &= \epsilon_0(J+\chi_s)\mathbf{E}_0\left[\left(\mathbf{C}^{-1}\otimes\mathbf{C}^{-T}\right)^{\overset{23}{T}}\mathbf{E}_0\right] - \frac{1}{2}\epsilon_0 J\mathbf{C}^{-1}\left[\mathbf{E}_0\cdot\left(\mathbf{C}^{-\mathbf{1}}\mathbf{E}_0\right)\right] - \gamma_\alpha\epsilon_0\chi_s\mathbf{E}_0\left({\mathbf{C}_{\text{v}_\alpha}}^{-1}\mathbf{E}_0\right).
\end{aligned}
\tag{4.3.9}
$$

or in indices

$$
\begin{aligned}
S_{\text{vol}_{ij}} &= \frac{1}{2}K(C_{kk}-3)\delta_{ij}, \\
S_{\text{dev}_{0ij}} &= G\left[(C_{ij}-\delta_{ij}) - \frac{1}{3}(C_{kk}-3)\delta_{ij}\right], \\
S_{\text{v}_\alpha ij} &= \beta_\alpha\, G\left[{C_{\text{v}_\alpha}}_{ik}^{-1}\left(C_{kl}{C_{\text{v}_\alpha}}_{lj}^{-1} - \delta_{kj}\right) - \frac{1}{3}\left(C_{kl}{C_{\text{v}_\alpha}}_{lk}^{-1} - 3\right){C_{\text{v}_\alpha}}_{ij}^{-1}\right], \\
S^{\text{E}}_{ij} &= \epsilon_0\left(J+\chi_s\right)E_{0\,k}{C_{ki}}^{-1}{C_{jl}}^{-1}E_{0\,l} - \frac{1}{2}\epsilon_0 J E_{0\,p}{C_{pq}}^{-1}E_{0\,q}{C_{ij}}^{-1} - \gamma_\alpha\epsilon_0\chi_s\, E_{0\,k}\, C^{-1}_{\text{v}_\alpha ki}E_{0\,j}.
\end{aligned}
\tag{4.3.10}
$$

The material tangent $\mathbf{k}^{\text{MM}}$ is calculated using $\tilde{\mathbb{C}} = 2\partial\mathbf{S}/\partial\mathbf{C}$.[6] The fractions are given as[7]

$$
\begin{aligned}
\tilde{\mathbb{C}}_{\text{vol}} &= K\left(\mathbf{1}\otimes\mathbf{1}\right), \\
\tilde{\mathbb{C}}_{\text{dev}} &= 2G\left(\mathbb{1} - \frac{1}{3}\left(\mathbf{1}\otimes\mathbf{1}\right)\right), \\
\tilde{\mathbb{C}}_{\text{v}_\alpha} &= 2\beta_\alpha G\left(\mathbf{C}^{-1}_{\text{v}_\alpha}\mathbf{C}^{-1}_{\text{v}_\alpha} - \frac{1}{3}\mathbf{C}^{-1}_{\text{v}_\alpha}\mathbf{C}^{-1}_{\text{v}_\alpha}\right),
\end{aligned}
\tag{4.3.11}
$$

or in indices

$$
\begin{aligned}
\tilde{C}_{\text{vol}\,ijkl} &= K\delta_{ij}\delta_{kl}, \\
\tilde{C}_{\text{dev}\,ijkl} &= 2G\left(\delta_{ik}\delta_{jl} - \frac{1}{3}\delta_{kl}\delta_{ij}\right), \\
\tilde{C}_{\text{v}_\alpha\,ijkl} &= 2\beta_\alpha\, G\left({C_{\text{v}_\alpha}}_{ik}^{-1}{C_{\text{v}_\alpha}}_{lj}^{-1} - \frac{1}{3}{C_{\text{v}_\alpha}}_{lk}^{-1}{C_{\text{v}_\alpha}}_{ij}^{-1}\right).
\end{aligned}
\tag{4.3.12}
$$

[5] Here, $\overset{23}{T}$ means that the second and the third index must be permuted.

[6] For details see appendix A.12.

[7] To compare simulation results of both implementation types of electro-viscoelasticity for large deformation, a formulation for $\mathbf{S}^{\text{E}}$ according to Eq. (5.1.18) and $\tilde{\mathbb{C}}^{\text{E}}$ defined in Eq. (A.8.5) is chosen.

4.3.3 Numerical treatment

The tangent $\mathbf{k}^{\mathrm{MM}}$ is updated in each time increment using a linear rate equation for viscoelastic stresses as proposed in Bonet [82]

$$\left.\frac{\mathrm{d}\mathbf{S}_{\mathrm{v}_\alpha}}{\mathrm{d}t}\right|_{\mathbf{C}=\text{const.}} = -\frac{1}{T_\alpha}\mathbf{S}_{\mathrm{v}_\alpha}. \tag{4.3.13}$$

An incremental form of the left side of Eq. (4.3.13) is given by

$$\left.\frac{\mathrm{d}\mathbf{S}_{\mathrm{v}_\alpha}}{\mathrm{d}t}\right|_{\mathbf{C}=\text{const.}} = \frac{1}{\Delta t}\left[\mathbf{S}_{\mathrm{v}_\alpha}\left(\mathbf{C}^{n+1}, \mathbf{C}_{\mathrm{v}_\alpha}^{n+1}\right) - \mathbf{S}_{\mathrm{v}_\alpha}\left(\mathbf{C}^{n+1}, \mathbf{C}_{\mathrm{v}_\alpha}^{n}\right)\right]. \tag{4.3.14}$$

Inserting Eq. (4.3.13) into Eq. (4.3.14) yields

$$\mathbf{S}_{\mathrm{v}_\alpha}\left(\mathbf{C}^{n+1}, \mathbf{C}_{\mathrm{v}_\alpha}^{n+1}\right) = \frac{T_\alpha}{T_\alpha + \Delta t}\,\mathbf{S}_{\mathrm{v}_\alpha}\left(\mathbf{C}^{n+1}, \mathbf{C}_{\mathrm{v}_\alpha}^{n}\right). \tag{4.3.15}$$

Bonet interprets the stresses $\mathbf{S}_{\mathrm{v}_\alpha}\left(\mathbf{C}^{n+1}, \mathbf{C}_{\mathrm{v}_\alpha}^{n}\right)$ as a kind of trial stresses known from plasticity theory. The viscous material tangent is updated similarly in every time step using the same pre-factor as for the viscous stresses

$$\tilde{\mathbf{C}}_{\mathrm{v}_\alpha}\left(\mathbf{C}^{n+1}, \mathbf{C}_{\mathrm{v}_\alpha}^{n+1}\right) = \frac{T_\alpha}{T_\alpha + \Delta t}\,2\beta_\alpha\, G\left(\mathbf{C}_{\mathrm{v}_\alpha}{}^{-1^n}\mathbf{C}_{\mathrm{v}_\alpha}{}^{-1^n} - \frac{1}{3}\mathbf{C}_{\mathrm{v}_\alpha}{}^{-1^n}\mathbf{C}_{\mathrm{v}_\alpha}{}^{-1^n}\right). \tag{4.3.16}$$

Internal variables are iterated in the current time step after viscous stress and material tangent are updated. A Newton-Raphson scheme is used to determine the α unknown tensorial variables; six times α equations are given by the third equation in Eq. (4.3.10). The derivatives were approximated numerically by using the backward difference quotient.

4.4 Model validation

Benchmark and patch tests are conducted for the validation of large deformation models; the simulation results of relaxation and creep tests are compared to analytical solutions of the Generalised Maxwell model. Analytical solutions are not split into hydrostatic and deviatoric parts, a direct comparison to numerical solutions is therefore only given for a Poisson's ratio of 0.5, which is however difficult in numerical studies. A maximum Poisson's ratio of 0.499 is therefore assumed in the following paragraphs. The Young's modulus of the single spring with Y_0=500 MPa is in the order of the Young's modulus of FEP at room temperature. In the benchmark tests, which use one element, and in the patch tests on a cube of eight elements, a homogeneous tensile stress or strain, and in voltage-controlled tests, a homogeneous electric field perpendicular to the upper cube surface is prescribed. The edge length of the cube geometries is chosen with 1 µm, the bottom is fixed perpendicular to surface and symmetry boundary conditions are given on the two lateral edges. For creating diagrams GNU Octave was used to compare curves for different viscous parameters.

4.4.1 Validation model B

In this subsection results of benchmark tests using model B and analytical solutions are compared to validate model B.

Relaxation and creep due to mechanical stress

The analytical solution for a relaxation test is given as

$$\sigma(t) = \varepsilon(0) \left(Y_0 + \sum_{\alpha=1}^{N} Y_\alpha e^{-\frac{t}{T_\alpha}} \right), \tag{4.4.1}$$

and for a creep test as[8]

$$\begin{gathered} \epsilon(t) = \sigma(0) \left[C_g + (C_r - C_g) \left(1 - e^{-\frac{t}{T \frac{C_r}{C_g}}} \right) \right] \\ \text{with } C_g = \frac{1}{Y_0 + Y_j},\ C_r = \frac{1}{Y_0}. \end{gathered} \tag{4.4.2}$$

The following figures show creep and relaxation tests for one volume element for changing viscous parameters, Poisson's ratios and mechanical impacts.

[8] See [147].

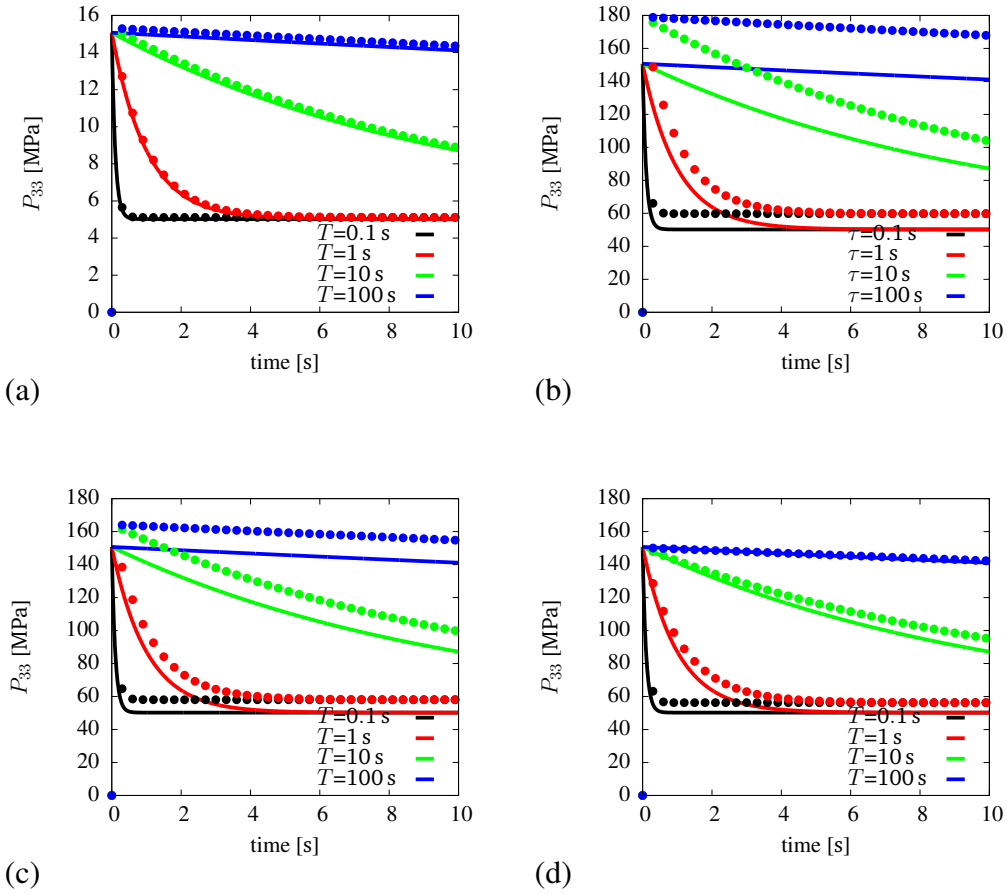

Figure 4.4.1.: Relaxation test, model B versus analytical solution for β=2.0: (a) ε=1 %, ν=0.499, (b) ε=10 %, ν=0.499, (c) ε=10 %, ν=0.45, (d) ε=10 %, ν=0.4. Dots show numerical solutions.

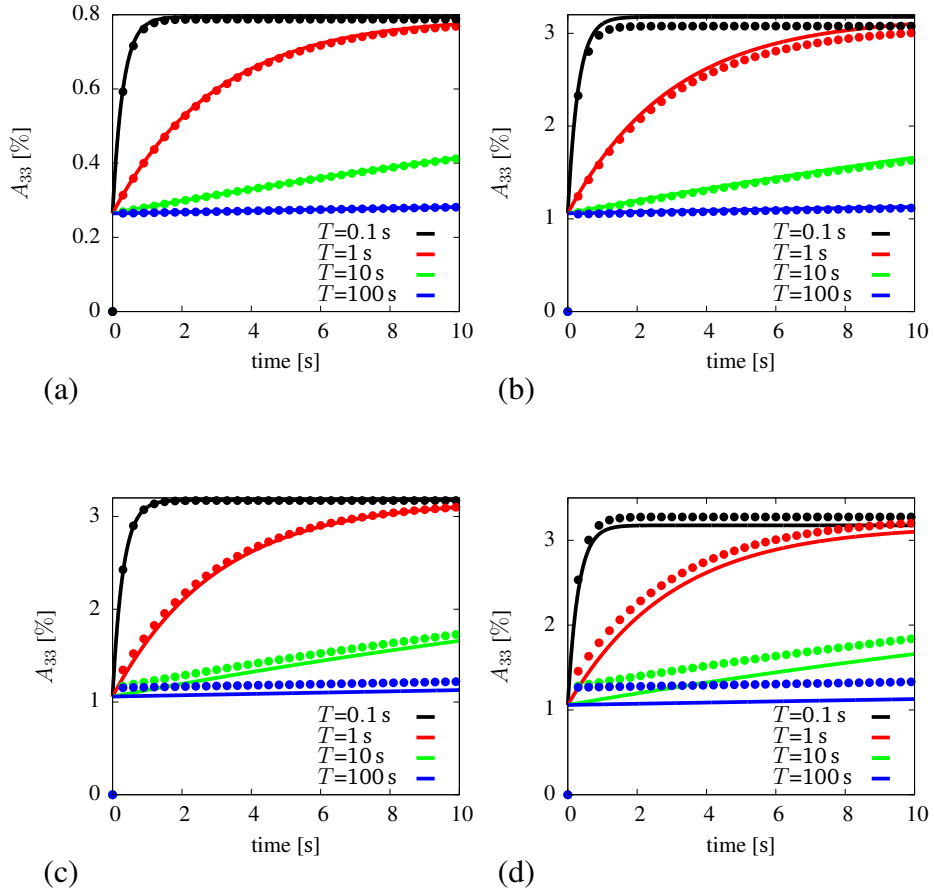

Figure 4.4.2.: Creep test, model B versus analytical solution: (a) Applied P_{33}=4 MPa, ν=0.499, (b) Applied P_{33}= 16 MPa, ν=0.499 (c) Applied P_{33}=16 MPa, ν=0.45 (d) Applied P_{33}=16 MPa, ν=0.4. Dots show numerical solutions.

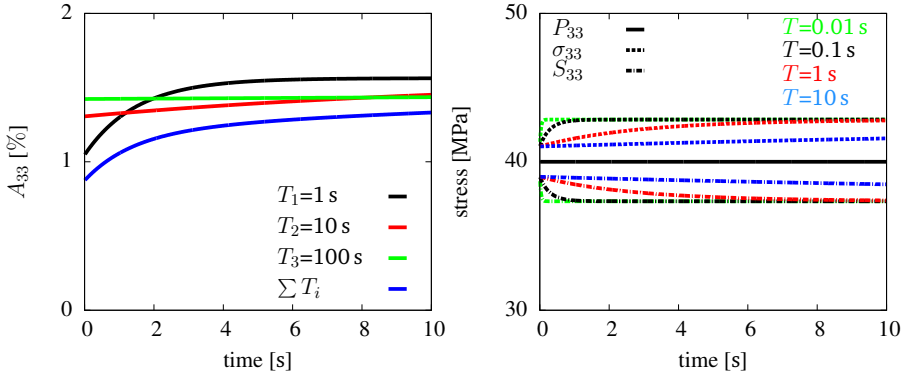

Figure 4.4.3.: Creep test for an applied P_{33}=40 MPa using a Generalised Maxwell model of three Maxwell elements with β_1=0.5, β_2=0.2, β_3=0.1 : (a) Green-Lagrange strain, (b) Different stress measures.

For small deformation due to strains about $1\,\%$, analytical and numerical solutions of relaxation and creep tests are identical what can be observed in Fig. 4.4.1a and Fig. 4.4.2a. An increase of strain or stress for a Poisson's ratio of 0.499 leads to a divergence of analytical and numerical solution, which is particular pronounced in relaxation tests for long relaxation times T and in creep tests if T is shorter than 10 s. The deviation is decreased by a reduction of Poisson's ratio to 0.45 or 0.4 in case of relaxation and increased for creep for long relaxation times.

Creep due to voltage

Fig. 4.4.4a shows a cube model that is used for the patch test consisting of eight volume elements. To distort the element the centre node of the cube is displaced slightly from the centre point. A homogeneous voltage of ϕ=1 kV is applied on the upper cube surface and induces a linear distribution of voltage and displacement u_{33} over the cube height, shown in Fig. 4.4.4b and c.

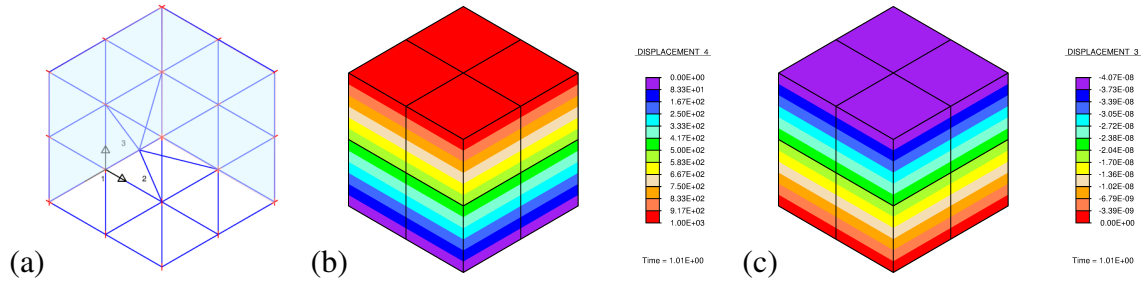

Figure 4.4.4.: Patch test: (a) Geometry and boundary conditions, light blue areas are symmetry planes, (b) ϕ [V], (c) u_{33} [m].

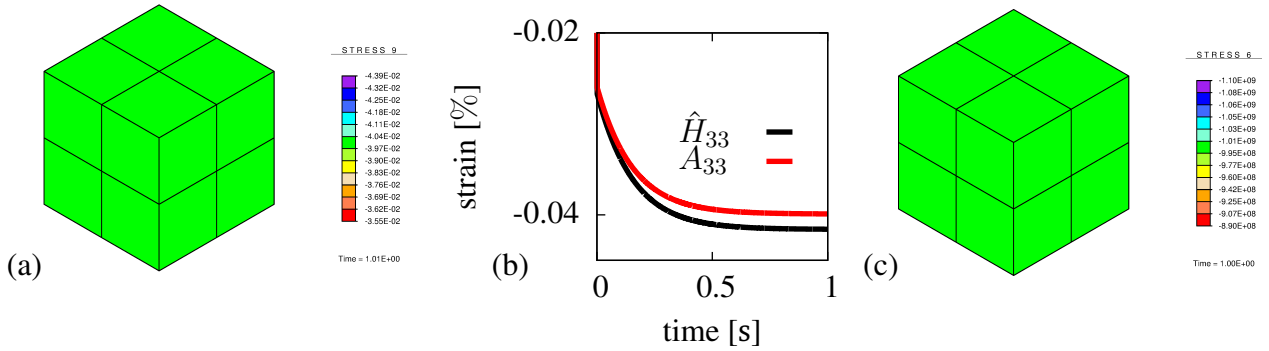

Figure 4.4.5.: Patch test for β_1=0.5, β_2=0.2, β_3=0.1, β_4=0.05 and T_1=0.1 s, T_2=1 s, T_3=10 s, T_4=100 s: (a) Green-Lagrange strain A_{33}, (b) Hencky strain $\hat{H}_{33}$, (c) Electric field at t=1s.

The Green-Lagrange strain A_{33} in Fig. 4.4.5a is homogeneous in the cube volume. As demonstrated in Fig. 4.4.5b, A_{33} and Hencky strain $\hat{H}_{33}$ decrease within a time interval of 1 s whereby the offset between both is enlarged. The electric field, shown in Fig. 4.4.5a, is homogeneous.

4.4.2 Validation model C

In this subsection results of benchmark tests using model C and B are compared to validate model C.

Relaxation due to mechanical stress

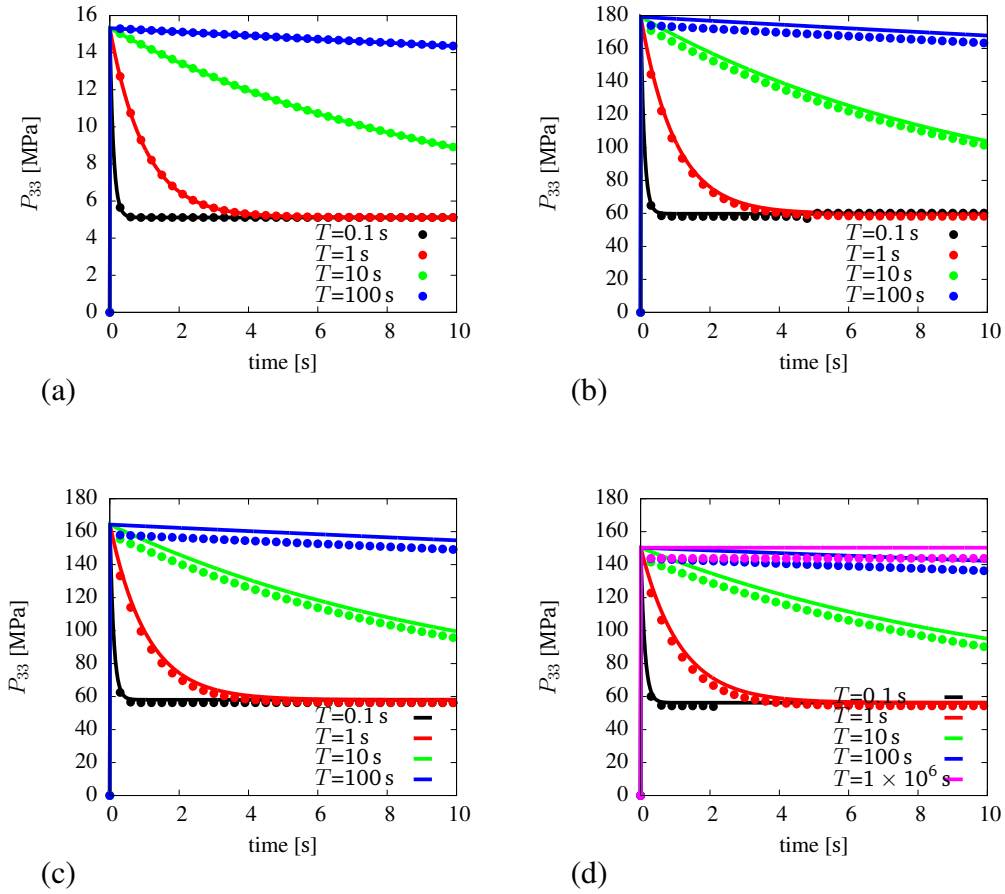

Figure 4.4.6.: Relaxation test, model C versus model B for β=2.0: (a) ε=1 %, ν=0.499, (b) ε=10 %, ν=0.499, (c) ε=10 %, ν=0.45, (d) ε=10 %, ν=0.4. Dots show solutions for model C.

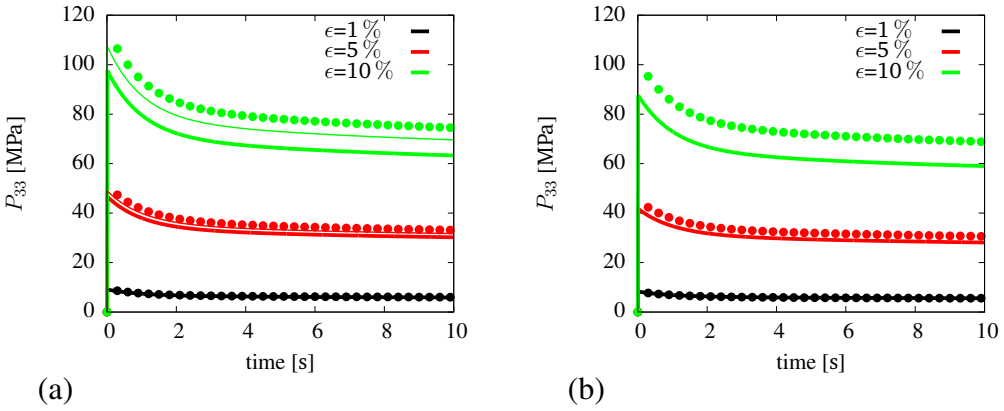

Figure 4.4.7.: Relaxation test, model C and B versus analytical solution using a Generalised Maxwell model of three Maxwell elements with β_1=0.5, β_2=0.2, β_3=0.1, T_1=1 s, T_2=10 s, T_3=100 s: (a) ν=0.499, (b) ν=0.4. Thick lines show solutions for model B, dots show solutions for model C and thin lines the analytical solution.

It is observable in the relaxation tests in Fig. 4.4.6a and b that the deviation between model B and C is slight, even for a strain of 10 % and a relaxation time of 100 s; the offset is not influenced by the Poisson's ratio that is shown in Fig. 4.4.6c and d. For a simultaneous activity of three Maxwell elements however, the offset between B and C is clearly visible in Fig. 4.4.7 for strains larger than 5 %.

Creep due to voltage

The patch test described in section 4.4.1 was used to compare B and C under voltage control.

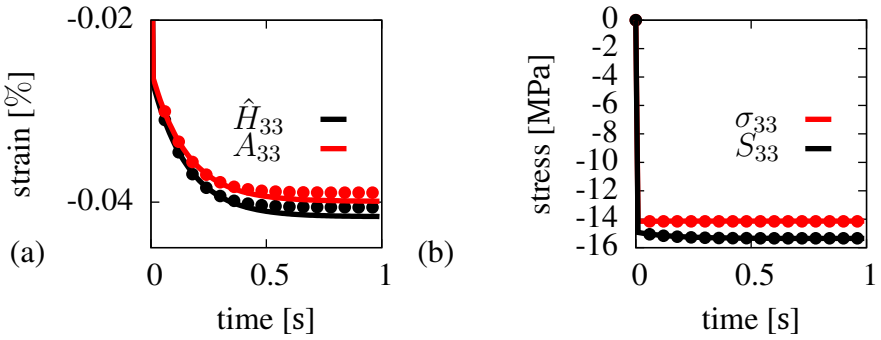

Figure 4.4.8.: Patch test, model C versus model B using a Generalised Maxwell model of four Maxwell elements with β_1=0.5, β_2=0.2, β_3=0.1, β_4=0.05 and T_1=0.5, T_2=0.2 s, T_3=0.1 s, T_4=0.05 s: (a) A_{33} and $\hat{H}_{33}$, (b) S_3 and σ_3. Dots show solutions for model C.

As shown in Fig. 4.4.8a, a divergence of resulting strains A_{33} and $\hat{H}_{33}$ is noticeable with a strain of 4 %. Both models yield a similar time function for Cauchy and 2.Piola-Kirchhoff stress, see Fig. 4.4.8b.
Both large deformation models fit the analytical solution for small deformation. In case several Maxwell elements are active, an offset between B, C and analytical solution is given for strains above 5 % for an incompressible material. In voltage-controlled tests, B and C diverge with strains above 5 %. All discussed tests show reasonable results and confirm the validity of the numerical coding.

5 3D model for layered polymeric ferroelectrets

5.1 Introduction

A 2D continuum model for the electric breakdown induced charging process and deformation behaviour of polymeric ferroelectrets has been introduced in Xu et al. and Gross and Xu [148, 149, 150]. This model is presented here in a 3D formulation and variants for small and large deformation to simulate lossless and transient behaviour. It consists of two subroutines implemented in FEAP, one for bulk elements, and one for interface elements. The linear model variant for bulk is similar to the linear standard electromechanical model for polarisation. Large deformation bulk models use a geometric non-linear formulation with St.Vernant material for the lossless behaviour, or apply the numerical schemes discussed in chapter 4 for transient behaviour. Electric field quantities are formulated in the reference configuration. The interface models adopt the bulk material and a subiteration is conducted for interface nodes to describe the accumulation of free charge after electric breakdown.

The chapter is organised as follows: In the subsection 5.1.1 the lossless linear model is described which is later used to investigate the piezoelectric behaviour. The non-linear bulk model is derived in subsection 5.1.2. The model for interface charging is revised in subsection 5.1.3. In section 5.2 numerical expressions for the element stiffness matrix in bulk and interface elements are explained.

5.1.1 Linear model, bulk

Material laws, kinematics and balance laws for a dielectric bulk material are described in the following. The mechanical stress tensor is written for Hookean material: $\boldsymbol{\sigma} = \mathbb{C}\boldsymbol{\varepsilon}$. $\boldsymbol{\sigma}$ and $\boldsymbol{\varepsilon}$ are second order tensors of stress and strain field. $\boldsymbol{\varepsilon} = \frac{1}{2}\left[(\nabla \mathbf{u})^T + \nabla \mathbf{u}\right]$ is the linearised strain tensor whereby $\mathbf{u}$ specifies the field of mechanical displacement. $\mathbb{C}$ is the fourth order elasticity tensor, which has 9 entries different from zero in the isotropic material assumed here. $\mathbb{C}$ is formulated as

$$\mathbb{C} = \lambda(\mathbf{1} \otimes \mathbf{1}) + 2\mu\mathbb{1}, \tag{5.1.1}$$

where $\otimes$ defines the dyadic or tensorial product. λ and μ are the Lamé constants whereby μ is equal to shear modulus G. $\mathbf{1}$ and $\mathbb{1}$ are unit tensors of second and fourth order. For an ideal dielectric material follows

$$\mathbf{E} = -\text{grad}\,\phi, \tag{5.1.2}$$

$$\mathbf{D} = \epsilon_0 \epsilon_r \mathbf{E}. \tag{5.1.3}$$

E and **D** are the vectors of electric and dielectric displacement field, ϵ_0 is the vacuum permittivity, ϕ represents the scalar field of electrostatic potential and $\epsilon_r = 1 + \frac{\chi_s}{J}$ is the relative permittivity. The susceptibility χ_s is divided by J, which is the volume change of an infinitesimal volume element during deformation. For convenience it is not written explicitly in expressions for fields mentioned so far that they depend on current position **x**, but this dependence is used to calculate J by the determinant of deformation gradient.

$$J = \det \mathbf{F} = \det \left(\mathbf{1} + \frac{\partial \mathbf{u}}{\partial \mathbf{X}} \right). \tag{5.1.4}$$

In McMeeking and Landis [95] an electrostatic stress for a proportional dependence of susceptibility on density as $\chi = \chi_s \frac{\rho}{\rho_0} = \chi_s \frac{1}{J}$ is derived.[1] The electrostatic stress is formulated as

$$\boldsymbol{\sigma}^{\mathrm{E}} = \mathbf{E} \otimes \mathbf{D} - \frac{1}{2} \epsilon_0 \frac{\chi_s}{J} (\mathbf{E} \cdot \mathbf{E}) \mathbf{1}. \tag{5.1.5}$$

Coupling between electrical and mechanical material properties is achieved via a definition of a total stress [94, 96]

$$\boldsymbol{\sigma}^{\mathrm{tot}} = \boldsymbol{\sigma} + \boldsymbol{\sigma}^{\mathrm{E}}. \tag{5.1.6}$$

The mechanical and electric balance law are given as

$$\operatorname{div} \boldsymbol{\sigma} + \mathbf{f} = 0, \tag{5.1.7}$$

$$\operatorname{div} \boldsymbol{\sigma}^{\mathrm{E}} - \mathbf{f}^{\mathrm{E}} = 0 \tag{5.1.8}$$

$$\operatorname{div} \mathbf{D} - \varrho = 0 \tag{5.1.9}$$

where **f** is the vector of mechanical body force density and $\mathbf{f}^{\mathrm{E}}$ the vector of electric force density. ϱ is the charge density.

5.1.2 Geometric non-linear model, bulk

Reference and current configuration for all field quantities is distinguished to consider geometric non-linear effects. The choice of configuration and work-conjugated stress and strain measure is influenced by material formulation and numerical transformability, as well as by requirements with regard to experimental verification. Here, the model is formulated in the reference configuration since it is a light version of the model for polarised dielectrics introduced in section 4.3.2. 2.Piola-Kirchhoff stress tensor **S** for St.Vernant material is defined by

$$\mathbf{S}(\mathbf{A}) = \lambda(\mathbf{A}) \mathbf{1} + 2\mu \mathbf{A}, \tag{5.1.10}$$

[1] This means that the polarisation energy ψ_P per unit mass is proportional to the square of the dipole moment per unit mass: $\psi_P = \frac{\rho_0}{2\epsilon_0 \chi_s} \left(\frac{P_k}{\rho} \right) \left(\frac{P_k}{\rho} \right)$.

or in indices as

$$S_{ij} = \lambda \delta_{ij} A_{kk} + 2\mu A_{ij}. \tag{5.1.11}$$

A is the Green-Lagrange strain tensor. For the mechanical tangent stiffness follows

$$\mathbb{C} = 2\frac{\partial \mathbf{S}}{\partial \mathbf{C}} = \lambda(\mathbf{1} \otimes \mathbf{1}) + 2\mu \mathbb{1}, \tag{5.1.12}$$

or in indices as

$$C_{ijkl} = \lambda \delta_{ij} \delta_{kl} + 2\mu \delta_{ik} \delta_{jl}. \tag{5.1.13}$$

Electric field quantities are defined in reference to Dorfmann and Ogden [94]

$$\mathbf{E}_0 = -\text{GRAD}\, \phi, \tag{5.1.14}$$

$$\mathbf{E}_0 = \mathbf{F}^T \mathbf{E}, \tag{5.1.15}$$

$$\mathbf{D}_0 = J\mathbf{F}^{-1}, \tag{5.1.16}$$

$$\mathbf{D}_0 = \epsilon_0 \left(J + \chi_s\right) \mathbf{C}^{-1} \mathbf{E}_0, \tag{5.1.17}$$

$$\mathbf{S}^{\mathrm{E}} = \left(\mathbf{C}^{-1}\mathbf{E}_0\right) \otimes \mathbf{D}_0 - \frac{1}{2}\epsilon_0 J \left[\mathbf{E}_0 \cdot \left(\mathbf{C}^{-1}\mathbf{E}_0\right)\right] \mathbf{C}^{-1}. \tag{5.1.18}$$

$\mathbf{E}_0$ and $\mathbf{D}_0$ are electric and dielectric displacement field vector in the reference configuration, **C** is right Cauchy-Green tensor.

5.1.3 Charging process, interface

This subsection introduces a model for the charging of a non-polarised polymer generated by free charges produced by electric breakdown of a gas. The interface charge density p is the difference between normal components of dielectric displacement in adjoining dielectrics with permittivities ϵ_{r_1} and ϵ_{r_2}.[2] Charging starts when the breakdown field E_{B} is reached

$$\begin{aligned} p &= [[\mathbf{D} \cdot \mathbf{n}]] = (\mathbf{D}^+ - \mathbf{D}^-) \cdot \mathbf{n} \\ &= \epsilon_0 \epsilon_{r_2} E_{\mathrm{m}} - \epsilon_0 \epsilon_{r_1} E_{\mathrm{B}} \quad \text{where} \quad \epsilon_{r_2} > \epsilon_{r_1}. \end{aligned} \tag{5.1.19}$$

$E_{\mathrm{m}} = -\mathbf{E}_{\mathrm{FEP}} \cdot \mathbf{m}$ is the normal component of the electric field in the polymer pointing into the broken down medium.

[2] See Eq. (2.2.25)

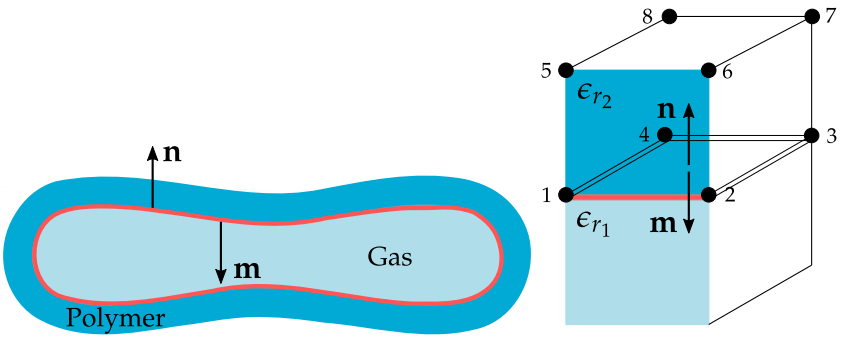

Figure 5.1.1.: (a) Orientation of vectors $\mathbf{m}$ and $\mathbf{n}$. The red line symbolises the interface. (b) Combination of bulk and interface element.

Accumulation of free charge is modelled by a return mapping algorithm similar to the numerical description of 1D plasticity with kinematic hardening [151]. Like a flow rule, a function to govern the charging is derived from Eq. (5.1.19)[3]

$$f(E_{\mathrm{m}}) := |E_{\mathrm{m}}| - \frac{\epsilon_{r_1}}{\epsilon_{r_2}} E_{\mathrm{B}} \leq 0. \tag{5.1.20}$$

Eq. (5.1.20) implies two cases. $f(E_{\mathrm{m}}) < 0$ means no charge is accumulated, since $|E_{\mathrm{m}}|$ is smaller than $\frac{\epsilon_{r_1}}{\epsilon_{r_2}} E_{\mathrm{B}}$. $f(E_{\mathrm{m}}) = 0$ defines the threshold for the case E_{m} is on the yield surface. A numerical iteration takes place for $f(E_{\mathrm{m}_{n+1}}) > 0$. For kinematic hardening, a linear increase of tensile stress shifts the centre of yield surface in the stress/strain diagram, the threshold value for accumulation of plastic strain due to compression is reduced. Such a behaviour is called Bauschinger effect that is observed for metals and alloys. Based on empirical observation [153], a similar behaviour, illustrated in Fig. 5.1.2, is assumed for the electric field component E_{m} as function of interface charge p. A second internal variable $q = -2E_{\mathrm{B0}} + E_{\mathrm{B1}}$ is installed to include this in the flow rule

$$f(E_{\mathrm{m}}, q) := |E_{\mathrm{m}} - q| - \frac{\epsilon_{r_1}}{\epsilon_{r_2}} E_{\mathrm{B}} \leq 0. \tag{5.1.21}$$

q is denoted as “back field“. The rate of p is constant and given by

$$\dot{p} = \gamma \, \mathrm{sign}(E_{\mathrm{m}} - q). \tag{5.1.22}$$

The signum function defines the direction of $\dot{p}$. During loading, see green curve section in Fig. 5.1.2, $f(E_{\mathrm{m}}) > 0$. It follows $\dot{p} = \gamma$. During unloading, see red curve section, $\dot{p} = -\gamma$ is held. p is only

[3] Compare with the formulation of 1D plasticity, see Simo and Hughes [152]

changed if the threshold value $f(E_\mathrm{m}) = 0$ is reached. The Kuhn-Tucker condition $\gamma f(E_\mathrm{m}) = 0$ can be derived from this.

$$\left.\begin{array}{rcl} f(E_\mathrm{m}) < 0 & \Rightarrow & \gamma = 0 \\ \gamma > 0 & \Rightarrow & f(E_\mathrm{m}) = 0 \end{array}\right\} \quad \gamma f(E_\mathrm{m}) = 0 \tag{5.1.23}$$

$f(E_\mathrm{m}) = 0$ has to be guaranteed for every time point; the Kuhn-Tucker condition in Eq. 5.1.23 is therefore also valid for $\dot{f}$ leading to the persistency or consistency condition

$$\gamma \dot{f}(E_\mathrm{m}) = 0. \tag{5.1.24}$$

γ is known as consistency parameter and can be interpreted as Lagrange multiplier. The relation between the internal variables is given as[4]

$$p = \epsilon_0 \epsilon_{r_2} q. \tag{5.1.25}$$

An evolution equation for q is defined by

$$\dot{q} = \frac{1}{\epsilon_0 \epsilon_{r_2}} \dot{p} = \gamma \, \mathrm{sign}(E_\mathrm{m} - q) \frac{1}{\epsilon_0 \epsilon_{r_2}}. \tag{5.1.26}$$

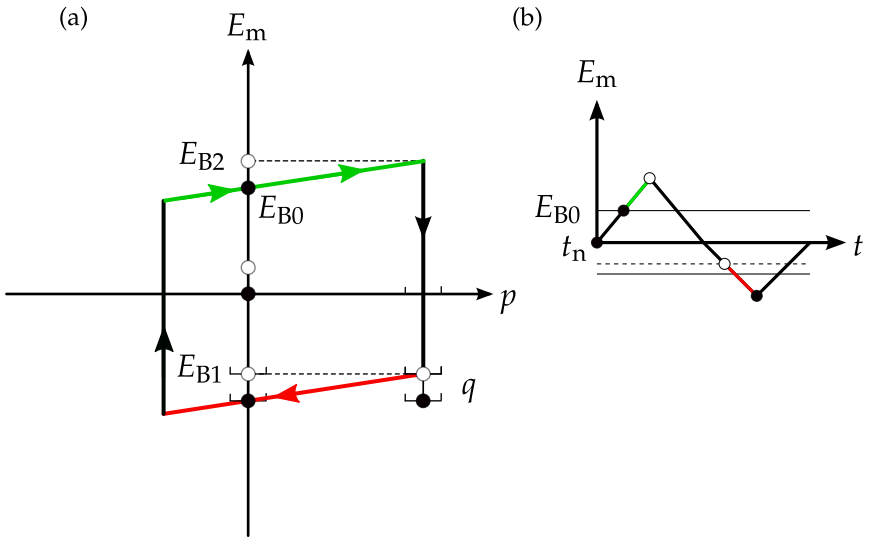

Figure 5.1.2.: (a) Hysteresis of charge accumulation: Green line marks loading, red line unloading. q is the offset of yield surface midpoint. (b) Time function of E_m.

[4] The model in [148] assumes a linear curve progression of p. This fits well Eq. (5.1.25). Measurements of polarisation dynamics of FEP/ePTFE/FEP sandwich structures have however shown that charge accumulation is non-linear with time [154]. A non-linear hardening rule can be used to improve the correlation to experimental data.

Eq. (5.1.19)-Eq. (5.1.26) form a differential-algebraic system of equations (DAEs) for time t_{n}. A time-discretisation is performed using a backward Euler scheme which approximates a solution for time points $t > t_{\mathrm{n}}$. The present initial value problem is classified as a constrained problem of evolution whereby the constraint is given by Eq. (5.1.21) which governs also the update of internal variables p and q. Time increments of internal variables p_{n} and q_{n} are updated if $f(E_{\mathrm{m}_{n+1}}) > 0$. The update of the electrostatic force t^{C} between two opposite polarised surfaces is governed by the constraint condition as well.[5] This condition is queried in the algorithm presented in Fig.5.1.3 by $f^{\mathrm{trial}}_{n+1} > 0$. An iterative process of query and update is repeated until $f^{\mathrm{trial}}_{n+1} \leq 0$. This iterative procedure is also referred to as return mapping.

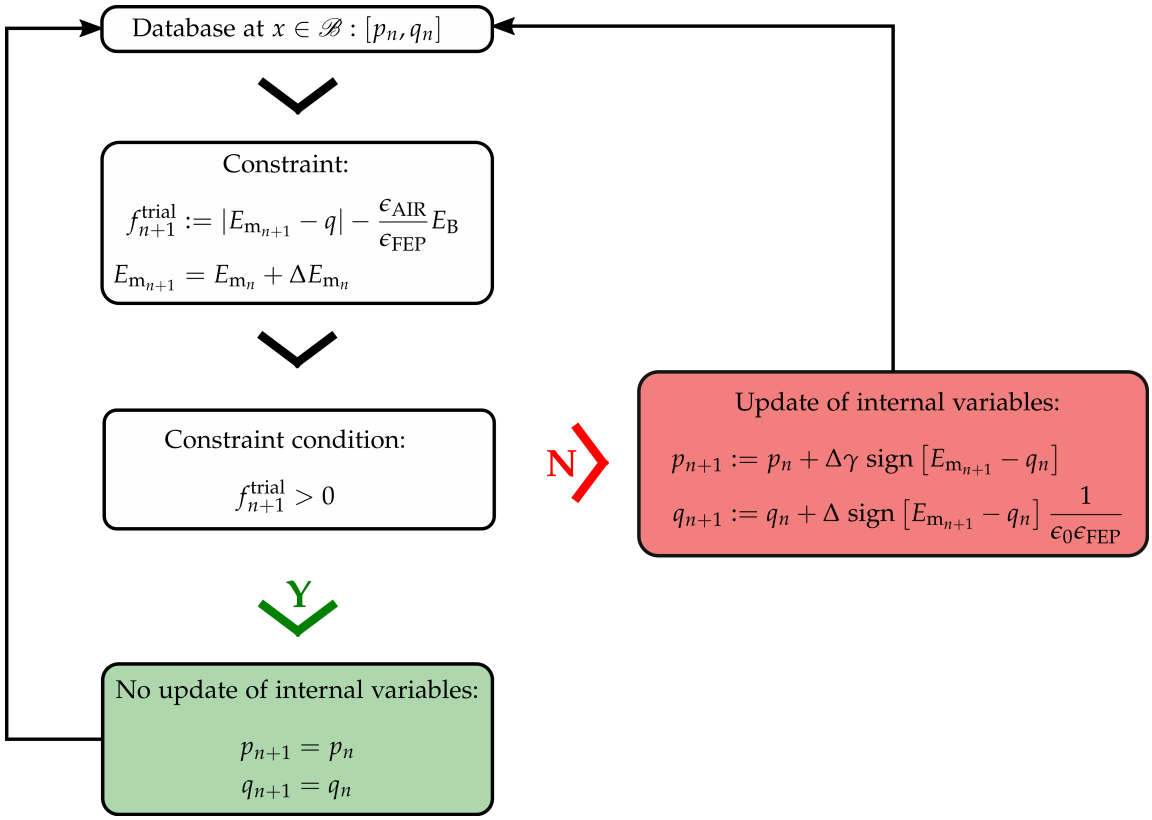

Figure 5.1.3.: Return mapping algorithm to describe charge accumulation in the interface: $\Delta\gamma = \gamma_{\mathrm{n+1}} + \Delta t \geq 0$, is the algorithmic counterpart of the consistency parameter $\gamma \geq 0$.[6]

Before electric breakdown, when $E_{r_1} < E_{\mathrm{B}}$, the electric field in the gas is calculated by transforming Eq. (5.1.19) to

$$E_{r_1} = \frac{p}{\epsilon_0 \epsilon_{r_1}} + \frac{\epsilon_{r_2}}{\epsilon_{r_1}} E_{\mathrm{m}}. \tag{5.1.27}$$

[5] For a detailed description see appendix A.7.

5.2 Numerical implementation

5.2.1 Linear model, bulk

Numerical implementation starts with the formulation of weak forms of balance laws referred to body $\mathscr{B}$ with volume Ω. The weak form of balance is equivalent to the work done by a virtual displacement $\delta\mathbf{u}$ and a virtual potential $\delta\phi$ on a volume Ω

$$\begin{aligned} &+\underbrace{\int_{\Omega} \mathbf{D}\cdot\delta\mathbf{E}\,dv}_{\delta W^{\mathrm{E}}_{\mathrm{int}}} + \underbrace{\int_{\partial\Omega_q} \mathbf{D}\cdot\mathbf{n}\,\delta\phi\,ds}_{\delta W^{\mathrm{E}}_{\mathrm{ext}}} = 0, \\ &-\underbrace{\int_{\Omega} (\boldsymbol{\sigma}+\boldsymbol{\sigma}^{\mathrm{E}}) : \delta\mathbf{H}\,dv}_{\delta W^{\mathrm{M}}_{\mathrm{int}}} + \underbrace{\int_{\partial\Omega_t} \mathbf{t}^{\mathrm{tot}}\cdot\delta\mathbf{u}\,ds}_{\delta W^{\mathrm{E}}_{\mathrm{ext}}} = 0. \end{aligned} \tag{5.2.1}$$

$\mathbf{t}^{\mathrm{tot}} = (\boldsymbol{\sigma}+\boldsymbol{\sigma}^{\mathrm{E}})\mathbf{n}$ is the total Cauchy stress vector, $\mathbf{D}\cdot\mathbf{n}$ is the surface charge density. $\delta\mathbf{H} = \operatorname{grad}\delta\mathbf{u}$ and $\delta\mathbf{E} = -\operatorname{grad}\delta\phi$ are the gradients of virtual displacement and electric field. δW_{ext} and δW_{int} are the virtual external and internal work of electric and mechanical forces, respectively. Due to the first law of thermodynamics, $\delta W_{\mathrm{int}} = \delta W_{\mathrm{ext}}$. Solutions of Eqs. (5.2.1) are obtained by using the Finite-Element method whereby a discretisation of volume and degrees of freedom is carried out. Geometry, virtual displacement and electric field are discretised using trilinear shape functions.[7] A standard interval for the Gauss quadrature is given by the natural coordinates $\xi \in [-1,1]$, $\eta \in [-1,1]$ and $\zeta \in [-1,1]$. The interval boundaries define the positions of 8 boundary nodes of a cube volume in the parameter space. Two residuals remain from the numerical solution of the balances. For the element nodes $a = 1,...,8$, their discrete form is described by[8]

$$\begin{aligned} R^{\mathrm{E}}_a &= -\int_{\Omega_h} (\mathbf{B}^{\mathrm{E}}_a)^T\cdot\mathbf{D}\,dv, \\ \mathbf{R}^{\mathrm{M}}_a &= -\int_{\Omega_h} (\mathbf{B}^{\mathrm{M}}_a)^T(\boldsymbol{\sigma}+\boldsymbol{\sigma}^{\mathrm{E}})\,dv. \end{aligned} \tag{5.2.2}$$

$\mathbf{B}^{\mathrm{E}}_a$ is a 3-dimensional vector of derivatives of shape functions of the virtual electric potential. In Voigt notation, $\mathbf{B}^{\mathrm{M}}_a$ is a 6x3 matrix of derivatives of shape functions of the virtual displacement. Vector and matrix are described in appendix A.6. $\boldsymbol{\sigma}$ and $\boldsymbol{\sigma}^{\mathrm{E}}$ are given in Voigt notation, residual $\mathbf{R}^{\mathrm{M}}_a$ is therefore a 3-dimensional vector. Since the Newton method is used, a tangential stiffness matrix describes the change

[7] See appendix A.5.

[8] The index $_h$ means discretised.

of the residual by variation of a kinematic variable. Three partial derivatives are given for the electromechanical coupled system since for linear theory the electric field does not depend on displacement. The discretised entries of the tangential stiffness matrix are noted down for any possible combination of element nodes a and b.[9]

$$\begin{bmatrix} k_{ab}^{\mathrm{EE}} & 0 \\ \mathbf{k}_{ab}^{\mathrm{ME}} & \mathbf{k}_{ab}^{\mathrm{MM}} \end{bmatrix}, \text{ for } a,b = 1,...,8 \text{ with}$$

$$\underbrace{k_{ab}^{\mathrm{EE}} = -\frac{\partial R_a^{\mathrm{E}}}{\partial \phi_b}}_{\text{scalar value}}, \quad \underbrace{\mathbf{k}_{ab}^{\mathrm{ME}} = -\frac{\partial \mathbf{R}_a^{\mathrm{M}}}{\partial \phi_b}}_{\text{vector}}, \quad \underbrace{\mathbf{k}_{ab}^{\mathrm{MM}} = -\frac{\partial \mathbf{R}_a^{\mathrm{M}}}{\partial u_b}}_{3\times 3 \text{ matrix}}. \tag{5.2.3}$$

5.2.2 Linear model, interface

The numeric modelling of charge accumulation and Coulomb force requires a formulation of the virtual work on interfaces between polymer and gas, given as

$$\begin{aligned} \delta\tilde{W}_{\mathrm{ext}}^{\mathrm{E}} &= -\int_{\partial\Omega_q} (\mathbf{D}^{+} - \mathbf{D}^{-}) \cdot \mathbf{n}\, \delta\phi \, ds = -\int_{\partial\Omega_q} p\, \delta\phi \, ds. \\ \delta\tilde{W}_{\mathrm{ext}}^{\mathrm{M}} &= \int_{\partial\Omega_t} (\mathbf{t}^{\mathbf{E}} \cdot \mathbf{m})\mathbf{m} \cdot \delta\mathbf{u} \, ds = \int_{\partial\Omega_t} t^{\mathrm{C}}\, \mathbf{m} \cdot \delta\mathbf{u} \, ds, \\ &= -\int_{\partial\Omega_t} t^{\mathrm{C}}\, \mathbf{n} \cdot \delta\mathbf{u} \, ds. \end{aligned} \tag{5.2.4}$$

$\mathbf{t}^{\mathrm{E}} = -\boldsymbol{\sigma}^{\mathrm{E}}\mathbf{n}$ is the electric Cauchy stress vector. t^{C} is the Coulomb force due to the attraction of polarised surfaces. An extension by $\mathbf{m} \cdot \mathbf{m}$ is necessary in case t^{C} is formulated by means of the Coulomb force in a parallel plate capacitor that is a scalar expression. The field inside the capacitor is a superposition of fields due to charges on each of both capacitor plates; one half of E_{r_1}[10] has to be taken into account to calculate t^{C}

$$t^{\mathrm{C}} = \frac{1}{2}|p\, E_{\mathrm{r}_1}|. \tag{5.2.5}$$

[9] The entries of the stiffness matrix are described more detailed in appendix A.6.

[10] At the end of the charging process E_{r_1} is equal to E_{B}, see appendix A.7. For simplification it is assumed that E_{B} is not changed by mechanical compression. This is an approximation. In reality, the breakdown field of air is defined via Paschen's curve which is a function of the gap between poled surfaces. A development of a continuum model for a deformation-dependent breakdown field could be of interest.

Discretised interface residuals are written as

$$\begin{aligned}\hat{\mathrm{R}}_c^{\mathrm{E}} &= -\int_{\partial\Omega_q^h} N_c\, p\, ds,\\ \hat{\mathbf{R}}_c^{\mathrm{M}} &= -\int_{\partial\Omega_t^h} N_c\, t^C \mathbf{n}\, ds.\end{aligned} \tag{5.2.6}$$

where $c = 1, ..., 4$ are the four interface nodes in Fig. 5.1.1. An additional stiffness matrix contribution for these nodes is

$$\begin{bmatrix} \hat{\mathrm{k}}_{cb}^{\mathrm{EE}} & \mathbf{0} \\ \hat{\mathbf{k}}_{cb}^{\mathrm{ME}} & \mathbf{0} \end{bmatrix}, \text{ with}$$

$$\hat{\mathrm{k}}_{cb}^{\mathrm{EE}} = -\frac{\partial \hat{\mathrm{R}}_c^{\mathrm{E}}}{\partial \phi_b},\ \hat{\mathbf{k}}_{cb}^{\mathrm{ME}} = -\frac{\partial \hat{\mathbf{R}}_c^{\mathrm{M}}}{\partial \phi_b}. \tag{5.2.7}$$

5.2.3 Geometric non-linear model, bulk

A total stress is assumed equivalent to Eq. (5.1.6) but using the 2.Piola-Kirchhoff stress tensor for St. Vernant material. $\mathbf{S}^{\mathrm{tot}} = \left(\mathbf{S} + \mathbf{S}^{\mathrm{E}}\right)$. $\mathbf{T}^{\mathrm{tot}}$ is then the total Cauchy stress vector. Weak forms of equilibrium are defined by

$$\begin{aligned}&+\int_{\Omega_0} \mathbf{D}_0 \cdot \partial \mathbf{E}_0\, dV + \int_{\partial\Omega_{0_q}} \mathbf{D}_0 \cdot \mathbf{N}\delta\phi\, dS = 0\\ &-\int_{\Omega_0} (\mathbf{S} + \mathbf{S}^{\mathrm{E}}) : \delta\mathbf{A}\, dV + \int_{\partial\Omega_{0_t}} \mathbf{T}^{\mathrm{tot}} \cdot \delta\mathbf{u}\, dS = 0,\end{aligned} \tag{5.2.8}$$

in Voigt notation as

$$\delta\mathbf{A}^h = \begin{bmatrix} \delta A_{11} \\ \delta A_{22} \\ \delta A_{33} \\ 2\delta A_{23} \\ 2\delta A_{13} \\ 2\delta A_{12} \end{bmatrix} = \sum_{a=1}^{n} \mathbf{B}_a^{\mathrm{M}} \delta\mathbf{u}_a, \tag{5.2.9}$$

or written in indices as

$$\delta A_{ij} = \frac{1}{2} \sum_{a=1}^{n} \left[F_{ik} N_{a,j} + N_{a,i} F_{kj}\right] \delta u_{ka}. \tag{5.2.10}$$

Matrix $\mathbf{B}^{\mathrm{M}}$ for large deformation is described in appendix A.8. $\mathbf{B}^{\mathrm{E}}$ is similar to the linear formulation. Residuals for the bulk are

$$\begin{aligned} \mathrm{R}^{\mathrm{E}} &= -\int_{\Omega_0^h} (\mathbf{B}_a^{\mathrm{E}})^T \cdot \mathbf{D}\, dV, \\ \mathbf{R}_a^{\mathrm{M}} &= -\int_{\Omega_0^h} (\mathbf{B}_a^{\mathrm{M}})^{\mathrm{T}} (\mathbf{S} + \mathbf{S}^{\mathrm{E}})\, dV. \end{aligned} \tag{5.2.11}$$

The element stiffness matrix is given by

$$\begin{bmatrix} \mathrm{k}_{ab}^{\mathrm{EE}} & \mathbf{k}_{ab}^{\mathrm{EM}} \\ \mathbf{k}_{ab}^{\mathrm{ME}} & \mathbf{k}_{ab}^{\mathrm{MM}} \end{bmatrix}, \text{ for } a, b = 1, ..., 8 \text{ with}$$

$$\underbrace{\mathrm{k}_{ab}^{\mathrm{EE}} = -\frac{\partial \mathrm{R}_a^{\mathrm{E}}}{\partial \phi_b}}_{\text{scalar value}}, \underbrace{\mathbf{k}_{ab}^{\mathrm{EM}} = -\frac{\partial \mathrm{R}_a^{\mathrm{E}}}{\partial \mathbf{u}_b}}_{\text{vector}}, \underbrace{\mathbf{k}_{ab}^{\mathrm{ME}} = -\frac{\partial \mathbf{R}_a^{\mathrm{M}}}{\partial \phi_b}}_{\text{vector}}, \underbrace{\mathbf{k}_{ab}^{\mathrm{MM}} = -\frac{\partial \mathbf{R}_a^{\mathrm{M}}}{\partial \mathbf{u}_b}}_{3\times 3 \text{ matrix}}. \tag{5.2.12}$$

5.2.4 Geometric non-linear model, interface

The residuals for interface nodes in the current configuration are assumed to be similar to linear theory.[11] A transformation into reference configuration can be performed by two ways, for the residual containing the Coulomb force can be interpreted as virtual work of a direction-dependent load. Nanson's law or the concept for deformation-dependent load, explained in section 2.7.1, can be applied. The latter is chosen here and outlined subsequently.[12]

Tangent vectors $\mathbf{g}_\alpha = \boldsymbol{\chi}_{,\alpha}^h$ are obtained by the partial derivative of position vector $\boldsymbol{\chi}^h$ with respect to the convective coordinates ξ and η.[13] The tangent vectors discretised by quadrilinear shape functions are written as

$$\begin{aligned} \boldsymbol{\chi}^h &= \sum_{c=1}^{4} N_c(\xi, \eta) \boldsymbol{\chi}_c, \\ \boldsymbol{\chi}_{,\alpha}^h &= \sum_{c=1}^{4} N_c(\xi, \eta)_{,\alpha}\, \boldsymbol{\chi}_c\,. \end{aligned} \tag{5.2.13}$$

The surface normal with respect to the reference configuration $\tilde{\mathbf{N}}$ is expressed using Eq. (2.7.4)

$$\tilde{\mathbf{N}}^h = \boldsymbol{\chi}_{,\xi}^h \times \boldsymbol{\chi}_{,\eta}^h = \begin{bmatrix} x_{2,\xi} x_{3,\eta} - x_{3,\xi} x_{2,\eta} \\ x_{3,\xi} x_{1,\eta} - x_{1,\xi} x_{3,\eta} \\ x_{1,\xi} x_{2,\eta} - x_{2,\xi} x_{1,\eta} \end{bmatrix}. \tag{5.2.14}$$

[11] See Eqs. (5.2.6)
[12] Compare with [92]
[13] $\alpha = 1$ complies with ξ and $\alpha = 2$ with η.

By assuming Eq. (5.2.6), the discretised interface residuals are given as

$$\begin{aligned}\hat{\mathrm{R}}_c^{\mathrm{E}} &= -\int\limits_{\partial\Omega_{p_q}^h} N_c\, p\, ||\boldsymbol{\chi}_{,\xi}^h \times \boldsymbol{\chi}_{,\eta}^h||\, d\xi d\eta, \\ \hat{\mathbf{R}}_c^{\mathrm{M}} &= -\int\limits_{\partial\Omega_{p_t}^h} N_c\, t^C \tilde{\mathbf{N}}^h\, d\xi d\eta.\end{aligned} \tag{5.2.15}$$

$\partial\Omega_p^h$ is the discretised surface in the parameter space. The stiffness matrix entries are[14]

$$\hat{\mathbf{k}}_{cb} = \int\limits_{\partial\Omega_p^h} t^C N_c \left(N_{b,\xi}\bar{\mathbf{N}}_{,\eta} - N_{b,\eta}\bar{\mathbf{N}}_{,\xi}\right) d\xi d\eta. \tag{5.2.16}$$

The entries of matrix $\bar{\mathbf{N}}_{,\alpha}$ are

$$\bar{\mathbf{N}}_{,\alpha} = \begin{bmatrix} 0 & \bar{x}_{3,\alpha} & -\bar{x}_{2,\alpha} \\ -\bar{x}_{3,\alpha} & 0 & \bar{x}_{1,\alpha} \\ \bar{x}_{2,\alpha} & -\bar{x}_{1,\alpha} & 0 \end{bmatrix}. \tag{5.2.17}$$

Due to large deformation theory two additional submatrices $\hat{\mathbf{k}}_{cb}^{\mathrm{EM}}$ and $\hat{\mathbf{k}}_{cb}^{\mathrm{MM}}$ containing partial derivatives of the electric and mechanical residual with respect to the mechanical displacement are supplemented.

$$\begin{bmatrix} \hat{\mathrm{k}}_{cb}^{\mathrm{EE}} & \hat{\mathbf{k}}_{cb}^{\mathrm{EM}} \\ \hat{\mathbf{k}}_{cb}^{\mathrm{ME}} & \hat{\mathbf{k}}_{cb}^{\mathrm{MM}} \end{bmatrix}. \tag{5.2.18}$$

A detailed description of 5.2.18 is given in appendix A.9.[15]

[14] Compare with Wriggers [92], p.144.

[15] For 2D case, the stiffness matrices using Nansons's formula are reported in [150].

6 Structural effects on ferroelectret parameters

6.1 Introduction

It is shown that electromechanical performance of polymeric ferroelectrets is primarily determined by their mechanical compliance [155]. For truss-like and eye shaped geometries it has been reported that the wall thickness regulates the effective Young's modulus [156]. The structure variant at hand consists of lined-up cells, illustrated in Fig. 6.1.1; it has a wall thicknesses between 50 µm and 150 µm. A very low Young's modulus of 0.3 MPa and a high piezoelectric coefficient of about 150 pC N^{-1} was measured for stress levels up to 0.01 MPa for a wall thickness of 50 µm. Since for the given wall thickness a higher Young's modulus was expected, a numerical investigation of structural properties by means of FE-simulation is carried out. In particular the cell geometry, which is formed by buckling during manufacturing, and the impact of mechanical boundary conditions are examined with regard to charge accumulation and piezoelectric coefficient.

Literature research revealed just a few works related to this topic since numerical investigation of charging and piezoelectric behaviour of polymeric ferroelectrets is a less covered topic. In Tuncer et al. [157], a linear electromechanical model, coupled via electrostatic stress has been applied to simulate d_{33} coefficients of layered electret systems whereby the charge distribution in the interface is prescribed. A further d_{33} simulation for an idealized, closed cellular PP structure can be found in Wan and Zhong [158]. Herein, single cells are modelled by hollow oblate tetrakaidecahedrons. A prediction method of effective electromechanical properties of cellular ferroelectrets based on the Eshelby's model is explained in [159].

The chapter is structured as follows: In the subsequent section 6.2 buckling of FEP-tubes is investigated by means of FE-simulation; the hot-forming of a single tube is simulated in subsection 6.2.1. Subsection 6.2.2 is focussed on the deformation behaviour of a set of tubes that form a cell array. Sections 6.3 and 6.4 describe simple schemes to estimate the effective Young's modulus and the d_{33}.

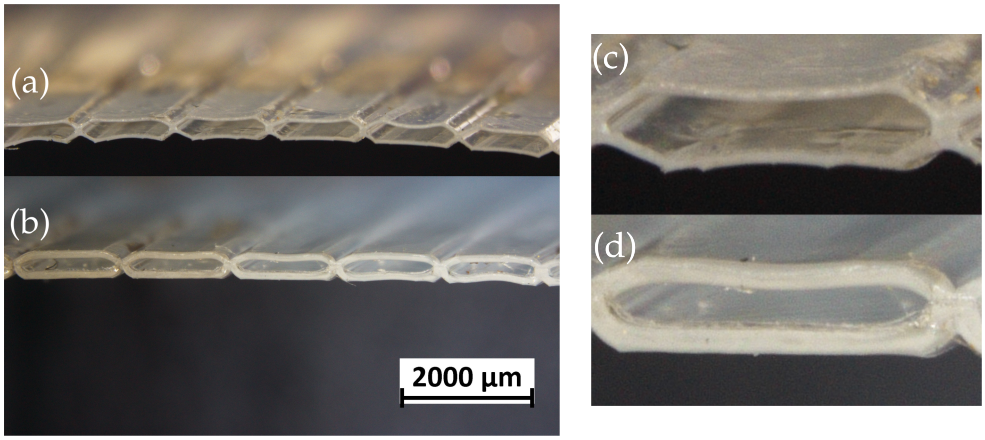

Figure 6.1.1.: Cell array from FEP-tubes: (a) and (c) 50 µm, (b) and (d) 100 µm [160].

6.2 From single tube to cell array

Many concepts to form ferroelectret geometries out of polymer films have been introduced in literature [161]-[162]. A FEP-array with tubular air channels is one structure variant introduced in Altafim et al. [163]. The array is obtained by fusing two films using a PTFE mask. Tubular channels can be formed also using a template-based lamination technology presented in [163, 164, 165]. The array structure at hand is produced by hot-forming of merchantable FEP-tubes. A set of tubes with a length about 5 cm is compressed between two metal plates like illustrated in Fig. 6.2.1. The plates are heated up to

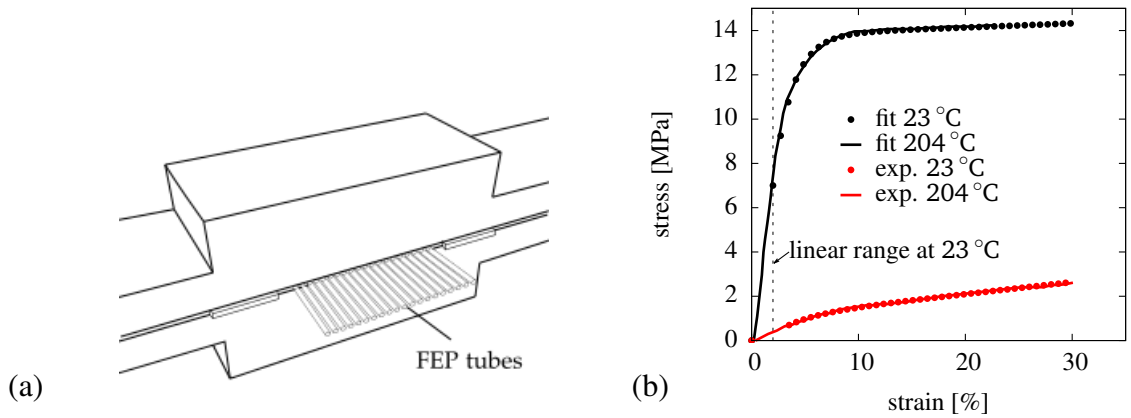

Figure 6.2.1.: (a) Set-up for preparation of array structures. 20-25 tubes are compressed and merged by hot-forming between two plates. (b) Fitted material curves of FEP100.

a temperature of 270 °C and melt together during a hold time of 10 min. In a time interval of 45 min the setup is cooled down to room temperature. Generated arrays have a well ordered structure down to a wall thickness t of 50 µm. For wall a thickness of 25 µm, the structure is unstable and shows diverse buckling modes.[1]

[1] The observed modes are similar to post-buckling modes described in [166]

6.2.1 Single tube

Deformation behaviour and stress distribution in tubes and circular rings induced by differently applied forces is subject of engineering and mathematical description since the beginning of the 20th century [167]. In 1969 a thick rubber ring compressed by two flat platens was experimentally examined in Durelli et al. [168]. The original circular cross section of the ring was deformed to an oval shape. An eight-shaped buckling mode has been observed during the hot-forming of FEP-tubes at 250 °C. A mathematical description of both deformation modes is given in Flaherty and Rubinow [169] where buckling modes with n-fold symmetries were calculated. The oval section is the first buckling mode that occurs if outside minus the inside pressure p is equal to buckling pressure p_{bn}. Higher buckling modes occur for $p_{bn} > p$. The observed eight-shaped mode can be ranged between p_{bn} and p_{cn} where p_{cn} is the pressure in case opposite longitudinal tube sides are just touch each other.

Deformation of tubes by compression between two plates is mapped by FE-simulation subsequently. The model assembly is shown in Fig. 6.2.2. Contact surfaces Surf.1 and Surf.2 are active. A surface to surface contact with finite sliding is applied. Default hard-contact using a Lagrange multiplier method is set normal to surface, and frictionless contact tangential to surface. Surf.2 is fixed for all degrees of freedom, Surf.1 is free to move in normal direction. A standard elasto-plastic material of ABAQUS that considers isotropic hardening is applied. Elasto-plastic material data is therefore extracted from stress/strain curves of FEP100 for 23 °C and 204 °C [170]. Matlab is used for the parameter fitting demonstrated in Fig. 6.2.1b. An FE-mesh is generated by 20-node quadratic brick elements with reduced integration. Non-linear geometry is assumed. The analysis is stabilised by a dissipated energy fraction of 0.002 %. The maximum ratio of stabilisation to strain energy is 0.05.

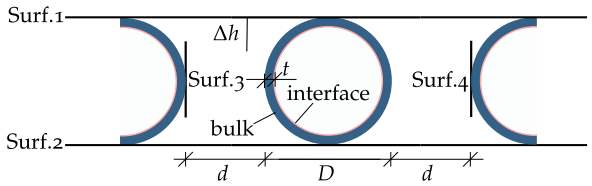

Figure 6.2.2.: Assembly of the FE-model: t is the tube thickness, d is distance between tubes, D the outer tube diameter.

Simulation results of displacement driven simulation at 204 °C show that upper and lower cell edge are displaced inhomogeneously. The outer cell edges are stronger shifted than middle area. The tube section is bent around the x-axis as it can be seen particularly in Fig. 6.2.3a and d. For both geometries the von Mises stress is maximal in the region of the folded edges. As it can be observed in Fig. 6.2.3b and e, the maximum value is higher in the tube with a wall thickness of 150 µm due to its higher stiffness. Fig. 6.2.3c and f show the displacement in compression direction.

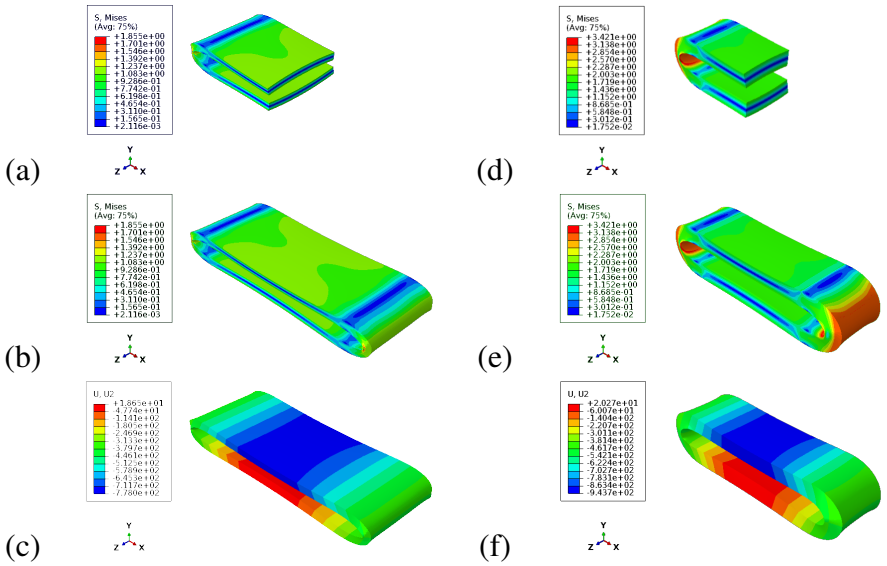

Figure 6.2.3.: Compressed tube at 204 °C, (a)-(c) D=940 µm, t=50 µm, (d)-(f) D=1400 µm, t=150 µm. Von Mises stress in [MPa], displacement in [µm]. (a) and (d) Von Mises stress in a tube half, (b) and (e) Von Mises stress, (c) and (f) Displacement in compression direction.

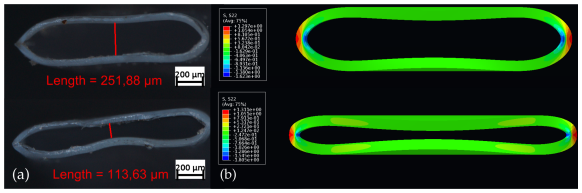

Figure 6.2.4.: Compressed FEP-tube with D=940 µm and t=50 µm: (a) Experiment at T=250 °C, (b) Simulation at T=204 °C, stress component S_{yy}.

A comparison of experiment and simulation is presented in Fig. 6.2.4. The compression test in Fig. 6.2.4a shows an eight shaped form that can be recognized also in the simulation. Stress in compression direction S_{yy} is concentrated on the left and right lateral edge. The outer edges are stretched (red region) and the inner are compressed (blue region).

6.2.2 Cell array

By additionally assuming lateral contact surfaces, Surf.3 and Surf.4 shown in Fig. 6.2.2, the compression of a set of tubes to an array structure is simulated using Virtual Performance Solution (VPS). Lateral contact is defined using a friction free Lagrange node to segment contact. An 8-node hexahedral element that applies mean a dilatation method is used.

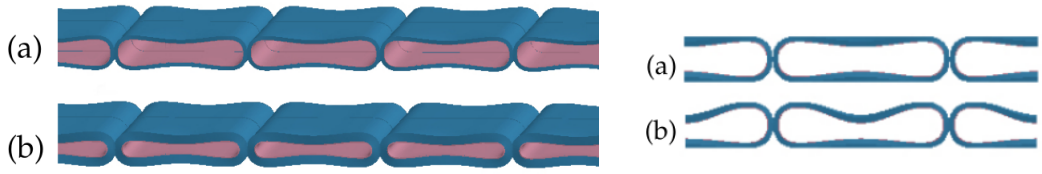

Figure 6.2.5.: Compressed set of tubes with D=1000 µm at T=204 °C. Left picture, (a) t=50 µm, (b) t=100 µm. Right picture, t=50 µm, (a) Surf.3 and Surf.4 just touch each other, (b) Distance d between tubes is slightly reduced.

Simulation results for tubes with an outer diameter D=1000 µm are presented in the left pictures in Fig. 6.2.5. Herein, the overall compression is 65 % what is equal to the experimental specification for a wall thickness of 50 µm. The right picture demonstrates that buckling of the upper edge is more pronounced in case where the tubes are positioned closer together. The buckling is stronger also if temperature is lower because the material's and the effective Young's modulus is higher. This relationship is demonstrated by Fig. 6.2.6 that shows the influence of temperature on deformation behaviour. An explanation for the outlined relationship is that for higher cell stiffness, higher contact pressure is necessary to compress the cell to a certain level; for a restricted movement of lateral edges, the contact pressure perpendicular to compression, in x-direction, is growing thereby. The minimal contact pressure in x-direction is for 23 °C about 18 % higher than for 204 °C what can be see Fig.6.2.7a and d.

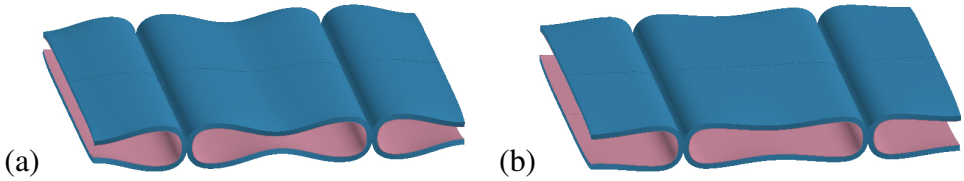

Figure 6.2.6.: Influence of temperature: (a) 23 °C, (b) 204 °C.

Comparing the manufactured arrays in Fig. 6.1.1 with the virtual structures in Fig. 6.2.5 shows different geometries for a wall thickness of 50 µm; in the real structure a cant has developed during hot-forming, while in the simulation lateral cell edges are rounded. A reason for this is the neglection of creep effects in the used material model. This assumption is confirmed by Fig. 6.2.8a and Fig. 6.2.8b that show that the geometries of real structure and simulation deviate just at those locations of maximal von Mises stresses and equivalent plastic strain.

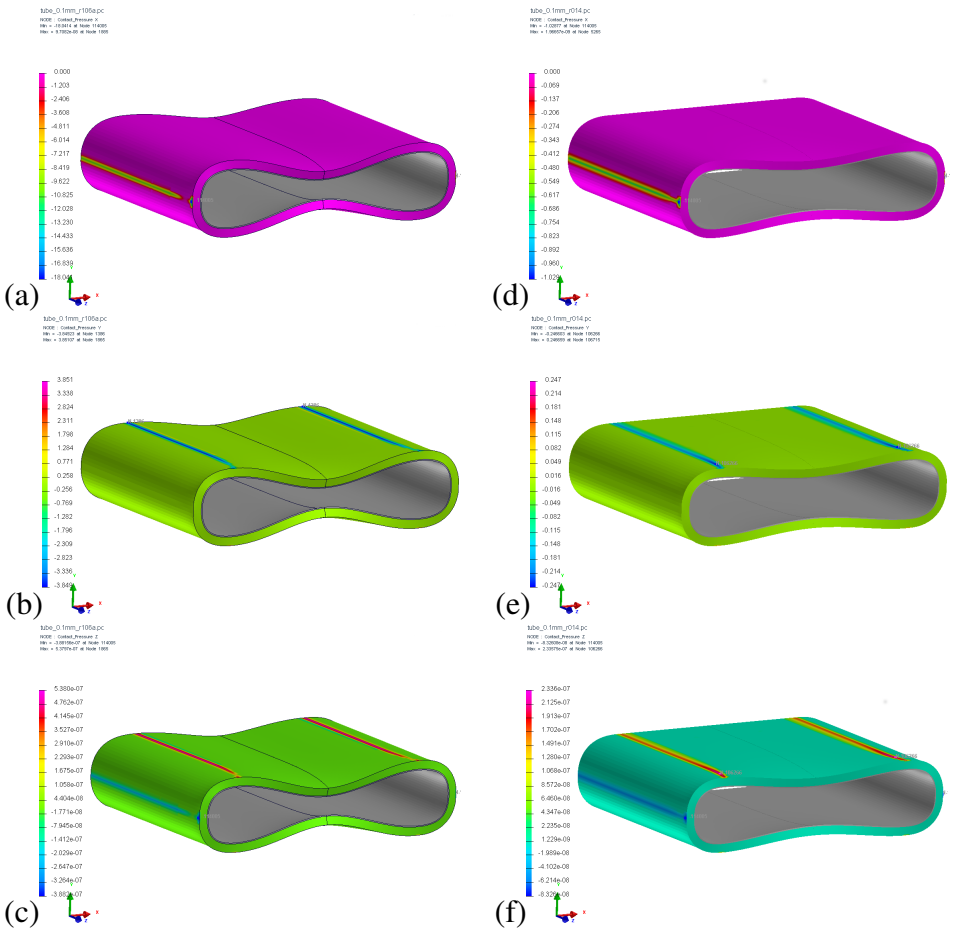

Figure 6.2.7.: Contact pressure in [MPa], (a)-(c) 23 °C, (d)-(f) 204 °C: (a) and (d) Contact pressures in x-direction, (b) and (e) Contact pressures in y-direction, (b) and (e) Contact pressures in z-direction, for a wall thickness of 50 µm.

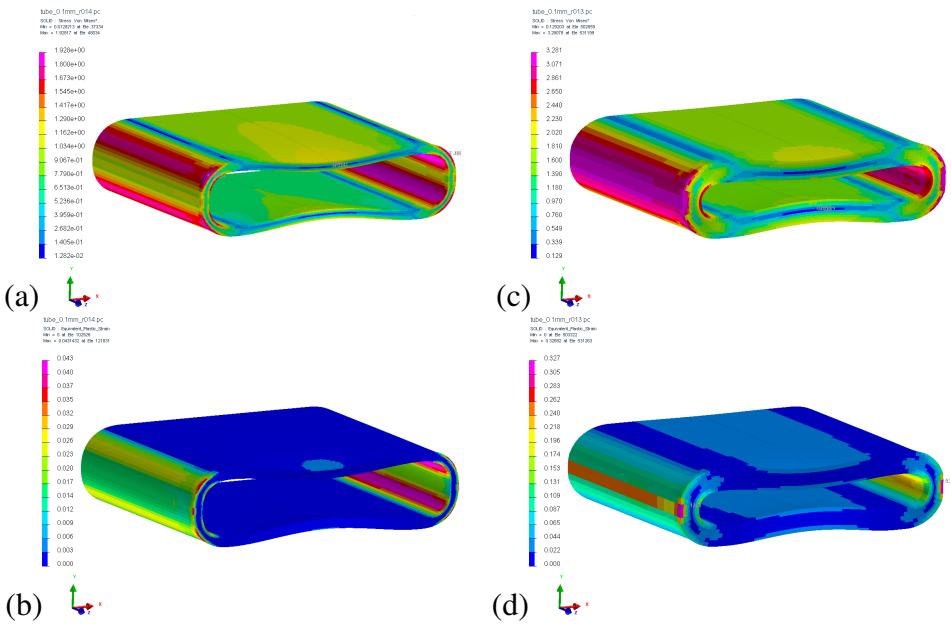

Figure 6.2.8.: (a) and (b) Von Mises stress in [MPa], (c) and (d) equivalent plastic strain at 204 °C, for wall thicknesses of 50 µm and 100 µm. Von Mises stress and plastic strain are maximal in the magenta regions.

Summing up, two parameters can be identified from FE-simulation which influence the buckling: The Young's modulus of tube material and the distance between adjacent tubes.

6.3 Effective Young's modulus

Since the effective Young's modulus of the cell, here denoted as Y_{E}, is an essential parameter for the d_{33} coefficient, an approximation of Y_{E} based on FE-simulation is identified. Boundary conditions on lateral edges, Young's modulus of FEP and cell geometry are varied. For each case a separate cell is investigated that is compressed by $1\,\%$. The cell geometry in the FE-model is derived from a dimensioned photomicrograph shown in Fig. 6.3.1a. Only the FEP-frame, identifiable by the blue elements in

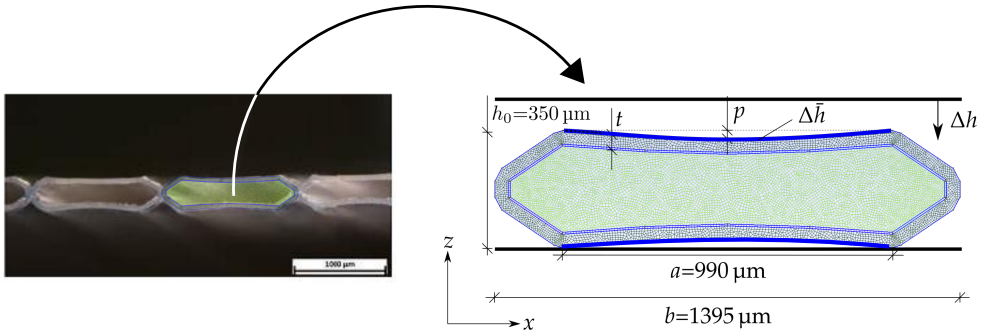

Figure 6.3.1.: Cell array for t=50 µm and FE-Model for electromechanical simulation

Fig. 6.3.1, is discretised using linear volume elements and linear elastic material to estimate Y_{E}, which is calculated using the mean compression strain $\bar{\varepsilon}_{33}$, defined by

$$\bar{\varepsilon}_{33} = \frac{\Delta\bar{h}}{h_0}. \tag{6.3.1}$$

h_0 is the initial height of the cell, $\Delta\bar{h}$ the mean value of the displacement of nodes on upper cell surface, see Fig. 6.3.1. The mean value of compression stress is defined by

$$\bar{\sigma}_{33} = \frac{\sum F_{\mathrm{reac}}}{A_0}. \tag{6.3.2}$$

A_0 in Fig. 6.3.2 is the contact surface where mechanical load is transferred. A_0 is assumed as reference surface that applies also for buckled cells where the reaction force F_{reac} acts in the four edge points. $\sum F_{\mathrm{reac}}$ is the sum of reaction forces on the half of the symmetric system. The effective Young's modulus of the structure can be determined by

$$Y_{\mathrm{E}} = \frac{\bar{\sigma}_{33}}{\bar{\varepsilon}_{33}}. \tag{6.3.3}$$

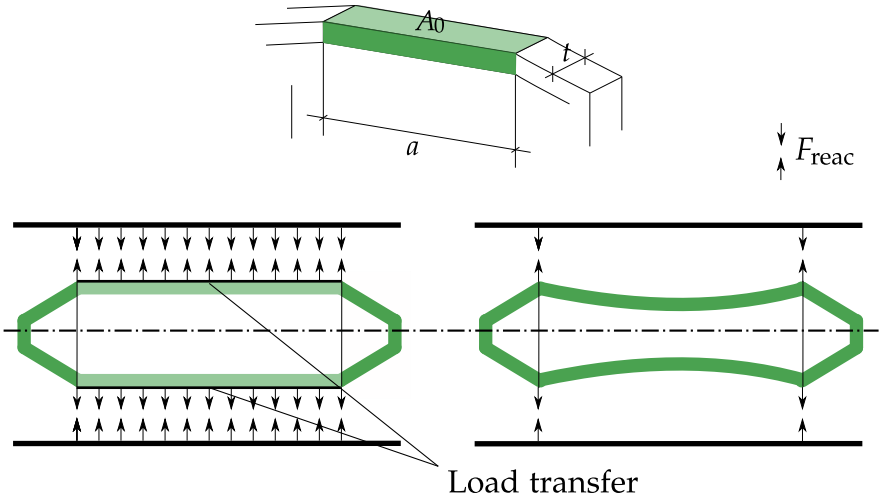

Figure 6.3.2.

In Tab. 6.1 four cell variants are distinguished. Cell 1 has straight longitudinal edges and cell 2 has buckled longitudinal edges. In both cells lateral movement is not restricted. The buckled geometry is assumed also for cell 3 and 4, but lateral boundary conditions differ. Lateral boundary nodes of cell 3 are forced to have an equal lateral displacement, and for cell 4 lateral boundaries are fixed. Y_{E} is calculated for values of the FEP's Young's modulus Y_{FEP} of 350 MPa, 440 MPa, and 500 MPa.

Y_{FEP} [MPa]	350	440	500
Cell variant	Y_{E} [MPa]		
1 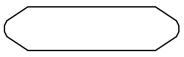	0.91	1.14	2.52
2 	0.26	0.33	0.38
3 	0.27	0.34	0.39
4 	0.97	1.22	1.39

Table 6.1.: Y_{E} for cell variants and variation of Y_{FEP}. Blue marked values are in the range of the measured Y_{E} for a wall thickness of 50 µm.

The best match with the experimental Y_E of 0.3 MPa for a cell array of 20 tubes with a wall thickness of 50 µm and a Y_{FEP} of 500 MPa [160, 171] is achieved by the free moveable, buckled cell 2.[2] By the calculated Y_E of cell 3 is shown that the constraint of linking the lateral cell movement, which can be interpreted as friction effect, has almost no influence for the small number of tubes. A significant increase of Y_E is given for cell 1 where the contact force is transferred via a larger area, and for cell 4 that is stiffened by fixed boundaries.

6.4 Piezoelectric coefficient

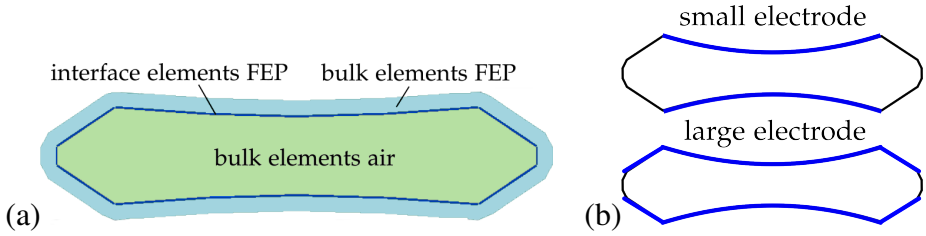

Figure 6.4.1.: (a) Element set-up, (b) Compliant electrode surface.

The electromechanical sensitivity of the ferroelectret structures investigated in context of this work is described by the d_{33} piezoelectric coefficient.[3] To derive a d_{33} from FE-simulation for the cell variants 2-4 in Tab. 6.1, following definition is assumed

$$d_{33} = \frac{\Delta D_{FEP}}{\Delta \bar{\sigma}_{33}}. \tag{6.4.1}$$

Δ is related to the time interval $\Delta t = t_1 - t_0$, the operation phase in which mechanical load is applied on the poled structure. ΔD_{FEP} is the dielectric displacement in the middle of upper cell boundary calculated by an electromechanical simulation using lossless, linear bulk and interface element formulations introduced in section 5.1.1. $\Delta\bar{\sigma}_{33} = \bar{\sigma}_{33}(t_1) - \bar{\sigma}_{33}(t_0)$ is the mean value of mechanical stress defined in Eq. (6.3.2). ΔD_{FEP} and $\Delta\sigma_{33}$ are obtained during a simulation with a load history shown in Fig. 6.4.2 whereby the strain in the second phase is prescribed with 1 % of the maximal cell height. The material definition of elements is demonstrated in Fig. 6.4.1a. The electric breakdown field is assumed with 6 kV mm^{-1}, χ_{AIR}=0 and χ_{FEP}=1.1. A fictive Young's modulus of air is assumed as 1.0×10^{-3} MPa,[4] ν_{AIR} is 0.49. Y_{FEP} is 500 MPa and ν_{FEP} is 0.49.

For variation of electrode surface and peak voltage ϕ_{max}, results for d_{33} are shown in Fig. 6.4.2b. With all boundary conditions d_{33} is strongly influenced by ϕ_{max}. This observation is supported by

[2] If alternatively a reference surface A_0 in Eq. (6.3.2) is chosen which includes the whole cell width b, see Fig. 6.3.2, values for Y_E are reduced. At a ratio of nonload-transferring to load-transferring surface of b/a=1.4, illustrated in Fig. 6.3.2, the reduction factor is 0.71. This determines Y_E between 0.23 MPa and 0.28 MPa what slightly underestimates the measured value of 0.3 MPa.

[3] The measured d_{33} coefficient can vary due to the applied measurement method [172, 173], the calculated coefficient due to its definition. It is therefore important to assume similar measurement parameters and definitions to compare d_{33}.

[4] For chosen values of 0.5×10^{-3} MPa and 5.0×10^{-3} MPa respectively, no change of dielectric displacement are observed.

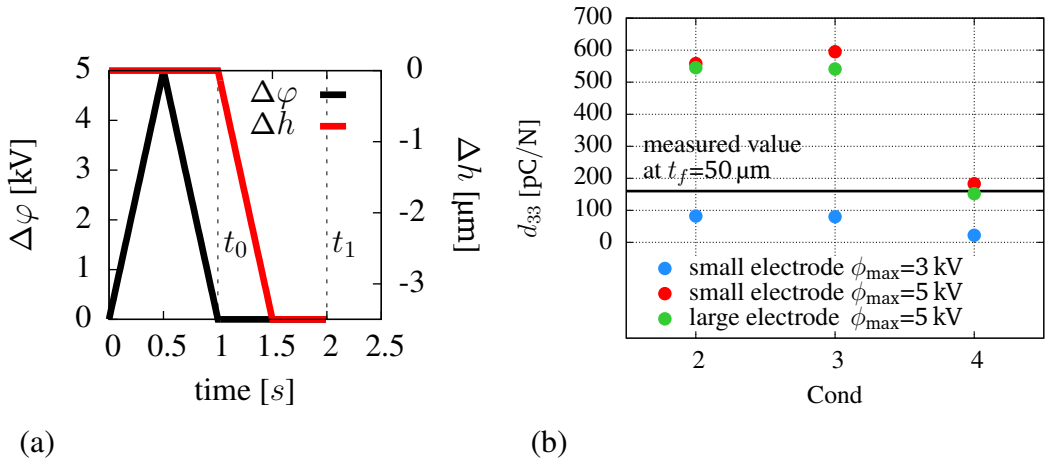

Figure 6.4.2.: (a) Applied electric potential and displacement in a time interval of 2 s, (b) Calculated d_{33} in dependence on boundary conditions and electrode surface at t=0.46 µm for a variation of the maximum potential $\phi_{\max}$ during charging.

measurements of interface charges in Zhukov et al. [171] and Sun et al. [165]. The influence of electrode size is on the other hand rather small and is observed primarily for cell 3 where d_{33} for the large electrode surface is smaller.

Summing up can be said that the simulation results show a dependence of d_{33} on the effective Young's modulus and peak voltage what confirms measurements and already known relations. However, the question rises if the effective Young's modulus, which is a mean value, is a sufficient parameter since it does not represent the deformation behaviour during poling that influences distribution and amount of the remanent polarisation.

7 FE-modelling of ferroelectret cells

7.1 Introduction

The previous chapter 6 is concerned with the influence of geometric effects directly characterised by the parameters Y_{E} and d_{33}. In this chapter, a more differentiated consideration is undertaken by evaluation and illustration of field output for cell geometries that are analysed to compare material formulations. Furthermore, the numerical code should be validated. Three cell geometries are therefore regarded, the ideal cell discussed in chapter 6, a simple rectangular disk and a virtual geometry that was derived from the elasto-plastic simulation of tube compression in section 6.2.2. Material parameters in all lossless models were chosen like follows: Y_{AIR}=1 $\times$ 10^{-3}, ν_{AIR}=0.49, Y_{FEP}=500, ν_{FEP}=0.49, electric susceptibilities of air and FEP were assumed to be 0 and 1.1, the electric breakdown field was set to $6\,\mathrm{kV\,mm^{-1}}$.

The chapter is organised as follows: In section 7.2 the ideal cell is investigated with the linear lossless model, in particular, hysteresis behaviour in 7.2.1, and electric field quantities during poling phase in 7.2.2. To map the transient mechanical behaviour, the large deformation electro-viscoelastic model B is used in 7.2.3. Section 7.3 investigates voltage driven transient deformation with model B in 7.3.1, compares results of the linear and geometric non-linear lossless model in 7.3.2 and gives information about possible causes for the instability of a rectangular ferroelectret disk in 7.3.3. Finally in section 7.4, transient field output and deformation of the virtual cell, which is poled and compressed subsequently, is shown using model B.

7.2 Ideal Cell

An ideal cell geometry was chosen to have a reference to experimental results and to record a current state of structure design by a continuum model.

7.2.1 Polarisation hysteresis, small deformation

The hysteresis for interface charge and dielectric displacement due to a triangular voltage function shown in Fig. 7.2.1 is studied using the linear lossless model from section 5.1.1. An ideal cell according to Fig. 7.2.2a is investigated. On the left lateral cell edge a symmetry condition is assumed in x-direction, on the right, equal x-displacement ("linking" of nodes) is prescribed. One side of the x-z-plane is fixed in y-direction. Hystereses are shown for two elements, 307 and 249 that lie in the interface, and for two nodes on the upper surface, see Fig. 7.2.2a. The peak voltage ϕ_{max} is varied between 3 kV and 5 kV.

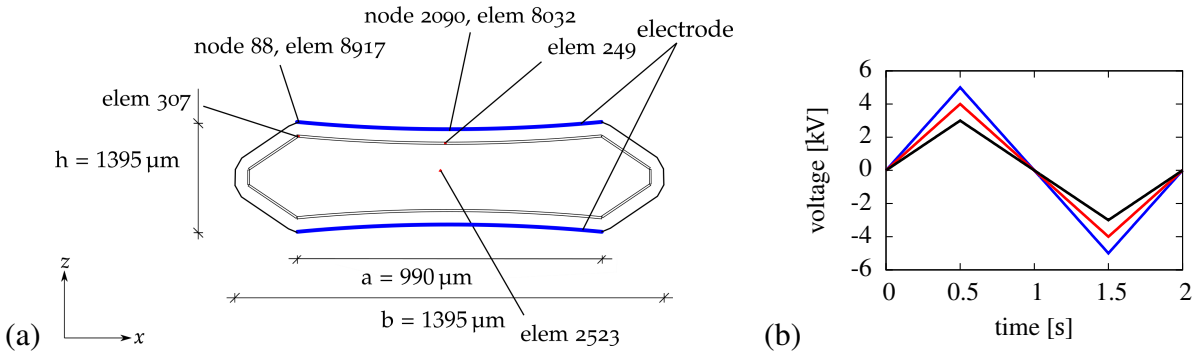

Figure 7.2.1.: (a) Cell geometry, position of reference elements and nodes, (b) Voltage functions.

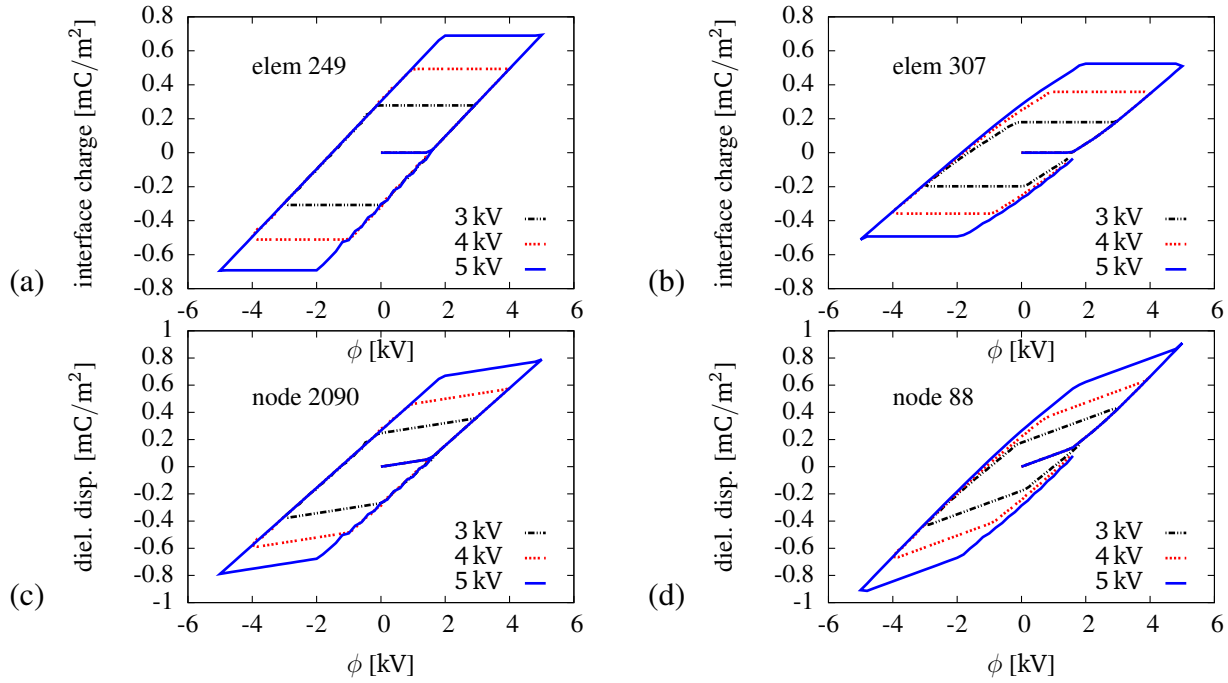

Figure 7.2.2.: Hystereses for triangular voltage functions with peak voltages ϕ_{max} of 3 kV, 4 kV and 5 kV: (a) and (b) Interface charge, (c) and (d) Dielectric displacement. A dependence of remanent interface charge and dielectric displacement on ϕ_{max} is observable for element 307 and node 88.

From the hystereses in Fig. 7.2.2 can be seen that remanent interface charge and dielectric displacement depend on ϕ_{max} for some locations. In element 307 and node 88, near the edges of the buckled surface, an influence of ϕ_{max} is given, however no change of remanent values is observed for the middle of the upper surface in element 249 and node 2090.

7.2.2 Field output poling phase, small deformation

The field output for electric and dielectric displacement during poling is shown for a triangular voltage function similar to Fig. 6.4.2 with ϕ_{max}=5 kV. Boundary conditions for cell 3 in Tab. 6.1 are assumed,

which has two linked lateral edges for x-displacement and an electrode surface appropriate to Fig. 7.2.3a.

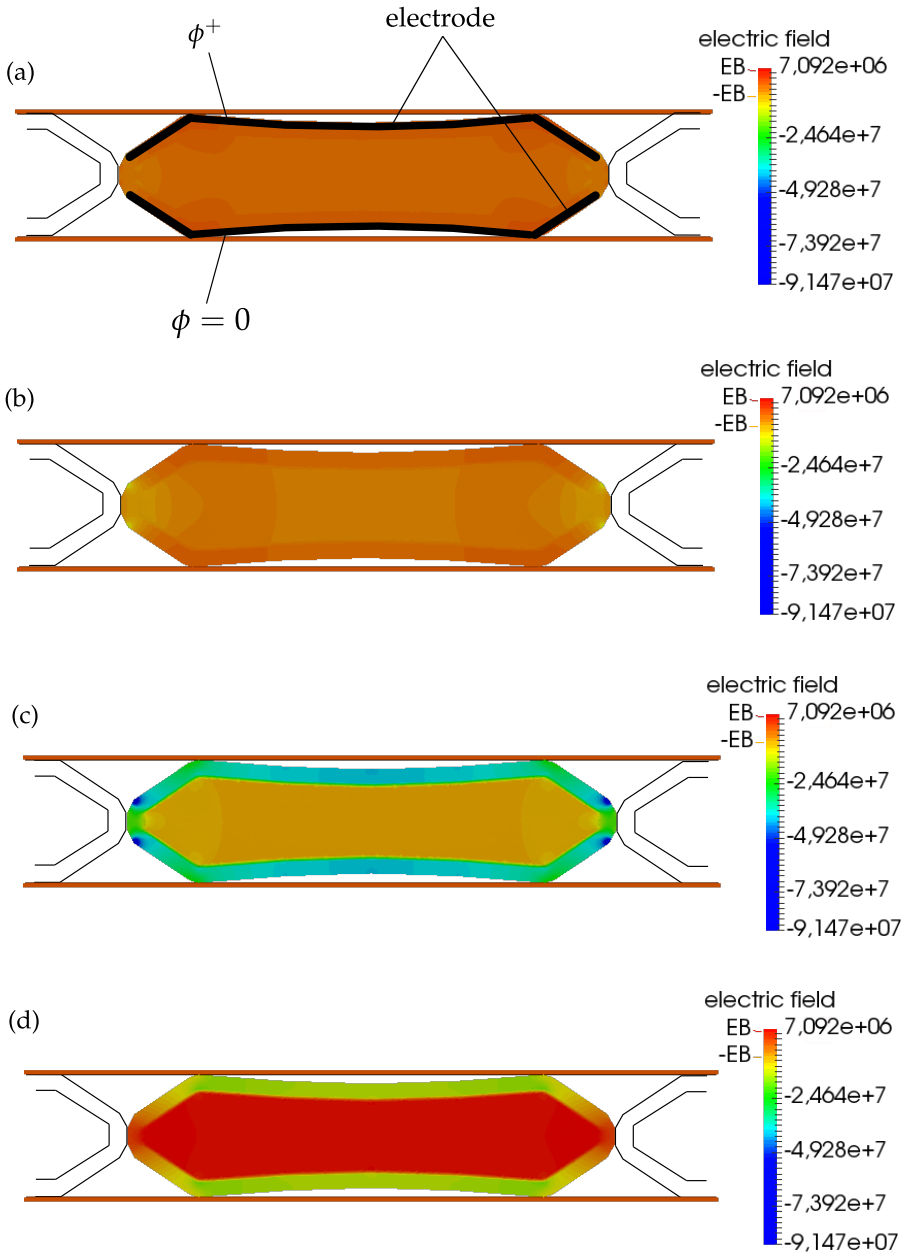

Figure 7.2.3.: Electric field during poling: (a) 0.05 s, $E < E_B$, the electric field is maximal at left and right cell edges where the gap between charged surfaces is the smallest, (b) 0.1 s, $E_{\text{AIR}} > E_B$, (c) 0.5 s, $\phi = \phi_{\text{max}}$, (d) 1 s, electric field at the end of poling phase for short-circuit.

In Fig. 7.2.3a it can be seen that the electric field is maximal in the region of lateral edges where the cell height is minimal. Electric breakdown is first initiated at the lateral edges and eventually in the middle of cell, see Fig. 7.2.3b. Fig. 7.2.3c shows the situation when ϕ_{max} is reached; singularities arise then in four edge points. The electric field distribution is inhomogeneous and different in lower and upper FEP-frame. When the voltage becomes zero, a homogeneous field with magnitude E_{B} is

observable within the whole cell; it has an opposite sign than the initial breakdown field. In case a short-circuit is created, a reversal of the breakdown field was monitored also in experiments.

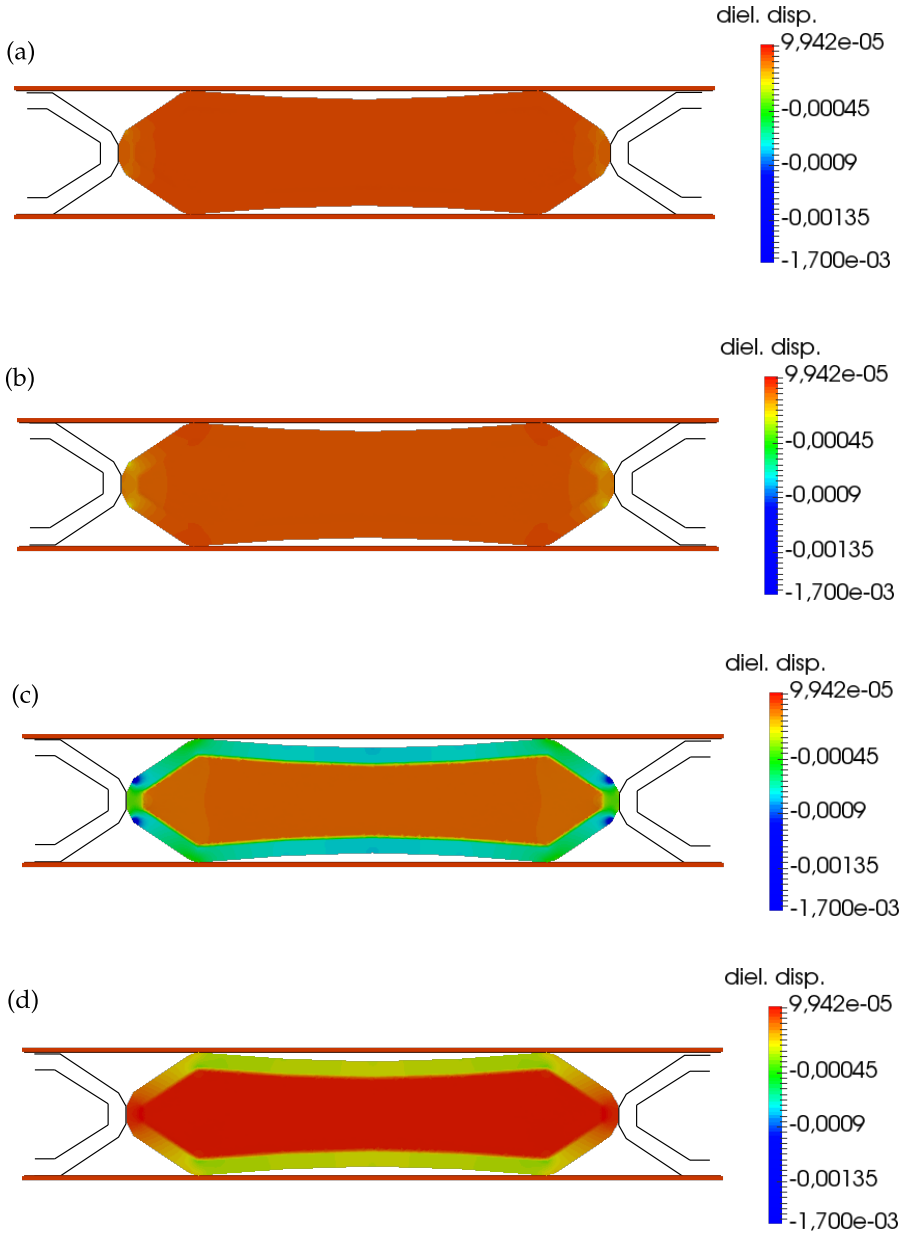

Figure 7.2.4.: Dielectric displacement during polarisation: (a) 0.05 s, (b) 0.1 s, (c) 0.5 s, (d) 1 s.

In case E_B is not reached yet, the dielectric displacement is equal in FEP and air, like observable in Fig. 7.2.4a. Fig. 7.2.4b shows clearly that electric breakdown is initiated first at lateral edges. A comparison of Fig. 7.2.4c and Fig. 7.2.4d identifies a smaller remanent D_{FEP} at the end of the poling phase than for ϕ_{max}; this corresponds to hysteresis diagrams. The dielectric displacement is larger in the buckled parts of FEP-frame than in the flattened edge regions. Fig. 7.2.5 demonstrates that the dielectric displacement field is influenced by mechanical boundary conditions that govern the structure's Young's modulus and deformation behaviour during poling. The maximal dielectric displacement, as well as its distribution are changed by the lateral boundary conditions. This is an interesting point because it may

be derived that a specification of mechanical boundary conditions or pre-deformation can reduce the poling voltage and increase the remanent interface charge.

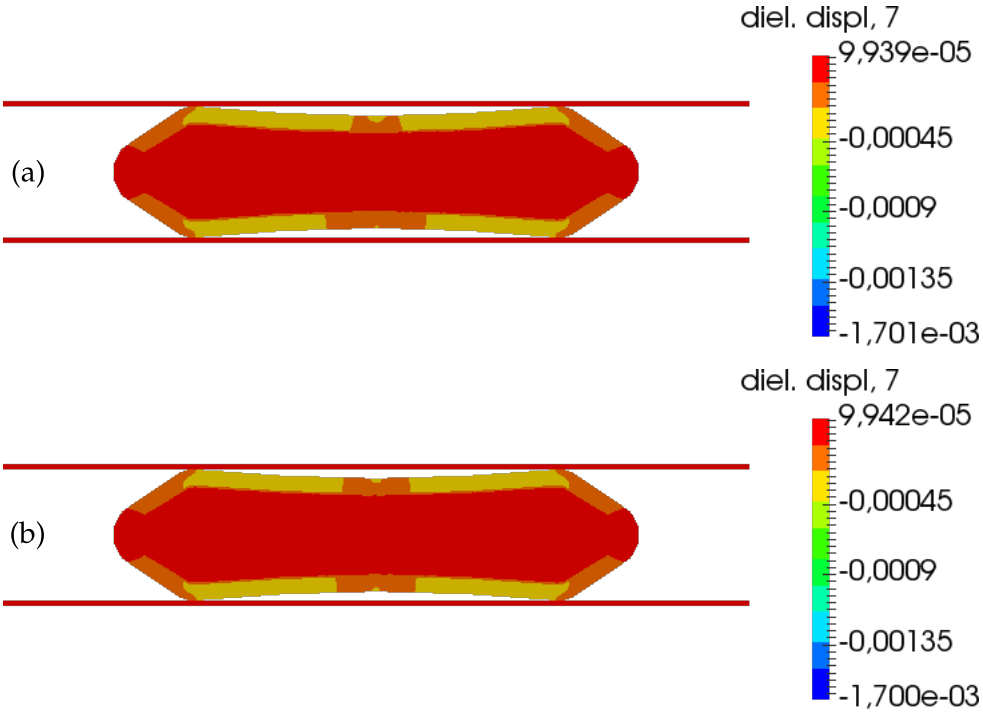

Figure 7.2.5.: Remanent dielectric displacement for cells in Tab. 6.1: (a) Cell 2, (b) Cell 3.

7.2.3 Force driven transient, large deformation

In this section, the time-dependent behaviour of an ideal cell for large deformation is illustrated with the stress-strain hystereses for a variation of the viscoelastic material parameters. An FE-mesh of the FEP-frame is generated with linear volume elements using model B from section 4.3; the frame is compressed by forces shown in Fig. 7.2.6a, which are applied on the four edge nodes of the cell and have a hold time of 0.16 s. The time curves of displacement and reaction force are illustrated exemplary in Fig.7.2.6b and c for ten Maxwell elements with β_α=0.8 and T_α=0.1 s.

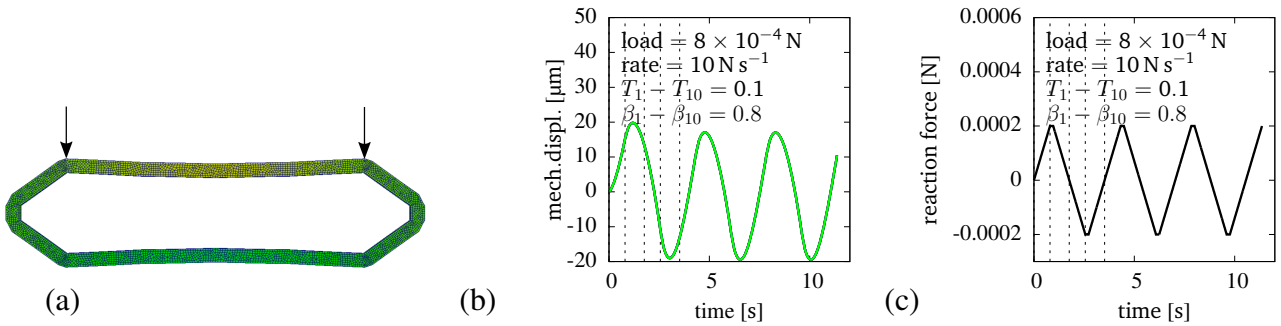

Figure 7.2.6.: (a) FEP-frame ideal cell, (b) Displacement, (c) Reaction force.

Parameter studies for β_α and T_α are shown subsequently in Fig. 7.2.7, Fig. 7.2.8 and Fig. 7.2.9, whereby stress and strain are mean values that are calculated by Eq. (6.3.1) and Eq. (6.3.2). Fig. 7.2.7 illustrates hystereses for a constant number of Maxwell elements, constant β_α, force, and force speed or loading rate. A force of $8 \times 10^{-4}\,\mathrm{N}$ with a loading rate of $10\,\mathrm{N\,s^{-1}}$ is adjusted to experiments in which the cyclic behaviour of cell arrays was investigated with compression tests. The relaxation time T_α, which is equal in all Maxwell elements, is varied with $1 \times 10^{-5}\,\mathrm{s}$, $1.0\,\mathrm{s}$ and $1 \times 10^{5}\,\mathrm{s}$. As it can be seen in Fig.7.2.7, the effective Young's modulus Y_E is increased by increasing the relaxation time since the springs in the Maxwell elements contribute longer to the total stiffness. Energy dissipation is recognisable only for T_α=1.0 s shown in Fig.7.2.7b.

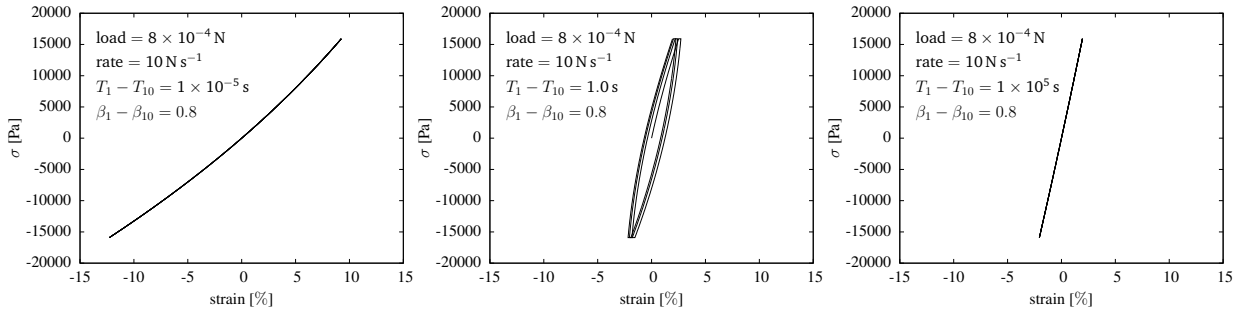

Figure 7.2.7.: Variation of T.

Fig. 7.2.8a and b show that by keeping β_α and T_α unchanged and increasing the loading rate, dissipative losses rise since the energy of the total system is raised. Fig. 7.2.9a-d illustrate hystereses for a constant load of $8 \times 10^{-4}\,\mathrm{N}$, a loading rate of $8 \times 10^{-3}\,\mathrm{N\,s^{-1}}$, β_α of 0.5 and T_α of 0.1 s; it is observed that the slope of cycles and thus Y_E grows with the number of Maxwell elements. In all first cycles strain is larger than in the following ones, what mirrors the typical development of a time-function of a damped oscillation.

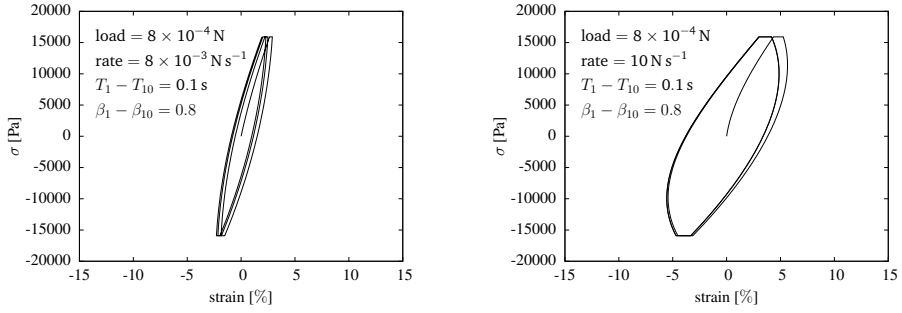

Figure 7.2.8.: Variation of loading rate.

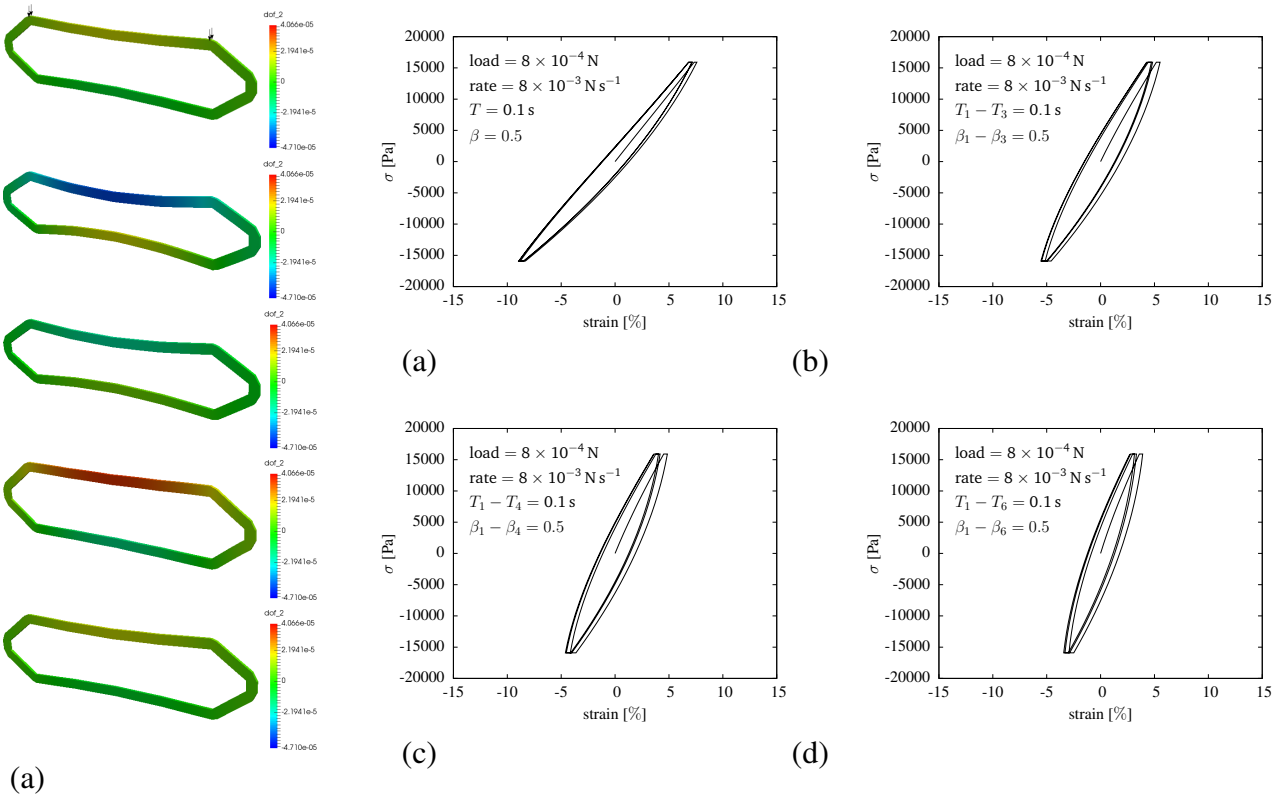

Figure 7.2.9.: Variation of the number of Maxwell elements.

7.3 Rectangular disk

A rectangular geometry is examined since thus a comparison to a previous publication of Xu et al. [148] is given where a similar geometry was investigated using a Neo-Hooke material law.

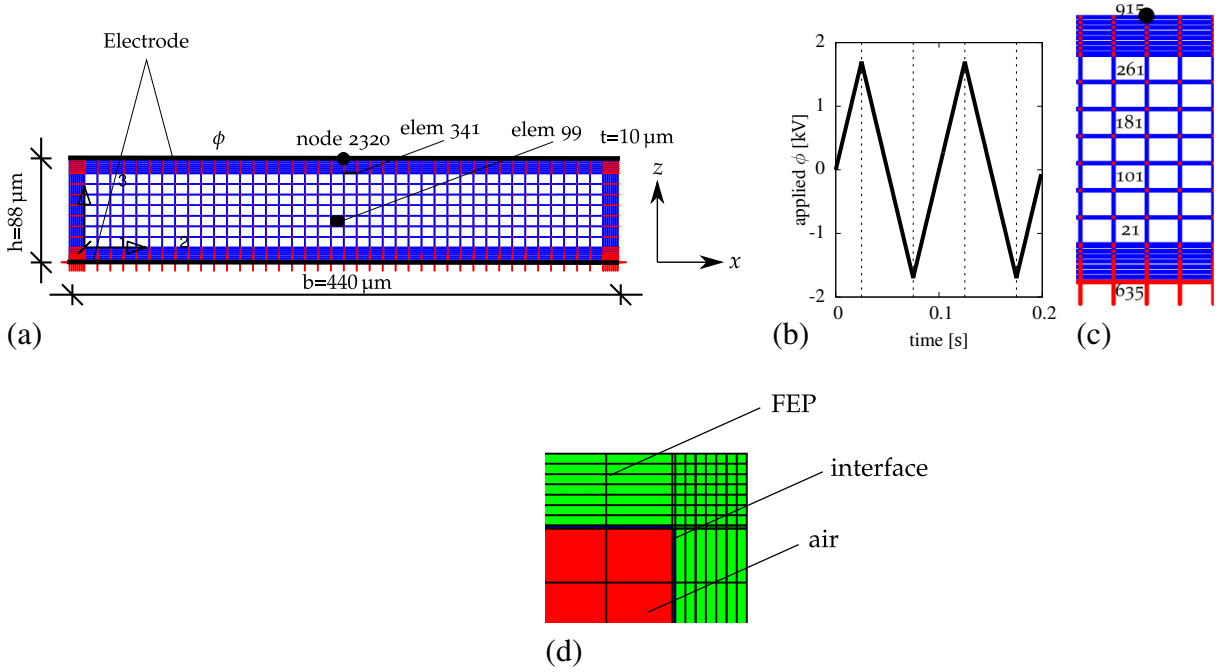

Figure 7.3.1.: (a) Rectangular structure, (b) Voltage function, (c) Reference elements, (d) Material definition of elements.

7.3.1 Voltage driven transient, large deformation

On the upper surface of a rectangular ferroelectret structure shown in Fig. 7.3.1a, a triangular voltage function according to Fig. 7.3.1c with ϕ_{max}=1.7 kV is applied. The bottom of the structure and the y-direction of one side of the xz-plane are fixed. Fig. 7.3.1b shows the reference elements that are considered for evaluation. The material definition is shown in Fig. 7.3.1d, FEP elements are green, air elements are red and interface elements are blue. The large deformation viscous model B is used for the analysis of the electro-viscoelastic behaviour of FEP which is modelled using one Maxwell element with a β of 0.5. The relaxation time T is varied with 1×10^{-5} s, 0.1 s and 1×10^{5} s. The lossless large deformation model is applied for air. In the following, interface charge-voltage hystereses and time functions of interface charge, dielectric displacement and electric field are shown whereby the interface charge refers to element 341 and the dielectric displacement to node 2320. The electric field is displayed in FEP for element 915 and in air for element 99.

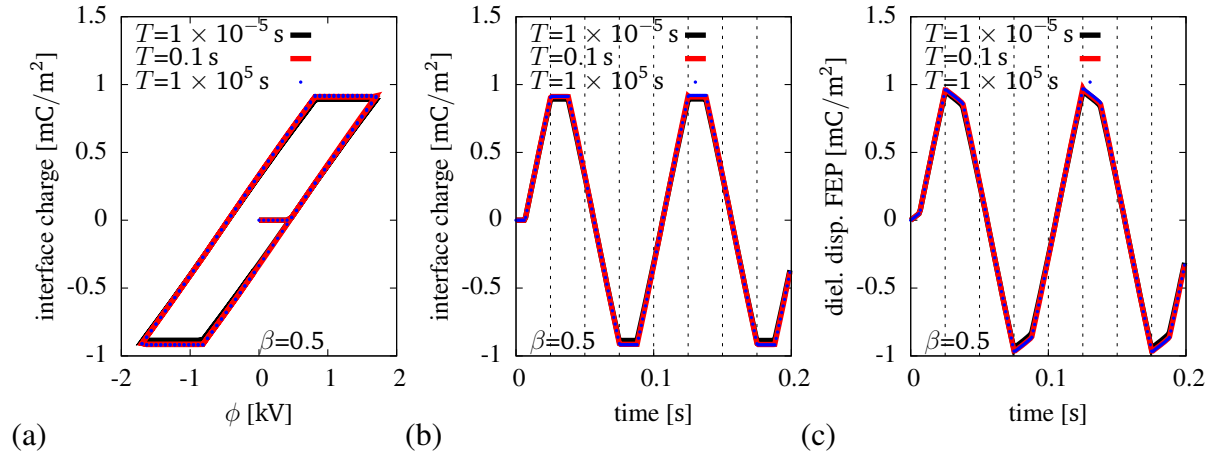

Figure 7.3.2.: (a) Hysteresis for different relaxation times T, (b) Interface charge p, (c) Dielectric displacement FEP.

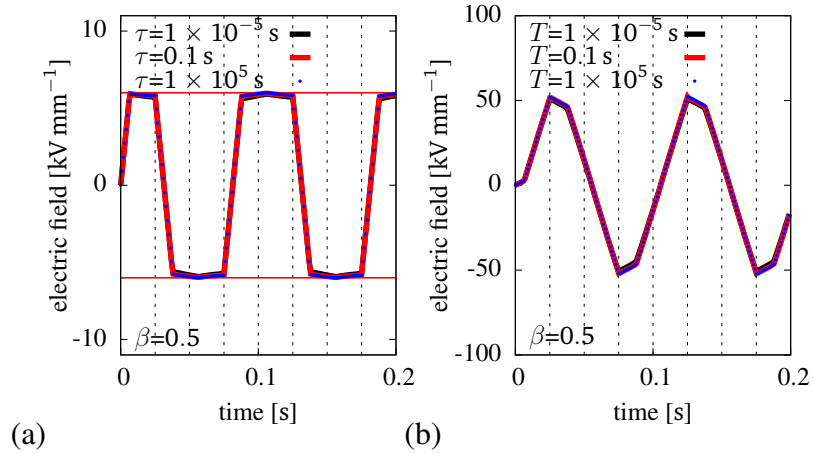

Figure 7.3.3.: (a) E_{AIR}, (b) E_{FEP} at different relaxation times T

From Fig. 7.3.2 to Fig. 7.3.3 can be seen that a variation of the relaxation time of one Maxwell element has almost no influence on the electric- and dielectric displacement field. A qualitative comparison to results for the non-linear lossless model, which is discussed later in section 7.3.2, shows for the viscoelastic model during charge accumulation and removal a decrease of E_{AIR} for positive p, and an increase for negative p.

The following Fig. 7.3.4 shows the displacement u_{zz} of node 2320 and the total 2.Piola-Kirchhoff stress S_{zz}^{tot} in element 914. Damping effects are observable for a T of 0.1 s and 1×10^5 s. The maximum values for compression and 2.Piola-Kirchhoff stress, which appear in case the voltage is maximal, are reduced due to viscoelastic effects. This is seen by comparing the curves for 1×10^{-5} s and 0.1 s. An increase of relaxation time above 0.1 s does hardly change the values, but leads to a time-shift of the curve. To some degree a shift of displacement and stress amplitude between the first and following cycles can be recognized.

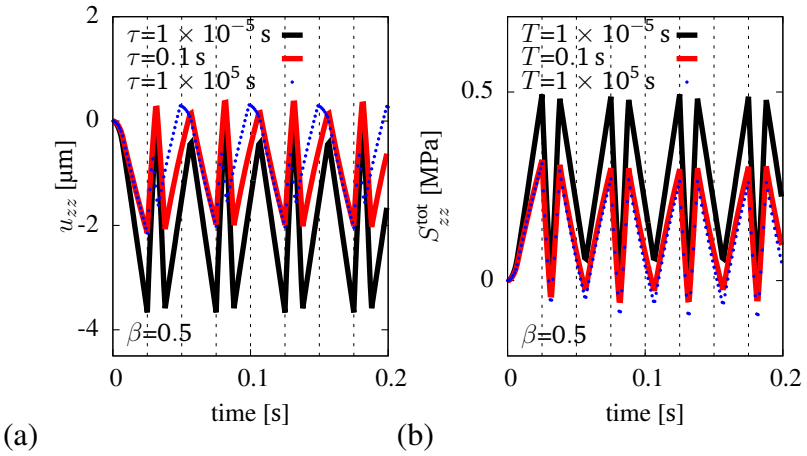

Figure 7.3.4.: (a) Displacement u_{zz}, (b) Total stress $S_{zz}^{\mathrm{tot}} = S_{zz} + S_{zz}^{\mathrm{E}}$

Fig. 7.3.5 shows Green-Lagrange and Hencky strain A_{zz} and $\hat{H}_{zz}$ for certain elements in Fig. 7.3.1. The strain in the elements 915 and 635, which are in the FEP-frame, is smaller than 2 %; the maximum compression is in the air elements 101 and 181. A difference between Green-Lagrange and Hencky strain is hardly visible.

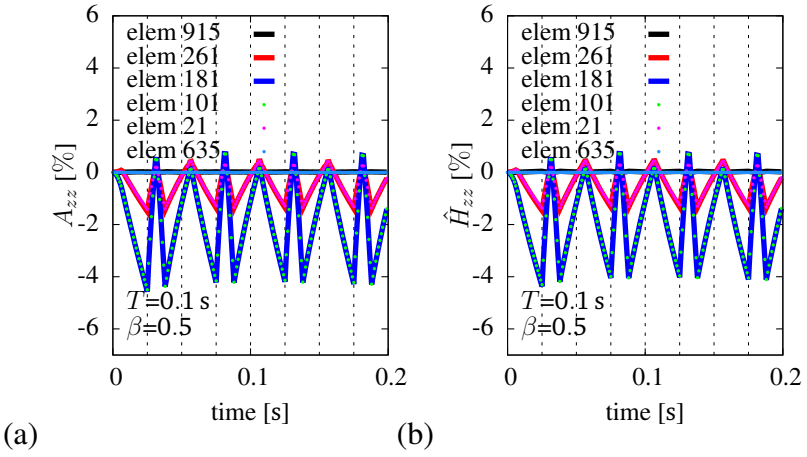

Figure 7.3.5.: (a) Green-Lagrange strain A_{zz}, (b) Hencky strain $\hat{H}_{zz}$.

Fig. 7.3.6 shows field distributions of the electric and dielectric displacement field for time points: 0.025 s when voltage is maximal, 0.031 s at the begin of reduction of interface charge and 0.05 s at the zero crossing of voltage. A homogeneous field distribution is observed in FEP and air for all time points. Displacement and total 2.Piola-Kirchhoff stress in z-direction is shown in Fig. 7.3.6. The maximal displacement u_{zz} occurs when voltage reaches its maximum in the middle of the upper cell surface, see Fig. 7.3.7a. The cell is stretched due to viscous effects at the zero crossing of voltage, see Fig. 7.3.6b. Compression stress shows on lateral edges of the plane-side where boundary conditions generate a restriction, and in the corners between interface and bulk.

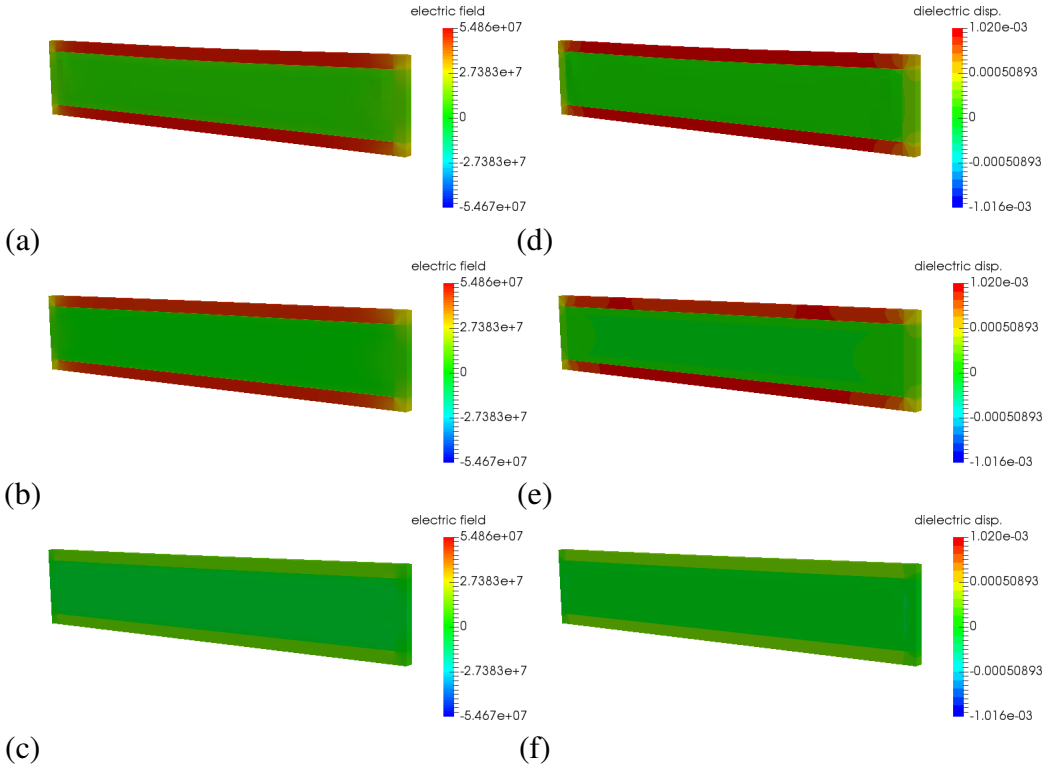

Figure 7.3.6.: (a)-(c) Electric field [V/m], (d)-(f) u_{zz} [m] for times 0.025 s, 0.031 s and 0.050 s, T=0.1 s, β=0.5.

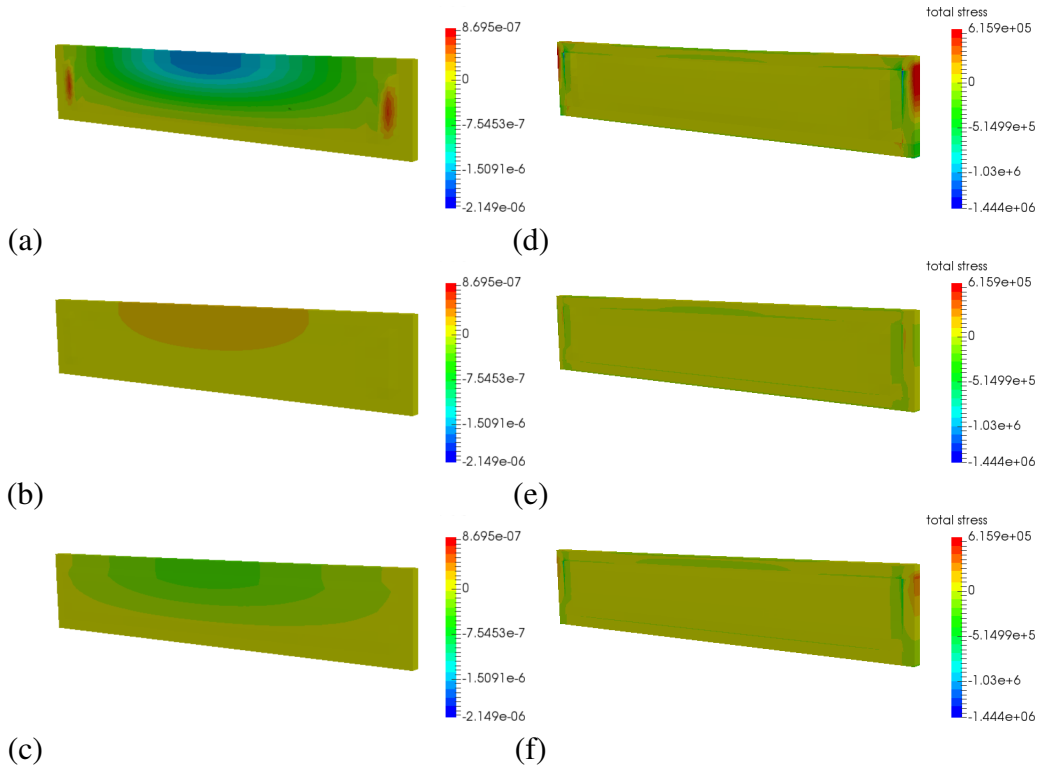

Figure 7.3.7.: (a)-(c) u_{zz} [m], (d)-(f) S_{zz} [N/m^2] for times 0.025 s, 0.031 s and 0.050 s, T=0.1 s, β=0.5.

In Fig.7.3.8 the Hencky strain is shown for maximal and minimal voltage at 0.025 s and 0.075 s, and at the end of cycle at 0.2 s. The distributions at 0.025 s and 0.075 s are almost identical; the strain in the FEP is homogeneous. Fig. 7.3.8c shows that the viscous stretch is not completely relaxed at the end of cycle.

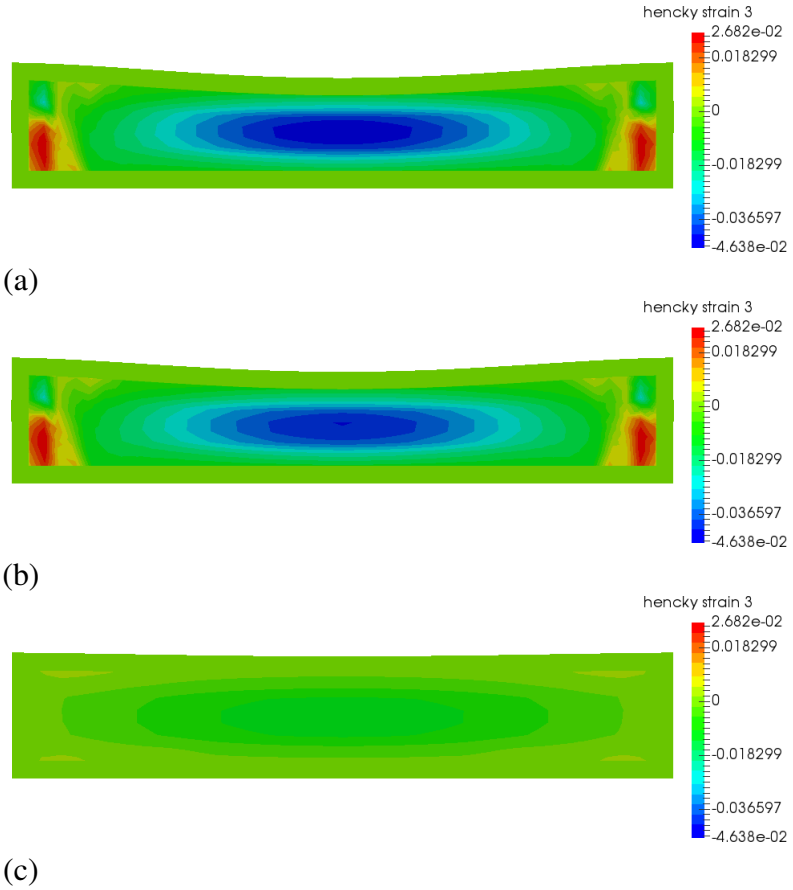

Figure 7.3.8.: Hencky strain $\hat{H}_{zz}$: (a) 0.025 s, (b) 0.075 s, (c) 0.2 s

7.3.2 Comparison linear/non-linear lossless model

Fig. 7.3.9 gives a comparison between the linear and geometric non-linear lossless model. A maximal peak voltage is assumed with $\phi_{\max}$=1.7 kV. Curves of electric quantities, monitored for node 2320, show no deviation between the models. The displacement u_{zz} shows a larger compression amplitude and thus a softer behaviour for the non-linear model. Cauchy stress σ_{zz} is almost identical for both models. The field distribution of u_{zz} for the non-linear model in Fig. 7.3.10 shows wrinkles in the region of air elements, although deformation of the structure is small.

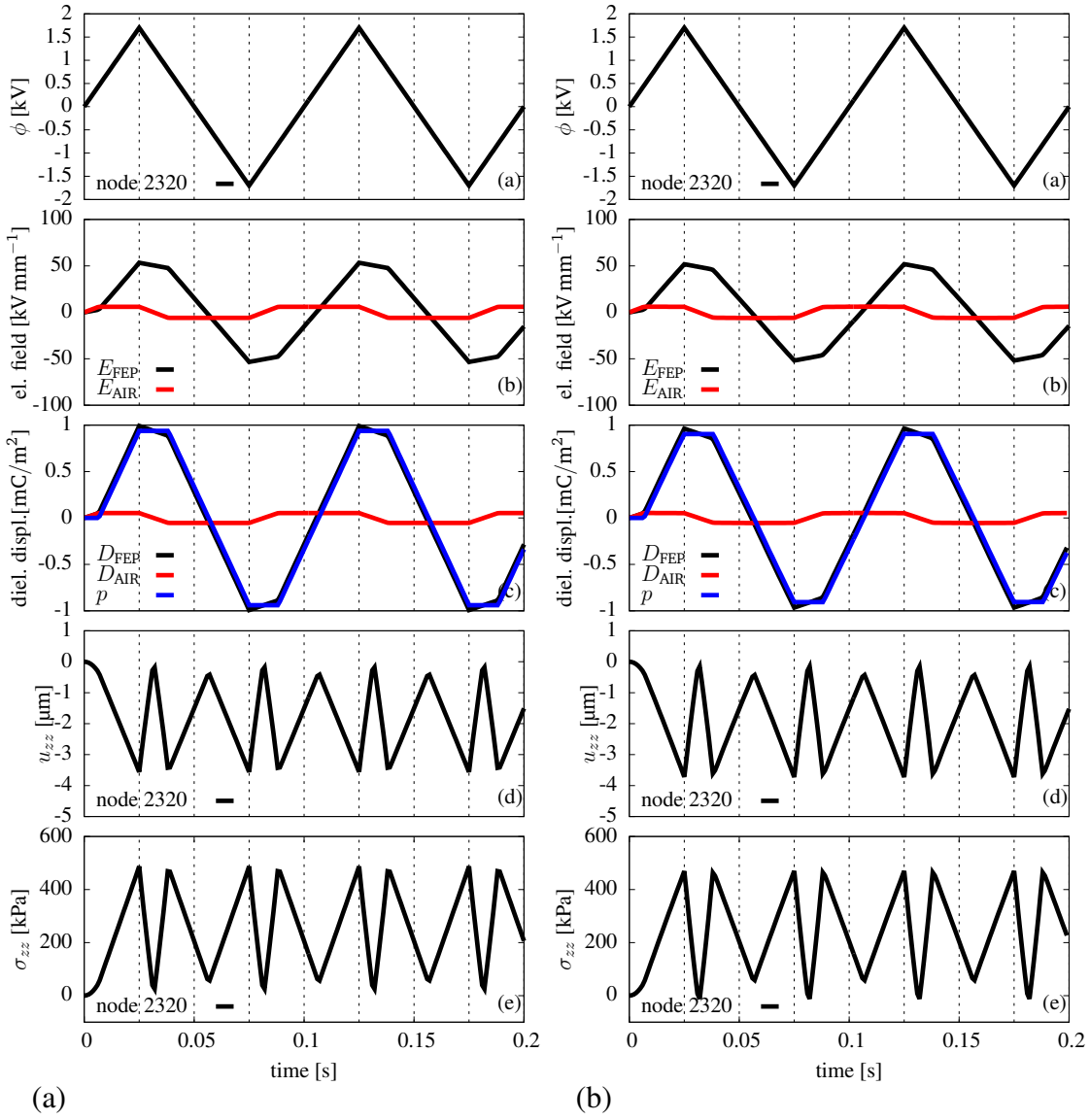

Figure 7.3.9.: Elastic material behaviour for an applied voltage of $1.7\,\mathrm{kV}$: (a) Linear lossless model, (b) Geometric non-linear lossless model.

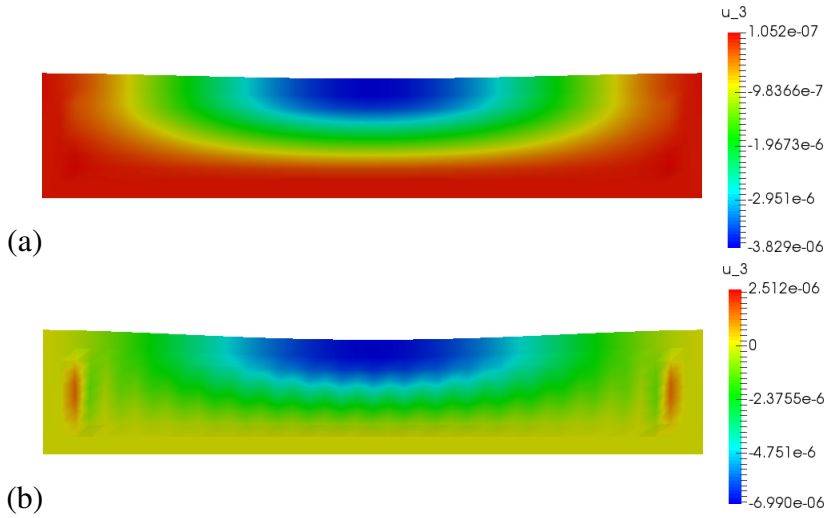

Figure 7.3.10.: Deformation u_{zz}: (a) Linear lossless model, $\phi_{\max}$=$1.8\,\mathrm{kV}$, (b) Geometric non-linear lossless model, $\phi_{\max}$=$2.8\,\mathrm{kV}$. Wave shaped deformation can be recognized.

7.3.3 Cell stability

To analyse convergence problems for lossless models additional simulation is performed. The FEP-frame is modelled using linear volume elements and merely the mechanical behaviour is investigated. The results for a force driven analysis assuming distributed load and of a displacement driven contact analysis are shown in Fig. 7.3.11. In the force driven analysis where force is linearly increased stepwise, the upper frame buckles or deforms like a bending beam like shown in Fig. 7.3.11a-d. The numerical solution is stable and deformation is reversible if the force is stepwise decreased, whereas the contact analysis shows various buckling modes in dependence on penalty stiffness and contact tolerances, see Fig. 7.3.11e-h. Fig. 7.3.11h shows an irreversible breakthrough.

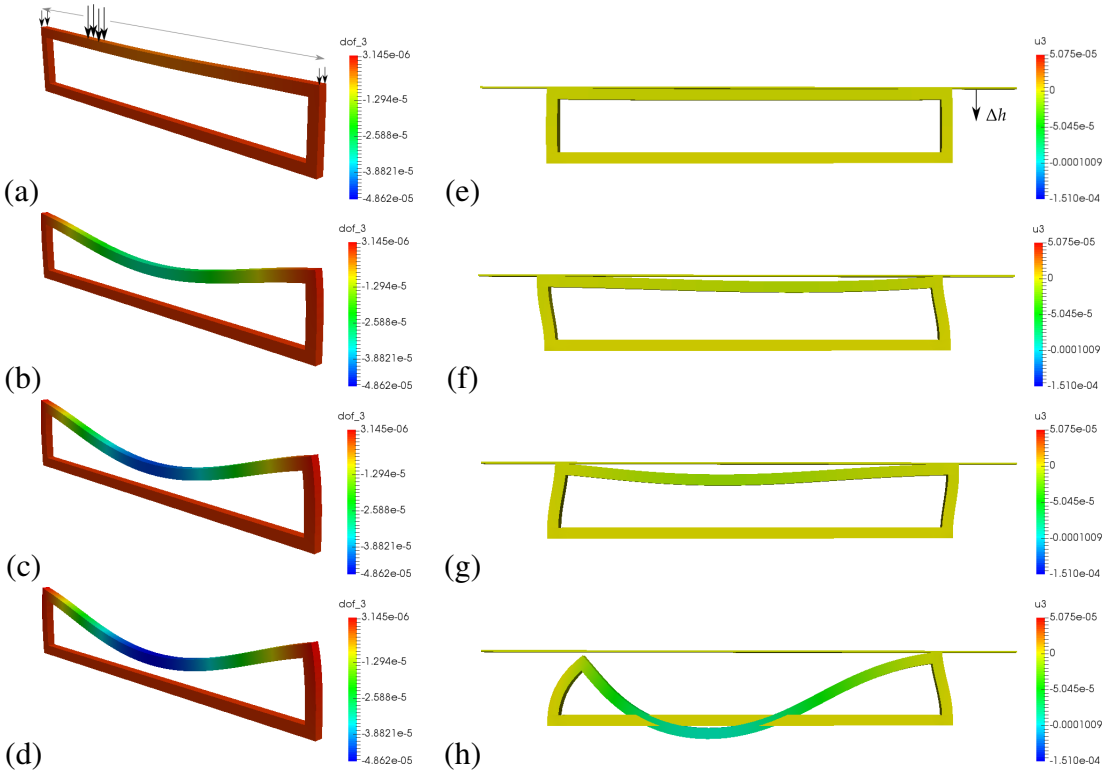

Figure 7.3.11.: Deformation of FEP frame. (a) Force driven analysis, (b) Contact analysis.

The numerical stability for electromechanical coupling is investigated using the triangular voltage function illustrated in the previous subsection. The resulting deformation field is displayed in Fig. 7.3.12 for two solution steps before calculation is terminated. For the linear model, a breakthrough of the structure is observed in Fig. 7.3.12b. For the non-linear model, as already mentioned, winkling is observed.

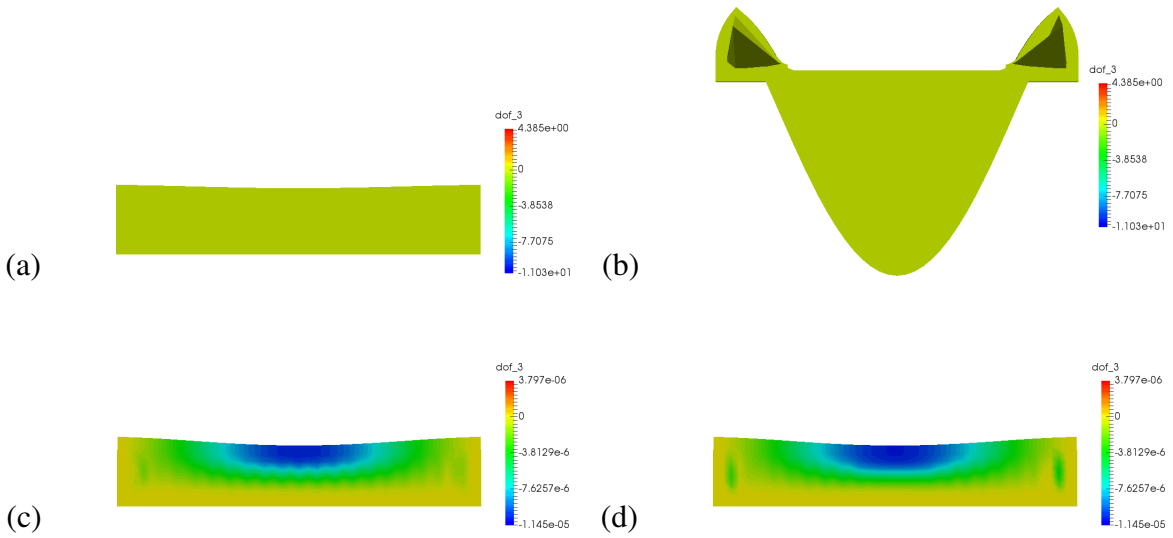

Figure 7.3.12.: Deformation resulting from voltage driven simulation for two solution steps before calculation is terminated: (a) and (b) Linear model, (c) and (d) Geometric non-linear model.

More information is given by looking at residuals in Fig. 7.3.13 and Fig. 7.3.14. A sudden increase of initial and final residual arise after the switch-over point of voltage for the linear model. For the non-linear model the initial residual increases linearly up to a point were also the final residual is diverging; the begin of divergence of initial residual is simultaneous to the appearance of wrinkles.

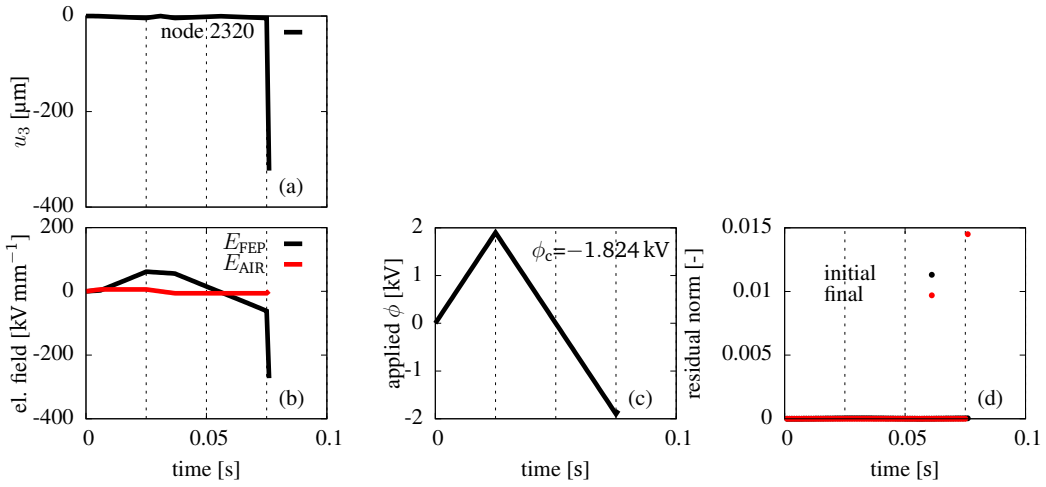

Figure 7.3.13.: (a)-(d) Linear model, termination at ϕ=−1.824 kV, (a) Jump of displacement in node 2320, (b) Jump of electric field in node 2320, (c) Voltage function, (d) Residuals.

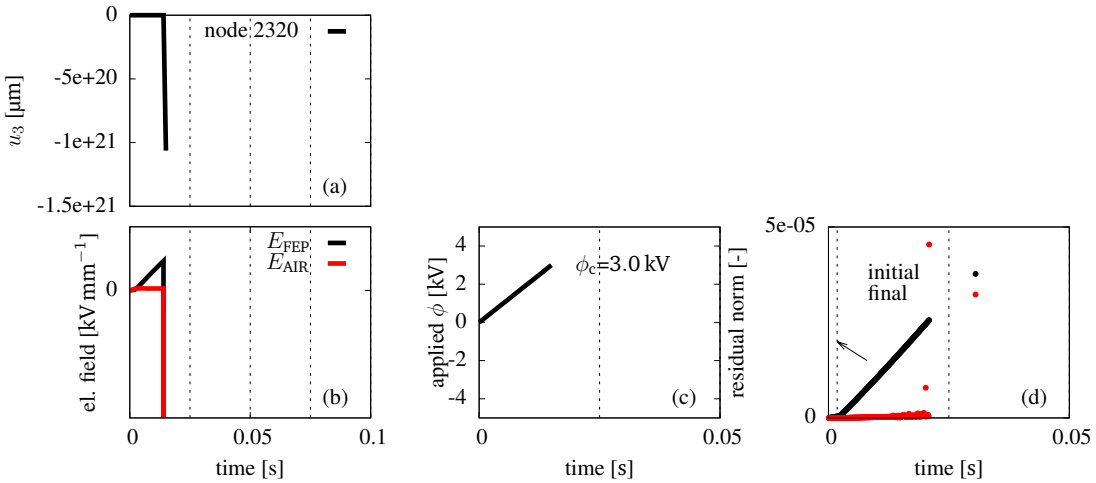

Figure 7.3.14.: (a)-(d) Non-linear model, termination at ϕ=3 kV. (a) Jump of displacement in node 2320, (b) Jump of electric field in node 2320, (c) Voltage function, (d) Residuals. The arrow in (d) marks the time point when initial residual is diverging. This point can be associated with appearance of wrinkles.

7.4 Virtual cell

A virtual cell geometry is taken over from elasto-plastic simulation of FEP-tube compression at 204 °C shown in section 6.2. Node and element data was exported from VPS files and converted into an input file for FEAP.

7.4.1 Polarisation and operation phase transient, large deformation

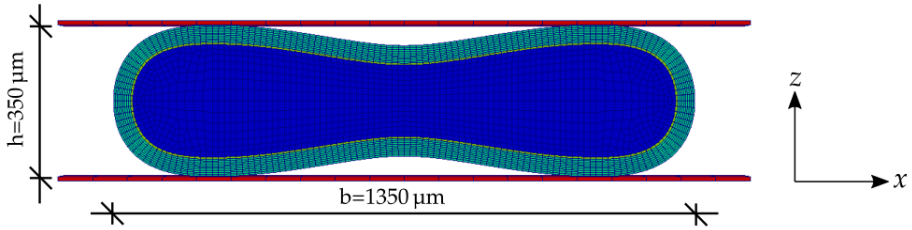

Figure 7.4.1.: Virtual Cell.

A contact analysis using model C for FEP and the lossless large deformation model for air is conducted for poling an subsequent compression like shown in Fig. 6.4.2a, assuming $\phi_{\max}$=5 kV and an applied compression of $h/4$. One lateral edge is fixed, the nodes one the other are linked in x-direction. In y-direction a symmetry boundary condition is prescribed for one xz-plane. Viscous parameters are assumed with β_1-β_{10}=0.8 and T_1-T_{10}=0.1 s.

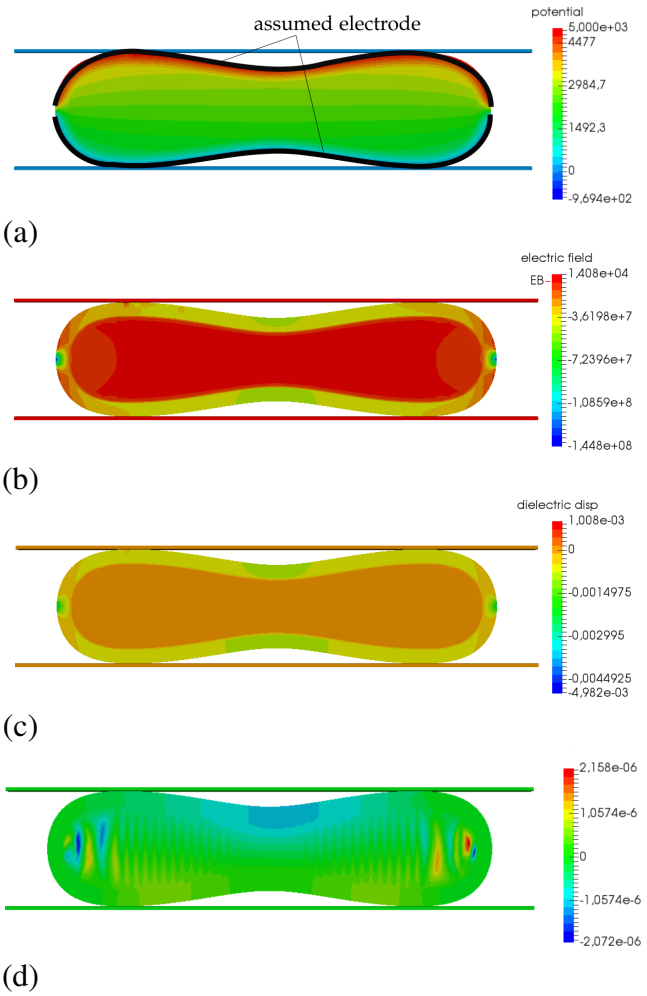

Figure 7.4.2.: t=0.5 s: (a) Electric potential, (b) Electric field, (c) Dielectric displacement, (d) Displacement u_{zz} .

Fig. 7.4.2 shows the field output for maximum voltage. The electric potential field is illustrated in Fig. 7.4.2a. Fig. 7.4.2b shows the electric field after electric breakdown where the distribution is almost homogeneous in the air. The electric and dielectric displacement field in FEP is inhomogeneous, see Fig. 7.4.2b and Fig. 7.4.2c. Apart from singularities that arise at lateral edges and which are irrelevant for the piezoelectric behaviour, the maximum values are located in the region of maximal buckling. For u_{zz} a wrinkle pattern can be observed in Fig. 7.4.2d. Fig. 7.4.3 shows u_{zz} in the operation phase. The simulation is terminated when an instability occurs in the air elements.

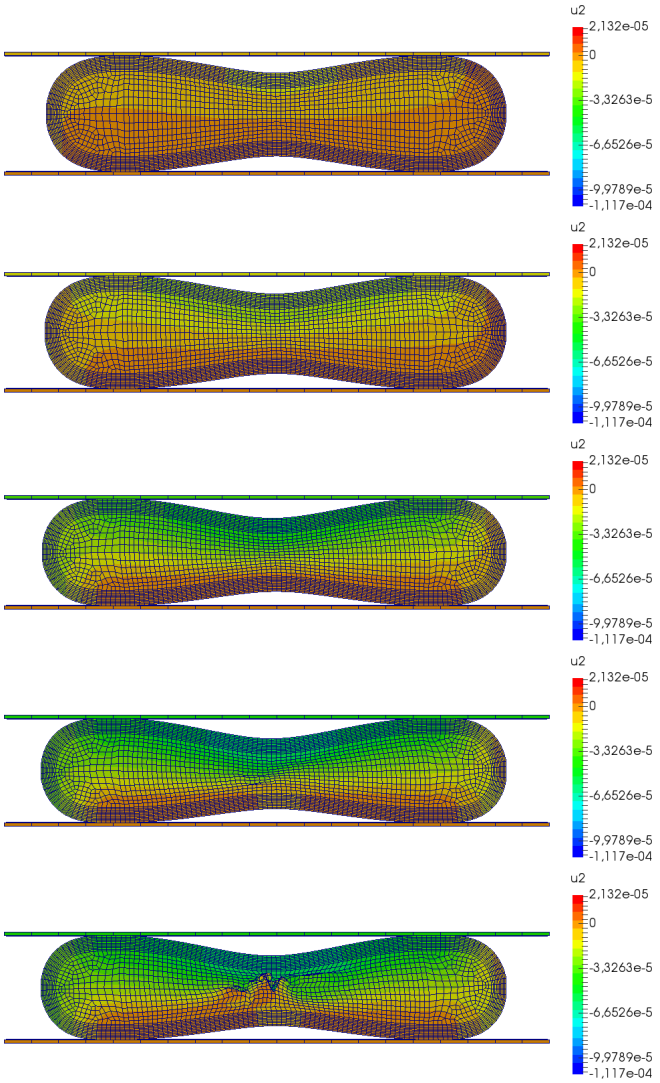

Figure 7.4.3.: Displacement u_{zz}

8 Conclusion and outlook

In the last chapter 7 simulation examples have shown that transient and lossless linear models work well for ideal cell. For the rectangular cell, numerical instabilities arise after the switch-over point of voltage. Viscous and lossless geometric non-linear FE-models in the present form, in which air is modelled similar to a solid body, work well up to a certain degree of deformation for the thin structures analysed here. For voltage governed simulations, a termination of the calculation is initiated by the formation of wrinkles in the air elements, which are collapsing also under mechanical compression of the virtual cell.

A simple concept for an estimation of the effective Young's modulus and the piezoelectric d_{33} coefficient of ferroelectret cells based on mean values was introduced in chapter 6. It was shown that a lateral freely moveable cell is a sufficient replacement for a cell array structure of about 20 cells, manufactured from FEP-tubes. It is questionable, however, in how far a parameter estimation based on mean values is suitable to map inhomogeneous field distributions which arise in arbitrary cell geometries and by variation of mechanical boundary conditions. To verify the assumption that mechanical boundary conditions can improve charge accumulation during the polarisation of ferroelectrets, experiments to determine the penetration depth of charge should to be performed.

In chapter 4 two formulations of visco-electromechanical behaviour for a St. Vernant material are introduced. In model B the stress tensor is split, in model C the free energy and deformation gradient is separated in instantaneous and viscous, time-dependent parts. By benchmark tests for relaxation and creep in reference to analytical descriptions was shown that below $5\,\%$, analytical- and numerical solution of the models are very close together. Dielectric dissipation is included in the energy formulation for model C. In case the poling behaviour or an accelerated voltage is regarded, dielectric dissipation should be considered also in the implementation.

Viscous, dynamic deformation behaviour and Pull-in instability was investigated for a rectangular dielectric elastomer membrane under voltage control in chapter 3. The numerical solution of the equation of motion and phase diagrams show a delayed Pull-in for electric fields below the critical electric field. A consideration of inertia effects lowers the critical electric field and makes the dynamic system more sensitive for Pull-in.

Insights in continuum mechanical modelling of dielectrics were given in this thesis. Nevertheless, improvements can be made in the electromechanical classification of FEP. This concerns primarily the determination of frequency-dependent viscous and dielectric loss factors, which are crucially needed to estimate a time-dependent d_{33}. A more exact model to describe the thermoplastic behaviour of the fluoropolymer FEP appears useful also. The filling medium of the cells should be simulated as fluid to represent the physical conditions more accurately. By switching to a particle level, the collision of particles can be taken into account which allows a description of the electric breakdown by statistical parameters.

Bibliography

[1] E. P. Otocu. Physical properties of ionic polymers. *J. Macromol. Sci.-Revs. Macromol. Chem.*, pages 275–294, 1971.

[2] D. Mecerreyes, editor. *Applications of Ionic Liquids in Polymer Scienceand Technology*. Springer, 2015. doi: 10.1007/978-3-662-44903-5.

[3] M. El Lallart, P.-J. Cottinet, D. Guyomar, and L. Lebrun. Electrostrictive polymers for mechanical energy harvesting. *J. Polym. Sci.*, 50:523–535, 2011. doi: 10.1002/polb.2304.

[4] L.D. Landau and E.M. Lifshitz. *Electrodynamics of Continuous Media, Course of theoretical Physics*, volume 8. Pergamon Press, 1960.

[5] A. K. Jonscher. Dielectric relaxation in solids. *J. Phys. D: Appl. Phys.*, 32, 1999.

[6] H. S. Nalwa, editor. *Ferroelectric Polymers*. Dekker, 1995.

[7] K.P. Menard. *Dynamic Mechanical Analysis, A Practical Introduction*. CRC Press, 1999.

[8] L. Malcolm, R. Williams, and J. D. Ferry. The temperature dependence of relaxation mechanisms in amorphous polymers and other glass-forming liquids. *J. Am. Chem. Soc*, 77:3701–3707, 1955. doi: 10.1021/ja01619a008.

[9] R. H. Boyd. Relaxation processes in crystalline polymers: experimental behaviour- a review. *Polym. Rev.*, 26:323–347, 1984. doi: 10.1016/0032-3861(85)90192-2.

[10] R. H. Boyd. Relaxation processes in crystalline polymers: molecular interpretation — a review. *Polym. Rev.*, 26:1123–1133, 1985. doi: 10.1016/0032-3861(85)90240-X.

[11] G. Kofod. The static actuation of dielectric elastomer actuators: how does pre-stretch improve actuation? *J. Phys. D: Appl. Phys.*, 41:215405, 2008. doi: 10.1088/0022-3727/41/21/215405.

[12] B. Chen, M. Kollosche, M. Stewart, J Busfield, and F. Carpi. Electrical breakdown of an acrylic dielectric elastomer: effects of hemispherical probing electrode's size and force. *International Journal of Smart and Nano Materials*, 6(4), 2015. doi: 10.1080/19475411.2015.1130974.

[13] J. Zhang, L. Tang, Y. Li, B. amd Wang, and H. Chen. Modeling of the dynamic characteristic of viscoelastic dielectric elastomer actuators subject to different conditions of mechanical load. *J. Appl. Phys.*, 117, 2015. doi: 10.1063/1.4913384.

[14] W. Kaiser. *Kunststoffchemie für Ingenieure*. Carl Hanser Verlag GmbH & Co. KG, 2015.

[15] G. Calleja, A. Jourdan, B. Ameduri, and J.-P. Habas. Where is the glass transition temperature of poly(tetrafluoroethylene)? a new approach by dynamic rheometry and mechanical tests. *Eur. Polym. J.*, 49(8):2214–2222, 2013. doi: 10.1016/j.eurpolymj.2013.04.028>.

[16] H. Teng. Overview of the development of the fluoropolymer industry. *Appl. Sci.*, 2:496–512, 2012. doi: 10.3390/app2020496 10.3390/app2020496.

[17] G.H Bowers and E. R. Lovejoy. Cross linking of teflon 100 fep-fluorocarbon resin by radiations. Division of Industrial and Engineering Chemistry, 140th Meeting, ACS, Chicago, III, September 1962.

[18] M. Destrade and D. Saccomandi. Finite amplitude elastic waves propagating in compressible solids. *Phys. Rev. E.* doi: 10.1103/PhysRevE.72.016620.

[19] D. J. McCoul. *Dielectric Elastomers for Fluidic and Biomedical Applications*. PhD thesis, University of California, Los Angeles, 2015.

[20] P. Galich and S. Rudykh. Manipulating pressure and shear waves in dielectric elastomers via external electric stimuli. *Int J. Solid Struct.*, 91, 2016. doi: 10.1016/j.ijsolstr.2016.04.032.

[21] S. Michel, X.Q. Zhang, M. Wissler, C. Löwe, and G. Kovacs. A comparison between silicone and acrylic elastomers as dielectric materials in electroactive polymer actuators. *Polym. Int.*, 59, 2009. doi: 10.1002/pi.2751.

[22] F. Capri, D.D. Rossi, R. Kornbluh, R. Pelrine, and P. Sommer-Larsen, editors. *Dielectric Elastomers as Electromechanical Transducers*. 2007.

[23] R. E. Pelrine, R. D. Kornbluh, and J. P. Joseph. Electrostriction of polymer dielectrics with compliant electrodes as a means of actuation. *Sens. Actuators, A*, 64:77–85, 1998. doi: 10.1016/S0924-4247(97)01657-9.

[24] R. Kornbluh, G. B. Andeen, and Eckerle J. Artificial muscle: the next generation of robotic actuators. volume MS91-331. SME, 1991. presented at the 4th World Conference of Robotics Research , Pittsburgh, PA.

[25] D. M. Opris, C. Molberg, M.and Walder, Y. S. Ko, B. Fischer, and F. A. Nuesch. New silicone composites for dielectric elastomer actuator applications in competition with acrylic foil. *Adv. Funct. Mater.*, 21:3531–3539, 2011. doi: 10.1002/adfm.201101039.

[26] R. K. Sahu and K. Patra. Rate-dependent mechanical behavior of vhb 4910 elastomer. *Mech. Adv. Mater. Struc.*, 23:170–179, 2015. doi: 10.1080/15376494.2014.949923.

[27] J. Guo, R. Xiao, H. S. Park, and T. D. Nguyen. The temperature-dependent viscoelastic behavior of dielectric elastomers. *J. Appl. Mech.*, 82, 2015. doi: 10.1115/1.4030850.

[28] G Kofod, R. Kornbluh, R. Pelrine, and P. Sommer-Larson. Actuation response of polyacrylate dielectric elastomers. *Proc. SPIE*, 4329, 2001. doi: 10.1117/12.432638.

[29] J-S. Plante and S. Dubowsky. Large-scale failure modes of dielectric elastomer actuators. *Int. J. Solids Struct.*, 43:7727, 2006. doi: 10.1016/j.ijsolstr.2006.03.026.

[30] S.M. Ha, Q. Yuan, W.and Pei, R. Pelrine, and S. Stanford. Interpenetrating polymer networks for high-performance electroelastomer artificial muscles. *Adv. Mater.*, 18:887–891, 2006. doi: 10.1002/adma.200502437.

[31] J. Sheng, H. Chen, J. Qiang, and Y Wang. Thermal, mechanical, and dielectric properties of a dielectric elastomer for actuator applications. *J. Macromol. Sci. B*, 51:2093–2104, 2012. doi: 10.1080/00222348.2012.659617.

[32] H. Mark, editor. *Encyclopedia of Polymer Science and Technology*. Wiley. doi: 10.1038/s41598-018-22918-1.

[33] M. Eguchi. *Proc. Phys. Math. Soc. Japan*, 1919-1923.

[34] K.C. Kao. *Dielectric phenomena in dielectric solids. With Emphasis on Physical Concepts of Electronic Processes*. Elsevier Academic Press, 2004.

[35] D. B. Go and A. Venkattraman. Microscale gas breakdown: ion-enhanced field emission and the modified paschen's curve. *J. Phys. D: Appl. Phy.*, 47:503001, 2014. doi: 10.1088/0022-3727/47/50/503001.

[36] S. Bönisch, W. Kalkner, and D. Pommerenke. Modeling of short-gap ESD under consideration of different discharge mechanisms. *IEEE Trans. Plasma Sci.*, 31(4), 2003. doi: 10.1109/TPS.2003.815823.

[37] A. Mellinger and 0. Mellinger. Breakdown threshold of dielectric barrier discharges in ferroelectrets: Where paschen's law fails. *IEEE Trans. Dielectr. Electr. Insul.*, 18(1):43–48, 2011. doi: 10.1109/TDEI.2011.5704491.

[38] H. von Seggern, S. Zhukov, and S. Fedosov. Importance of geometry and breakdown field on the piezoelectric d_{33} coefficient of corona charged ferroelectret sandwiches. *IEEE Trans. Dielectr. Electr. Insul.*, 18(1), 2011. doi: 10.1109/TDEI.2011.5704492.

[39] K. V. Kozlov, H. E. Wagner, R. Brandenburg, and P. Michel. Spatio-temporally resolved spectroscopic diagnostics of the barrier discharge in air at atmospheric pressure. *J. Phys. D: Appl. Phys.*, 34:3164–3176, 2001.

[40] M. Lindner, S. Bauer-Gogonea, S. Bauer, M. Paajanen, and J. Raukola. Dielectric barrier microdischarges: Mechanism for the charging of cellular piezoelectric polymers. *J. Appl. Phys.*, 91, 2002. doi: 10.1063/1.1459751.

[41] X. Qiu, A. Mellinger, M. Wegener, W. Wirges, and R. Gerhard. Barrier discharges in cellular polypropylene ferroelectrets: How do they influence the electromechanical properties? *J. Appl. Phys.*., 101, 2007. doi: 10.1063/1.2735410.

[42] X. Qiu, A. Mellinger, and R. Gerhard. Influence of gas pressure in the voids during charging on the piezoelectricity of ferroelectrets. *Appl. Phys. Lett.*, 92:052901, 2007. doi: 10.1063/1.2841037.

[43] . URL `https://www.gore.com/about/technologies`.

[44] . URL `https://www.kwo-ptfe.de/en/ptfe-technology/ptfe-properties`.

[45] A. Mellinger, M. Wegener, W. Wirges, R. R. Mallepally, and R. Gerhard-Multhaupt. Thermal and temporal stability of ferroelectret films made from cellular polypropylene/air composites. *Ferroelectrics*, 331:189–199, 2006. doi: 10.1080/00150190600737933.

[46] Z. Hu and H. von Seggern. Breakdown-induced polarization buildup in porous fluoropolymer sandwiches: a thermally stable piezoelectret. *J. Appl. Phys.*., 99:024102, 2006. doi: 10.1063/1.2161825.

[47] Y. Wan, L. Xie, X. Zhang, and Z. Zhong. Time dependence of piezoelectric d_{33} coefficient of cellular ferroelectret polypropylene film. *Appl. Phys. Lett.*, 98:122902, 2011. doi: 10.1063/1.3569950.

[48] M. Gaal, V. Bovtun, W. Stark, A. Erhard, Y. Yakymenko, and M. Kreutzbruck1. Viscoelastic properties of cellular polypropylene ferroelectrets. *J. Appl. Phys.*, 119:125101, 2016. doi: 10.1063/1.4944798.

[49] R. Kressmann. Linear and nonlinear piezoelectric response of charged cellular polypropylene. *J. Appl. Phys.*, 90, 2001. doi: 10.1063/1.1398597.

[50] M. Curtin, B. Wright, and Rahmi. O. Viscoelastic properties of fluorinated ethylene-propylene (fep) random copolymers. In *APS March Meeting Abstracts*, 2016. URL `http://adsabs.harvard.edu/abs/2016APS..MAR.M1137C`.

[51] Ron Pelrine, Roy Kornbluh, Jose Joseph, and Seiki Chiba. Electrostriction of polymer films for microactuators. In *Tenth Annual International Workshop on Micro Electro Mechanical Systems*, 1997. doi: 10.1109/MEMSYS.1997.581811.

[52] R. Pelrine, R. Kornbluh, J. Joseph, R. Heydt, Q. Pei, and S. Chiba. High-field deformation of elastomeric dielectrics for actuators. *Mater. Sci. Eng., C*, 11:89, 2000.

[53] G. Kovacs, P. Lochmatter, and M. Wissler. An arm wrestling robot driven by dielectric elastomer actuators. *Smart Materials and Structures*, 16(2):S306, 2007. doi: 10.1088/0964-1726/16/2/S16. URL `http://stacks.iop.org/0964-1726/16/i=2/a=S16`.

[54] H. Wang, L. Li, Y. Zhu, and W. Yang. Analysis and application of a rolled dielectric elastomer actuator with two degrees of freedom. *Smart Materials and Structures*, 25(12):125008, 2016. doi: 10.1088/0964-1726/25/12/125008. URL http://stacks.iop.org/0964-1726/25/i=12/a=125008.

[55] F. Carpi, C. Salaris, and D. De Rossi. Folded dielectric elastomer actuators. *Smart Materials and Structures*, 16(2):S300, 2007. doi: 10.1088/0964-1726/16/2/S15. URL http://stacks.iop.org/0964-1726/16/i=2/a=S15.

[56] R. Kornbluh, R. Pelrine, Q. Pei, R. Heydt, S. Stanford, S. Oh, and J. Eckerl. Electroelastomers: Applications of dielectric elastomer transducers for actuation, generation and smart structures. *Proc. SPIE*, 4698:254–270, 2002. doi: 10.1117/12.475072.

[57] A. O'Halloran, F. O'Malley, and McHugh P. A review on dielectric elastomer actuators, technology, applications, and challenges. *J. Appl. Phys.*, 104:071101, 2008. doi: 10.1063/1.2981642.

[58] I. Polyakov and J. R. Heim, 2011.

[59] E. Rustighi, W. Kaal, S. Herold, and A. Kubbara. Experimental characterisation of a flat dielectric elastomer loudspeaker. *Actuators*, 7(28), 2018. doi: 10.3390/act7020028.

[60] Rocco Vertechy, Antonio Frisoli, Massimo Bergamasco, Federico Carpi, Gabriele Frediani, and Danilo De Rossi. Modeling and experimental validation of buckling dielectric elastomer actuators. *Smart Materials and Structures*, 21(9):094005, 2012. URL http://stacks.iop.org/0964-1726/21/i=9/a=094005.

[61] R. Pelrine, P. Sommer-Larsen, R.D. Kornbluh, R. Heydt, G. Kofod, and P. Pei, Q.and Gravesen. Applications of dielectric elastomer actuators. *Proc. SPIE*, 4329, 2001. doi: 10.1117/12.432665.

[62] *Applications of pressure-sensitive dielectric elastomer sensors*, volume 9798, 2016. doi: 10.1117/12.2220808. URL https://doi.org/10.1117/12.2220808.

[63] D. Xu, A. Tairych, and I. A. Anderson. Stretch not flex: programmable rubber keyboard. *Smart Materials and Structures*, 25(1):015012, 2016. doi: 10.1088/0964-1726/25/1/015012. URL http://stacks.iop.org/0964-1726/25/i=1/a=015012.

[64] B. W. An, J. H. Shin, S.-Y. Kim, J. Kim, S. Ji, J. Park, Y. Lee, J. Jang, Y.-G. Park, E. Cho, S. Jo, and J.-U. Park. Smart sensor systems for wearable electronic devices. *Polymers*, 9(303), 2017. doi: 10.3390/polym9080303.

[65] URL https://www.stretchsense.com/.

[66] URL https://leaptechnology.com.

[67] D. Meschede. *Gerthsen Physik*. Springer, 2010. doi: 10.1007/978-3-642-12894-3.

[68] R. Arora and W. Mosch. *High voltage insulation engineering*. New Age International, 2004.

[69] A. Wipf. Lecture notes in electrodynamics, WS 2006/2007.

[70] T. Fließbach. *Elektrodynamik*. Spektrum Akademische Verlag Heidelberg, 2008.

[71] S.M.A. Jiménez and R. M. McMeeking. Deformation dependent dielectric permittivity and its effect on actuator performance and stability. *Int. J. Non-Lin. Mech.*, 2013.

[72] G. Kofod, P. Sommer-Larson, R. Kornbluh, and R. Pelrine. Actuation response of polyacrylate dielectric elastomers. *J. Intell. Mater. Syst. Struct.*, 14, 2003. doi: 10.1177/104538903039260.

[73] Mazza E. and M. Wissler. Electromechanical coupling in dielectric elastomer actuators. *Sens. Actuators, A*, 138(2), 2007. doi: 10.1016/j.sna.2007.05.029.

[74] H. Altenbach. *Kontinuumsmechanik*. Springer, 2012.

[75] H. D. Baehr. *Thermodynamik*. 1989.

[76] G.A. Holzapfel. *Nonlinear Solid Mechanics: A Continuum Approach for Engineering*. 2000.

[77] E. B. Tadmor, R.E. Miller, and R. S. Elliott. *Continuum Mechanics and Thermodynamics*. Cambridge University Press, 2012.

[78] B.D. Coleman and W. Noll. The thermodynamics of elastic materials with heat conduction and viscosity. *Arch. Rational Mech. Anal.*, 13, 1963.

[79] S. Reese and S. Govindjee. A theory of finite viscoelasticity and numerical aspects. *Int J. Solid Struct.*, 35:3455–3482, 1998. doi: 10.1016/S0020-7683(97)00217-5.

[80] S. Reese and S. Govindjee. Theoretical and numerical aspects in the thermo-viscoelastic material behavior of rubber-like polymers. *Mech. Time Depend. Mater.*, 1:357–396, 1998.

[81] A. Ask, A. Menzel, and M. Ristinmaa. Phenomenological modeling of viscous electrostrictive polymers. *Int. J. Non-Lin. Mech.*, 47, 2011. doi: 10.1016/j.ijnonlinmec.2011.03.020.

[82] J. Bonet. Large strain viscoelastic constitutive models. *Int. J. Solids Struct.*, 38:2953, 2000. doi: 10.1016/S0020-7683(00)00215-8.

[83] F. R. Schwarzl. *Polymermechanik*. Springer, 1990.

[84] T.G. Mezger. *Das Rheologie Handbuch, 3. Auflage*. Vincentz Network, 2010.

[85] R. L. Bagley and P. J. Torvik. Fractional calculus-a different approach to the analysis of viscvis-coelastic damped structures. *AiAA J.*, 21(5):741–748, 1983. doi: 10.2514/3.8142.

[86] R. L. Bagley. Power law and fractional calculus model of viscoelasticity. *AIAA J.*, 27(10):1412–1417, 1987. doi: 10.2514/3.10279.

[87] L. H. Sperling. *Introduction to the physical polymer science*. John Wiley & Sons, 2006.

[88] X. Chen. Nonlinear electro-thermo-viscoelasticity. *Acta Mech.*, 211:49–59, 2009. doi: 10.1007/s00707-009-0217-9.

[89] M. Mehnert, M. Hossain, and P. Steinmann. On nonlinear thermo-electro-elasticity. *Proc. Math. Phys. Eng. Sci.*, 2016. doi: 10.1098/rspa.2016.0170.

[90] T.J.R. Hughes. *The Finite Element Method: Linear Static and Dynamic Finite Element Analysis*. Dover Publications, INC., New York, 2000.

[91] R.D. Cook, D.S. Malkus, M. E. Plesha, and R.J. Witt. *Concepts and Applications of Finite Element Analysis, 4. Edition*. John Wiley & Sons, 2002.

[92] P. Wriggers. *Nonlinear Finite Element Method*. Springer, 2008.

[93] G.A. Maugin. *Nonlinear Electromechanical Couplings*. John Wiley & Sons, 1992.

[94] A. L. Dorfmann and R. W. Ogden. Nonlinear electroelasticity. *Acta Mech.*, 174:167, 2005. doi: 10.1007/s00707-004-0202-2.

[95] R. M. McMeeking and C. M. Landis. Electrostatic Forces and Stored Energy for Deformable Dielectric Materials. *J. Appl. Mech.*, 72:581, 2005. doi: 10.1115/1.1940661.

[96] A. L. Dorfmann and R. W. Ogden. Nonlinear Electroelastic Deformations. *J. Elasticity*, 82:99, 2006. doi: 10.1007/s10659-005-9028-y.

[97] M. Wissler and E. Mazza. Modeling and simulation of dielectric elastomer actuators. *Smart Mater. Struct.*, 14:1396, 2005. doi: 10.1088/0964-1726/14/6/032.

[98] W. Hong. Modeling viscoelastic dielectrics. *J. Mech. Phys. Solids*, 59:637–650, 2011. doi: 10.1016/j.jmps.2010.12.003.

[99] F. Vogel, S. Göktepe, P. Steimann, and E. Kuhl. Modeling and simulation of viscous electro-active polymers. *Eur. J. Mech. A-Solid*, 48:112, 2014. doi: 10.1016/j.euromechsol.2014.02.001.

[100] K. A. Khan, H. Wafai, and T. El Sayed. A variational constitutive framework for the nonlinear viscoelastic response of a dielectric elastomer. *Comput. Mech.*, 52:345, 2013. doi: 10.1007/s00466-012-0815-6.

[101] H. S. Park and T. D. Nguyen. Viscoelastic effects on electromechanical instabilities in dielectric elastomers. *Soft Matter*, 9:1031, 2013. doi: 10.1039/c2sm27375f.

[102] A. Büschel, S. Klinkel, and Werner Wagner. Dielectric elastomers – numerical modeling of nonlinear visco-electroelasticity. *Int. J. Numer. Meth. Engng.*, 93, 2013. doi: 10.1002/nme.4409.

[103] A. Ask, A. Menzel, and M. Ristinmaaa. Modelling of viscoelastic dielectric elastomers with deformation dependent electric properties. *Procedia IUTAM*, 12, 2015. doi: 10.1016/j.piutam.2014.12.015.

[104] J. Bergström and L. B. Hilbert. A constitutive model for predicting the large deformation thermomechanical behavior of fluoropolymers. *Mech. Mater.*, 37:899–913, 2003. doi: 10.1016/j.mechmat.2004.09.002.

[105] H. Godaba, Z. Zhang, U. Gupta, C.C. Foo, and J. Zhu. Dynamic pattern of wrinkles in a dielectric elastomer. *Soft Matter*, 2017. doi: 10.1039/c7sm00198c.

[106] J. W. Fox and N. C. Goulbourne. On the dynamic electromechanical loading of dielectric elastomer membranes. *J. Mech. Phys. Solids*, 56:2669, 2008. doi: 10.1016/j.jmps.2008.03.007.

[107] P. B. Gonçalves, D. Pamplona, P. B. C. Teixeira, R. L. C. Jerusalmi, I. A. Cestari, and A. A. Leirner. Dynamic non-linear behavior and stability of a ventricular assist device. *Int. J. Solids Struct.*, 40:5017, 2003. doi: 10.1016/S0020-7683(03)00252-X.

[108] X. Zhao and Z. Suo. Method to analyze electromechanical stability of dielectric elastomers. *Appl. Phys. Lett.*, 91, 2007. doi: 10.1063/1.2768641.

[109] X. Zhao, S. Koh, and Z. Suo. Nonequilibrium thermodynamics of dielectric elastomers. *Int. J. Appl. Mech.*, 3:203, 2011. doi: 10.1142/S1758825111000944.

[110] A. N. Norris. Comment on "Method to analyze electromechanical stability of dielectric elastomers". *Appl. Phys. Lett.*, 92, 2008. doi: 10.1063/1.2833688.

[111] J. Leng, L. Liu, Y. Liu, K. Yu, and S. Sun. Electromechanical stability of dielectric elastomer. *Appl. Phys. Lett.*, 94, 2009. doi: 10.1063/1.3138153.

[112] R. Díaz-Calleja, E. Riande, and M. J. Sanchis. On electromechanical stability of dielectric elastomers. *Appl. Phys. Lett.*, 93, 2008. doi: 10.1063/1.2972124.

[113] B. Xu, R. Mueller, M. Klassen, and D. Gross. On electromechanical stability analysis of dielectric elastomer actuators. *Appl. Phys. Letters*, 97, 2010. doi: 10.1063/1.3504702.

[114] J. Zhu, S. Cai, and Z. Suo. Resonant behavior of a membrane of a dielectric elastomer. *Int J. Solid Struct.*, 47, 2010. doi: 10.1016/j.ijsolstr.2010.08.008.

[115] S. Rudykh, K. Bhattacharya, and G. deBotton. Snap-through actuation of thick-wall electroactive balloons. *Int J. Nonlinear Mech.*, 47, 2012. doi: 10.1016/j.ijnonlinmec.2011.05.006.

[116] T. Li, C. Keplinger, R. Baumgartner, S. Bauer, W. Yang, and Z. Suo. Giant voltage-induced deformation in dielectric elastomers near the verge of snap-through instability. *J. Mech. Phys. Solids*, 61, 2013. doi: 10.1016/j.jmps.2012.09.006.

[117] D. De Tommasi, G. Puglisi, G. Saccomandi, and G. Zurlo. Pull-in and wrinkling instabilities of electroactive dielectric actuators. *J. Phys. D: Appl. Phys.*, 43(32), 2010. doi: 10.1088/0022-3727/43/32/325501.

[118] Z. Suo, X. Zhao, and W. H. Greene. A nonlinear field theory of deformable dielectrics. *J. Mech. Phys. Solids*, 43:467–486, 2008.

[119] A. L. Dorfmann and R. W. Ogden. Nonlinear electroelastostatics: Incremental equations and stability. *Int J. Eng. Sci*, 48, 2008. doi: doi:10.1016/j.ijengsci.2008.06.005.

[120] A. L. Dorfmann and R. W. Ogden. Instabilities of an electroelastic plate. *Int J. Eng. Sci*, 77, 2014. doi: 10.1016/j.ijengsci.2013.12.007.

[121] S. Rudykh and G. Bhattacharya, K. deBotton. Stability of anisotropic electroactive polymers with application to layered media. *ZAMP*, 62, 2011. doi: 10.1007/s00033-011-0136-1.

[122] S. Rudykh and G. Bhattacharya, K. deBotton. Multiscale instabilities in soft heterogeneous dielectric elastomers. *P. Roy. Soc. A*, 2013. doi: 10.1098/rspa.2013.0618.

[123] N. J. Hoff. Buckling and stability,. *J. Roy. Aero. Soc.*, 58, 1954.

[124] N. J. Hoff. Creep buckling. *Aero. Quart.*, 7:1–51, 1956.

[125] G.N. Rabotnov and Shesterikov. Creep stability of colums and plates. *J. Mech. Phys. Solids*, 6: 27–34, 1957.

[126] Hans Ziegler. Die Stabilitätskriterien der Elastomechanik. *Ing. Arch.*, 20:49–56, 1952.

[127] N. J. Hoff. Dynamic stability of structures. Technical report, Aeronautics and Astronautics Stanford University, 1965.

[128] B. Xu, R. Mueller, A. Theis, M. Klassen, and D. Gross. Dynamic analysis of dielectric elastomer actuators. *Appl. Phys. Lett.*, 100:112903–1, 2012. doi: 10.1063/1.3694267.

[129] J. Zhu. Instabilitiy in nonlinear oscillation of dielectric elastomers. *J. Appl. Mech.*, 82, 2015. doi: 10.1115/1.4030075.

[130] M. M. Joglekar. An energy-based approach to extract the dynamic instability parameters of dielectric elastomer actuators. *J. Appl. Mech.*, 81, 2014. doi: 10.1115/1.4027925.

[131] M. M. Joglekar. Dynamic-instability parameters of dielectric elastomer actuators with equal biaxial prestress. *AIAA J.*, 53(10), 2015. doi: 10.2514/1.J054062.

[132] D. Eder-Goy, Y. Zhao, and B-X. Xu. Dynamic pull-in instability of a prestretched viscous dielectric elastomer under electric loading. *Acta. Mech.*, 2017. doi: 10.1007/s00707-017-1930-4.

[133] P. Steinmann, M. Hossain, and G. Possart. Hyperelastic models for rubber-like materials: consistent tangent operators and suitability for treloar's data. *Arch. Appl. Mech.*, 82(9):1183–1217, 2012. doi: 10.1007/s00419-012-0610-z.

[134] M. C. Boyce and Arruda E. M. Constitutive models for rubberelasticity, a review. *Rubber Chem. Technol.*, 73, 1992.

[135] S. Reese. A micromechanically motivated material model for the thermo-viscoelastic material behaviour of rubber-like polymers. *Int. J. Plast.*, 19:909–940, 2003.

[136] R.L. Taylor, K.S. Pister, and G.L. Goudreau. Thermomechanical analysis of viscoelastic solids. *Int. J. Numer. Meth. Eng.*, 2:45–59, 1970.

[137] J.C. Simo. On a fully three dimensional finite-strain viscoelastic damage model: Formulation and computational aspects. *Comput. Methods Appl. Mech. Eng.*, 60:153–173, 1987.

[138] H. Kaliske, M.and Rothert. Formulation and implementation of three-dimensional viscoelasticity at small and finite strains. *Comput. Mech.*, 19:228–239, 1997. doi: 10.1007/s004660050171.

[139] S. Govindjee and S. Reese. A presentation and comparison of two large deformation viscoelastic models. *J. Eng. Mater. Technol.*, 119:251–255, 1997.

[140] M.S. Green and A.V. Tobolsky. A new approach to the theory of relaxing polymeric media. *J. Chem. Phys.*, 14:80–92, 1946.

[141] J. Lubliner. A model of rubber viscoelasticity. *Mech. Research Comm.*, 12:93–99, 1985.

[142] F. Sidoroff. Un modèle viscoélastique non linéaire avec configuration intermédiairess. *J. Mec.*, 13:679–713, 1974.

[143] P. Saxena, D. K. Vu, and P. Steinmann. On rate-dependent dissipation effects in electro-elasticity. *Int J. Nonlinear Mech.*, 62:1–11, 2014. doi: 10.1016/j.ijnonlinmec.2014.02.002.

[144] J. Lubliner. *Plasticity Theory*. Dover, 2008.

[145] R. Faria. A direct current piezoelectric effect in fluorinated ethylene-propylene copolymer due to space charge. *Appl. Phys. Lett.*, 69, 1996. doi: 10.1063/1.117639.

[146] N. Nepal, R. A. P. Altafim, and A. Mellinger. Space charge deposition in tubular channel ferroelectrets: A combined fluorescence imaging/limm study with finite element analysis. *J. Appl. Phys.*, 121, 2017. doi: 10.1063/1.4990280.

[147] David Roylance. *Engineering Viscoelasticity*. Department of Materials Science and Engineering, MIT, Cambrige, MA 02139, 2001.

[148] B-X. Xu, H. von Seggern, S. Zhukov, and D. Gross. Continuum modeling of charging process and piezoelectricity of ferroelectrets. *J. Appl. Phys.*, 114:094103, 2013. doi: 10.1063/1.4819441.

[149] D. Gross and B-X. Xu. Micromechanical modelling of cellular ferroelectrets by using internal variables. *Proc. IUTAM*, 12:62–72, 2015. doi: doi: 10.1016/j.piutam.2014.12.008.

[150] B-X. Xu, H. von Seggern, S. Zhukov, and D. Gross. An internal-variable-based interface model for the charging process of ferroelectrets. *Eur. J. Mech. A Solids*, 48:97–111, 2014. doi: 10.1016/j.euromechsol.2013.12.011.

[151] J. Betten. *Kontinuumsmechanik*. Springer Berlin Heidelberg, 1993. doi: 10.1007/978-3-662-08168-6.

[152] J.C. Simo and T.J.R Hughes. *Computational inelasticity*. Springer, 1998.

[153] S. Zhukov, Fedosov. S., and H. von Seggern. Piezoelectrets from sandwiched porous polytetrafluoroethylene (eptfe) films: influence of porosity and geometry on charging properties. *J. Phys. D*, 44:105501, 2011. doi: 10.1088/0022-3727/44/10/105501.

[154] H. von Seggern, H., S. Zhukov, and S. Fedosov. Poling dynamics and thermal stability of FEP/ePTFE/FEP sandwiches. *IEEE Trans. Dielectr. Electr. Insul.*, 17(4):1070–9878, 2010. doi: 10.1109/TDEI.2010.5539675.

[155] M. Wegener, W. Wirges, R. Gerhard-Multhaupt, M. Dansachmüller, R. Schwödiauer, S. Bauer-Gogonea, S Bauer, M. Paajanen, H. Minkkinen, and J. Raukola. Controlled inflation of voids in cellular polymer ferroelectrets: Optimizing electromechanical transducer properties. *Appl. Phys. Lett.*, 84(3), 2004. doi: 10.1063/1.1641171.

[156] E. Tuncer. Numerical calculations of effective elastic properties of two cellular structures. *J. Phys. D: Appl. Phys.*, 38:497–503, 2005. doi: 10.1088/0022-3727/38/3/023.

[157] E. Tuncer, M. Wegener, and R. Gerhard-Multhaupt. Modeling electro-mechanical properties of layered electrets: Application of the finite-element method. *J. Electrostat.*, 63:21–35, 2005. doi: 10.1016/j.elstat.2004.06.002.

[158] Y-P. Wan and Z. Zhong. Effective electromechanical properties of cellular piezoelectret: A review. *Acta. Mech. Sin.*, 28::951–959, 2012. doi: 10.1007/s10409-012-0125-4.

[159] Y-P. Wan, L. Xie, and Z. Zhong. Micromechanical prediction the effective elctromechanical properties of cellular ferroelectrets. *J. Appl. Phys.*, 108:054101, 2010. doi: 10.1063/1.3481435.

[160] S. Zhukov, D. Eder-Goy, C. Biethan, S. Fedosov, B-X. Xu, and H. von Seggern. Tubular fluoropolymer arrays with high piezoelectric response. *Smart Mater. Struct.*, 27(1), 2017. doi: 10.1088/1361-665X/aa9a63.

[161] W. Künstler, Z. Xia, T. Weinhold, A. Pucher, and R. Gerhard-Multhaupt. Piezoelectricity of porous polytetrafluoroethylene single- and multiple-film electrets containing high charge densities of both polarities. *Appl. Phys. A*, 70(1):5–8, 2000. doi: 10.1007/s003390050002.

[162] X. Qiu, W. Wirges, and R. Gerhard. Thermal poling of ferroelectrets: How does the gas temperature influence dielectric barrier discharges in cavities? *Appl. Phys. Lett.*, 108:252901, 2016. doi: 10.1063/1.4954263.

[163] R.A.P. Altafim, X. Qiu, W. Wirges, R. Gerhard, R. A. C. Altafim, H. C. Basso, W. Jenninger, and J. Wagner. Template-based fluoroethylenepropylene piezoelectrets with tubular channels for transducer applications. *J. Appl. Phys.*, 106:014106, 2009. doi: 10.1063/1.3159039.

[164] X. Zhang, J. Hillenbrand, and G. M. Sessler. Ferroelectrets with improved thermal stability made from fused fluorocarbon layers. *J. Appl. Phys.*, 101:054114, 2006. doi: 10.1063/1.2562413.

[165] Z. Sun, X. Zhang, Z. Xia, X. Qiu, W. Wirges, R. Gerhard, C. Zeng, C. Zhang, and B. Wang. Polarization and piezoelectricity in polymer films with artificial void structure. *Appl. Phys. A*, 105:197–205, 2011. doi: 10.1007/s00339-011-6481-2.

[166] S. Houliara and S.A. Karamanos. Buckling and post-buckling of long pressurized elastic thin-walled tubes under in-plane bending. *Int. J. Non Linear Mech.*, 41:491–511, 2004. doi: 10.1016/j.ijnonlinmec.2005.11.002.

[167] S. P. Timoshenko and J. N. Goodier. *Theory of Elasticity*. McGraw-Hill, 1970.

[168] A. J. Durelli, V. J. Parks, and T.L. Chen. Stress and finite-strain analysis of a circular ring under diametral compression. *Experimental Mechanics*, 9(5):210–214, 1969. doi: 10.1007/BF02326537.

[169] J.B. Flaherty, J.E.and Keller and S.I. Rubinow. Post buckling behavior of elastic tubes and rings with opposite sides in contact*. *Siam J. Appl. Math.*, 23(4), 1972. doi: 10.1137/0123047.

[170] URL `http://www.rjchase.com`.

[171] S. Zhukov, D. Eder-Goy, S. Fedosov, B-X. Xu, and H. von Seggern. Analytical prediction of the piezoelectric d33 response of fluoropolymer arrays with tubular air channels. *Sci. Rep.*, 8, 2018. doi: 10.1038/s41598-018-22918-1.

[172] J. Zhang, H. Chen, J. Sheng, Liu L., Y. Wang, and S. Jia. Dynamic performance of dissipative dielectric elastomers under alternating mechanical load. *Appl. Phys. A*, 116:59, 2014. doi: 10.1007/s00339-013-8092-6.

[173] A. Mohebbi, F. Mighri, A. Ajji, and D. Rodrigue. Cellular polymer ferroelectret: A review on their development and their piezoelectric properties. *Adv. Polym. Tech.*, 0(0):21686, 2016. doi: 10.1002/adv.21686.

[174] J. Sheng, H. Chen, L. Liu, J. Zhang, Y. Wang, and S. Jia. Dynamic electromechanical performance of viscoelastic dielectric elastomers. *Appl. Phys. Letters*, 114, 2013. doi: 10.1063/1.4823861.

A Appendix

A.1 Point charge/continuous charge

$$\begin{aligned}\varrho(\mathbf{x}) &= \int\limits_{V_{\text{ref}}} d^3x'\,\varrho(\mathbf{x}')\delta(\mathbf{x}-\mathbf{x}')\,dV = \sum_{i=1}^{N}\int\limits_{V_i} d^3x'\,\varrho(\mathbf{x}')\delta(\mathbf{x}-\mathbf{x}')\,dV \\ &\approx \sum_{i=1}^{N}\left(\int\limits_{V_i} d^3x'\,\varrho(\mathbf{x}')\right)\delta(\mathbf{x}-\mathbf{x}_i)\,dV = \sum_{i=1}^{N} q_i\,\delta(\mathbf{x}-\mathbf{x}_i)\end{aligned} \tag{A.1.1}$$

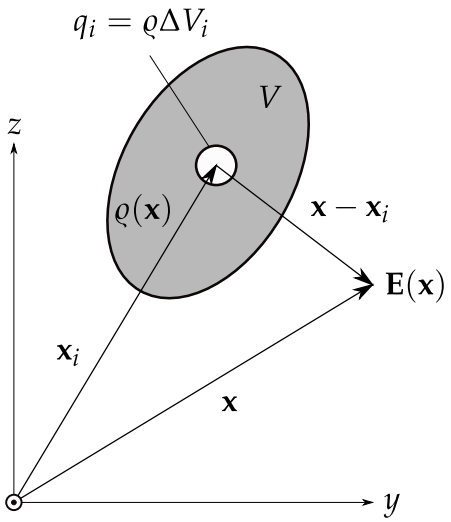

A.2 Glass transition in amorphous polymers

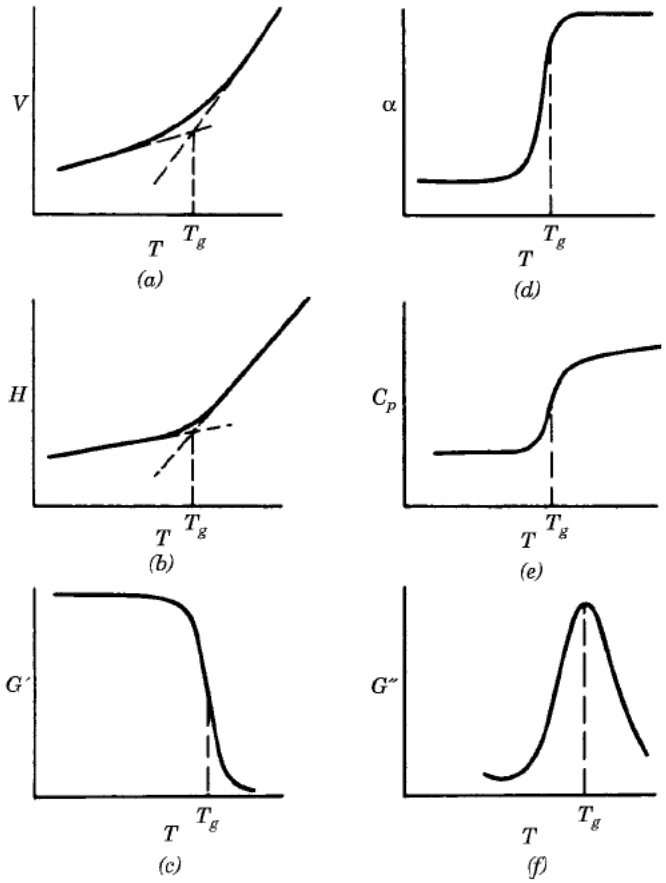

A.3 Indices

Indices:

$i, j, k, l, m = 1, 2, 3$
$p, q = 1, ..., 6$
$a, b = 1, ..., 8$
$c = 1, ..., 4$

A.4 Material parameters

	Mat.1 [174]	Mat.2 (based on measured data, uniaxial tests) [109]	
ρ	1.2×10^3		$\mathrm{kg/m^3}$
μ	1.6966×10^4	2.28×10^4	Pa
β	2.333	2.85	[-]
T	72.377	200	s
ϵ	4.758×10^{-11}	4.1595×10^{-11}	As/Vm

A.5 Shape functions

Shape functions for a 8-node trilinear volume element [90], a is the index for the regarded node

$$N_a(\xi,\eta,\zeta) = \frac{1}{8}(1+\xi_a\xi)(1+\eta_a\eta)(1+\zeta_a\zeta), \tag{A.5.1}$$

where a is the specific node. For the discretisation of the real and the virtual displacements and the real an the virtual potential follows

$$\begin{aligned} u_i^h(\xi,\eta,\zeta) &= \sum_{a=1}^{8} N_a(\xi,\eta,\zeta)u_{ia} \\ \delta u_i^h(\xi,\eta,\zeta) &= \sum_{a=1}^{8} N_a(\xi,\eta,\zeta)\delta u_{ia} \\ \phi^h(\xi,\eta,\zeta) &= \sum_{a=1}^{8} N_a(\xi,\eta,\zeta)\phi_a \\ \delta\phi^h(\xi,\eta,\zeta) &= \sum_{a=1}^{8} N_a(\xi,\eta,\zeta)\delta\phi_a. \end{aligned} \tag{A.5.2}$$

Due to the isoparametric concept the geometry is discretised by using the same shape functions. Therefore

$$\begin{aligned} x(\xi,\eta,\zeta) &= \sum_{a=1}^{8} N_a(\xi,\eta,\zeta)x_a \\ y(\xi,\eta,\zeta) &= \sum_{a=1}^{8} N_a(\xi,\eta,\zeta)y_a \\ z(\xi,\eta,\zeta) &= \sum_{a=1}^{8} N_a(\xi,\eta,\zeta)z_a, \end{aligned} \tag{A.5.3}$$

$x_a(x,y,z)$ are the nodal coordinates in the physical space.

A.6 Stiffness matrix bulk material, small deformation

Matrices of the derivatives of shape functions in Voigt notation

$$B^{\mathrm{M}}_{pi\,a} = \begin{bmatrix} N_{a,1} & 0 & 0 \\ 0 & N_{a,2} & 0 \\ 0 & 0 & N_{a,3} \\ 0 & N_{a,3} & N_{a,2} \\ N_{a,3} & 0 & N_{a,1} \\ N_{a,2} & N_{a,1} & 0 \end{bmatrix}, \; B^{\mathrm{E}}_{i\,a} = \begin{bmatrix} N_{a,1} \\ N_{a,2} \\ N_{a,3} \end{bmatrix}. \tag{A.6.1}$$

Discretised partial derivatives

$$\frac{\partial}{\partial \phi_b} = \frac{\partial}{\partial E_i}\frac{\partial E_i}{\partial \phi_b} = -\frac{\partial}{\partial E_i} B^{\mathrm{E}}_{i\,b}. \tag{A.6.2}$$

Submatrices of material tangents for the bulk material

$$\begin{aligned} k^{\mathrm{EE}}_{ab} &= -\frac{\partial R^{\mathrm{E}}_a}{\partial \phi_b} = \int_{\Omega^h} (B^{\mathrm{E}}_{i\,a})^T \frac{\partial D_i}{\partial E_j}\frac{\partial E_j}{\partial \phi_b}\, d\boldsymbol{v} = -\int_{\Omega^h} (B^{\mathrm{E}}_{i\,a})^T \frac{\partial D_i}{\partial E_j} B^{\mathrm{E}}_{j\,b}\, d\boldsymbol{v}, \\ k^{\mathrm{ME}}_{i\,ab} &= -\frac{\partial R^{\mathrm{M}}_{i\,a}}{\partial \phi_b} = \int_{\Omega^h} B^{\mathrm{M}}_{ip\,a} \frac{\partial \sigma^{\mathrm{E}}_p}{\partial E_k}\frac{\partial E_k}{\partial \phi_b}\, d\boldsymbol{v} = -\int_{\Omega^h} B^{\mathrm{M}}_{ip\,a} \frac{\partial \sigma^{\mathrm{E}}_p}{\partial E_k} B^{\mathrm{E}}_{k\,b}\, d\boldsymbol{v}, \\ k^{\mathrm{MM}}_{ij\,ab} &= -\frac{\partial R^{\mathrm{M}}_{i\,a}}{\partial u_{j\,b}} = \int_{\Omega^h} B^{\mathrm{M}}_{ip\,a} \frac{\partial \sigma_p}{\partial \epsilon_q}\frac{\partial \epsilon_q}{\partial u_{j\,b}}\, d\boldsymbol{v} = \int_{\Omega^h} B^{\mathrm{M}}_{ip\,a} \frac{\partial \sigma_p}{\partial \epsilon_q} B^{\mathrm{M}}_{qj\,b}\, d\boldsymbol{v}. \end{aligned} \tag{A.6.3}$$

The partial derivatives in Voigt notation are

$$\begin{aligned} \frac{\partial D_i}{\partial E_j} =& \epsilon_0 \begin{bmatrix} 1+\frac{\chi_s}{J} & 0 & 0 \\ 0 & 1+\frac{\chi_s}{J} & 0 \\ 0 & 0 & 1+\frac{\chi_s}{J} \end{bmatrix}, \\ \frac{\partial \sigma^{\mathrm{E}}_p}{\partial E_k} =& \epsilon_0 \begin{bmatrix} E_1[2(1+\frac{\chi_s}{J})-1] & -E_2 & -E_3 \\ -E_1 & E_2[2(1+\frac{\chi_s}{J})-1] & -E_3 \\ -E_1 & -E_2 & E_3[2(1+\frac{\chi_s}{J})-1] \\ 0 & 2E_3(1+\frac{\chi_s}{J}) & 2E_2(1+\frac{\chi_s}{J}) \\ 2E_3(1+\frac{\chi_s}{J}) & 0 & 2E_1(1+\frac{\chi_s}{J}) \\ 2E_2(1+\frac{\chi_s}{J}) & 2E_1(1+\frac{\chi_s}{J}) & 0 \end{bmatrix}, \\ \frac{\partial \sigma_p}{\partial \epsilon_q} =& \tilde{C}_{pq} = \begin{bmatrix} \lambda+2\mu & \lambda & \lambda & 0 & 0 & 0 \\ \lambda & \lambda+2\mu & \lambda & 0 & 0 & 0 \\ \lambda & \lambda & \lambda+2\mu & 0 & 0 & 0 \\ 0 & 0 & 0 & 2\mu & 0 & 0 \\ 0 & 0 & 0 & 0 & 2\mu & 0 \\ 0 & 0 & 0 & 0 & 0 & 2\mu \end{bmatrix}. \end{aligned} \tag{A.6.4}$$

A.7 Stiffness matrix interface, small deformation

Discretised partial derivatives

$$\frac{\partial E_{\mathrm{m}}}{\partial \phi_b} = \frac{\partial(-E_i m_i)}{\partial \phi_b} = B^{\mathrm{E}}_{i\,b} m_i. \tag{A.7.1}$$

Submatrices of material tangents for the interface in the parameter space

$$\begin{aligned}
\hat{k}^{\mathrm{EE}}_{cb} &= -\frac{\partial \hat{R}^{\mathrm{E}}_c}{\partial \phi_b} = +\int\limits_{\partial\Omega_{p^h_q}} N_c \frac{\partial p}{\partial E_{\mathrm{m}}} \frac{\partial E_{\mathrm{m}}}{\partial \phi_b} ||\boldsymbol{\chi}^h_{,\xi} \times \boldsymbol{\chi}^h_{,\eta}||\, d\xi d\eta = -\int\limits_{\partial\Omega_{p^h_q}} N_c \frac{\partial p}{\partial E_{\mathrm{m}}} B^{\mathrm{E}}_{i\,b} \left[\boldsymbol{\chi}^h_{,\xi} \times \boldsymbol{\chi}^h_{,\eta}\right]_i d\xi d\eta, \\
\hat{k}^{\mathrm{ME}}_{i\,cb} &= -\frac{\partial \hat{R}^{\mathrm{M}}_{i\,c}}{\partial \phi_b} = +\int\limits_{\partial\Omega_{p^h_t}} N_c \frac{\partial t^C}{\partial E_{\mathrm{m}}} \frac{\partial E_{\mathrm{m}}}{\partial \phi_b} \left[\boldsymbol{\chi}^h_{,\xi} \times \boldsymbol{\chi}^h_{,\eta}\right]_i d\xi d\eta \\
&= -\int\limits_{\partial\Omega_{p^h_t}} N_c \frac{\partial t^C}{\partial E_{\mathrm{m}}} B^{\mathrm{E}}_{i\,b} n_i \left[\boldsymbol{\chi}^h_{,\xi} \times \boldsymbol{\chi}^h_{,\eta}\right]_i d\xi d\eta.
\end{aligned} \tag{A.7.2}$$

With the definition of p using Eq. (5.1.19) follows

$$\frac{\partial p}{\partial E_{\mathrm{m}}} = \epsilon_0 \epsilon_{r_2}. \tag{A.7.3}$$

The stiffness matrix entry $\hat{k}^{\mathrm{EE}}_{cb}$ is only considered if the constraint condition is violated, that means p is changed. The derivative of t^{C} with respect to E_{m} is case sensitive. If the constraint condition is not violated, it follows from Eq. (5.1.19)

$$E_{r_1} = \left(\frac{-p + \epsilon_0 \epsilon_{r_2} E_{\mathrm{m}}}{\epsilon_0 \epsilon_{r_1}}\right), \tag{A.7.4}$$

$$t^{\mathrm{C}} = \frac{1}{2}|p\, E_{r_1}|, \tag{A.7.5}$$

$$\frac{\partial t^{\mathrm{C}}}{\partial E_{\mathrm{m}}} = \frac{1}{2}|p|\frac{\epsilon_{r_2}}{\epsilon_{r_1}}. \tag{A.7.6}$$

For a violation the following is valid

$$t^{\mathrm{C}} = \frac{1}{2}|p\, E_{r_1}|, \tag{A.7.7}$$

$$\frac{\partial t^{\mathrm{C}}}{\partial E_{\mathrm{m}}} = \frac{1}{2}|\epsilon_0 \epsilon_{r_2}| E_{\mathrm{B}}. \tag{A.7.8}$$

A.8 Stiffness matrix bulk material, large deformation

Submatrices of material tangents for the bulk material: Matrices of the derivatives of shape functions in Voigt notation [92] S.124

$$B^{\mathrm{M}}_{pi\ a} = \begin{bmatrix} F_{11}N_{a,1} & F_{21}N_{a,1} & F_{31}N_{a,1} \\ F_{12}N_{a,2} & F_{22}N_{a,2} & F_{32}N_{a,2} \\ F_{13}N_{a,3} & F_{23}N_{a,3} & F_{33}N_{a,3} \\ F_{12}N_{a,3} + F_{13}N_{a,2} & F_{22}N_{a,3} + F_{23}N_{a,2} & F_{32}N_{a,3} + F_{33}N_{a,2} \\ F_{11}N_{a,3} + F_{13}N_{a,1} & F_{21}N_{a,3} + F_{23}N_{a,1} & F_{31}N_{a,3} + F_{33}N_{a,1} \\ F_{11}N_{a,2} + F_{12}N_{a,1} & F_{21}N_{a,2} + F_{22}N_{a,1} & F_{31}N_{a,2} + F_{32}N_{a,1} \end{bmatrix}, \; B^{\mathrm{E}}_{i\ a} = \begin{bmatrix} N_{a,1} \\ N_{a,2} \\ N_{a,3} \end{bmatrix}. \tag{A.8.1}$$

Discretised partial derivatives

$$\frac{\partial}{\partial \phi_b} = \frac{\partial}{\partial E_{0_i}} \frac{\partial E_{0_i}}{\partial \phi_b} = -\frac{\partial}{\partial E_{0_i}} B^{\mathrm{E}}_{i\ b}, \tag{A.8.2}$$

$$\frac{\partial}{\partial u_{i\ b}} = \frac{\partial}{\partial C_{kl}} \frac{\partial C_{kl}}{\partial u_{i\ b}} = 2\frac{\partial}{\partial C_{kl}} B^{\mathrm{M}}_{pi\ b}, \text{with } kl \to p. \tag{A.8.3}$$

Submatrices of material tangents for the bulk material

$$\begin{aligned}
k^{\mathrm{EE}}_{ab} &= -\frac{\partial R^{\mathrm{E}}_a}{\partial \phi_b} = -\int_{\Omega^h_0} (B^{\mathrm{E}}_{i\ a})^T \frac{\partial D_{0_i}}{\partial E_{0_j}} B^{\mathrm{E}}_{j\ b}\, dV, \\
k^{\mathrm{EM}}_{i\ ab} &= -\frac{\partial R^{\mathrm{E}}_a}{\partial u_{i\ b}} = \int_{\Omega^h_0} (B^{\mathrm{E}}_{j\ a})^T \frac{\partial D_{0_j}}{\partial u_{i\ b}}\, dV = 2\int_{\Omega^h_0} (B^{\mathrm{E}}_{j\ a})^T \frac{\partial D_{0_j}}{\partial C_{p\ b}} B^{\mathrm{M}}_{pi\ b}\, dV, \\
k^{\mathrm{ME}}_{i\ ab} &= -\frac{\partial R^{\mathrm{M}}_{i\ a}}{\partial \phi_b} = \int_{\Omega^h_0} B^{\mathrm{M}}_{ip\ a} \frac{\partial S^{\mathrm{E}}_p}{\partial E_{0_k}} \frac{\partial E_{0_k}}{\partial \phi_b}\, dV = -\int_{\Omega^h_0} B^{\mathrm{M}}_{ip\ a} \frac{\partial S^{\mathrm{E}}_p}{\partial E_{0_k}} B^{\mathrm{E}}_{k\ b}\, dV, \\
k^{\mathrm{MM}}_{ij\ ab} &= -\frac{\partial R^{\mathrm{M}}_{i\ a}}{\partial u_{j\ b}} = \int_{\Omega^h_0} \frac{\partial \left[B^{\mathrm{M}}_{ip\ a}(S_p + S^{\mathrm{E}}_p)\right]}{\partial u_{j\ b}}\, dV = \int_{\Omega^h_0} \frac{\partial B^{\mathrm{M}}_{ip\ a}}{\partial u_{j\ b}}(S_p + S^{\mathrm{E}}_p)\, dV + \int_{\Omega^h_0} B^{\mathrm{M}}_{ip\ a} \frac{\partial (S_p + S^{\mathrm{E}}_p)}{\partial u_{j\ b}}\, dV \\
&= \tilde{G}_{ik\ ab} + 2\int_{\Omega^h_0} B^{\mathrm{M}}_{ip\ a} \frac{\partial (S_p + S^{\mathrm{E}}_p)}{\partial C_{q\ b}} B^{\mathrm{M}}_{qj\ b}\, dV.
\end{aligned} \tag{A.8.4}$$

$\tilde{G}_{ik\ ab}$ is the geometric part of stiffness matrix that considers the geometric non-linearity in the displacement. The partial derivatives were derived by using the index notation. Afterwards a contradiction of indices to gain the Voigt notation was performed.

The partial derivatives were calculated as follows

$$
\begin{aligned}
\frac{\partial D_{0_i}}{\partial E_j} =& \epsilon_0 (J + \chi_s) C^{-1}_{ij}, \\
\frac{\partial D_{0_i}}{\partial C_{ij}} =& \epsilon_0 \frac{1}{2} J C^{-1}_{ij} C^{-1}_{kl} E_l \\
&+ \epsilon_0 (J + \chi_s)(-C_{ki} C^{-1}_{jl}) E_l, \\
\frac{\partial S^{\mathrm{E}}_{ij}}{\partial E_k} =& C^{-1}_{ik} \epsilon_0 (J + \chi_s) C^{-1}_{jq} E_q \\
&+ C^{-1}_{ip} E_p \epsilon_0 (J + \chi_s) C^{-1}_{jk} \\
&- \frac{1}{2} \epsilon_0 J C^{-1}_{kn} E_n C^{-1}_{ij} \\
&- \frac{1}{2} \epsilon_0 J E_{\mathrm{m}} C^{-1}_{mk} C^{-1}_{ij}, \\
\frac{\partial S^{\mathrm{E}}_{ij}}{\partial C_{kl}} =& \frac{1}{2} \tilde{C}_{ijkl}, \\
\frac{\partial S^{\mathrm{E}}_{ij}}{\partial C_{kl}} =& (-C^{-1}_{ik} C^{-1}_{lp} E_p) \epsilon_0 (J + \chi_s) C^{-1}_{jq} E_q \\
&+ C^{-1}_{ip} E_p \left[\frac{1}{2} \epsilon_0 J C^{-1}_{kl} C^{-1}_{jq} E_q + \epsilon_0 (J + \chi_s)(-C^{-1}_{jk} C^{-1}_{lq}) E_q \right] \\
&- \frac{1}{4} \epsilon_0 J C^{-1}_{kl} E_{\mathrm{m}} C^{-1}_{mn} E_n C^{-1}_{ij} \\
&- \frac{1}{2} \epsilon_0 J E_{\mathrm{m}} C^{-1}_{mn} E_n (-C^{-1}_{ik} C^{-1}_{lj}) \\
&- \frac{1}{2} \epsilon_0 J E_{\mathrm{m}} (-C^{-1}_{mk} C^{-1}_{ln}) E_n C^{-1}_{ij}.
\end{aligned}
\tag{A.8.5}
$$

A.9 Stiffness matrix interface, large deformation

Discretised partial derivatives

$$\begin{aligned}
\frac{\partial E_{\mathrm{m}}}{\partial \phi_b} &= -\left(F^{-1}_{ji}\frac{\partial E_{0_j}}{\partial \phi_b}\right) m_i = \left(F^{-1}_{ji} B^{\mathrm{E}}_{j\,b}\right) m_i, \\
\frac{\partial E_{\mathrm{m}}}{\partial u_{k\,b}} &= -\left(\frac{\partial F^{-1}_{ji}}{\partial u_{k\,b}} E_{0_j}\right) m_i - E_i \frac{\partial F_{ij}}{\partial u_{k\,b}} M_j, \\
\frac{\partial F_{ij}}{\partial u_{k\,b}} &= N_{b,j}\delta_{ik}.
\end{aligned} \tag{A.9.1}$$

Submatrices of material tangents for the interface in the parameter space

$$\begin{aligned}
\hat{k}^{\mathrm{EE}}_{cb} = -\frac{\partial \hat{R}^{\mathrm{E}}_c}{\partial \phi_b} &= + \int_{\partial\Omega^h_{p^h_q}} N_c \frac{\partial p}{\partial E_{\mathrm{m}}} \frac{\partial E_{\mathrm{m}}}{\partial \phi_b} ||\boldsymbol{\chi}^h_{,\xi} \times \boldsymbol{\chi}^h_{,\eta}||\, d\xi d\eta, \\
\hat{k}^{\mathrm{EM}}_{i\,cb} = -\frac{\partial \hat{R}^{\mathrm{E}}_c}{\partial u_{i\,b}} &= + \int_{\partial\Omega^h_{p^h_q}} N_c \frac{\partial p}{\partial E_{\mathrm{m}}} \frac{\partial E_{\mathrm{m}}}{\partial u_{i\,b}} ||\boldsymbol{\chi}^h_{,\xi} \times \boldsymbol{\chi}^h_{,\eta}||\, d\xi d\eta \\
&\quad + \int_{\partial\Omega^h_{p^h_q}} N_c\, p \left[N_{b,\xi}\bar{\mathbf{N}}_{,\eta} - N_{b,\eta}\bar{\mathbf{N}}_{,\xi}\right]_{ji} \tilde{N}^h_j\, ||\boldsymbol{\chi}^h_{,\xi} \times \boldsymbol{\chi}^h_{,\eta}||\, d\xi d\eta \\
&\quad + \int_{\partial\Omega^h_{p^h_q}} N_c\, p \tilde{N}^h_j \left[N_{b,\xi}\bar{\mathbf{N}}_{,\eta} - N_{b,\eta}\bar{\mathbf{N}}_{,\xi}\right]_{ji} ||\boldsymbol{\chi}^h_{,\xi} \times \boldsymbol{\chi}^h_{,\eta}||\, d\xi d\eta, \\
\hat{k}^{\mathrm{ME}}_{i\,cb} = -\frac{\partial \hat{R}^{\mathrm{M}}_{i\,c}}{\partial \phi_b} &= + \int_{\partial\Omega^h_{p^h_t}} N_c \frac{\partial t^C}{\partial E_{\mathrm{m}}} \frac{\partial E_{\mathrm{m}}}{\partial \phi_b} \tilde{N}^h_i\, d\xi d\eta, \\
\hat{k}^{\mathrm{MM}}_{ij\,cb} = -\frac{\partial \hat{R}^{\mathrm{M}}_{i\,c}}{\partial u_{j\,b}} &= + \int_{\partial\Omega^h_{p^h_t}} N_c \frac{\partial t^C}{\partial E_{\mathrm{m}}} \frac{\partial E_{\mathrm{m}}}{\partial u_{j\,b}} \tilde{N}^h_i\, d\xi d\eta \\
&\quad + \int_{\partial\Omega^h_{p^h_t}} N_c\, t^C \left[N_{b,\xi}\bar{\mathbf{N}}_{,\eta} - N_{b,\eta}\bar{\mathbf{N}}_{,\xi}\right]_{ij} d\xi d\eta.
\end{aligned} \tag{A.9.2}$$

A.10 Deviatoric part second order tensor

$\underline{t}$ is a second order tensor in the current configuration

$$\mathrm{dev}(\underline{t}) := \underline{t} - \frac{1}{3}\mathrm{tr}\,\underline{t}. \tag{A.10.1}$$

$\underline{T}$ is a second order tensor in the reference configuration

$$\mathrm{dev}(\underline{T}) := \underline{T} - \frac{1}{3}\mathrm{tr}\,\underline{T}. \tag{A.10.2}$$

A.11 Partial derivatives of stresses, split of deformation gradient

$$\begin{aligned}\Psi_{\text{vol}} =& K\frac{1}{8}\left[\left(C_{kl}-\delta_{kl}\delta_{kl}\right)\right]^2\\ =& K\frac{1}{8}\left(C_{kk}-3\right)^2\end{aligned} \tag{A.11.1}$$

$$\begin{aligned}2\frac{\partial\Psi_{\text{vol}}}{\partial C_{ij}} =& K\frac{1}{2}\left(C_{kk}-3\right)\frac{\partial C_{mm}}{\partial C_{ij}}\\ =& K\frac{1}{2}\left(C_{kk}-3\right)\delta_{mi}\delta_{mj}\\ =& K\frac{1}{2}\left(C_{kk}-3\right)\delta_{ij}\end{aligned} \tag{A.11.2}$$

$$\begin{aligned}\Psi_{\text{dev}} =& G\left[\frac{1}{4}\left(C_{kl}-\delta_{kl}\right)\left(C_{lm}-\delta_{lm}\right)\delta_{km}-\frac{1}{12}\left[\left(C_{kl}-\delta_{kl}\right)\delta_{kl}\right]^2\right]\\ =& G\left[\frac{1}{4}\left(C_{kl}-\delta_{kl}\right)\left(C_{lk}-\delta_{lk}\right)-\frac{1}{12}\left(C_{kk}-3\right)^2\right]\end{aligned} \tag{A.11.3}$$

$$\begin{aligned}2\frac{\partial\Psi_{\text{dev}}}{\partial C_{ij}} =& G\left[\frac{1}{2}\left[\frac{\partial C_{kl}}{\partial C_{ij}}\left(C_{lk}-\delta_{lk}\right)+\frac{\partial C_{lk}}{\partial C_{ij}}\left(C_{kl}-\delta_{kl}\right)\right]-\frac{1}{3}\left(C_{kk}-3\right)\frac{\partial C_{mm}}{\partial C_{ij}}\right]\\ =& G\left[\frac{1}{2}\left[\delta_{ki}\delta_{lj}\left(C_{lk}-\delta_{lk}\right)+\delta_{li}\delta_{kj}\left(C_{kl}-\delta_{kl}\right)\right]-\frac{1}{3}\left(C_{kk}-3\right)\delta_{mi}\delta_{mj}\right]\\ =& G\left[\frac{1}{2}\left[\left(C_{ji}-\delta_{ji}\right)+\left(C_{ji}-\delta_{ji}\right)\right]-\frac{1}{3}\left(C_{kk}-3\right)\delta_{ij}\right]\\ =& G\left[\left(C_{ji}-\delta_{ji}\right)-\frac{1}{3}\left(C_{kk}-3\right)\delta_{ij}\right]\end{aligned} \tag{A.11.4}$$

$$\begin{aligned}\Psi_{\text{v}_\alpha} =& \beta_\alpha\, G\left[\frac{1}{4}\left[\left(C_{ij}{C_{\text{v}_\alpha}jk}^{-1}-\delta_{ik}\right)\left(C_{kl}{C_{\text{v}_\alpha}lm}^{-1}-\delta_{km}\right)\delta_{im}\right]-\frac{1}{12}\left[\left(C_{ij}{C_{\text{v}_\alpha}jk}^{-1}-\delta_{ik}\right)\delta_{ik}\right]^2\right]\\ =& \beta_\alpha\, G\left[\frac{1}{4}\left[\left(C_{ij}{C_{\text{v}_\alpha}jk}^{-1}-\delta_{ik}\right)\left(C_{kl}{C_{\text{v}_\alpha}li}^{-1}-\delta_{ki}\right)-\frac{1}{12}\left(C_{ij}{C_{\text{v}_\alpha}ji}^{-1}-3\right)^2\right]\end{aligned} \tag{A.11.5}$$

$$
\begin{aligned}
2\frac{\partial \Psi_{\mathrm{v}_\alpha}}{\partial C_{pq}} =& \beta_\alpha\, G \Bigg[\frac{1}{2} \left[\frac{\partial C_{ij}}{\partial C_{pq}} {C_{\mathrm{v}_\alpha jk}}^{-1} \left(C_{kl} {C_{\mathrm{v}_\alpha li}}^{-1} - \delta_{ki} \right) + \frac{\partial C_{kl}}{\partial C_{pq}} {C_{\mathrm{v}_\alpha li}}^{-1} \left(C_{ij} {C_{\mathrm{v}_\alpha jk}}^{-1} - \delta_{ik} \right) \right] \\
& - \frac{1}{3} \frac{\partial C_{mj}}{\partial C_{pq}} {C_{\mathrm{v}_\alpha jm}}^{-1} \left(C_{kn} {C_{\mathrm{v}_\alpha nk}}^{-1} - 3 \right) \Bigg] \\
=& \beta_\alpha\, G \Bigg[\frac{1}{2} \left[\delta_{ip}\delta_{jq} {C_{\mathrm{v}_\alpha jk}}^{-1} \left(C_{kl} {C_{\mathrm{v}_\alpha li}}^{-1} - \delta_{ki} \right) + \delta_{kp}\delta_{lq} {C_{\mathrm{v}_\alpha li}}^{-1} \left(C_{ij} {C_{\mathrm{v}_\alpha jk}}^{-1} - \delta_{ik} \right) \right] \\
& - \frac{1}{3} \delta_{mp}\delta_{jq} {C_{\mathrm{v}_\alpha jm}}^{-1} \left(C_{kn} {C_{\mathrm{v}_\alpha nk}}^{-1} - 3 \right) \Bigg] \\
=& \beta_\alpha\, G \Bigg[\frac{1}{2} \left[{C_{\mathrm{v}_\alpha qk}}^{-1} \left(C_{kl} {C_{\mathrm{v}_\alpha lp}}^{-1} - \delta_{kp} \right) + {C_{\mathrm{v}_\alpha qi}}^{-1} \left(C_{ij} {C_{\mathrm{v}_\alpha jp}}^{-1} - \delta_{ip} \right) \right] \\
& - \frac{1}{3} {C_{\mathrm{v}_\alpha qp}}^{-1} \left(C_{kn} {C_{\mathrm{v}_\alpha nk}}^{-1} - 3 \right) \Bigg]
\end{aligned}
\tag{A.11.6}
$$

A.12 Partial derivatives of material tangents, split of deformation gradient

$$
\begin{aligned}
2\frac{\partial S_{\mathrm{vol}_{ij}}}{\partial C_{pq}} =& K\frac{\partial\left(C_{kk}\delta_{ij}-3\delta_{ij}\right)}{\partial C_{pq}} \\
=& K\left(\delta_{kp}\delta_{kq}\delta_{ij}\right)=K\delta_{pq}\delta_{ij}
\end{aligned}
\tag{A.12.1}
$$

$$
\begin{aligned}
2\frac{\partial S_{\mathrm{dev}_{ij}}}{\partial C_{pq}} =& 2G\frac{\partial\left[\left(C_{ji}-\delta_{ji}\right)-\frac{1}{3}\left(C_{kk}-3\right)\delta_{ij}\right]}{\partial C_{pq}} \\
=& 2G\left[\frac{\partial C_{ji}}{\partial C_{pq}}-\frac{1}{3}\frac{\partial C_{kk}}{\partial C_{pq}}\delta_{ij}\right] \\
=& 2G\left[\delta_{jp}\delta_{iq}-\frac{1}{3}\delta_{pq}\delta_{ij}\right]
\end{aligned}
\tag{A.12.2}
$$

$$
\begin{aligned}
2\frac{\partial S_{\mathrm{v}_\alpha ij}}{\partial C_{pq}} =& 2\beta G\frac{\partial\left[{C_{\mathrm{v}_\alpha jk}}^{-1}\left(C_{kl}{C_{\mathrm{v}_\alpha li}}^{-1}-\delta_{ki}\right)-\frac{1}{3}\left(C_{kj}{C_{\mathrm{v}_\alpha jk}}^{-1}-3\right){C_{\mathrm{v}_\alpha ji}}^{-1}\right]}{\partial C_{pq}} \\
=& 2\beta G\left[{C_{\mathrm{v}_\alpha jk}}^{-1}\left(\frac{\partial C_{kl}}{\partial C_{pq}}{C_{\mathrm{v}_\alpha li}}^{-1}\right)-\frac{1}{3}\frac{C_{kj}}{C_{pq}}{C_{\mathrm{v}_\alpha jk}}^{-1}{C_{\mathrm{v}_\alpha ji}}^{-1}\right] \\
=& 2\beta G\left[{C_{\mathrm{v}_\alpha jk}}^{-1}\delta_{kp}\delta_{lq}{C_{\mathrm{v}_\alpha li}}^{-1}-\frac{1}{3}\delta_{kp}\delta_{jq}{C_{\mathrm{v}_\alpha jk}}^{-1}{C_{\mathrm{v}_\alpha ji}}^{-1}\right] \\
=& 2\beta G\left[{C_{\mathrm{v}_\alpha jp}}^{-1}{C_{\mathrm{v}_\alpha qi}}^{-1}-\frac{1}{3}{C_{\mathrm{v}_\alpha qp}}^{-1}{C_{\mathrm{v}_\alpha ji}}^{-1}\right]
\end{aligned}
\tag{A.12.3}
$$